INVESTIGATIONS INTO THE GENERALITY OF METALLOINSERTION AT DNA DEFECTS

Thesis by

Brian Matthew Zeglis

In Partial Fulfillment of the Requirements

for the Degree of

Doctor of Philosophy in Chemistry

California Institute of Technology

Pasadena, California

2010

(Defended June 10, 2009)

ACKNOWLEDGEMENTS

First and foremost, I would like to thank my research advisor, Professor Jacqueline K. Barton. It has been a privilege to spend the last four years in your laboratory. Truth be told, it is nearly impossible for me to distill my appreciation down to only a few sentences. I am grateful for your knowledge, guidance, patience, and encouragement. I am especially indebted to the freedom you have given me to pursue my own ideas. Furthermore, I appreciate and admire your ability to bring together and support such an intelligent and talented group of people. The enthusiasm, optimism, and creativity with which you approach science have been and will continue to be constant sources of inspiration.

I would also like to express my appreciation for my faculty committee, Professors Harry Gray, Steve Mayo, and Doug Rees. Your guidance, suggestions, and support have been invaluable along the way.

I am tremendously indebted to Maureen Renta for her tireless work, invaluable advice, and tremendous patience.

A large number of Barton laboratory members, past and present, deserve a tremendous amount of thanks for their help and support: Jon Hart, for teaching me the right way to do things and being a great friend; Brian Jackson, for pioneering the study of mismatch-specific metalloinsertors; Irv Lau, for making the corner a fun place to work; Eddie Merino, for teaching me everything I know about molecular biology and being a superb role model; Mi Hee Lim, for her synthetic expertise and engaging conversations; Hang Song, for her advice, enthusiasm, and patience (I know sitting next to me isn't

always easy); Joey Genereux, for conversations that are always one part stimulating and one part hilarious; Cindy Puckett, for her willingness to help and her generous glass-ware loan policies; and Jennifer Boland, for her enthusiasm and dedication. I would also like to thank Benjamin Elias, Takanori Tanaki, Makiko Tanaka, Natalie Muren, Christine Romano, and Eric Olmon for helpful discussions, teaching me new things, and making the laboratory a fantastic place to work.

I would also particularly like to thank Jens Kaiser and Valerie Pierre, whose hard work and guidance made the crystallography project possible.

I would especially like to express my gratitude for four people that have made my time at Caltech particularly special. Pam Sontz, I am deeply thankful for your positive outlook, steadfast friendship, and sense of humor. Marisa Buzzeo, I cannot thank you enough for the kindness and support you have given me and the conversations and the laughter we have shared. Russ Ernst, it has been a joy, privilege, and honor to have you as a friend and to work alongside you for the past four years. You have been a support in more ways and in more settings than I can count, spanning from the laboratory to the basketball court and everything in between. And, last but not least, Paul Lee. It is hard to know where to begin; suffice it to say that I don't know anyone else who would walk with me from Pasadena to the Pacific Ocean. Friends like you do not come around often.

Finally, I would like to thank my family: Mom, Dad, Mark, Julie, Allison, Jeff, Samantha, Austin, Herman, Sophia, Sydney, Aidan, and Alex. Words cannot describe how grateful I am for your support and love, particularly over the past five years. This thesis is dedicated to you.

ABSTRACT

Metalloinsertors are substitutionally inert, octahedral transition metal complexes that bind to thermodynamically destabilized mismatched sites in duplex DNA with high affinity and selectivity. The complexes approach DNA from the minor groove, eject the mismatched bases into the major groove, and replace the displaced bases in the helical π-stack with their own sterically expansive ligands. Herein, we describe a series of five investigations aimed at elucidating the generality of metalloinsertion at DNA defects.

In an effort to develop a diagnostic for mismatched DNA, a bifunctional, mismatch-specific conjugate with rhodium metalloinsertor and fluorophore subunits has been constructed. A proof-of-concept conjugate was successfully produced that displays an almost fourfold fluorescence enhancement in the presence of mismatched versus matched DNA.

To investigate the range of metal complexes capable of mismatch-specific metalloinsertion, a ruthenium bisdipyridyl complex bearing the heptacyclic eilatin ligand has been synthesized and characterized. Electrophoresis competition experiments illustrate that the complex does display mismatch-preferential, though not necessarily mismatch-selective, binding.

To probe the generality of metalloinsertion at other common thermodynamically destabilized DNA defects, the binding of rhodium metalloinsertors at abasic sites and single base bulges has been studied. It was determined that metalloinsertors bind abasic sites with high affinity and specificity, without regard to the identity of the unpaired base and with little dependence on the sequence context of the defect. Single base bulge

recognition proved more elusive, with both the identity of the unpaired base and the sequence context influencing recognition.

To determine the structural generality of metalloinsertion, single crystal X-ray diffraction was employed to determine the structure of Δ-$Rh(bpy)_2(chrysi)^{3+}$ bound to an oligonucleotide duplex containing two A•A mismatches. Two structures were obtained at < 2 Å resolution, and each provides an archetypical picture of metalloinsertion: the bulky rhodium complex inserts into the mismatched site from the minor groove, ejecting the mismatched bases and replacing the displaced base pair with its own sterically expansive ligand.

Finally, two mismatch-specific conjugates have been designed for chemotherapeutic applications: a metalloinsertor-oxaliplatin conjugate for the selective delivery of platinum chemotherapeutics to mismatch repair deficient cells and a metalloinsertor-Auger electron emitter conjugate for the selective irradiation of mismatch-containing DNA.

TABLE OF CONTENTS

LIST OF FIGURES AND TABLES

CHAPTER 1: INTRODUCTION[ζ]

1.1: METAL COMPLEXES AS DNA-BINDING AGENTS

DNA is the library of the cell, simultaneously storing and dispensing the information required for life. Molecules that can bind and react with specific DNA sites provide a means to access this cellular information. Over the past fifty years, small molecules that bind DNA have shown significant promise as diagnostic probes, reactive agents, and therapeutics. Naturally, a tremendous amount of attention has focused on the design of organic DNA-binding agents.[1] However, over the past twenty five years, some of this focus has shifted to another class of non-covalent DNA-binding agents: substitutionally inert, octahedral transition metal complexes.

At first glance, transition metal complexes seem an odd choice for DNA molecular recognition agents. Certainly, Nature herself offers very little precedent in this regard. With few exceptions, biological transition metals are confined to coordination sites in proteins or cofactors, not in discrete, free-standing coordination complexes.[2] Further, the cell generally employs organic moieties for the binding and recognition of DNA. Yet despite the lack of many natural examples, transition metal complexes offer two singular advantages as DNA-binding agents. First and foremost, coordination complexes offer a uniquely modular system. The metal center acts in essence as an anchor, holding in place a rigid, three-dimensional scaffold of ligands that can, if desired, bear recognition elements. The DNA-binding and recognition properties of a complex can thus be varied relatively easily via the facile interchange of ligands. Second, transition metal centers benefit from rich photophysical and electrochemical properties,

[ζ] Adapted from Zeglis, B. M.; Pierre, V. P.; Barton, J. K. Metallointercalators and metalloinsertors. *Chem. Comm.* **2007**, 4565−4579.

thus extending their utility far beyond that of mere passive molecular recognition agents. Indeed, these characteristics have allowed metal complexes to be used in a wide range of capacities, from fluorescent markers to DNA foot-printing agents to electrochemical probes.[3]

With very few exceptions, non-covalent, DNA-binding metal complexes share a set of fundamental characteristics. All are kinetically inert, a requisite trait due to the paramount importance of stability. Indeed, the vast majority of complexes are d^6 octahedral or d^8 square-planar. In addition, most exhibit a rigid or mostly rigid three-dimensional structure, an important facet considering that in many cases undue fluxionality could negate recognition. Moreover, the stereochemistry of a complex can dramatically influence recognition and specificity, an understandable notion given the chirality of the DNA target. Finally, most of the complexes that have been prepared are, by design, photochemically or photophysically active, properties that confer tremendous utility in probing metal complex-DNA interactions and nucleic acid structure.

1.2: A STRUCTURAL INTRODUCTION TO DNA

Before embarking on our discussion of the binding and recognition of DNA, a brief description of the structure of DNA may be helpful. DNA is a polymer of individual deoxyribonucleotides, each of which is composed of a heterocyclic base, a ribose sugar, and a phosphate (**Figure 1.1**). The most common form of DNA (and the form addressed almost exclusively in these pages) is the double-stranded, anti-parallel, right-handed double helix termed B-DNA, though the less common, right-handed A-form and left-handed Z-form will occasionally enter the discussion.[4, 5] Within the polynucleotide

assembly, the heterocyclic bases – adenine (A), guanine (G), cytosine (C), and thymine (T) – are bound to the sugars in an *anti* orientation with a disposition perpendicular to the helical axis. The base pairs collectively form a central π-stack that runs parallel to the helical axis between the two strands of the sugar-phosphate backbone. Each base forms hydrogen bonds with its complement on the opposite, anti-parallel strand, adenine with thymine and cytosine with guanine. The rise per base is 3.4 Å, and there are ten base pairs per helical turn. Surrounding the central base stack, the polyanionic sugar-phosphate backbone forms two distinct grooves, a wide major groove and a narrow minor groove. All of these structural characteristics can and have been exploited for molecular recognition.

1.3: EARLY WORK ON DNA-BINDING METAL COMPLEXES

The earliest research into the interactions between metals and DNA focused almost exclusively on the binding strength and location of metal-aquo ions, both those with and without biological significance.[6] Perhaps as a result of these studies, the potential utility of metal-DNA interactions was realized early on. For example, melting temperature measurements for DNA in the presence of each of the first row transition metal ions were obtained to assess which metal ions stabilize or destabilize the duplex,[7] and the use of uranyl-bound nucleosides was investigated as a possible tool for electron microscopy-based DNA sequence determination.[8] Moreover, studies of the binding of mercury to non-thiolated and thiolated guanosine residues also further portended the

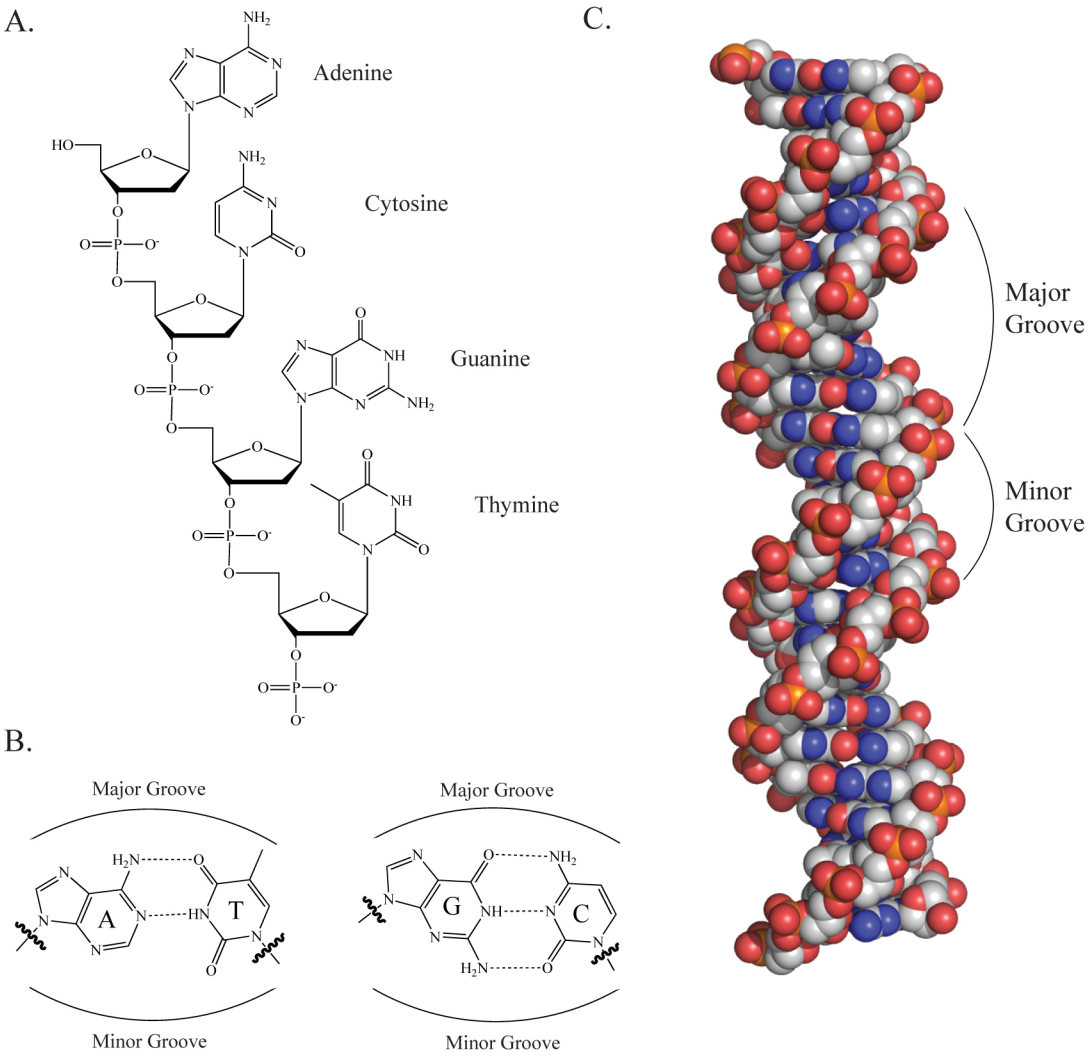

Figure 1.1: Deoxyribonucleic Acid. (A) Structures of the 4 natural DNA bases attached to the sugar phosphate backbone. (B) The Watson-Crick base pairs with major and minor grooves illustrated. (C) Model of double-stranded, B-form DNA. The major and minor grooves are indicated. Carbon, oxygen, nitrogen, and phosphorus atoms are grey, red, blue, and orange, respectively.

growing interest in metals as DNA probes.[9] Importantly, these studies all focused upon the coordination of metal ions to DNA and as such employed either aquo-ions or complexes with open coordination sites. Our interest, however, is in the non-covalent binding of coordinatively saturated metal complexes to DNA. With respect to this area, clues suggesting the interaction of inert metal complexes and DNA were evident as early as the 1950s, most notably in F.P. Dwyer's work on the biological activity of metal polypyridyl complexes.[10] Simple tris(chelate) complexes of Ru(II) and Ni(II) were found to have antiviral and bacteriostatic activities, in some cases with stereoselective biological activity **(Figure 1.2)**.

It was not until the mid-1970s, however, that a progenitor non-covalent DNA-binding complex was prepared by S. J. Lippard and co-workers.[11] During their work on the binding of metals to thiolated bases, it was observed that the planar complex Pt(2,2',2"-terpyridine)$(Cl)^+$ induced a spectral shift for 4-thiouridine in the presence of tRNA. Follow up studies, this time using Pt(terpyridine)$(SCH_2CH_2OH)^+$ to eliminate the labile coordination site, employed a variety of techniques to establish the intercalative binding mode of the complex with DNA. X-ray fiber diffraction patterns provided further evidence for intercalation, revealing a periodicity of one platinum unit every 10 angstroms (every other base pair) and a partial un-winding of the phosphate backbone.[12] Subsequent investigations expanded the family of intercalators to include other complexes with planar heterocyclic ligands, Pt(bpy)$(en)^{2+}$ and Pt(phen)$(en)^{2+}$, established binding constants in the realm of 10^4–10^5 M^{-1} for the family with DNA base pairs, and probed the effects of sequence context and ionic strength on intercalation.[13]

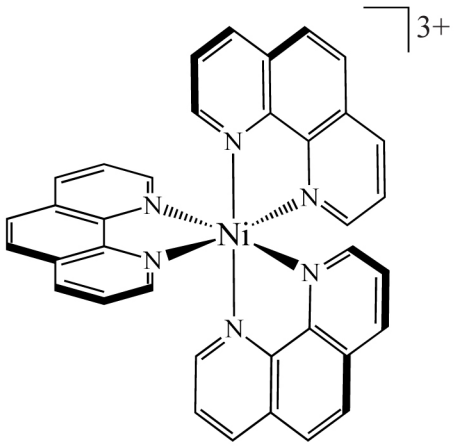

Δ–[Ni(phen)$_3$]$^{2+}$

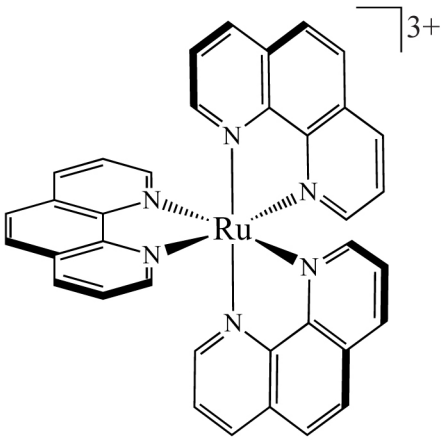

Δ–[Ru(phen)$_3$]$^{2+}$

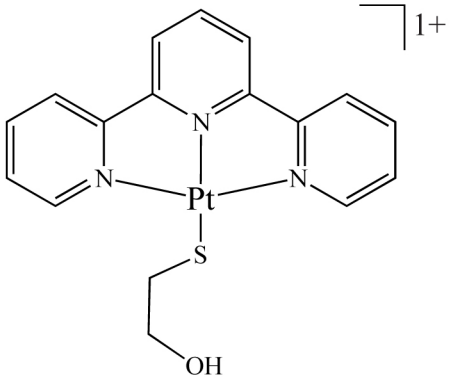

[Pt(terpy)(SCH$_2$CH$_2$OH)]$^+$

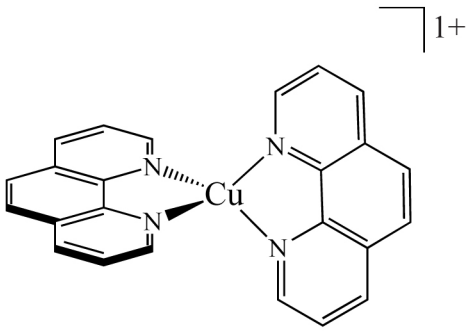

[Cu(phen)$_2$]$^+$

Figure 1.2: Examples of early DNA-binding metal complexes. (Clockwise from top left): Δ-Ni(phen)$_3^{2+}$, Δ-Ru(phen)$_3^{2+}$, Cu(phen)$_2^+$, Pt(terpy)(SCH$_2$CH$_2$OH)$^+$

Just as Lippard's platinum complexes laid the groundwork for future research on intercalative binding, the study of another complex, $Cu(phen)_2^+$, in the lab of D. S. Sigman during the late 1970s and early 1980s unearthed the rich chemistry of groove-binding metal complexes.[14] The complex was serendipitously discovered to degrade DNA during investigations into the inhibition of *E. coli* DNA polymerase by 1,10-phenanthroline, and it was soon learned that the DNA cleavage reaction was oxygen-dependent.[15] Product isolation and analysis led to a proposed mechanism that suggested minor-groove binding by $Cu(phen)_2^+$ formed *in situ*, a hypothesis later confirmed through elegant labeling experiments.[16, 17] Additional reactivity studies revealed that the complex binds and cleaves not only B-form duplex DNA but also A-form DNA, RNA, and other folded nucleic acid structures.[18]

1.4: NATURE'S EXAMPLE: FE-BLEOMYCIN

It is important to address, at least briefly, Nature's lone example of a non-covalent DNA-binding metal complex: metallobleomycin. First isolated from *Streptomyces verticillus* in the late 1960s, bleomycins are a widely-studied family of glycopeptide antibiotics that have been used successfully in the treatment of some forms of cancer.[19] The structure of bleomycins can be broken down into three domains: a metal-binding domain containing a pyrimidine moiety and five nitrogen atoms for octahedral metal coordination, a peptide linker region bearing a disaccharide side-chain, and a bithiazole unit with an appended, positively charged tail (**Figure 1.3**). While the metal-binding

A.

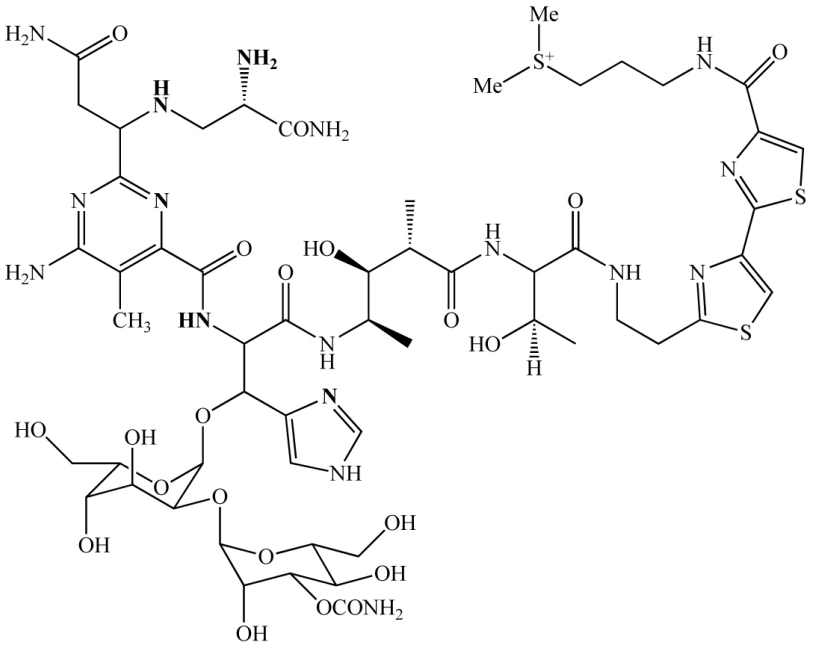

B.

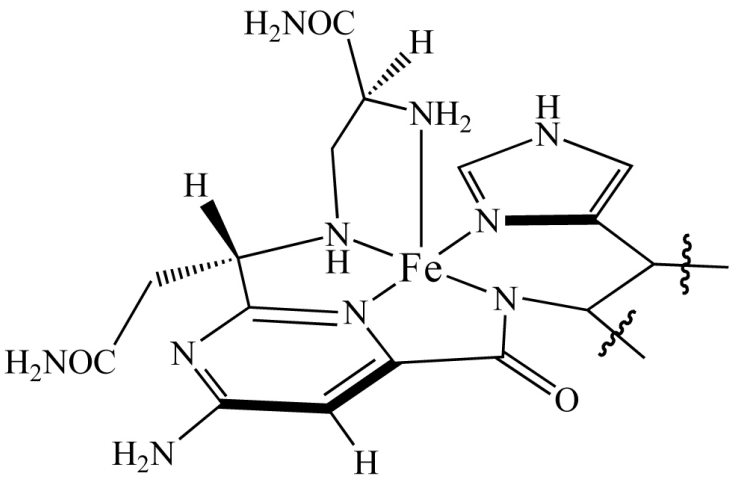

Figure 1.3: Bleomycin. Structures of (A) apo-bleomycin A_2 with coordinating nitrogens in bold and (B) the Fe coordination environment of bleomycin

region can coordinate a variety of metals, including Zn(II), Cu(II), and Co(III), the majority of research has focused on Fe-bleomycin complexes.[20] Significantly, exposure of the Fe bleomycin complex to oxygen and a reductant leads to the formation of activated bleomycin, a species that can, in turn, affect both single-stranded and double-stranded DNA cleavage via 4'-hydrogen atom abstraction by a high valent Fe-oxo species.

Metallobleomycins bind DNA via the minor groove, though neither affinity nor specificity is particularly high. Over the past twenty years, extensive synthetic and spectroscopic studies have helped elucidate the contribution of each structural moiety to DNA-binding and reactivity.[20] The bithiazole subunit and positively-charged tail are considered to play the most important roles in DNA-binding. The charge of the cationic tail is generally agreed to provide electrostatic impetus for binding. The role of the bithiazole, however, is subject to considerably more debate. And while the bulk of the evidence suggests that this moiety intercalates between base-pairs neighboring the binding site of the complex[21, 22], others have suggested that the bithiazole interacts with the DNA primarily in the minor groove.[23] To continue, hydrogen-bonding of the pyrimidine moiety in the metal-binding region is thought to help confer 5'-G-Py-3' cleavage selectivity.[24] The definitive roles of the linker region and disaccharide have proven more subtle and elusive, with the linker region likely of conformational importance and the disaccharide having been assigned roles ranging from DNA binding to metal chelation to cellular uptake and localization.

Finally, it is also both interesting and important to note that metallobleomycins, unlike many of the metal complexes discussed below, are exquisitely sensitive to

structural changes, for attempts to alter any of the domains have been met with dramatically reduced binding and cleavage efficiencies.[20]

1.5: TRIS(PHENANTHROLINE) COMPLEXES

The earliest work on the DNA-binding of octahedral metal centers focused on tris(phenanthroline) complexes of ruthenium, cobalt, zinc, and nickel.[25–30] Extensive photophysical and NMR experiments suggested that these complexes bound to DNA via two distinct modes: (a) hydrophobic interactions in the minor groove and (b) partial intercalation of a phenanthroline ligand from the major groove. Perhaps more important than the discovery of these dual binding modes, however, was the revelation these complexes provided regarding the importance of chirality in the binding of octahedral metal complexes to DNA. [31] In the case of $Ru(phen)_3^{2+}$, for example, the Δ-enantiomer is preferred in the intercalative binding mode, while the complementary Λ-enantiomer is favored in the minor groove binding mode (**Figure 1.4**). In subsequent years, it was discovered that metal centers bearing more sterically demanding phenanthroline ligand derivatives, such as diphenylphenanthroline (DIP), display even more dramatic chiral discrimination. Luminescence and hypochromism assays have revealed enantioselective binding on the part of $Ru(DIP)_3^{2+}$: the Δ-enantiomer binds enantiospecifically to right-handed B-DNA, while the Λ-enantiomer binds only to left-handed Z-DNA.[32] This enantiospecificity has been exploited to map left-handed Z-DNA sites in supercoiled plasmids using Λ-$Co(phen)_3^{3+}$.[33] Indeed, the trend in enantiomeric selectivity for octahedral tris(chelate) complexes — matching the symmetry of the

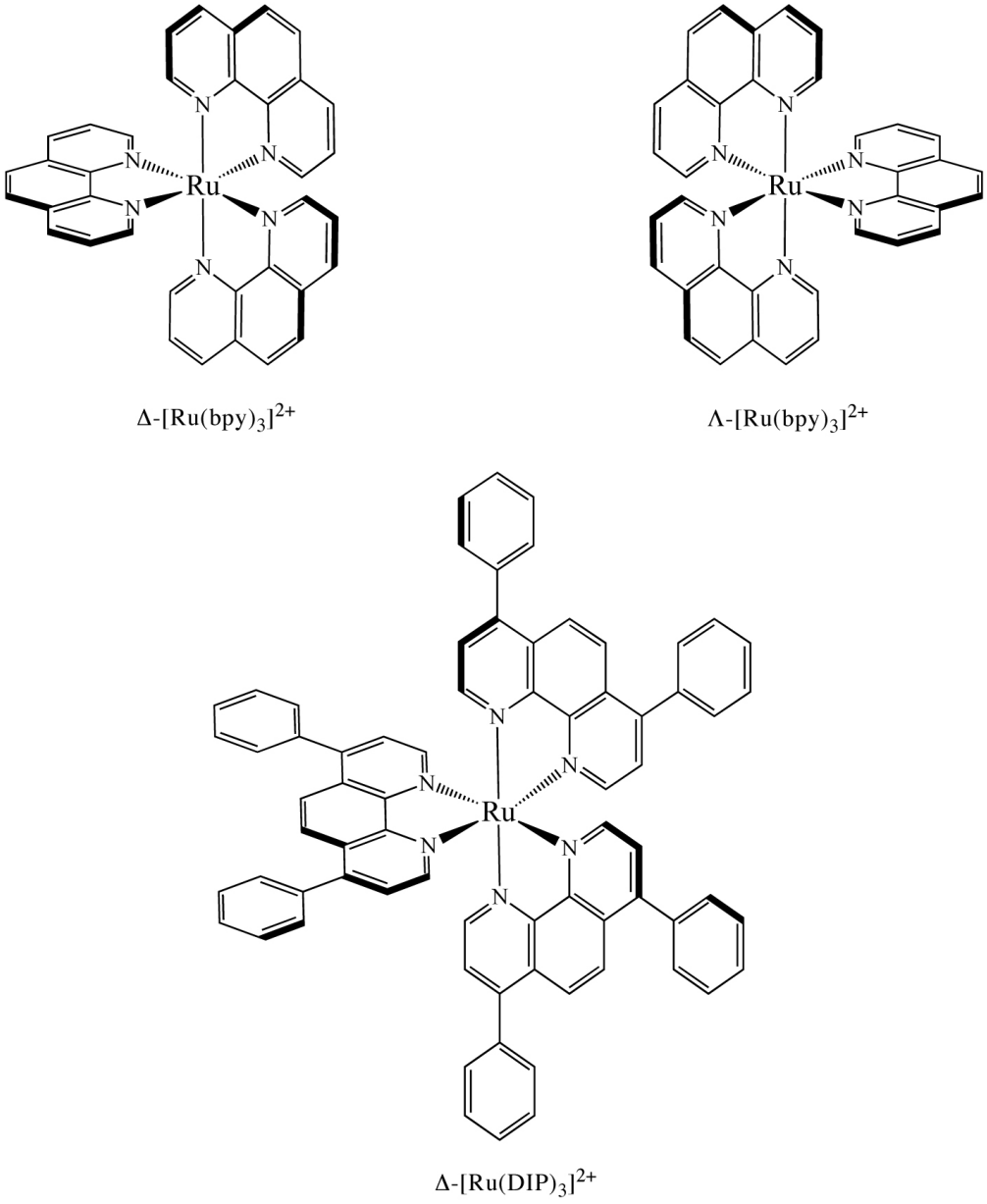

Figure 1.4: Ruthenium tris(phenanthroline) complexes

complex to that of DNA helix — has repeatedly and consistently been observed for non-covalent DNA-binding complexes developed in the years since these initial discoveries.[34]

These earliest tris(phenanthroline) complexes do not, of course, represent the only examples of complexes that bind DNA via the minor or major grooves. The extensively studied $Cu(phen)_2^+$, for instance, has been shown to bind DNA via the minor groove. Indeed, these particular groove-binding complexes not only bind DNA but also cleave the macromolecule in the presence of hydrogen peroxide.[16, 35] Metal complexes that bind in the groove have come a long way since these first studies and are now quite sophisticated. Turro, for instance, developed an artificial photonuclease by linking the metallogroove-binder $Ru(bpy)_3^{2+}$ to an electron-acceptor chain containing two viologen units. Interestingly, the chemistry of metallogroove-binders also extends to supramolecular self-assembly. Following the initial work of Lehn on the interaction and cleavage of DNA with a cuprous double-helicate,[36] Hannon and coworkers designed a triple-helicate capable of recognizing three-way junctions in DNA. This intricate recognition has recently been characterized by single crystal X-ray crystallography.[37–39]

1.6: METALLOINTERCALATORS

1.6.1: GENERAL ARCHITECTURE OF THE BINDING MODE

Intercalators are small organic molecules that unwind DNA in order to π-stack between two base pairs. Metallointercalators, it then follows, are metal complexes that bear at least one intercalating ligand. As their name suggests, these ligands, oriented parallel to the base pairs and protruding away from the metal center, can readily π-stack in the DNA duplex. Further, upon binding, the ligands behave as a stable anchor for the

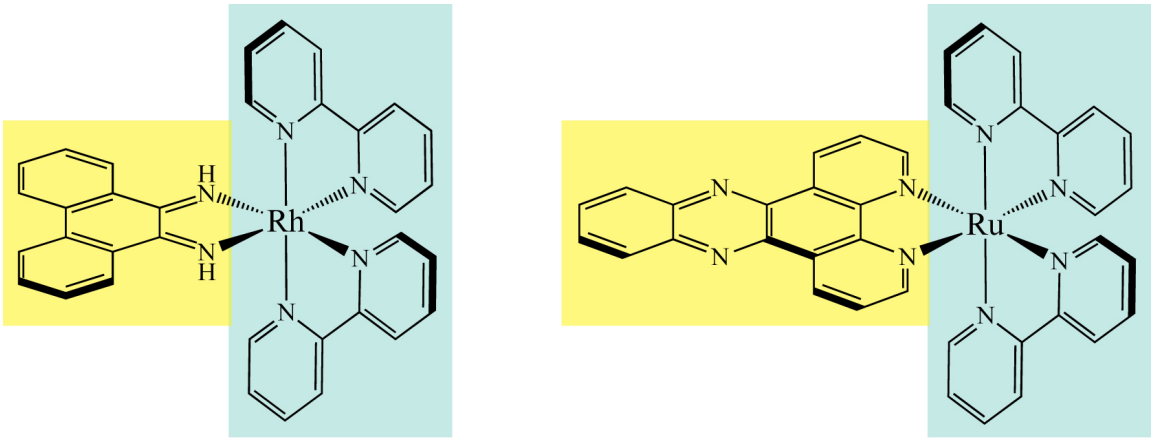

Δ–Rh(bpy)$_2$(phi)$^{3+}$ Δ–Ru(bpy)$_2$(dppz)$^{2+}$

Figure 1.5: Chemical structure of Δ-Rh(bpy)$_2$(phi)$^{3+}$ and Δ-Ru(bpy)$_2$(dppz)$^{2+}$. The intercalating ligands are highlighted in yellow, the ancillary ligands in cyan.

metal complex with respect to the double helix and direct the orientation of the ancillary ligands with respect to the DNA duplex. Two well-known examples of intercalating ligands are phi (9,10-phenanthrenequinone diimine) and dppz (dipyrido[3,2-*a*:2',3'-c]phenazine) (**Figure 1.5**).[3]

Ligand intercalation was first demonstrated by photophysical studies.[40–46] However, it was not until extensive NMR studies[47–50] and high resolution crystal structures had been performed that the structural details of this binding mode were properly illuminated.[51] Metallointercalators bind DNA from the major groove, with the intercalating ligand acting in effect as a new base pair. Intercalation results in a doubling of the rise and a widening of the major groove at the binding site. However, beyond these changes, this interaction distorts only minimally the structure of DNA. In the case of B-DNA, for example, the sugars and bases all maintain their original C_2'-endo and *anti* conformations, respectively. Indeed, only the opening of the phosphate angles, not any base or sugar perturbations, is necessary for intercalation.

Three crystal structures of a metal complex intercalated within a duplex, two containing an octahedral rhodium complex bound to an oligonucleotide and one a square-planar platinum complex bound to a paired dinucleotide, each demonstrate that intercalation occurs via the major groove.[51–53] Yet this may not always be the case. NMR studies indicate that metal complexes bearing dpq (dipyrido[2,2-*d*:2',3'-*f*]quinoxaline), a close analogue of dppz lacking the terminal aromatic ring, favor binding via the minor groove.[54–56] Whether this binding by the more hydrophobic complex involves one or two binding modes, perhaps groove-binding from the minor groove along with intercalation, still needs to be confirmed.

1.6.2: EXPLOITING THE PHOTOPHYSICAL AND PHOTOCHEMICAL PROPERTIES OF METALLOINTERCALATORS

By design, metallointercalators are coordinatively saturated and substitutionally inert such that no direct coordination with DNA bases occurs. Nonetheless, they often possess rich photochemistry and photophysics that have been advantageously exploited both to probe their interaction with DNA and interrogate further various aspects of nucleic acid chemistry. The most studied example is almost certainly the molecular light switch complex, $Ru(phen)_2(dppz)^{2+}$. This ruthenium complex shows solvatochromic luminescence in organic solutions. In aqueous solutions, however, it does not luminesce, because water deactivates the excited state through hydrogen-bonding with the endocyclic nitrogen atoms of the intercalating ligand. Remarkably, however, the complex luminesces brightly upon the addition of duplex DNA (**Figure 1.6**). In this case, the metal complex intercalates into the DNA, and the surrounding duplex prevents water from gaining access to the intercalated ligand; thus, the DNA has created a local region of aprotic 'solvent' in which the metal complex, now free of any hydrogen bonds, can display its characteristic luminescence.[40, 57, 58]

Although there has been some debate over the binding orientation of $Ru(phen)_2(dppz)^{2+}$, it has now been established that the complex intercalates via the major groove. Direct competition titrations against both a minor groove binder (distamycin) and a well-characterized major groove intercalator (Δ-α-Rh[(R,R)-Me_2trien](phi)$^{3+}$, *vide infra*) clearly demonstrate that the molecular light switch intercalates via the major groove with a slight preference for poly-d(AT) regions over poly-d(GC) tracts.[59] This conclusion is further supported by detailed NMR studies

performed with complexes bearing selectively deuterated dppz ligands. The latter investigations, together with the observed biexponential decay of the luminescence of $Ru(phen)_2(dppz)^{2+}$, further stipulate the presence of two populations with slightly different intercalation geometries. Many analogues of the popular molecular light switch, such as Nordén's threading bis-intercalators,[60, 61] have been synthesized, and their photophysics extensively studied and reviewed.[62]

While ruthenium and dppz-based metallointercalators have proven to be powerful molecular light switches for the detection of DNA, rhodium intercalators have been shown to be efficient agents for photoactivated DNA strand cleavage. Importantly, this reactivity enables us to mark directly the site of intercalation and to characterize the recognition properties of each metallointercalator. In this case, the most well studied examples are rhodium complexes employing the phi ligand as the intercalating ligand, such as $Rh(bpy)_2(phi)^{3+}$, $Rh(phen)_2(phi)^{3+}$, and $Rh(phi)_2(bpy)^{3+}$.[63]

In many cases, DNA cleavage is observed after irradiation of the DNA-bound metal complex at short wavelengths (313−325 nm). This irradiation prompts the formation of an intercalating ligand-based radical that abstracts a hydrogen atom from the adjacent deoxyribose ring.[43] Subsequent degradation of the resultant sugar radical then leads to direct DNA strand scission. In the absence of dioxygen, the photolysis of intercalated rhodium complexes leads to the formation of 3'- and 5'-phosphate terminated strands as well as a free base. To contrast, in the presence of dioxygen, direct strand cleavage still occurs but instead produces a 5'-phosphate terminated strand, a 3'-phosphoglycaldehyde terminated strand, and a base propenoic acid. These observations

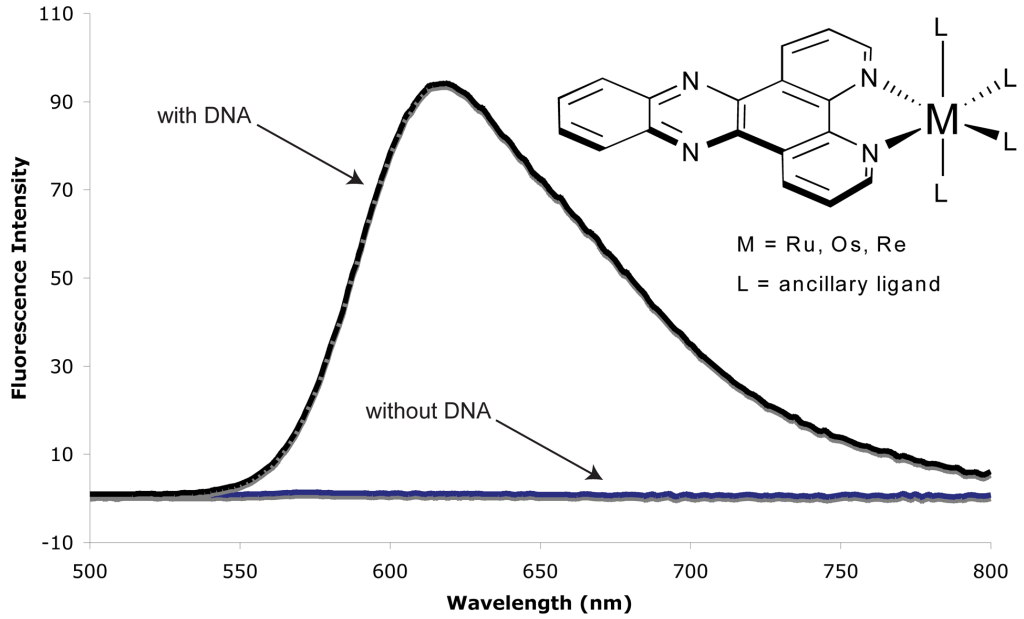

Figure 1.6: The light-switch effect of dppz-based metallointercalators. A representative plot of the effect of DNA on the luminescence of complexes of the general form $M(dppz)(L)_4$. In the absence of DNA (blue), hydrogen-bonding to the endocyclic phenazine nitrogens deactivates the fluorescence of the molecule. In the presence of DNA (black), the phenazine nitrogens are protected from water, and the complexes exhibit intense fluorescence.

are consistent with previously observed chemistry at the C3' position of the sugar. However, since both an atomic resolution crystal structure and a solution NMR study of a metal complex intercalated in the major groove of DNA indicate that the C2' hydrogen of the neighboring sugars is closer to the intercalating ligand than the C3' hydrogen, we propose that initially, the photoactivated intercalator abstracts the C2' hydrogen of the sugar. This is immediately followed by hydrogen migration to form the C3' radical and subsequent degradation of the sugar ring.

Although rhodium complexes efficiently cleave DNA upon photoactivation, many research laboratories find more convenient the use of DNA cleavage agents that cut without irradiation.[64] This can be achieved through the use of a bifunctional metallointercalator – peptide chimera in which a metal-coordinating peptide is covalently attached to $Rh(phi)_2(bpy')^{3+}$ (**Figure 1.7**). The metallointercalator acts as a targeting vector that delivers the metallopeptide to the sugar-phosphate backbone. The latter then promotes hydrolytic DNA strand cleavage.

In a similar approach, luminescent DNA cross-linking probes were achieved using bifunctional ruthenium intercalators conjugated to short peptides.[65] In the presence of an oxidative quencher, irradiation of the intercalated $Ru(phen)(bpy')(dppz)^{2+}$ oxidizes the oligonucleotide. The nearby tethered peptide then crosslinks with the oxidized site of the DNA. Although delivery of the peptide by the metallointercalator is not essential for cross-linking, this technique advantageously yields cross-linking adducts that are luminescent and are thus easily detectable. Furthermore, these cross-links may resemble those found *in vivo* under conditions of oxidative stress.

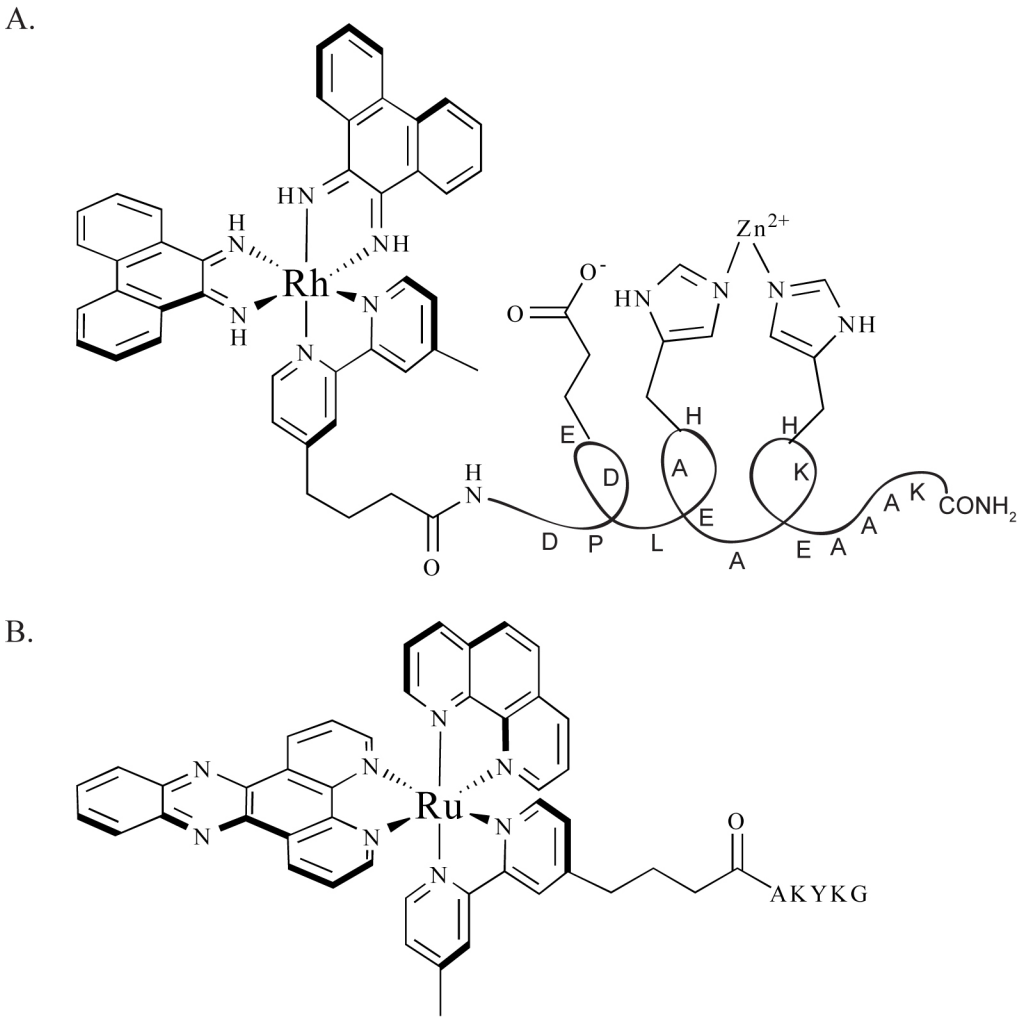

Figure 1.7: Metallointercalator conjugates. Chemical structures of (A) an artificial nuclease and (B) a luminescent cross-linking agent

1.6.3: SHAPE-SELECTIVE RECOGNITION

On the whole, metallointercalators are structurally rigid molecules with well-defined symmetry, making them particularly well suited for selective molecular recognition of specific DNA sequences. Importantly, because of the general rigidity of the complexes, both the overall shape and ancillary ligands of these complexes can also be exploited in the development of useful agents.

Perhaps not surprisingly, stereochemistry is of utmost importance in the construction of site-specific recognition agents. Indeed, one of the earliest findings in this field was the necessity of matching the chirality of the metallointercalator with that of the double helix: the Δ-enantiomer of the metal complex preferentially binds to right-handed B-DNA. This enantioselective discrimination is primarily steric in nature and depends on the size of the ancillary ligands relative to that of the DNA groove. For instance, poor enantioselectivity is observed with metallointercalators bearing small ancillary ligands such as phenanthroline and bipyridine, whereas complete enantiospecificity is achieved with bulkier ancillary ligands such as DPB (4,4'-diphenyl-bipyridine).[66, 67] The Δ-enantiomer of $Rh(phi)(DPB)_2^{3+}$, for example, readily cleaves the sequence 5'-CTCTAGAG-3' upon photoactivation, but no intercalation or cleavage is observed with the Λ-enantiomer, even with a thousand-fold excess of metallointercalator (**Figure 1.8**). For Z-DNA, which is a left-handed helix, little enantioselectivity for chiral metal complexes is observed because of the very shallow, almost convex major groove;[25] hence the Λ-isomer, which cannot bind at all to B-form DNA, becomes a selective probe for Z-DNA.

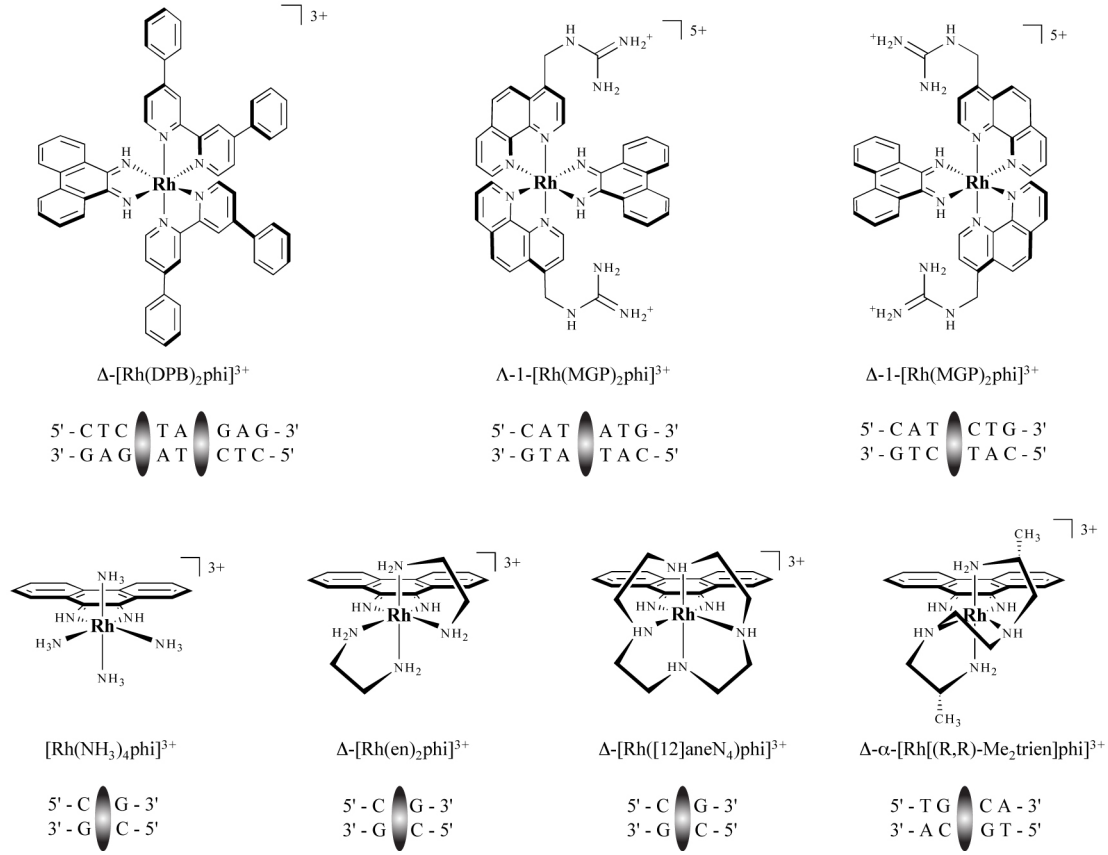

Figure 1.8: Sequence-specific metallointercalators and their target sequences. The name and recognition site of each metallointercalator is shown below the chemical structure of complex. The shaded grey ovals indicate the precise location of intercalation.

As a monomer, Δ-Rh(phi)$(DPB)_2^{3+}$ is geometrically capable of spanning only six base pairs; however, the metallointercalator is able to recognize a palindromic sequence eight base pairs long by dimerizing. The target sequence 5'-CTCTAGAG-3' can be considered as two overlapping 5'-CTCTAG-3' intercalation sites. Concomitant intercalation of two metal complexes, each at a central 5'-CT-3' of the 6-mer, favors stacking of the ancillary phenyls from both complexes over the central 5'-TA-3' step. This binding cooperativity, more common with DNA binding proteins, enhances the binding affinity of the second intercalator by 2 kcal. As a result, irradiation of the metallointercalators / DNA adduct cleaves both DNA strands with three base pairs separating the two cleavage sites.

The remarkable specificity and intricate binding mode of Δ-Rh(phi)$(DPB)_2^{3+}$ enables it to inhibit efficiently the activity of *Xba*I restriction endonuclease at the palindromic site.[46] Notably, no comparable inhibition of *Xba*I has been achieved with any other metallointercalators, and Δ-Rh(phi)$(DPB)_2^{3+}$ cannot inhibit restriction enzymes that bind different sites. Thus, metallointercalators have found use not only as probes for nucleic acid structures but also as mimics and, perhaps, inhibitors of DNA-binding proteins.

Interestingly, more moderate shape-based site recognition can be achieved with sterically smaller ancillary ligands like phenanthroline. $Rh(phen)_2(phi)^{3+}$, for instance, preferentially intercalates at sites with high propeller twisting toward the major groove.[63, 68−70] This intercalator preferentially photocleaves 5'-Py-Py-Pu-3' sites and occasionally 5'-Pu-Py-Pu-3' sites but not 5'-Pu-Pu-Py-3' sites. Comparison of photocleavage experiment results with the crystal structures of several B-form oligonucleotides reveals a

direct correlation between the binding preference of $Rh(phen)_2(phi)^{3+}$ and the increased propeller twisting at the sites of intercalation. Opening of the major groove in the 5'-Py-Py-Pu-3' sequence produces more steric leeway for the hydrogens of the ancillary phenanthroline ligands, thus enabling deeper intercalation by the metal complex. In the case of a 5'-Pu-Pu-Py-3' site, however, reduced propeller twisting creates a more sterically confining major grove at the intercalation site; in this instance, then, increased steric hindrance between the groove and the phenanthroline ligands pushes the intercalating phi ligand farther away from the DNA helical axis, thereby reducing the binding affinity of the complex.

Due to its unique properties, $Rh(phen)_2(phi)^{3+}$ has also been employed as a probe for RNA tertiary structure.[42, 71–73] As discussed above, the complex can only intercalate from the major groove side of DNA, a property which prevents it from binding via the sterically-altered groove of duplex RNA and binding instead preferentially to triplex RNA. In this capacity, the rhodium complex is able to compete for binding at the TAT protein binding site in the immunodeficiency virus TAR RNA.[74] $Rh(phen)_2(phi)^{3+}$ efficiently binds and photocleaves the U24 base involved in the base-triplex of the RNA hairpin that is essential to TAT binding. The metal complex similarly competes with and inhibits the binding of the bovine BIV-TAT peptide to its RNA target site. Mutants of the RNA oligomer lacking the base triplex and which can therefore no longer bind the TAT peptide are likewise no longer targeted by the metallointercalator.

1.6.4: SEQUENCE RECOGNITION BASED ON FUNCTIONALITY

Selective recognition of a DNA sequence by a metallointercalator can also be achieved by matching the functionality of the ancillary ligands positioned in the major groove with those of the targeted base pairs. Specific targeting of the sequence 5'-CG-3', for instance, is achieved with the complexes $Rh(NH_3)_4(phi)^{3+}$, $Rh([12]aneN_4)(phi)^{3+}$ and Δ-$Rh(en)_2(phi)^{3+}$.[75–78] In these examples, recognition is ensured both by the C2 symmetry of the metal complexes and hydrogen bonding between the axial ammines of the metallointercalators and the O6 atoms of the guanines. The Λ-enantiomer of $Rh(en)_2(phi)^{3+}$, in contrast, recognizes the sequence 5'-TA-3' due to van der Waals contact between the methylene groups on the backbone of the complex and the thymine methyls of the DNA.

The predictive design of sequence specific metallointercalators was expanded with Δ-α-$Rh[(R,R)\text{-}Me_2trien](phi)^{3+}$, a complex that specifically recognizes and photocleaves the sequence 5'-TGCA-3' (**Figure 1.9**).[79] The rhodium complex was designed to recognize this sequence via hydrogen bonding contacts between the axial ammine ligands and the O6 atoms of the guanines, as well as potential van der Waals contacts between the pendant methyl groups on the metal complex and the methyl groups on the flanking thymines. A high resolution NMR solution structure followed by the first crystal structure of a metallointercalator-DNA adduct later revealed at atomic resolution the details of the intercalation and recognition. In fact, it is because of the high sequence-specificity of this intercalator that a high resolution view of intercalation within a long DNA duplex could be obtained. In the DNA octamer containing the central 5'-TGCA-3'

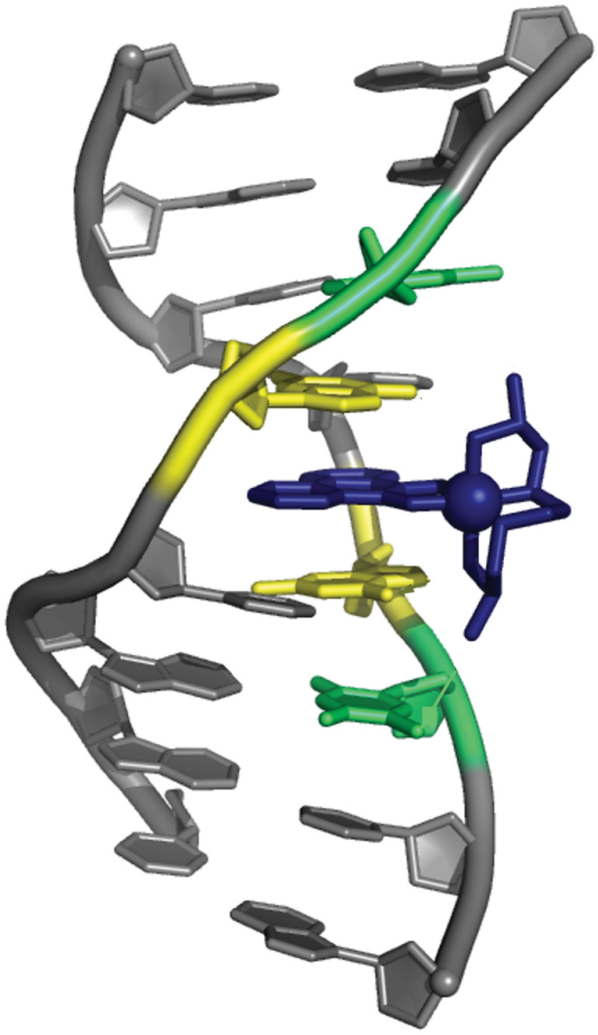

Figure 1.9: Crystal structure of the metallointercalator Δ−α-[Rh[(R,R)-Me_2trien]phi]$^{3+}$ bound to its target sequence, 5'-TGCA-3'. The recognition is conferred by two sets of interactions: (1) hydrogen bonding between the axial ammines of the complex and the O6 atoms of the guanines and (2) methyl-methyl interactions between the ligand methyl groups and those of the thymines.

site, the DNA unwinds to enable complete and deep intercalation of the phi ligand of the metal complex within the major groove. This results in a doubling of the rise at the intercalation site without any base ejection. The metallointercalator thus behaves as a newly added base pair that causes only minimal structural perturbation to the DNA. Furthermore, both the NMR study and crystal structure confirm that the sequence-specific recognition is, indeed, based on the anticipated hydrogen bonding and van der Waals interactions.

1.6.5: SEQUENCE RECOGNITION BASED ON SHAPE AND FUNCTIONALITY

Yet another metallointercalator provides an interesting example of sequence-specific recognition predicated on both shape *and* functionality. 1-$Rh(MGP)_2(phi)^{5+}$, a derivative of $Rh(phen)_2(phi)^{3+}$ containing pendant guanidinium groups on the ancillary phenanthroline ligands, was designed to bind a subset of the sequences recognized by the latter complex, specifically those 5'-Py-Py-Pu-3' triplets flanked by two G•C base pairs. Hydrogen bonding between the guanidinium groups on the ancillary ligands and the O6 atoms of the flanking guanines was expected to confer this selectivity.[80, 81] As predicted, NMR studies demonstrate that the Δ-enantiomer recognizes the sequence 5'-CATCTG-3' specifically.

Surprisingly, in spite of the large size of the ancillary ligands, the Λ-enantiomer also binds DNA and recognizes a different sequence, 5'-CATATG-3'. The expansive MGP ligands certainly prevent the left-handed isomer from entering the major groove of right-handed DNA. However, plasmid unwinding assays and NMR studies establish that the Λ-enantiomer of the metallointercalator binds DNA by unwinding it up to 70°. It is in

this conformation that the complex can span the entire six-base pair binding site and contact the N7 position of the flanking guanines with the pendant guanidinium groups. Replacing these flanking guanines with deazaguanines demonstrates that the absence of the N7 nitrogen atoms eliminates any site selectivity. Therefore, we can conclude that the guanidinium functionalities of the ancillary ligands are responsible for the recognition of the flanking guanines, whereas the shape of the metallointercalator enables the recognition of the "twistable" central 5'-ATAT-3' sequence.

Due to its high site-specificity, the Λ-enantiomer of this complex has found biological application as an inhibitor of transcription factor binding.[82] In a manner similar to $Rh(phen)_2(phi)^{3+}$, Λ-1-$Rh(MGP)_2(phi)^{5+}$ can site-specifically inhibit the binding of a transcription factor to its activator recognition region. In competition experiments with yeast Activator Protein 1 (yAP-1), the metal complex was able to compete with the protein for a domain that included both the binding region of yAP-1 and that of Λ-1-$Rh(MGP)_2(phi)^{5+}$ at concentrations as low as 120 nM. This result represents one of the first hints at the therapeutic potential of rhodium intercalators, a notion strongly supported by subsequent investigations illustrating that $Rh(phi)_2(phen)^{3+}$ and other rhodium bis(quinone diimine) complexes inhibit transcription *in vitro*.[83, 84]

1.7: METALLOINSERTORS

Without a doubt, the vast majority of non-covalent, DNA-binding metal complexes are either groove-binders or intercalators. However, the dearth of complexes that bind DNA via other means does not necessarily exclude the existence of alternative

modes. Indeed, L.S. Lerman, in his seminal article proposing intercalation as the DNA-binding mode for organic dyes, presciently proposed a third non-covalent binding mode: insertion.[85] A molecule, he posited, may bind "a DNA helix with separation and displacement of a base-pair." While Lerman was addressing organic moieties, we can apply this thinking to metal complexes quite easily. Metalloinsertors, like metallointercalators, contain a planar aromatic ligand that extends into the base-stack upon DNA-binding. However, while metallointercalators unwind the DNA and stack their planar ligand between two intact base pairs, metalloinsertors separate and eject the bases of a single base pair, with their planar ligand acting as a π-stacking replacement in the DNA base stack.

Until very recently, no examples of DNA-binding insertors, neither metallic nor organic, had been reported. However, our research into mismatch-specific DNA-binding agents has led to the discovery of a family of rhodium complexes that bind DNA via this unique mode. These novel complexes have been dubbed metalloinsertors (**Figure 1.10**).

1.7.1: MISMATCHED DNA

1.7.1.1: STRUCTURE

Genomic fidelity is vital to cellular survival and replication. However, a wide variety of DNA defects can arise in the lifetime of a cell to threaten the fidelity of the genome.[86] Non-canonical base pairs, commonly known as single base mismatches, are one particularly deleterious class of DNA defects. Eight possible mismatches exist, each thermodynamically destabilized relative to the A•T and C•G Watson-Crick base pairs: A•A, A•C, A•G, C•C, C•T, G•G, G•T, and T•T (**Figure 1.11**).

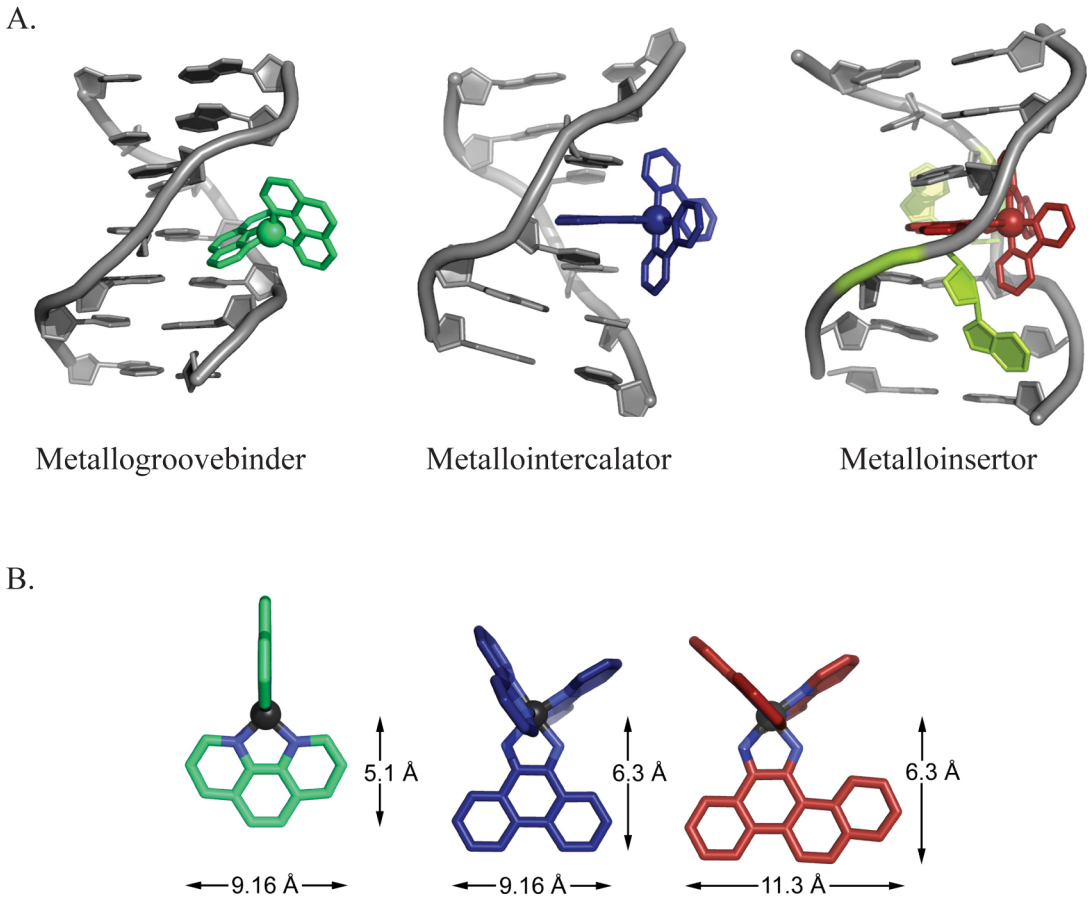

Figure 1.10: Three non-covalent binding modes for metal complexes and DNA. (A) Models of a metallogroove-binder (green), metallointercalator (blue), and metalloinsertor (red) bound to DNA; (B) Representative dimensions of a metallogroovebinder (green), metallointercalator (blue), and metalloinsertor (red)

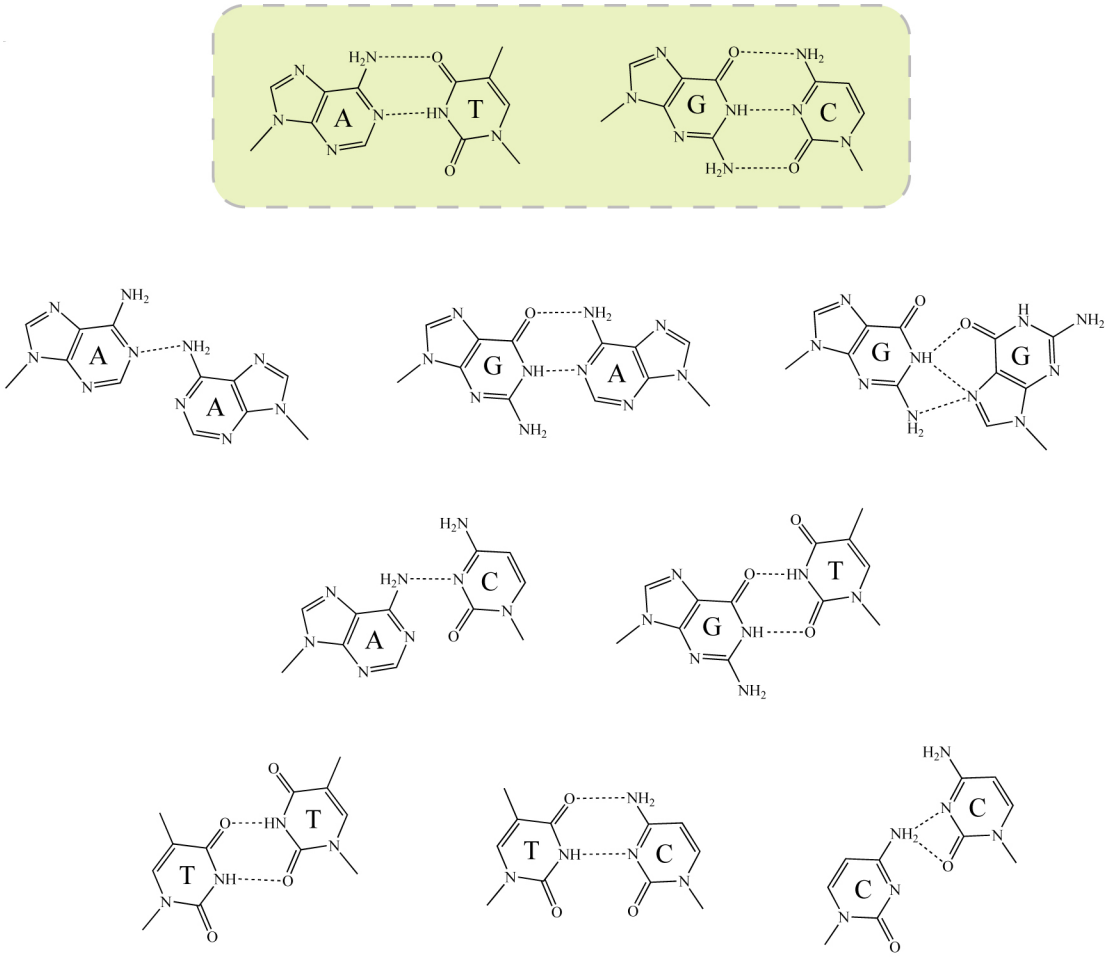

Figure 1.11: Mismatched DNA. The mismatched base pairs and their most probable hydrogen bonding interactions. The standard Watson-Crick base pairs are shown at the top, highlighted in green.

Several structures of DNA mismatches – specifically A•G, G•G, A•C, and G•T – in modified Drew-Dickerson dodecamers have been obtained by single crystal x-ray crystallography (**Figure 1.12**).[87–91] In each, the DNA adopts a B-form structure without kinks or extrahelical bases. Some perturbation at the mismatch sites is observed, however; the mismatched bases themselves adopt unusual conformations in order to maximize hydrogen-bonding and π-stacking interactions.

Nuclear magnetic resonance studies have provided complementary insights into the structure of mismatched DNA; while NMR cannot offer the level of resolution and detail characteristic of crystal structures, the technique is performed under far more physiologically relevant conditions and, importantly, can provide information on base dynamics.[92] Solution structures of various mismatched duplexes have confirmed an overall B-form structure. Further, experiments show that the hydrogen bonding schemes of certain mismatches (*e.g.* G•T) may change based on the identity of the base pairs flanking the mispair.[93, 94] Most important, though, is the observation that mismatched bases are characterized by a higher rate of proton exchange than their matched counterparts. For this to be the case, mismatches must undergo a conformational change to expose the base-pairing face of each nucleotide to bulk solvent. Whether this behavior is a slight opening of the mispaired bases or the adoption of a fully extrahelical conformation is unknown. Regardless of the detailed mechanics, however, one thing is certain: this behavior is indicative of thermodynamic destabilization at mismatched sites.

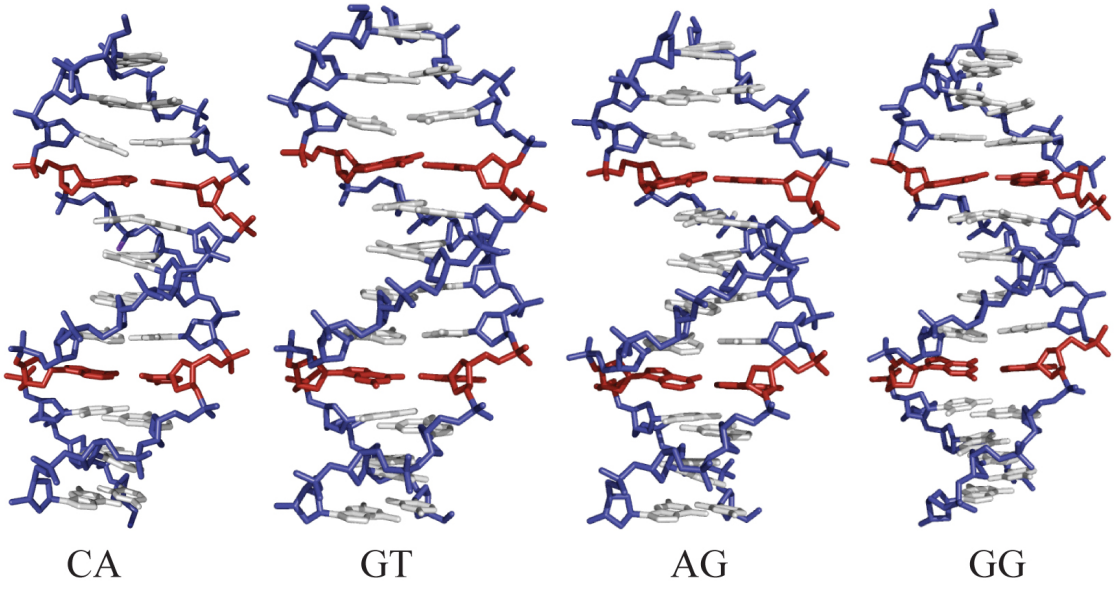

Figure 1.12: Crystal structures of mismatch-containing DNA duplexes. Each palindromic duplex is labeled with the mismatch it contains. While the mismatched bases appear slightly perturbed, the overall structure of the duplex is disrupted very little. The mismatches are shown in red.

1.7.1.2: THERMODYNAMICS

The energetics of single base mismatches have also been very thoroughly studied using both UV-Vis and NMR spectroscopy. UV-Vis measurements, which provide insight into the destabilizing influence a mismatch has on an oligonucleotide as a whole, have made the comparison of the stabilities of different mismatches quite easy. In general, then, a ranking of the stability of base pairs proceeds as follows: C•G > A•T > > G•G ~ G•T ~ A•G > > T•T ~ A•A > C•T ~ A•C > C•C.[94] The relative order does, admittedly, have some dependence on sequence context, but the trends generally remain similar.[95] The guanine-containing mismatches tend to be the most stable mispairs because of the particular ability of guanine to form hydrogen bonds, but they are still destabilized relative to Watson-Crick base pairs. The C•C mismatch is the most destabilizing mispair, a result of poor hydrogen-bonding and small aromatic surface area.

The combination of UV-Vis data with ^{1}H-NMR data has allowed for the creation of standard tables of ΔG° parameters for all base pairs in every sequence context (**Table 1.1**).[96–100] The 5'-AXC-3' sequence provides an example (**Figure 1.13**). In this particular sequence context, C•G and A•T Watson-Crick base pairs stabilize the duplex by 3.52 and 2.44 kcal/mol, respectively. In contrast, a C•C mismatch destabilizes the duplex by 2.12 kcal/mol. Indeed, regardless of the numbers, in all cases replacing a matched base pair with a mismatch will destabilize the duplex

GX/CY	A	C	G	T
A	0.17	0.81	-0.25	-1.30
C	0.47	0.79	-2.24	0.62
G	-0.52	-1.84	-1.11	0.08
T	-1.44	0.98	-0.59	0.45

CX/GY	A	C	G	T
A	0.43	0.75	0.03	-1.50
C	0.79	0.70	-1.84	0.62
G	0.11	-2.17	-0.11	-0.50
T	-1.28	0.40	-0.2	-0.10

AX/TY	A	C	G	T
A	0.61	0.88	0.14	-1.00
C	0.77	1.33	-1.44	0.64
G	0.02	-1.28	-0.13	0.71
T	-0.88	0.73	0.07	0.69

TX/AY	A	C	G	T
A	0.69	0.92	0.42	-0.6
C	1.33	1.05	-1.30	0.97
G	0.74	-1.45	0.44	0.43
T	-1.00	0.75	0.34	0.68

Table 1.1: Thermodynamics of mismatches. ΔG° values (kcal/mol) for different internal mismatches with neighboring matched base pairs. In all cases, the Watson-Crick base pairs, highlighted in red, are more stable than any of the possible mismatches. To obtain a value for a mismatch, C•C for example, in a sequence context, say 5'-AXC-3', add 1.33 + 0.79 to obtain a total of 2.12 kcal/mol destabilization. X refers to the row, while Y refers to the column.

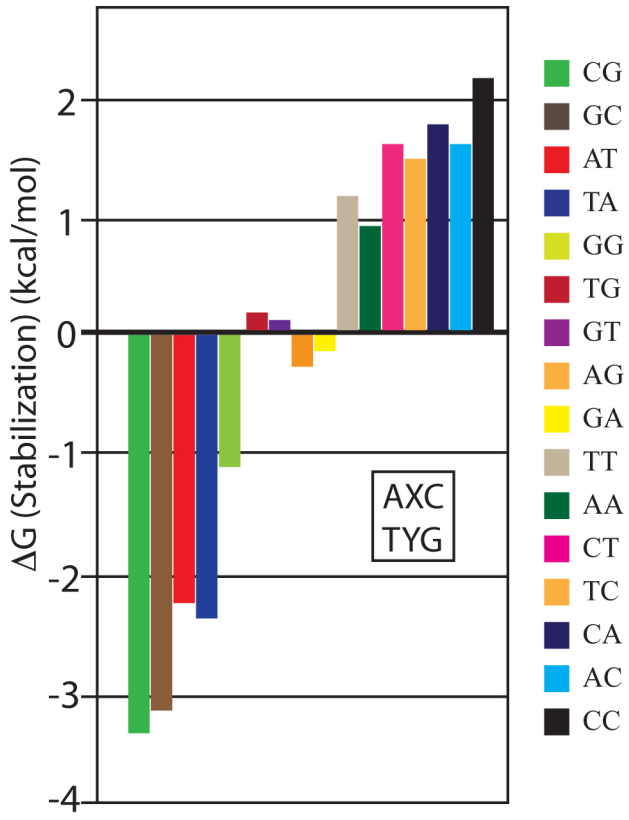

Figure 1.13: Thermodynamics of base pairs in a 5'-AXC-3' sequence context. The stabilization of different base pairs in the 5'-AXC-3' sequence is shown. The bars represent different base pairs (legend on the right), with negative ΔG° values net stabilizing and positive ΔG° values net destabilizing.

1.7.1.3: CAUSES

DNA replication is the most important source of mismatches *in vivo*.[101] Alone, the catalytic domain of a DNA polymerase will misincorporate one in 10^4 bases.[102] Needless to say, this is an unacceptably high level of infidelity for even the simplest organisms: upon a subsequent round of replication, unrepaired mismatches will become permanent mutations. To ensure the integrity of replication, most polymerases also employ proofreading domains which check the base pairs immediately after their incorporation and excise bases that have been incorrectly inserted. This dramatically increases the fidelity of the replication process to 1 incorrect base in $\sim 10^7 - 10^8$ bases.[103] The mismatch countermeasures do not stop here, however. Post-replication mismatch repair machinery (*vide infra*) can lower the misincorporation rate to as low as 1 base in 10^9 bases.

While the standard DNA replication process described above is quite accurate, under special circumstances, DNA synthesis can lead to higher rates of nucleotide misincorporation. The major polymerases involved in the replication of genomic DNA, Polymerase δ and Polymerase ε, are incapable of incorporating bases opposite chemically damaged bases.[104] When one of these two polymerases encounters such a site, they dissociate from the DNA and are temporarily replaced (100−1000 bases) by one of three translesion synthesis polymerases, Polymerase η, Polymerase ι, or Polymerase ζ.[105] These enzymes will readily incorporate a base opposite the chemically damaged site, but this functionality comes with a price; the translesion synthesis polymerases lack proof-reading domains and thus have far higher rates of nucleotide misincorporation than Pol δ and Pol ε.

A number of other, more minor processes can also create mismatches. During the genetic recombination of homologous chromatids, the sliding of the four-way Holliday junction intermediate can result in mismatch formation.[106] Cytosine deamination, a spontaneous chemical reaction in which the minor imine tautomeric form of cytosine is hydrolyzed to produce uracil, can create G•U mismatches.[107] These mismatches, if left unrepaired by the base excision repair machinery, will result in A•U mismatches and, ultimately, an A•T transversion. Interestingly, the action of an activated cytosine deaminase enzyme, AID, may be responsible for the creation of mismatches and consequent mutations during the process of intentional somatic hypermutation used by lymphocytes to increase genetic diversity in the production of immunoglobins.[107]

1.7.1.4: REPAIR

Regardless of their source, mismatches are recognized and repaired *in vivo* by the endogenous mismatch repair (MMR) machinery.[108] In prokaryotes, the repair pathway is mediated by the MutS, MutL, and MutH proteins; in higher organisms, homologs of these enzymes play the central roles. The machinery detects a mismatch, excises a fragment of DNA containing the mismatch, and replaces approximately 1 kb of DNA.[109]

In the prokaryotic pathway, the mechanistic details are murky, but a general sequence of events is accepted (**Figure 1.14**).[110] First, a MutS dimer will recognize and bind a mismatched site in the DNA. The binding event attracts a MutL dimer. Next, in a poorly understood step, the MutS/L complex differentiates between parent and daughter strands

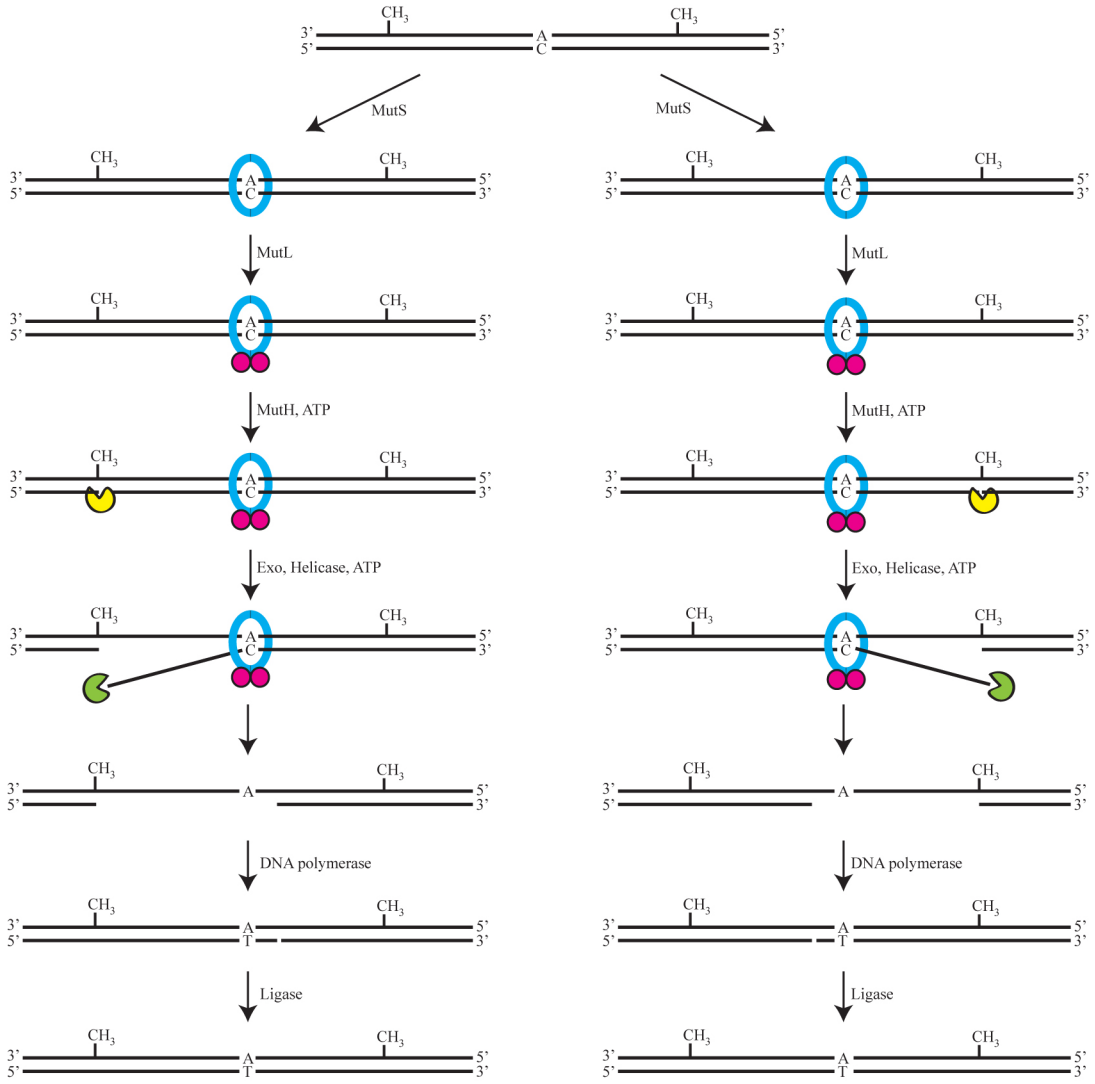

Figure 1.14: Mismatch repair in prokaryotes. A general scheme: (1) MutS recognizes and binds the mismatch; (2) MutL is recruited, and MutS/L identify the daughter strand; (3) MutH is recruited and nicks the daughter strand; (4) an exonuclease digests the nicked strand; (5) a DNA polymerase synthesizes a new daughter strand; (6) a ligase seals the nick, yielding intact, matched DNA.

and then recruits a third protein, the endonuclease MutH, to nick the daughter strand. The nicked strand is then digested by exonucleases traveling toward the mismatched site. Finally, a new DNA strand is synthesized by a polymerase, and the resultant nick is ligated to yield a fully repaired duplex. A similar, though slightly more complex, process governs mismatch repair in eukaryotes, with MSH2 replacing MutS, MLH1 replacing MutL, and an unknown endonuclease in place of MutH.[111]

1.7.1.5: CONSEQUENCES

Upon replication, uncorrected mismatches will become permanent mutations. As we have discussed above, the cell has evolved a complex mismatch repair (MMR) machinery to counter this threat. Abnormalities in this machinery, however, lead to dire consequences: the genomic accumulation of mismatches and their consequent mutations create a high likelihood for cancerous transformations. Indeed, mutations in MMR genes have been identified in 80% of hereditary non-polyposis colon cancers; further, 15−20% of biopsied solid tumors have shown evidence of somatic mutations associated with MMR.[112] Moreover, MMR deficiency has been linked to resistance to common chemotherapeutic and antineoplastic agents.[113] It thus becomes clear that the design, synthesis, and study of molecules able to specifically target single base mismatches is of tremendous importance to the development of new cancer diagnostics and therapeutics.

1.7.1.6: RECOGNITION BY SMALL MOLECULES

Given the biological importance of mismatches, it is not surprising that a number of organic, small molecule recognition agents have been developed. Two classes predominate: polyamides and naphthyridines.

Polyamides bind DNA through minor groove interactions, and the systematic modification of the chemical structural of polyamides has facilitated the recognition of almost any sequence.[114] Mismatches are no exception. The polyamide f-ImImIm, for example, has been designed for the specific recognition of G•T mismatches (**Figure 1.15a**).[115, 116] A dimer of the polyamide binds the mismatch through the minor groove with a relatively high affinity, approximately 5×10^6 M^{-1}. However, the ultimate applicability of mismatch-binding polyamides is significantly limited by both their lack of generality and poor selectivity.

The second class of mismatch recognition agents, naphthyridines, has been studied extensively by the Nakatani and Saito groups. Originally, 2-amino-7-methylnaphthryridine was investigated for its ability to recognize and stabilize single guanine bulges in DNA.[117] However, it was soon noted that dimers of naphthyridines are capable of recognizing a variety of different mismatches. For example, a naphthyridine dimer with an amide linker is capable of specific interactions with a G•G mismatch: the naphthyridines insert into the mismatch site, hydrogen bond with the mispaired guanines, and π–stack within the helix (**Figure 1.15b**). Somewhat surprisingly, a slightly different naphthyridine dimer with an alkyl linker is capable of the specific recognition of C•C, C•T, C•A, and T•T mismatches *via* a similar binding mode. In all cases, the binding

A.

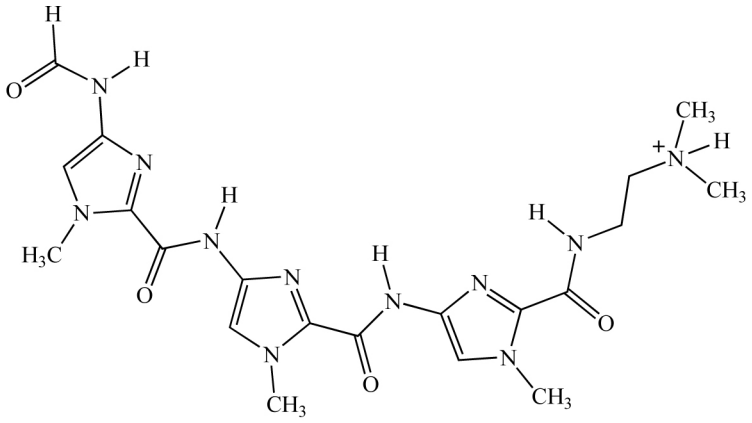

B.

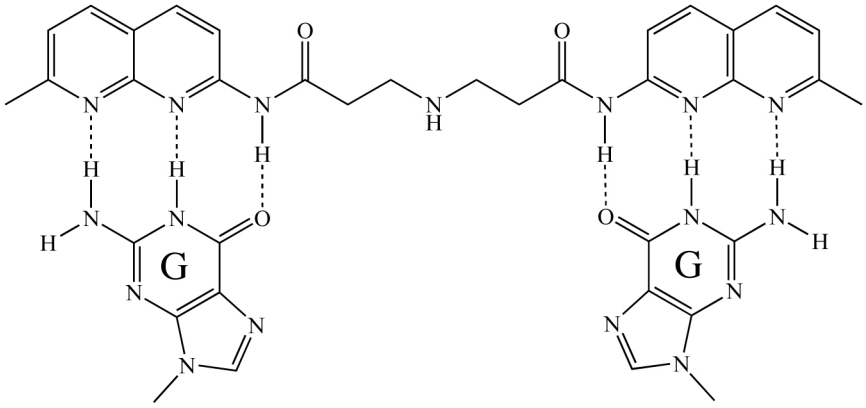

Figure 1.15: Organic mismatch recognition agents. (A) The polyamide f-ImImIm specifically recognizes G•T mismatches; (B) the amide-linked naphthyridine dimer specifically recognizes G•G mismatches.

constants hover around 1 x 10^6 M^{-1}; however, these complexes, like polyamides, are limited by their lack of generality, modest selectivity, and photochemical inactivity.

1.7.2: RATIONAL DESIGN OF MISMATCH-SPECIFIC METAL COMPLEXES

Over the past ten years, much of our laboratory's work in molecular recognition has been focused on the design, synthesis, and study of metal complexes that selectively bind mismatched sites in DNA. When compared to sequence-specific metallointercalators, the design of mismatch-specific complexes presents a peculiar challenge. In this case, the recognition target is not a unique sequence but rather a type of site, specifically a region in the duplex that is thermodynamically destabilized by the mismatch's imperfect hydrogen-bonding. Indeed, an ideal mismatch recognition agent would bind all possible mismatched sites (C•C, C•A, A•G, etc.) without regard to the sequence context surrounding the mismatch. Taken together, these requirements dictate that the recognition elements of our mismatch-selective complexes must move from the ancillary ligands to the intercalating ligand.

Somewhat surprisingly, mismatch-specificity was achieved simply by replacing the non-specific phi ligand with the similar but more sterically expansive chrysene-5,6-quinone diimine (chrysi) ligand (**Figure 1.16**). Specifically, the chrysi ligand is 0.5 Å wider than the span of matched DNA and 2.1 Å wider than its parent phi ligand. Unlike the phi ligand, which is the ideal size for intercalation between the backbones of matched DNA, the chrysi ligand, with its additional fused ring, is too bulky to intercalate at stable, matched sites due to inevitable steric clash with the sugar rings of the DNA. Single base mismatches, it was proposed, would be a different story altogether, for at these

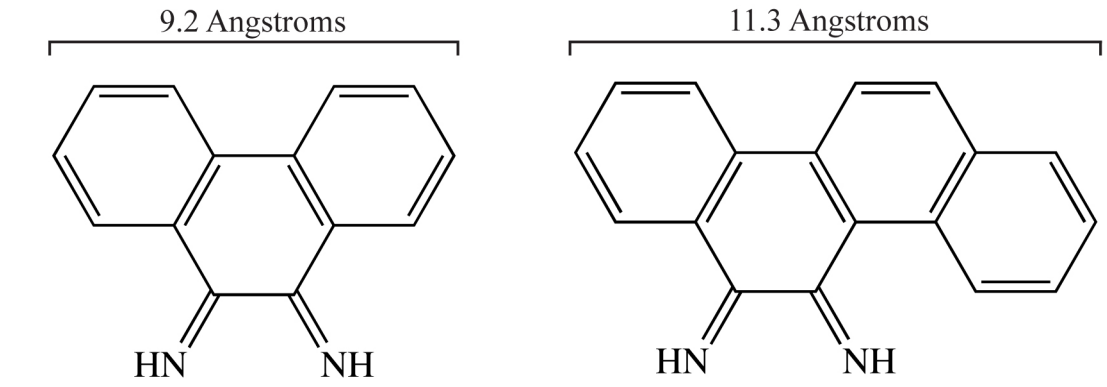

9,10-phenanthrenequinone diimine (phi) chrysene-5,6-quinone diimine (chrysi)

Figure 1.16: Structure of phi and chrysi ligands. The width of the phi ligand is well-suited for intercalation between the base pairs of well-matched DNA. The extra width of the chrysi ligand precludes binding at matched base pairs and instead confers selectivity for thermodynamically destabilized mismatched sites.

thermodynamically destabilized sites, the energetic benefit of the π-stacking ligand would outweigh the energetic cost of steric clash. In designing the complex, rhodium was again chosen as the metal primarily due its photophysical properties, most notably the ability of the non-specific rhodium complexes to promote strand scission upon irradiation.

1.7.3: RECOGNITION EXPERIMENTS

The first generation complex, $Rh(bpy)_2(chrysi)^{3+}$, was synthesized from $Rh(bpy)_2(NH_3)_2^{3+}$ and chrysene-5,6-quinone via base-mediated condensation of the quinone onto the ammine ligands of the metal ion (**Figure 1.17a**).[118] Initial photocleavage experiments showed that the complex does, indeed, bind mismatched sites and, upon photoactivation with UV-light, promotes direct strand cleavage of the DNA backbone adjacent to the mismatch site.[119] The compound also proved to be remarkably selective; mismatches are bound at least 1000 times tighter than matched base pairs. A dramatic enantiomeric effect is also observed, with the Δ-enantiomer binding and cleaving extremely well and the Λ-enantiomer almost completely inactive. While the preference for the Δ-isomer binding to right-handed DNA was anticipated, the remarkably high enantioselectivity was unexpected, given the relatively small bipyridine ancillary ligands. Further experiments were performed to test the specificity of the complex. Photocleavage experiments employing alkaline agarose and denaturing polyacrylamide gels revealed that $Rh(bpy)_2(chrysi)^{3+}$ cleaves at, and only at, a single mismatch incorporated into a linearized 2725 base-pair plasmid.[120]

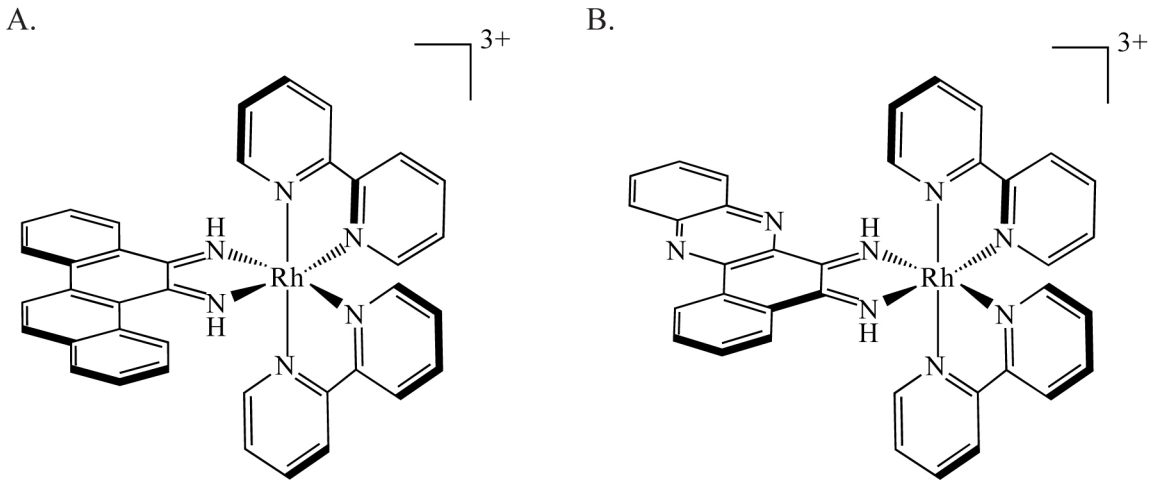

Δ-Rh(bpy)$_2$(chrysi)$^{3+}$ Δ-Rh(bpy)$_2$(phzi)$^{3+}$

Figure 1.17: Structures of Δ-Rh(bpy)$_2$(chrysi)$^{3+}$ and Δ-Rh(bpy)$_2$(phzi)$^{3+}$

Subsequent investigations established that $Rh(bpy)_2(chrysi)^{3+}$ binds and cleaves 80% of mismatch sites in all possible sequence contexts.[121] Furthermore, comparing the binding affinities of $Rh(bpy)_2(chrysi)^{3+}$ to independent measurements of mismatch destabilization revealed a clear correlation between mismatch stability and metal complex binding: in general, the more destabilized the mismatch, the tighter the binding. For example, the mismatch-selective binding constants of $Rh(bpy)_2(chrysi)^{3+}$ range from 3×10^7 M^{-1} for the dramatically destabilized C•C mismatch to 2.9×10^5 M^{-1} for the far more stable A•A mismatch.[120] Consistent with this relationship, $Rh(bpy)_2(chrysi)^{3+}$ almost completely fails to target the most stable mismatches, specifically those containing guanine nucleotides. In essence, the less destabilized mismatched sites "look" just like well-matched base-pairs to the metalloinsertor.

A second generation mismatch-specific metal complex, $Rh(bpy)_2(phzi)^{3+}$, was recently designed and synthesized (**Figure 1.17b**). The endocyclic nitrogens in the benzo[a]phenazine-5,6-quinone diimine (phzi) ligand enhance the π-stacking capability of the complex and thus raise its site-specific binding constant.[122] For example, the binding constants of this complex for C•A and C•C mismatches were measured to be 0.3 and 1×10^8 M^{-1}, respectively, affinities that allow for mismatch recognition and photocleavage at nanomolar concentrations. Importantly, the higher binding affinities are not accompanied by a concomitant decrease in selectivity, which remains at 1000-fold or greater. The increased affinity, however, is not sufficient to facilitate binding to the more stable G-containing mismatches.

1.7.4: STRUCTURE

While the above experiments provide comprehensive information on the range, strength, and specificity of mismatch recognition by $Rh(bpy)_2(chrysi)^{3+}$, they yield little, if any, information on the structure of the complex and DNA upon binding. Previous NMR and crystal structures of phi-bearing metallointercalators clearly indicate that these complexes bind by classical intercalation via the major groove.[123] There was, however, no guarantee that a mismatch recognition complex would bind DNA in a similar manner. Thus, the elucidation of the structure of $Rh(bpy)_2(chrysi)^{3+}$ bound to a mismatched site became of project of tremendous importance.

Δ-$Rh(bpy)_2(chrysi)^{3+}$ was co-crystallized with a self-complementary oligonucleotide containing two A•C mismatches (5'-CGG*A*AATT*C*CCG-3'). The structure was subsequently solved at atomic resolution (1.1 Å) using the single anomalous diffraction technique (**Figure 1.18**).[53] Quite surprisingly, the structure reveals *two* binding modes for $Rh(bpy)_2(chrysi)^{3+}$. In the crystal, not only is the complex bound to both mismatched sites as expected, but it is also intercalated at a matched site at the center of the oligonucleotide. However, a large volume of evidence, including a second crystal structure (*vide infra*), supports the idea that the binding observed at the matched site results entirely from crystal packing forces.

In stark contrast to other known metallointercalators, $Rh(bpy)_2(chrysi)^{3+}$ is bound to the mismatched DNA via the minor groove. Further, and perhaps more remarkably, the complex does not bind via classical *intercalation* but rather the previously unreported mode of *insertion*. Rather than stacking an intercalating ligand between base pairs,

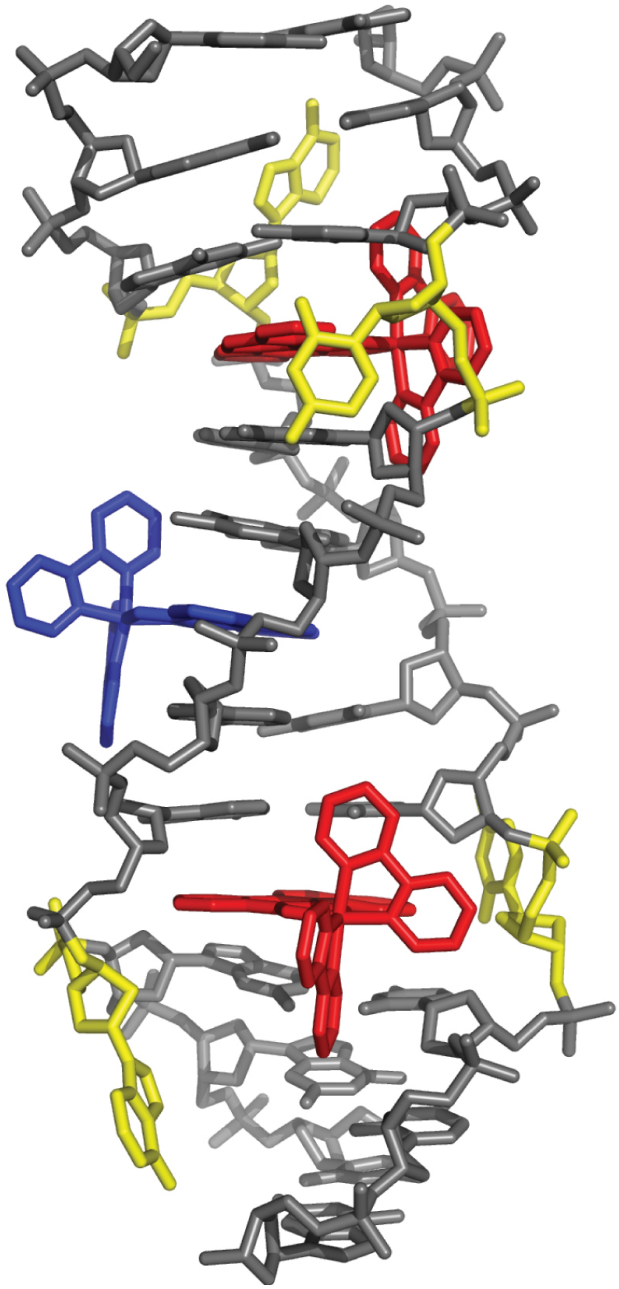

Figure 1.18: Crystal structure of Δ-Rh(bpy)$_2$(chrysi)$^{3+}$ bound to a C•A mismatch. Crystal structure (1.1 Å) of the metalloinsertor (red) bound to a palindromic oligonucleotide containing two C•A mismatches (yellow). The centrally intercalated rhodium complex is shown in blue.

thereby prompting an increase in the rise of the DNA, $Rh(bpy)_2(chrysi)^{3+}$ completely ejects the mismatched nucleotides from the base-stack and replaces the ejected bases with its own sterically expansive ligand. Despite this insertion, the complex does not significantly distort the DNA; all sugars maintain a C2'-*endo* puckering, and all bases remain in the *anti*-configuration. Instead, the DNA accommodates the bulky ligand by opening its phosphate backbone slightly. The chrysi ligand is inserted quite deeply into the base stack, so much so that the rhodium is only 4.7 Å from the center of the helical axis, and the chrysi ligand is solvent accessible from the opposite major groove. Interestingly, the complex itself is perturbed very little, though some flattening of the chrysi ligand (perhaps to augment π-stacking) is observed. These structural observations have been independently verified in a recent NMR investigation.[124]

The details provided by the crystal structure and NMR study help to explain three observations about which we could previously only hypothesize. First, the binding of the complex to the sterically smaller minor groove without an increase in rise explains the observed enantiospecific nature of recognition. Second, the minor groove insertion of the complex explains the different cleavage products created by $Rh(bpy)_2(chrysi)^{3+}$ and $Rh(bpy)_2(phi)^{3+}$ as observed via mass spectrometry.[125] The major groove binding mode of the metallointercalator positions it to cleave the DNA by abstracting the C2'H of the deoxyribose ring. Because it binds via the minor groove, $Rh(bpy)_2(chrysi)^{3+}$ is positioned to abstract preferentially the C1'H of the sugar adjacent to the mismatched site, and in this case, we see products consistent with C1'H abstraction. Finally, while we had previously demonstrated that the thermodynamic destabilization of the mismatch site is directly correlated to the binding affinity of the metal complex, the ejected bases

observed in the structure point to the concrete explanation. Since $Rh(bpy)_2(chrysi)^{3+}$ must displace the bases of the destabilized mismatched sites in order to bind the DNA, it follows that the more destabilized the site, the more easily the complex can eject the mispaired bases, and the tighter it can bind. Conversely, the complex cannot eject matched bases (or even more stable mismatched bases) because their hydrogen bonding interaction is too strong to allow for it.

1.7.5: DIAGNOSTIC APPLICATIONS

Considering the critical role of mismatches and mismatch repair deficiency in cancer susceptibility, the development of our unique recognition technology for diagnostic and therapeutic applications has also been a focus of our laboratory.

Fluorescence is a particularly attractive reporter in diagnostic applications and could be very useful in a sensitive early diagnostic for the detection of mismatches in genomic DNA. As a result, we have developed two different mismatch-specific fluorophores as potential diagnostics. The first probe, $Ru(bpy)_2(tactp)^{2+}$, sought to combine the DNA light-switch character of $Ru(dppz)(L)_2^{2+}$ complexes and the mismatch-specificity of the chrysi ligand in a single complex bearing a bulky chrysi/dppz hybrid ligand (**Figure 1.19a**).[126] However, while the complex does exhibit some light-switch behavior and mismatch-specific binding, the avid dimerization of the large aromatic ligand leads to non-specific fluorescence and thus dramatically limits its diagnostic potential. The second probe, a bifunctional conjugate combining a rhodium metalloinsertor with an organic fluorophore, will be discussed in the third chapter of this thesis.

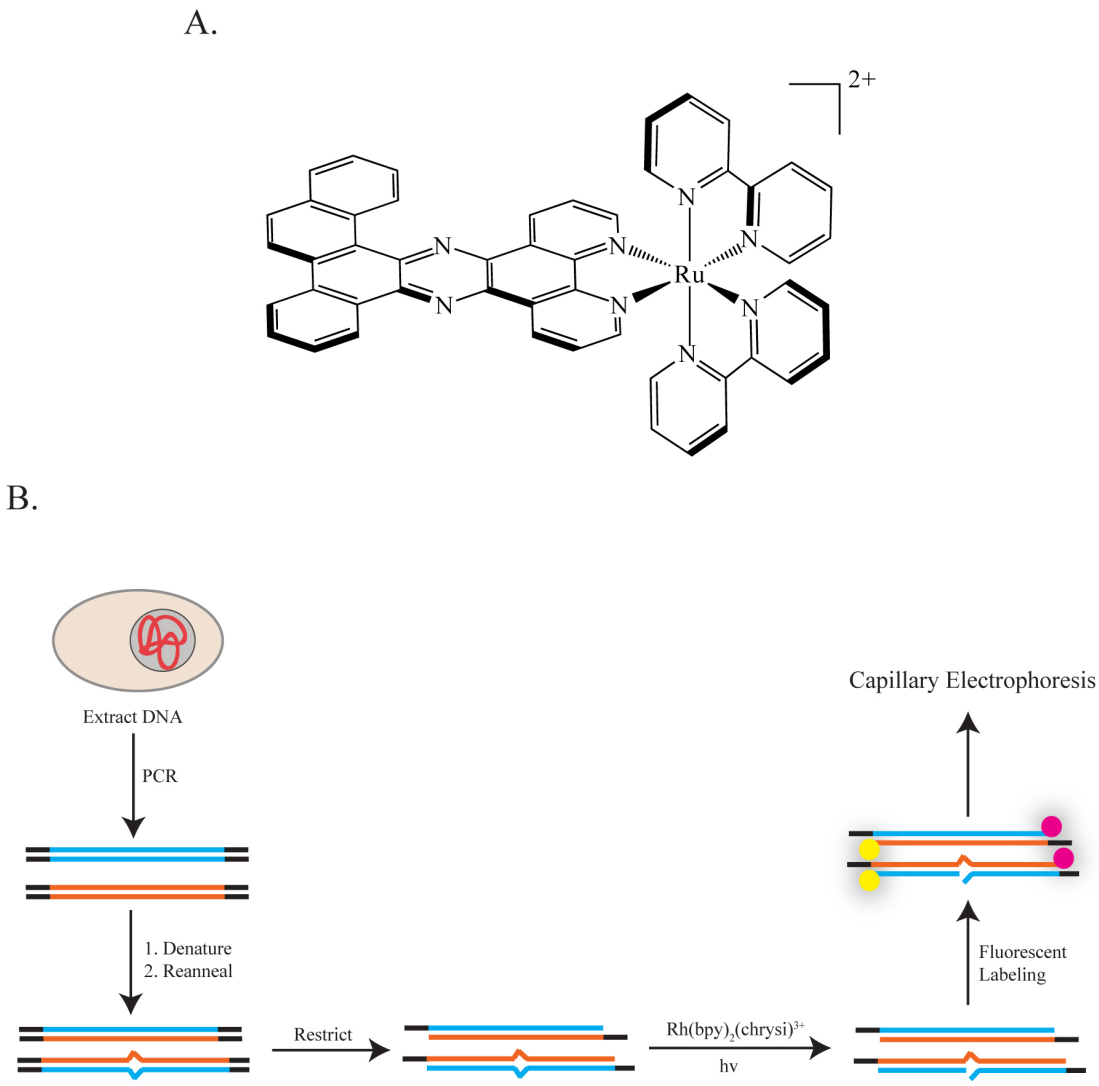

Figure 1.19: Diagnostic applications of metalloinsertors. (A) A complex designed as a mismatch-selective fluorophore, $Ru(bpy)_2(tactp)^{2+}$; (B) a schematic outline of a procedure for the detection of single nucleotide polymorphism using metalloinsertors

The site-specific photocleavage of both $Rh(bpy)_2(chrysi)^{3+}$ and $Rh(bpy)_2(phzi)^{3+}$ may also be exploited for diagnostic mismatch detection. Of course, the detection of mismatches in (labeled) oligonucleotides and synthetic plasmids does not hold particular diagnostic utility. Rather, the ideal system would allow for the quantification of the number of cleavage events (and thus mismatches) in the DNA from a particular cell sample or biopsy, thus indicating whether the tissue in question is MMR-deficient. $Rh(bpy)_2(phzi)^{2+}$, for example, has been used in conjunction with alkaline agarose electrophoresis to illustrate differences in site-specific cleavage frequencies in the DNA from MMR-proficient and -deficient cell lines. Further development of such a cleavage-based, whole-genome mismatch detection methodology using fluorescence is currently underway.

Mismatch-specific metalloinsertors have also been applied to the discovery of single nucleotide polymorphisms (SNPs).[127] SNPs are single base mutations that constitute the largest source of genetic variation in humans and can lead to variations in disposition to disease or response to pharmaceuticals. While other methodologies for SNP discovery exist, detection remains expensive, and false positive rates high.[128] In this application, a region of the genome suspected to contain an SNP is amplified via PCR, denatured, and then reannealed in the presence of a pooled sample (**Figure 1.19b**). If the region of interest had contained an SNP, the re-annealing process statistically generates a mismatch at the polymorphic site. The resultant mismatch-containing duplexes are then selectively cleaved via irradiation in the presence of $Rh(bpy)_2(chrysi)^{3+}$ or $Rh(bpy)_2(phzi)^{3+}$, fluorescently end-labeled, and analyzed via capillary gel electrophoresis. This new technique allows for the rapid identification of SNP sites with

single-base resolution. The methodology is further made useful by its sensitivity, for it allows for the detection of SNPs with allele frequencies as low as 5%.

1.7.6: THERAPEUTIC APPLICATIONS

The application of mismatch-specific metalloinsertors as a platform for new chemotherapeutics has also been of interest, especially considering that MMR-deficiency not only increases the likelihood of cancerous transformations but also decreases the efficacy of many common chemotherapeutic agents.[113]

Recently, it was discovered that both $Rh(bpy)_2(chrysi)^{3+}$ and $Rh(bpy)_2(phzi)^{3+}$ selectively inhibit cellular proliferation in MMR-deficient cells when compared to cells that are MMR-proficient.[129] Few small molecules have shown a similar cell-selective effect. Interestingly, enantiomeric differences are also observed associated with this inhibition. While the mismatch-binding, Δ-enantiomer of $Rh(bpy)_2(chrysi)^{3+}$ shows a high level of differential anti-proliferative effect, no such difference is seen using the non-binding Λ-enantiomer. This observation is important for two reasons. First, the mere presence of an enantiomeric difference strongly suggests that the causative agent is the intact complex, not some unknown degradation product or metabolite thereof. Second, the observation that the DNA-binding Δ-$Rh(bpy)_2(phzi)^{3+}$ and Δ-$Rh(bpy)_2(chrysi)^{3+}$ are the active enantiomers suggests that DNA mismatch binding plays at least some role in the anti-proliferative effect of these complexes. The surprise, however, was the observation that the biological effect occurs independent of irradiation with these complexes, even though they bind DNA only non-covalently.

More recently, the effect of ancillary ligand variation on the cytotoxicity of metalloinsertors has been explored.[130] A series of complexes with increasingly bulky ancillary ligands – $Rh(NH_3)_4(chrysi)^{3+}$, $Rh(bpy)_2(chrysi)^{3+}$, $Rh(HDPA)_2(chrysi)^{3+}$, $Rh(phen)_2(chrysi)^{3+}$, and $Rh(DIP)_2(chrysi)^{3+}$ – was synthesized and assayed for their DNA binding capability. Perhaps not surprisingly, it was found that the smaller the ancillary ligands, the tighter the complex binds mismatched DNA; for example, while $Rh(NH_3)_4(chrysi)^{3+}$ binds C•C mismatches with a binding affinity of greater than 1×10^8 M^{-1}, $Rh(DIP)_2(chrysi)^{3+}$ binds the same mismatched site with an affinity of less than 1×10^4 M^{-1}. The most interesting aspect of this study, however, comes to the fore when these complexes are employed in anti-proliferative assays: the tighter the complexes bind DNA (and thus the smaller the ancillary ligands), the greater the differential anti-proliferative effect in MMR-deficient and -proficient cells (**Figure 1.20**). This result not only further substantiates the role of mismatch binding in mediating the *in vivo* biological effect of these molecules but also marks a significant step forward in the development of more effective metalloinsertor-based chemotherapeutics. Currently, work is underway to understand the mechanism of cytotoxicity more fully and to maximize the differential effect of these complexes.

Several bifunctional, mismatch-specific conjugates have also been developed with a potential for chemotherapeutic application. In each, the rhodium moieties serve as the targeting vectors, delivering a cytotoxic cargo to mismatched DNA or, more generally, cells containing mismatched DNA, thereby tuning the reactivity of otherwise non-specific agents. Unlike $Rh(bpy)_2(chrysi)^{3+}$ or $Rh(bpy)_2(phzi)^{3+}$, these conjugates are

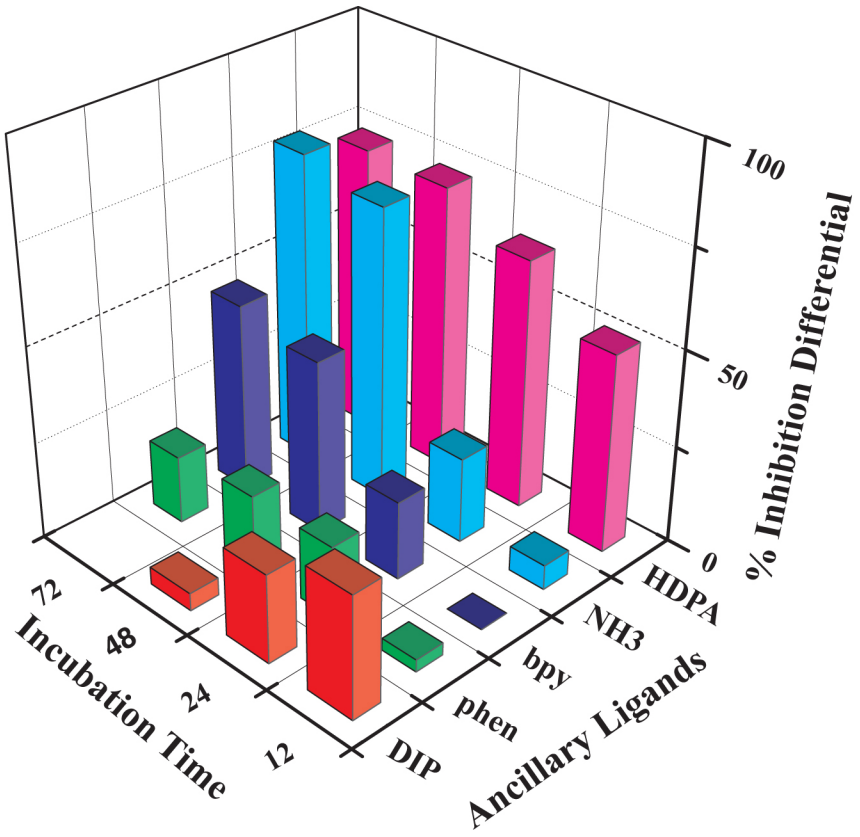

Figure 1.20: Differential anti-proliferative effects of metalloinsertors. A standard BrdU incorporation ELISA assay was employed to determine the anti-proliferative effects of a series of metalloinsertors as a function of ancillary ligand and incubation time.

trisheteroleptic, employing a tether-modified bipyridine ligand to establish the link between the two moieties. For example, in one conjugate the metalloinsertor is linked to a nitrogen mustard known to form covalent adducts at 5'-GXC-3' sites (**Figure 1. 21a**).[131] PAGE experiments with radiolabeled oligonucleotides confirm that the rhodium moiety successfully confers mismatch-selectivity on the alkylating agent. The two moieties neither abrogate nor attenuate each other's function. Significantly, independent of any chemotherapeutic application, this conjugate may also prove useful due to its ability to "mark" mismatch sites covalently.

Another bifunctional conjugate was created by linking a metalloinsertor moiety to an analogue of the well-known anticancer drug cisplatin, a Pt(II) complex that coordinates to single- and double-guanine sites in DNA and subsequently inhibits both transcription and replication (**Figure 1.21b**).[132] Like its alkylator cousin, this conjugate succeeds in tuning the reactivity of the platinum subunit; upon binding a mismatched site, the platinum moiety then forms a covalent adduct with a nearby site. It is clear that it is the mismatch-selective Rh complex that dictates binding; the Pt moiety is seen to form interstrand as well as intrastrand crosslinks in the DNA, even though without linkage to the Rh center, cisplatin substantially prefers forming intrastrand crosslinks. Clearly, it is hoped that imparting mismatch-selectivity on such a potent anti-cancer drug may lead to a therapeutic agent against MMR-deficient cell lines.

Most recently, a third conjugate has sought to create a light-free, mismatch-specific DNA cleavage agent by tethering a $Cu(phen)_2^+$ analogue to a selective metalloinsertor (**Figure 1.21c**).[133] The data reveal that this conjugate, like the others,

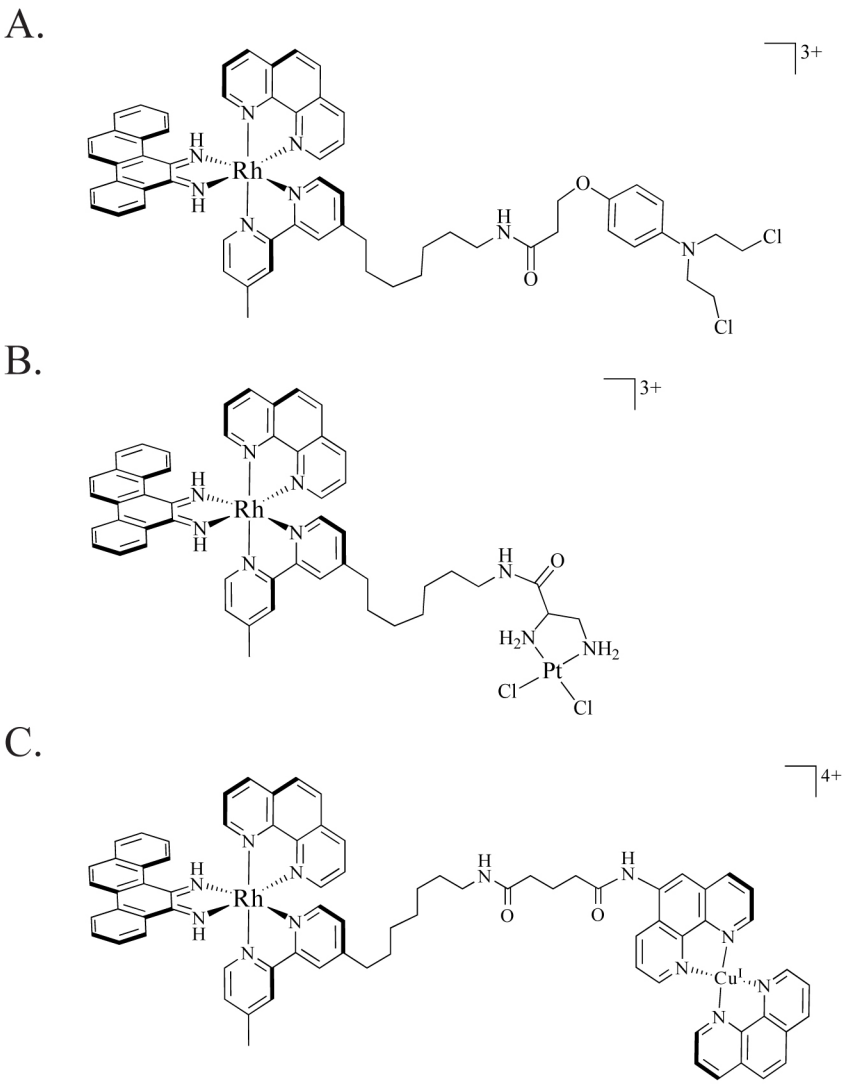

Figure 1.21: Three bifunctional, mismatch-selective conjugates. (A) A metalloinsertor-nitrogen mustard conjugate for mismatched strand-directed alkylation; (B) A metalloinsertor-cisplatin analogue conjugate for mismatched strand-directed platination; (C) A metalloinsertor-Cu(phen)$_2^+$ conjugate for the light-free cleavage of mismatched DNA.

successfully directs the reactivity of the copper oxidant. Upon the addition of a stoichiometric reductant to convert Cu(II) to the active Cu(I), light-independent DNA backbone cleavage is observed near the mismatch site at concentrations for which no cleavage is seen with untethered $Cu(phen)_2^+$ alone. Interestingly, however, the addition of the untethered rhodium metalloinsertor and copper moieties leads to similar, if not more pronounced, directed cleavage near the mismatched site, likely due to the slight opening of the minor groove caused by the Rh complex. Irrespective of potential chemotherapeutic applications, a mismatch-directed, DNA-cleaving conjugate could prove very useful, for it eliminates the need for a light source when cleaving mismatched sites. The antiproliferative effects of all three of these conjugates are currently being investigated, and the design and synthesis of other reactive conjugates are being explored (*vide infra*). Building upon the mismatch-selective binding of metalloinsertors through the design of bifunctional conjugates certainly offers new tools to probe MMR deficiencies in biological contexts.

1.7.7: CELLULAR UPTAKE

Whether for diagnostic or therapeutic applications, establishing the rapid and efficient cellular uptake of metal complexes is of fundamental importance. Cellular (and nuclear) delivery was first achieved through the conjugation of a D-octaarginine cell-penetrating peptide to the mismatch-binding rhodium complex (**Figure 1.22**).[134] The pendant peptide does not impair the ability of the rhodium moiety to bind and cleave mismatched sites; however, it does increase the non-specific binding by the complex, an

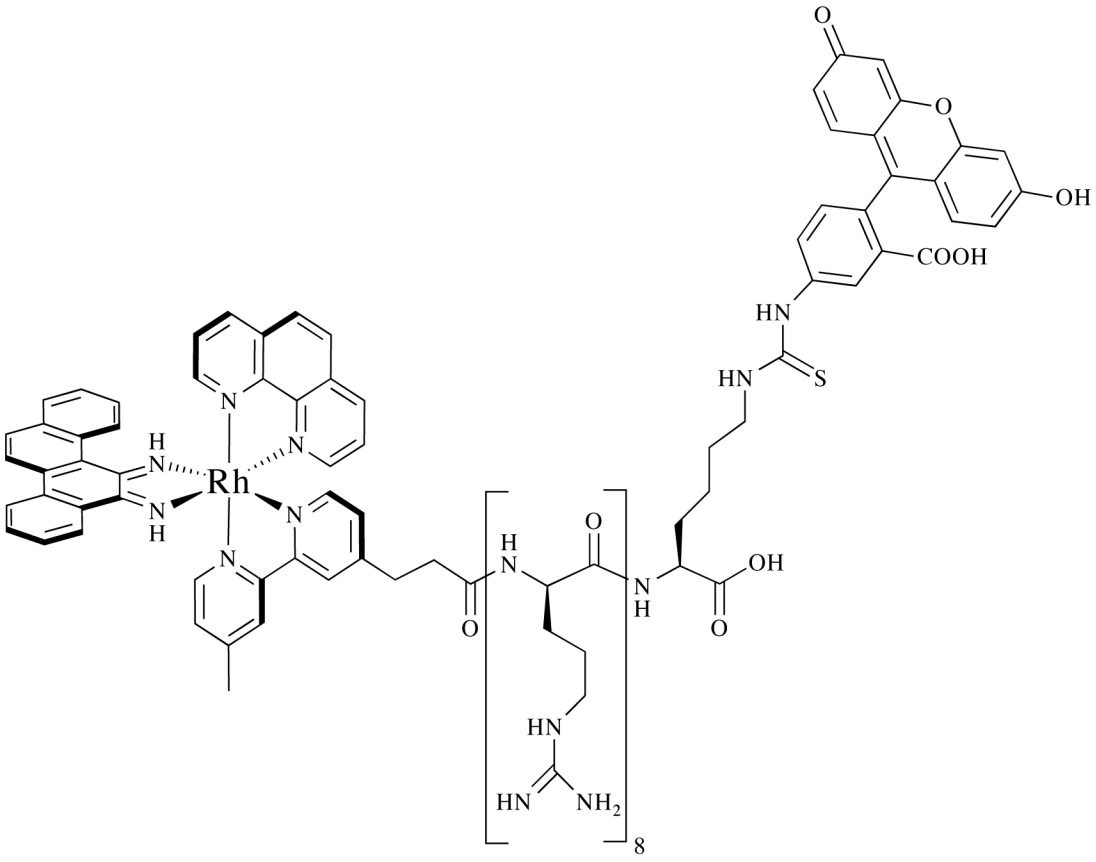

Figure 1.22. A trifunctional metalloinsertor-octaarginine-fluorophore conjugate

effect easily attributed to the strongly cationic character of the peptide. Confocal microscopy images of a similar trifunctional conjugate (this time containing a fluorophore in addition to rhodium and peptide) provide visual evidence for the rapid uptake of the conjugate into the nuclei of HeLa cells.

Despite the success of the peptide conjugate, it is becoming increasingly apparent that the cellular uptake properties of these metal complexes can be altered more simply by exploiting the modularity of their ancillary ligands. Indeed, systematic variation of the ancillary ligands offers a means to learn the characteristics of the metal complex that are essential to facilitate uptake. Using $Ru(L)_2(dppz)^{2+}$ as a scaffold, it has been shown that increasing the lipophilicity of the ancillary ligands of the complex can dramatically enhance their uptake by HeLa cells. For example, data from both fluorescent cell sorting experiments and confocal microscopy confirm that $Ru(phen)_2(dppz)^{2+}$ is more readily taken up than $Ru(bpy)_2(dppz)^{2+}$, while the extremely lipophilic $Ru(DIP)_2(dppz)^{2+}$ is taken up far better than the first two (**Figure 1.23**).[135] More recently, extensive mechanistic investigations have determined that passive diffusion is most likely the pathway for metal complex uptake.[136]

Needless to say, the lessons learned here beg to be employed directly in the study of the differential anti-proliferative effects of $Rh(bpy)_2(chrysi)^{3+}$ and $Rh(bpy)_2(phzi)^{3+}$ in mismatch repair proficient and deficient cells; one might easily suppose that maximizing uptake will augment the differential biological effect. In this case, however, the situation becomes more complicated. That metalloinsertion occurs from the sterically constrictive minor groove dictates that the ligands of any *in vivo* therapeutic must be tuned to strike a

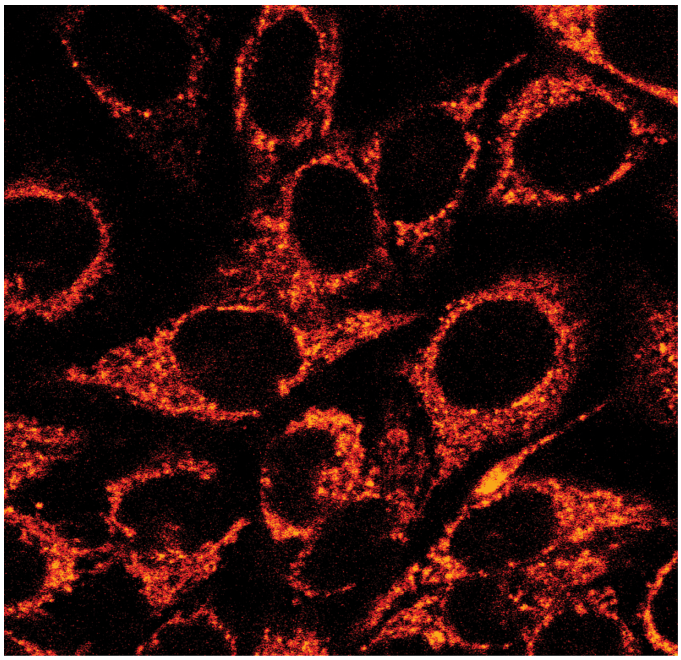

Figure 1.23. Confocal microscopy of HeLa cells incubated with $Ru(DIP)_2(dppz)^{2+}$

delicate balance between affinity (favoring small ligands) and uptake (favoring larger ligands).

1.7.8: OUTLOOK

One clear conclusion to be drawn from the work described here is that the field has witnessed explosive growth and advancement over the years, from Lerman's initial suggestion of the non-covalent binding modes possible for small molecules and DNA to the design of bifunctional mismatch-specific conjugates. Yet surely, much remains to be done. From a design and synthesis standpoint, myriad possibilities exist, including the exploitation of different metals for their unique characteristics, the recognition of more complex and varied sites, and the expansion of the nascent metalloinsertor family. However, the intersection of this field with biology holds the greatest potential for growth. Despite some significant strides, the employment of these complexes in biological systems as probes, diagnostics, or therapeutics represents a largely untapped area with potentially tremendous value.

1.8: REFERENCES

1. Demeunynck, M.; Bailly, W. D. *Small Molecule DNA and RNA Binders: From Synthesis to Nucleic Acid Complexes*. Wiley−VCH: Weinheim, 2002.
2. Lippard, S. J.; Berg, J. M. *Principles of Bioinorganic Chemistry* University Science Books: Mill Valley, CA, 1994.
3. Erkkila, K. E.; Odom, D. T.; Barton, J. K. *Chemical Reviews* **1999,** *99* (9), 2777−2795.
4. Watson, J. D.; Crick, F. H. C. *Nature* **1953,** *171* (4356), 737−738.
5. Bloomfield, V. A.; Crothers, D. M.; Tinoco, I. *Nucleic Acids: Structure, Properties, and Functions*. University Science Books: Sausalito, California, 2000.
6. Izatt, R. M.; Christen, J. J.; Rytting, J. H. *Chemical Reviews* **1971,** *71* (5), 439−481.
7. Eichhorn, G. L.; Shin, Y. A. *Journal of the American Chemical Society* **1968,** *90* (26), 7323−7238.
8. Beer, M.; Moudrianakis, E. N. *Proceedings of the National Academy of Sciences of the United States of America* **1962,** *48* (3), 409−416.
9. Heitner, H. I.; Sunshine, H. R.; Lippard, S. J. *Journal of the American Chemical Society* **1972,** *94* (25), 8936−8937.
10. Dwyer, F. P.; Gyarfas, E. C.; Rogers, W. P.; Koch, J. H. *Nature* **1952,** *170* (4318), 190−191.
11. Jennette, K. W.; Lippard, S. J.; Vassilia, G. A.; Bauer, W. R. *Proceedings of the National Academy of Sciences of the United States of America* **1974,** *71* (10), 3839−3843.

12. Bond, P. J.; Langridge, R.; Jennette, K. W.; Lippard, S. J. *Proceedings of the National Academy of Sciences of the United States of America* **1975,** *72* (12), 4825−4829.
13. Howe−Grant, M.; Lippard, S. J. *Biochemistry* **1979,** *18* (26), 5762−5769.
14. Sigman, D. S. *Accounts of Chemical Research* **1986,** *19* (6), 180−186.
15. Meijler, M. M.; Zelenko, O.; Sigman, D. S. *Journal of the American Chemical Society* **1997,** *119* (5), 1135−1136.
16. Chen, C. H. B.; Milne, L.; Landgraf, R.; Perrin, D. M.; Sigman, D. S. *Chembiochem* **2001,** *2* (10), 735−740.
17. Pope, L. E.; Sigman, D. S. *Proceedings of the National Academy of Sciences of the United States of America−Biological Sciences* **1984,** *81* (1), 3−7.
18. Sigman, D. S.; Bruice, T. W.; Mazumder, A.; Sutton, C. L. *Accounts of Chemical Research* **1993,** *26* (3), 98−104.
19. Chen, J. Y.; Stubbe, J. *Nature Reviews Cancer* **2005,** *5* (2), 102−112.
20. Stubbe, J.; Kozarich, J. W.; Wu, W.; Vanderwall, D. E. *Accounts of Chemical Research* **1996,** *29* (7), 322−330.
21. Boger, D. L.; Cai, H. *Angewandte Chemie−International Edition* **1999,** *38* (4), 448−476.
22. Burger, R. M. *Chemical Reviews* **1998,** *98* (3), 1153−1169.
23. Keck, M. V.; Manderville, R. A.; Hecht, S. M. *Journal of the American Chemical Society* **2001,** *123* (36), 8690−8700.
24. Dandrea, A. D.; Haseltine, W. A. *Proceedings of the National Academy of Sciences of the United States of America* **1978,** *75* (8), 3608−3612.

25. Barton, J. K.; Dannenberg, J. J.; Raphael, A. L. *Journal of the American Chemical Society* **1982,** *104* (18), 4967−4969.

26. Barton, J. K.; Danishefsky, A. T.; Goldberg, J. M. *Journal of the American Chemical Society* **1984,** *106* (7), 2172−2176.

27. Kumar, C. V.; Barton, J. K.; Turro, N. J. *Journal of the American Chemical Society* **1985,** *107* (19), 5518−5523.

28. Rehmann, J. P.; Barton, J. K. *Biochemistry* **1990,** *29* (7), 1701−1709.

29. Rehmann, J. P.; Barton, J. K. *Biochemistry* **1990,** *29* (7), 1710−1717.

30. Barton, J. K.; Raphael, A. L. *Proceedings of the National Academy of Sciences of the United States of America* **1985,** *82* (19), 6460−6464.

31. Barton, J. K. *Science* **1986,** *233*, 727−732.

32. Barton, J. K.; Basile, L. A.; Danishefsky, A. T.; Alexandrescu, A. *Proceedings of the National Academy of Sciences of the United States of America* **1984,** *82*, 6460−6468.

33. Barton, J. K.; Raphael, A. L. *Journal of the American Chemical Society* **1984,** *106* (8), 2466−2468.

34. Eriksson, M.; Leijon, M.; Hiort, C.; Norden, B.; Graslund, A. *Biochemistry* **1994,** *33* (17), 5031−5040.

35. Fu, P. K. L.; Bradley, P. M.; van Loyen, D.; Durr, H.; Bossmann, S. H.; Turro, C. *Inorganic Chemistry* **2002,** *41* (15), 3808−3810.

36. Schoentjes, B.; Lehn, J. M. *Helvetica Chimica Acta* **1995,** *78* (1), 1−12.

37. Hannon, M. J. *Chemical Society Reviews* **2007,** *36* (2), 280−295.

38. Oleksi, A.; Blanco, A. G.; Boer, R.; Uson, I.; Aymami, J.; Rodger, A.; Hannon, M. J.; Coll, M. *Angewandte Chemie−International Edition* **2006,** *45* (8), 1227−1231.

39. Uerpmann, C.; Malina, J.; Pascu, M.; Clarkson, G. J.; Moreno, V.; Rodger, A.; Grandas, A.; Hannon, M. J. *Chemistry−a European Journal* **2005,** *11* (6), 1750−1756.

40. Friedman, A. E.; Chambron, J. C.; Sauvage, J. P.; Turro, N. J.; Barton, J. K. *Journal of the American Chemical Society* **1990,** *112* (12), 4960−4962.

41. Friedman, A. E.; Kumar, C. V.; Turro, N. J.; Barton, J. K. *Nucleic Acids Research* **1991,** *19* (10), 2595−2602.

42. Jenkins, Y.; Friedman, A. E.; Turro, N. J.; Barton, J. K. *Biochemistry* **1992,** *31* (44), 10809−10816.

43. Hartshorn, R. M.; Barton, J. K. *Journal of the American Chemical Society* **1992,** *114* (15), 5919−5925.

44. Hiort, C.; Lincoln, P.; Norden, B. *Journal of the American Chemical Society* **1993,** *115* (9), 3448−3454.

45. Lincoln, P.; Broo, A.; Norden, B. *Journal of the American Chemical Society* **1996,** *118* (11), 2644−2653.

46. Tuite, E.; Lincoln, P.; Norden, B. *Journal of the American Chemical Society* **1997,** *119* (1), 239−240.

47. Franklin, S. J.; Barton, J. K. *Biochemistry* **1998,** *37* (46), 16093−16105.

48. Hudson, B. P.; Barton, J. K. *Journal of the American Chemical Society* **1998,** *120* (28), 6877−6888.

49. Dupureur, C. M.; Barton, J. K. *Journal of the American Chemical Society* **1994,** *116* (22), 10286−10287.

50. Collins, J. G.; Shields, T. P.; Barton, J. K. *Journal of the American Chemical Society* **1994,** *116* (22), 9840−9846.

51. Kielkopf, C. L.; Erkkila, K. E.; Hudson, B. P.; Barton, J. K.; Rees, D. C. *Nature Structural Biology* **2000,** *7* (2), 117−121.

52. Wang, A. H. J.; Nathans, J.; Vandermarel, G.; Vanboom, J. H.; Rich, A. *Nature* **1978,** *276* (5687), 471−474.

53. Pierre, V. C.; Kaiser, J. T.; Barton, J. K. *Proceedings of the National Academy of Sciences U. S. A.* **2007,** *103*, 429−434.

54. Greguric, I.; AldrichWright, J. R.; Collins, J. G. *Journal of the American Chemical Society* **1997,** *119* (15), 3621−3622.

55. Fry, J. V.; Collins, J. G. *Inorganic Chemistry* **1997,** *36* (13), 2919−&.

56. Collins, J. G.; Sleeman, A. D.; Aldrich−Wright, J. R.; Greguric, I.; Hambley, T. W. *Inorganic Chemistry* **1998,** *37* (13), 3133−3141.

57. Turro, C.; Bossmann, S. H.; Jenkins, Y.; Barton, J. K.; Turro, N. J. *Journal of the American Chemical Society* **1995,** *117* (35), 9026−9032.

58. Olson, E. J. C.; Hu, D.; Hormann, A.; Jonkman, A. M.; Arkin, M. R.; Stemp, E. D. A.; Barton, J. K.; Barbara, P. F. *Journal of the American Chemical Society* **1997,** *119* (47), 11458−11467.

59. Holmlin, R. E.; Stemp, E. D. A.; Barton, J. K. *Inorganic Chemistry* **1998,** *37* (1), 29−34.

60. Onfelt, B.; Lincoln, P.; Norden, B. *Journal of the American Chemical Society* **1999,** *121* (46), 10846−10847.

61. Onfelt, B.; Lincoln, P.; Norden, B. *Journal of the American Chemical Society* **2001,** *123* (16), 3630−3637.

62. Xiong, Y.; Ji, L. N. *Coordination Chemistry Reviews* **1999,** *185−6*, 711−733.

63. Sitlani, A.; Long, E. C.; Pyle, A. M.; Barton, J. K. *Journal of the American Chemical Society* **1992,** *114* (7), 2303−2312.

64. Fitzsimons, M. P.; Barton, J. K. *Journal of the American Chemical Society* **1997,** *119* (14), 3379−3380.

65. Copeland, K. D.; Lueras, A. M. K.; Stemp, E. D. A.; Barton, J. K. *Biochemistry* **2002,** *41* (42), 12785−12797.

66. Sitlani, A.; Barton, J. K. *Biochemistry* **1994,** *33* (40), 12100−12108.

67. Sitlani, A.; Dupureur, C. M.; Barton, J. K. *Journal of the American Chemical Society* **1993,** *115* (26), 12589−12590.

68. Pyle, A. M.; Long, E. C.; Barton, J. K. *Journal of the American Chemical Society* **1989,** *111* (12), 4520−4522.

69. Pyle, A. M.; Morii, T.; Barton, J. K. *Journal of the American Chemical Society* **1990,** *112* (25), 9432−9434.

70. Campisi, D.; Morii, T.; Barton, J. K. *Biochemistry* **1994,** *33* (14), 4130−4139.

71. Chow, C. S.; Barton, J. K. *Biochemistry* **1992,** *31* (24), 5423−5429.

72. Chow, C. S.; Behlen, L. S.; Uhlenbeck, O. C.; Barton, J. K. *Biochemistry* **1992,** *31* (4), 972−982.

73. Lim, A. C.; Barton, J. K. *Biochemistry* **1993,** *32* (41), 11029−11034.

74. Chow, C. S.; Hartmann, K. M.; Rawlings, S. L.; Huber, P. W.; Barton, J. K. *Biochemistry* **1992,** *31* (13), 3534−3542.

75. Krotz, A. H.; Kuo, L. Y.; Barton, J. K. *Inorganic Chemistry* **1993,** *32* (26), 5963−5974.

76. Krotz, A. H.; Kuo, L. Y.; Shields, T. P.; Barton, J. K. *Journal of the American Chemical Society* **1993,** *115* (10), 3877−3882.

77. Shields, T. P.; Barton, J. K. *Biochemistry* **1995,** *34* (46), 15037−15048.

78. Shields, T. P.; Barton, J. K. *Biochemistry* **1995,** *34* (46), 15049−15056.

79. Krotz, A. H.; Hudson, B. P.; Barton, J. K. *Journal of the American Chemical Society* **1993,** *115* (26), 12577−12578.

80. Terbrueggen, R. H.; Barton, J. K. *Biochemistry* **1995,** *34* (26), 8227−8234.

81. Terbrueggen, R. H.; Johann, T. W.; Barton, J. K. *Inorganic Chemistry* **1998,** *37* (26), 6874−6883.

82. Odom, D.; Parker, C. S.; Barton, J. K. *Journal of Inorganic Biochemistry* **1999,** *74* (1−4), 252−252.

83. Fu, P. K. L.; Bradley, P. M.; Turro, C. *Inorganic Chemistry* **2003,** *42* (3), 878−884.

84. Fu, P. K. L.; Turro, C. *Chemical Communications* **2001,** (03), 279−280.

85. Lerman, L. S. *Journal of Molecular Biology* **1961,** *3*, 18−30.

86. Marnett, L. J.; Plastaras, J. P. *Trends in Genetics* **2001,** *17*, 214−221.

87. Brown, T.; Hunter, W. N.; Kneale, G.; Kennard, O. *Proceedings of the National Academy of Sciences of the United States of America* **1996,** *83*, 2402−2406.

88. Hunter, W. N.; Brown, T.; Kennard, O. *Nucleic Acids Research* **1987,** *15*, 6589−6606.

89. Hunter, W. N.; Brown, T.; Kneale, G.; Anand, N. N.; Rabinovich, D.; Kennard, O. *Journal of Biological Chemistry* **1987,** *262*, 9962−9970.

90. Skelly, J. V.; Edwards, K. J.; Jenkins, T. C.; Neidle, S. *Proceedings of the National Academy of Sciences of the United States of America* **1993,** *90*, 804−808.

91. Drew, H. R.; Wing, R. M.; Takano, R.; Broa, C.; Tanaka, S.; Itakura, K.; Dickerson, R. E. *Proceedings of the National Academy of Sciences of the United States of America* **1981,** *78*, 2179−2183.

92. Arnold, F. H.; Wolk, S.; Cruz, P.; Tinoco, I. *Biochemistry* **1987,** *26*, 4068−4075.

93. Isaacs, R. J.; Rayens, W. S.; Spielmann, H. P. *Journal of Molecular Biology* **2002,** *319*, 191−207.

94. Peyret, N.; Seneviratne, P. A.; Allawi, H. T.; SantaLucia, J. *Biochemistry* **1999,** *38*, 3468−3477.

95. SantaLucia, J.; Hicks, D. *Annual Reviews in Biophysics and Biomolecular Structure* **2004,** *33*, 415−440.

96. Allawi, H. T.; SantaLucia, J. *Biochemistry* **1998,** *37* (26), 9435−9444.

97. Allawi, H. T.; SantaLucia, J. *Biochemistry* **1997,** *36* (34), 10581−10594.

98. Allawi, H. T.; SantaLucia, J. *Biochemistry* **1998,** *37* (8), 2170−2179.

99. Allawi, H. T.; Santalucia, J. *Nucleic Acids Research* **1998,** *26* (11), 2694−2701.

100. Allawi, H. T.; SantaLucia, J. *Nucleic Acids Research* **1998,** *26* (21), 4925−4934.

101. Kunkel, T. A. *Journal of Biological Chemistry* **2004,** *279*, 16895−16898.

102. Schaaper, R. M. *Journal of Biological Chemistry* **1993,** *268*, 23762−23765.

103. Drake, J. W.; Charlesworth, B.; Charlesworth, D.; Crow, J. F. *Genetics* **1998,** *148*, 1667−1686.

104. Kunkel, T. A. *Cancer Cell* **2003,** *3*, 105−110.

105. Lehmann, A. R. *FEBS Letters* **2005,** *579*, 873−876.

106. Gerton, J. L.; Hawley, R. S. *Nature Reviews Genetics* **2005,** *6*, 477−487.

107. Samaranayake, M.; Bujnicki, J. M.; Carpenter, N.; Bhagwat, A. S. *Chemical Reviews* **2006,** *106*, 700−719.

108. Iyer, R. R.; Pluciennik, A.; Burdett, V.; Modrich, P. *Chemical Reviews* **2006,** *106*, 302−323.

109. Kolodner, R. *Genes & Development* **1996,** *10* (12), 1433−1442.

110. Modrich, P. *Journal of Biological Chemistry* **2006,** *281* (41), 30305−30309.

111. Kolodner, R. D. *Trends in Biochemical Science* **1995,** *20*, 397−401.

112. Jacob, S.; Praz, F. *Biochemie* **2002,** *84*, 27−47.

113. Fink, D.; Aebi, S.; Howell, S. B. *Clinical Cancer Research* **1998,** *4* (1), 1−6.

114. Dervan, P. B.; Edelson, B. S. *Current opinion in Structural Biology* **2003,** *13*, 284−299.

115. Lacy, E. R.; Cox, K. K.; Wilson, W. D.; Lee, M. *Nucleic Acids Research* **2002,** *30*, 1834−1841.

116. Lacy, E. R.; Nguyen, B.; Le, M.; Cox, K. K.; Hartley, J. A.; Lee, M.; Wilson, W. D. *Nucleic Acids Research* **2004,** *32*, 2000−2007.

117. Nakatani, K.; Sando, S.; Saito, I. *Journal of the American Chemical Society* **2000,** *122*, 2172−2177.

118. Murner, H.; Jackson, B. A.; Barton, J. K. *Inorganic Chemistry* **1998,** *37* (12), 3007−3012.

119. Jackson, B. A.; Barton, J. K. *Journal of the American Chemical Society* **1997,** *119* (52), 12986−12987.

120. Jackson, B. A.; Alekseyev, V. Y.; Barton, J. K. *Biochemistry* **1999,** *38* (15), 4655−4662.

121. Jackson, B. A.; Barton, J. K. *Biochemistry* **2000,** *39* (20), 6176−6182.

122. Junicke, H.; Hart, J. R.; Kisko, J. L.; Glebov, O.; Kirsch, I. R.; Barton, J. K. *Proceedings of the National Academy of Sciences U. S. A.* **2003,** *100*, 3737−3742.

123. Hudson, B. P.; Dupureur, C. M.; Barton, J. K. *Journal of the American Chemical Society* **1995,** *117* (36), 9379−9380.

124. Cordier, C.; Pierre, V. C.; Barton, J. K. *Journal of the American Chemical Society* **2007,** *129*, 12287−12295.

125. Brunner, J.; Barton, J. K. *Journal of the American Chemical Society* **2006,** *128* (21), 6772−6773.

126. Ruba, E.; Hart, J. R.; Barton, J. K. *Inorganic Chemistry* **2004,** *43* (15), 4570−4578.

127. Hart, J. R.; Johnson, M. D.; Barton, J. K. *Proceedings of the National Academy of Sciences of the United States of America* **2004,** *101* (39), 14040−14044.

128. Rider, M. J.; Taylor, S. L.; Tobe, V. O.; Nickerson, D. A. *Nucleic Acids Research* **1998,** *26* (967−973).

129. Hart, J. R.; Glebov, O.; Ernst, R. J.; Kirsch, I. R.; Barton, J. K. *Proceedings of the National Academy of Sciences U. S. A.* **2006,** *103*, 15359−15363.

130. Ernst, R. J.; Song, H.; Barton, J. K. *Journal of the American Chemical Society* **2009,** *131* (6), 2359−2366.

131. Schatzschneider, U.; Barton, J. K. *Journal of the American Chemical Society* **2004,** *126* (28), 8630−8631.

132. Petitjean, A.; Barton, J. K. *Journal of the American Chemical Society* **2004,** *126* (45), 14728−14729.

133. Lim, M. H.; Lau, I. H.; Barton, J. K. *Inorganic Chemistry* **2007,** *46*, 9528−9530.

134. Brunner, J.; Barton, J. K. *Biochemistry* **2006,** *45* (40), 12295−12302.

135. Puckett, C. A.; Barton, J. K. *Journal of the American Chemical Society* **2007,** *129* (1), 46−47.

136. Puckett, C. A.; Barton, J. K. *Biochemistry* **2008,** *47* (45), 11711−11716.

CHAPTER 2: PROTOCOLS[ρ]

2.1: INTRODUCTION

Any doctoral thesis functions primarily as the synthesis and exposition of the writer's research. However, many theses, especially those from experimental laboratories, moonlight in a second, almost equally important role: reference work for future researchers. Indeed, these pages offer a singular opportunity to pass on the details of fundamental experimental protocols, unhastened and unabridged by the exigencies of publication.

In this chapter, a set of experimental procedures essential to the study of metalloinsertors is described.[1] Guidelines for both syntheses and nucleic acid experiments are addressed; however, procedures specific to a single line of investigation (e.g. the synthesis of eilatin or crystal structure refinement) are included in the pertinent chapter.

2.2: INSTRUMENTATION AND MATERIALS

All reagents were obtained from commercial sources and used as received without further purification. NMR spectra were recorded on a Varian 400 MHz spectrometer. Mass spectrometry was performed at either the Caltech mass spectrometry facility or in the Beckman Institute Protein/Peptide Micro Analytical Laboratory (PPMAL). Absorption spectra were recorded on a Beckman DU 7400 spectrophotometer, and circular dichroism spectra were recorded on a Jasco J-500A spectropolarimeter. Unless otherwise noted, all reactions were performed under ambient conditions.

[ρ] Parts of this chapter were adapted from Zeglis, B. M.; Barton, J. K. DNA base mismatch detection with bulky rhodium metallointercalators: synthesis and applications. *Nature Protocols.* **2007**, *2(2)*, 357−371.

Oligonucleotides were synthesized on an ABI 3400 DNA synthesizer and purified in duplicate (DMT-off and DMT-on) before use. HPLC purifications were performed on an HP1100 high-pressure liquid chromatography system equipped with a diode array detector using a Varian DynaMax C18 semipreparative column. Irradiations were performed using an Oriel Instruments solar simulator (320−440 nm). All PAGE experiments described employed denaturing 20% polyacrylamide gels (SequaGel, National Diagnostics) and were performed according to published procedures. Further, gels were developed using Molecular Dynamics phosphorimaging screens and a Molecular Dynamics Storm 820 phosphorimager and were subsequently visualized and quantified with Molecular Dynamics ImageQuant software. Further instrumentation and materials specific to individual investigations (e.g. X-ray irradiation sources, etc.) will be addressed in the relevant chapters.

2.3: Synthetic Protocols

2.3.1: Synthesis of *ortho*-quinone ligand precursors

2.3.1.1: Synthesis of chrysene-5,6-quinone

Chrysene-5,6-quinone was produced by the method of Graebe and Honigsburger with minor modifications.[2] A 250 mL round bottom flask was charged with 10.0 g (44 mmol) chrysene and 110 mL glacial acetic acid (**Figure 2.1**). Subsequently, 46 g sodium dichromate were added slowly with stirring to the reaction mixture, and the resultant slurry was heated to reflux. The reaction was then monitored until white solid could no longer be seen in the refluxing suspension (approximately 24−36 h). At this point, heating was stopped, the mixture was poured into 100 mL boiling water, and the product

was hot filtered through a medium glass frit. The resultant orange precipitate was washed three times with 100 mL boiling water and subsequently recrystallized from hot ethanol to yield the orange, crystalline product (85% yield).

^{1}H-NMR (CD_2Cl_2): 9.39 ppm (d, 1H); 8.16 ppm (m, 4H); 7.92 (d, 1H); 7.77 ppm (t of d, 2H); 7.57 ppm (t of d, 2H).

ESI-MS (m/z): 257 $[M+H]^+$

2.3.1.2: SYNTHESIS OF 3,4-BENZO[A]PHENAZINE QUINONE

The 3,4-benzo[a]-phenazine quinone ligand precursor was synthesized according to the procedure published by Junicke et al.[3, 4] A 250 mL round bottom flask was charged with 4.5 g (20 mmol) 2,3-dichloro-1,4-napthoquinone and 2.0 g (20 mmol) *o*-phenylene diamine in 125 mL pyridine (**Figure 2.2**). The solution was brought to reflux and allowed to stir with heating for 1 h. The reaction mixture was then allowed to cool to room temperature and was subsequently filtered on a medium glass frit to yield a brown-red solid (the intermediate, 6-pyridinium-benzo[a]phenazine-5-olate) in quantitative yield.

The red-brown solid was then freed from excess pyridine via rotary evaporation. After weighing, the solid was placed in a second round-bottom flask and dissolved in 10 mL glacial acetic acid and 1 mL concentrated nitric acid. Water (0.66 mL/g) was added accordingly. The resultant mixture was heated in a boiling water bath for 1 h (the reaction is complete when only yellow-orange precipitate remains). After heating, the product was precipitated by pouring the solution into 100 mL cold water, collected via filtration on a medium glass frit, and washed three times with ethanol (50 mL) and three times with

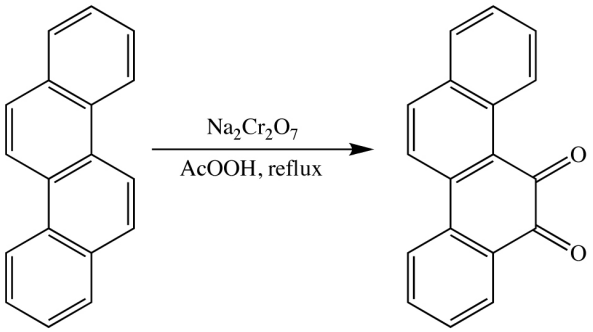

Figure 2.1: Synthesis of chrysene-5,6-quinone. Chrysene is oxidized to chrysene-5,6-quinone with sodium dichromate.

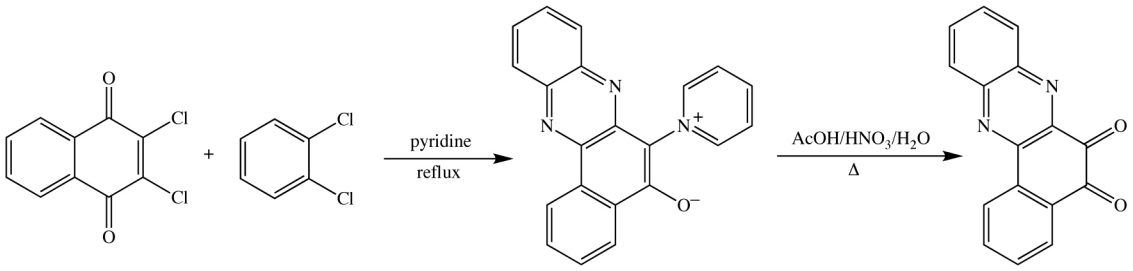

Figure 2.2: Synthesis of 3.4-benzo[a]phenazine quinone. 2,3-dichloro-1,4-naphthoquinone is reacted with *ortho*-phenylene diamine in pyridine to produce a zwitterionic intermediate (6-pyridinium-benzo[a]phenazine-5-olate) that is subsequently oxidized by nitric acid to form the desired product.

diethyl ether (50 mL). A yellow-green powder results (>75% yield) that can be re-crystallized from 7:3 chloroform:ethyl acetate (vol:vol).

^{1}H-NMR ($CDCl_3$): 8.78 ppm (d, 1H); 8.24 ppm (d, 1H); 8.21 ppm (d, 1H); 8.15 ppm (d, 1H); 8.01 ppm (t, 1H); 7.94 ppm (t, 1H); 7.90 ppm (t, 1H); 7.73 ppm (t, 1H).

ESI-MS: 261 $[M+H]^+$

2.3.2: SYNTHESIS OF BISDIPYRIDYL COMPLEXES

2.3.2.1: SYNTHESIS OF $[Rh(bpy)_2Cl_2]Cl$

[$Rh(bpy)_2Cl_2]^+$ was prepared by analogy to the method of Gillard and co-workers with minor modifications.[5, 6] A 50 mL round-bottom flask was charged with 0.64 g $RhCl_3$ (2.8 mmol) and 50 mg hydrazine monohydrochloride in 12.5 mL deionized water. A solution of 0.85 g (5.6 mmol) bipyridine in 12.5 mL ethanol was then added, and the resultant solution was deoxygenated via the freeze-pump-thaw technique. The degassed mixture was then brought to reflux under argon and heated until all the materials have dissolved (approximately 20 minutes) and formed a yellow-orange solution. While still hot, the resultant solution was filtered through a medium glass frit and immediately placed in a refrigerator to chill at 4 ºC overnight to promote crystallization. The next morning, the resulting yellow crystals (0.95 g, 70% yield) were collected by filtration and dried under vacuum. A synthetic scheme for this reaction and those described in 2.3.4−2.3.9 are shown in **Figure 2.3**.

^{1}H-NMR (d_6-DMSO): 9.71 ppm (d, 2H); 9.0 ppm (d, 2H); 8.91 ppm (d, 2H); 8.63 ppm (t, 2H); 8.33 ppm (t, 2H); 8.17 ppm (t, 2H); 7.82 ppm (d, 2H); 7.59 ppm (t, 2H).

ESI-MS: 486 $[M]^+$

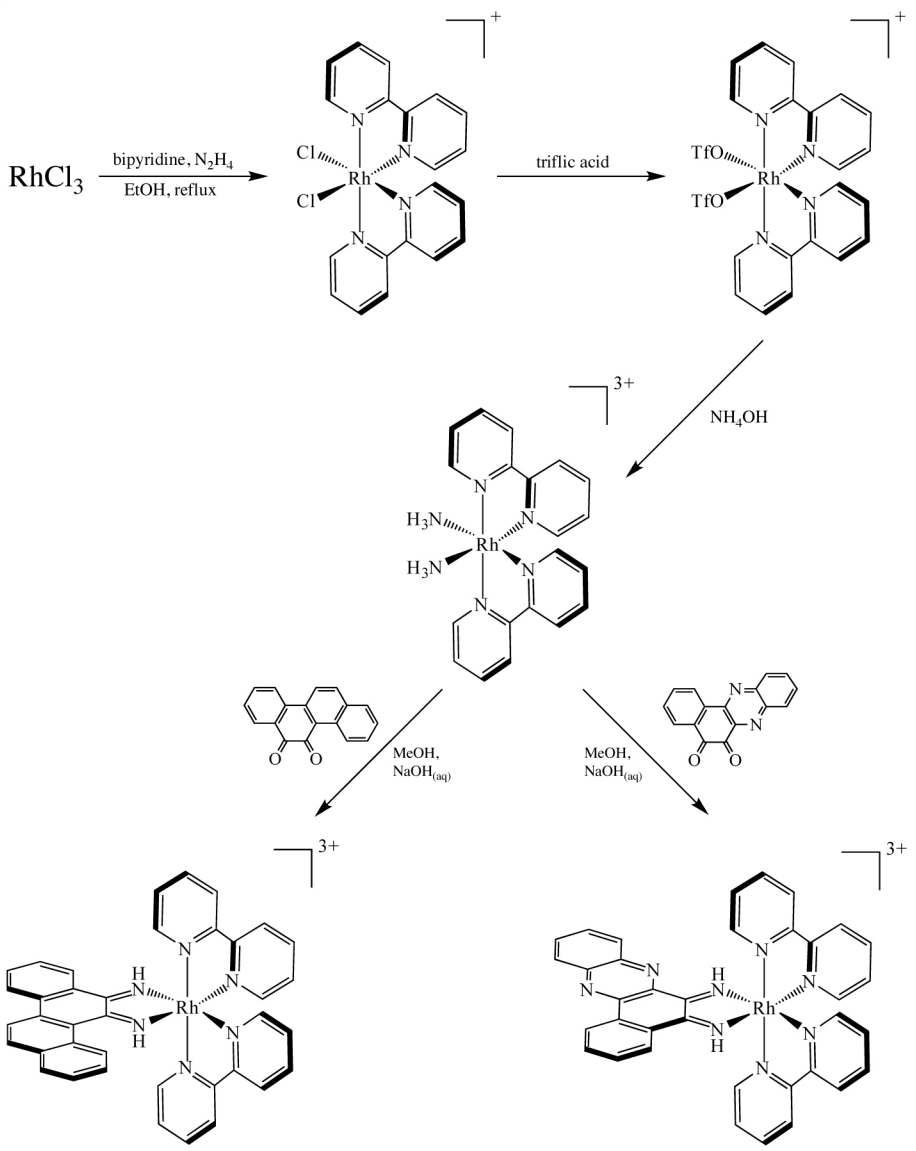

Figure 2.3: Scheme for the synthesis of *rac*-Rh(bpy)$_2$(chrysi)$^{3+}$ and *rac*-Rh(bpy)$_2$(phzi)$^{3+}$

2.3.2.2: SYNTHESIS OF $[Rh(bpy)_2(OTf)_2]OTf$

$[Rh(bpy)_2(OTf)_2]OTf$ and $[Rh(bpy)_2(NH_3)_2](X)_3$ were prepared by the method of Gidney and coworkers with minor modifications.[7] A 50-mL Schlenk flask was charged with 500 mg $Rh(bpy)_2(Cl)_2^+$ (~ 1 mmol) and deoxygenated by evacuating it and refilling with $Ar_{(g)}$ three times. Subsequently, 5 g triflic acid (excess) were added carefully to the reaction vessel under positive argon pressure (caution: triflic acid is very reactive, pyrophoric, and, to make matters worse, eats through gloves). After the addition of HOTf, the reaction vessel was closed with a rubber septum, the septum was pierced with a 16-gauge needle, and the flask was purged with argon for 60 seconds. The dark red reaction mixture was allowed to stir for 16 h with periodic $Ar_{(g)}$ purges to remove HCl generated by the reaction. After 16 h, the reaction mixture was added dropwise to 300 mL vigorously stirring diethyl ether cooled to -78 ºC. The resultant yellowish precipitate was collected via filtration on a Buchner funnel, washed with cold diethyl ether, and used as promptly as possible.

2.3.2.3: SYNTHESIS OF $[Rh(bpy)_2(NH_3)_2](X)_3$

In a 250-mL round-bottom flask fitted with a reflux condenser, 500 mg $Rh(bpy)_2(OTf)_2^+$ (0.6 mmol) were suspended in 50 mL concentrated NH_4OH. The suspension was stirred, brought to reflux, and heated until all of the material went into solution (15 min); over the course of heating, the insoluble, singly charged complex is converted to the more soluble, triply-charged complex. Depending on the desired counter-ion, the product can be isolated one of two ways: (a) if the PF_6^- salt is desired, excess NH_4PF_6 should be added to the solution, and the reaction mixture should be

cooled overnight to facilitate precipitation; (b) if the OTf^- counter-ion is desired, the NH_4OH should simply be removed by rotary evaporation at room temperature. Recoveries are best using the evaporation method and range from 80−100% depending on mechanical losses.

^1H NMR (d_6-acetone, PF_6^- salt): 9.45 ppm (d, 2H); 9.05 ppm (d, 2H); 8.89 ppm (d, 2H); 8.79 ppm (split t, 2H); 8.45 ppm (split t, 2H); 8.30 ppm (split t, 2H); 8.05 ppm (d, 2H); 7.74 ppm (split t, 2H); 5.06 ppm (broad s, 6H).

ESI-MS: 449 $[M-2H]^+$

2.3.2.4: METALLATION BY CONDENSATION

The metallation of the intercalating and inserting ligands (*i.e.* phi, chrysi, phzi) is accomplished via the condensation of the ligand *ortho*-quinones onto a metal *cis*-diammine complex (**Figure 2.4**).[6] This clean and facile reaction is based on the pioneering work of Sargeson on inter- and intramolecular condensation reactions.[8−13] Indeed, Schiff base condensations have been shown to be possible with coordinated ligands with retention of configuration at the metal center. Two alternative methods exist: (1) the metallation of the diamine followed by the air-mediated oxidation of the ligand to the corresponding diimine[14−16] and (2) the *in situ* deprotection and subsequent metallation of a trimethylsilylimine variant of the ligand of interest.[17] Both strategies, however, are severely limited by product yield and the requirement for cumbersome anaerobic conditions.

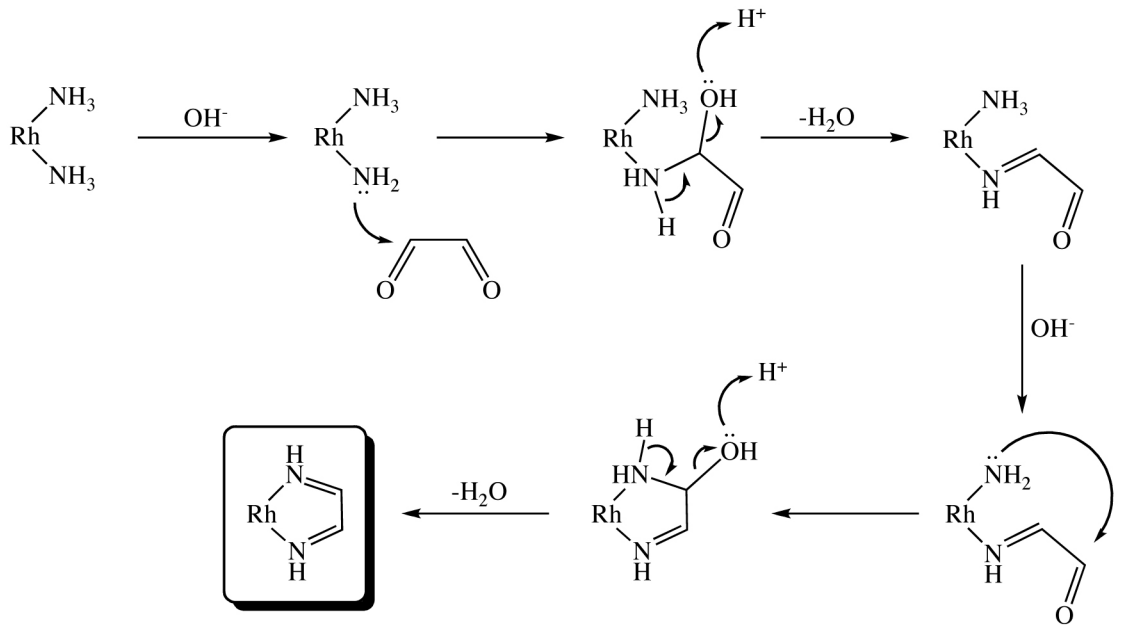

Figure 2.4: *O*-quinone condensation mechanism. One of the ammines in a *cis*-diammine complex is deprotonated by a base and attacks the quinone carbon to form a hemiaminal intermediate. This structure can then dehydrate to form an imine. This reaction is then followed by an identical, intramolecular condensation to form the desired diimine ligand.

In the condensation reaction, one of the ammines in a *cis*-diammine complex is deprotonated by a base and attacks the quinone carbon to form a hemiaminal intermediate, a structure that quickly and cleanly dehydrates to form an imine. This reaction is then followed by an identical, intramolecular condensation to form the desired diimine ligand. Many metal *cis*-ammine complexes can be employed for this reaction. However, one must pay particular attention to the pKa values for the coordinated ammines in question.[18, 19] *Cis*-ammine complexes of Rh(III) work well, because the pKa of the metal-bound ammines is approximately 10 and are thus readily deprotonated by aqueous NaOH. The pKa values of ammines in analogous Ru(II) complexes, in contrast, are higher and mostly likely require a stronger base to make the reaction proceed.

2.3.2.5: SYNTHESIS OF $[Rh(bpy)_2(chrysi)](Cl)_3$

In a 100-mL round-bottom flask, 195 mg $[Rh(bpy)_2(NH_3)_2](PF_6)_3$ (0.2 mmol) and 57 mg chrysene-5,6-quinone (0.22 mmol) were dissolved in 50 mL MeCN with rapid stirring under ambient conditions.[20, 21] After 10 min, 2 mL aqueous sodium hydroxide (0.4 M) were added, and the reaction vessel was closed to prevent evaporation. After 3 h, the reaction was halted by bringing the pH of the solution to 7.0 by adding a stoichiometric amount of $HCl_{(aq)}$. By this point, the reaction should have changed color dramatically from orange/yellow to dark red; the reaction can also be monitored by TLC using silica F plates in a solvent system of 3:1:1 MeCN/H_2O/MeOH (vol/vol/vol) with 0.1 M KNO_3. After neutralization, the MeCN and H_2O were removed *in vacuo* by rotary evaporation.

The resulting solid was re-dissolved in a minimum volume of water and purified via cation-exchange chromatography using Sephadex SP-C25 ion exchange resin. Four inches of resin pre-equilibrated with 0.05 M $MgCl_2$ were poured into a 1−1.5 inch diameter column and subsequently washed with copious (500 mL) deionized H_2O. The rhodium complex was loaded onto the column simply by passing the aqueous Rh solution through the resin (the rhodium complex will 'stick' to the top of the column, forming a thin, dark red band). The complex was then eluted by slowly increasing the [$MgCl_2$] in the eluent in 500-mL batches, starting with 0.05 M $MgCl_2$ and increasing in increments of 0.05 M until the red band of the metal complex has passed through the column. The resultant eluted solution was concentrated on a reverse-phase cartridge primed with MeOH and eluted with 1:1:0.001 H_2O/MeCN/TFA (vol/vol/vol). Finally, the solvent was removed by lyophilization to yield the product as a dark red powder (25 mg, 75%). The complex can be further purified via reverse-phase high-performance liquid chromatography using an HP1100 HPLC system, a Varian DynaMax C18 semipreparative column, and an elution gradient of 85:15 to 40:60 H_2O (0.1% TFA):MeCN (0.1% TFA) over 60 min.

^{1}H-NMR (d_4-methanol): 8.94 ppm (t, 2H); 8.86 ppm (t, 2H); 8.80 ppm (d, 1H); 8.77 ppm (d, 1H); 8.56 ppm (split t, 2H); 8.44 ppm (m, 5H); 8.40 ppm (d, 1H); 8.15 ppm (m, 1H); 8.03 ppm (m, 1H); 7.95 ppm (m, 3H); 7.86 ppm (d, 1H); 7.81 ppm (d, 1H); 7.64 ppm (m, 5H).

ESI-MS: 671 $[M-2H]^+$

UV-Vis (H_2O, pH 7.0, **Figure 2.5**): λ_{max} 302 nm (ε = 57,000 M^{-1}), 315 nm (ε = 52,200 M^{-1}), 391 nm (ε = 10,600 M^{-1}).

2.3.2.6: SYNTHESIS OF $[Rh(bpy)_2(phzi)](Cl)_3$

In a 100-mL round-bottom flask, 100 mg $[Rh(bpy)_2(NH_3)_2](PF_6)_3$ (0.1 mmol) and 35 mg 3,2-benzo[a]phenazine quinone (0.125 mmol) were dissolved in 50 mL MeCN with rapid stirring under ambient conditions.[3] After 10 min, 2 mL aqueous sodium hydroxide (0.4 M) were added, and the reaction vessel was closed to prevent evaporation. After 3 h, the reaction was halted by bringing the pH of the solution to 7.0 by adding a stoichiometric amount of $HCl_{(aq)}$. By this point, the reaction should have changed color dramatically from orange-yellow to dark brown-yellow; the reaction can also be monitored by TLC using silica F plates in a solvent system of 3:1:1 MeCN/H_2O/MeOH (vol/vol/vol) with 0.1 M KNO_3. After neutralization, the MeCN and H_2O were removed *in vacuo* by rotary evaporation.

The resulting solid was re-dissolved in a minimum volume of water and purified via cation-exchange chromatography using Sephadex SP-C25 ion exchange resin. Four inches of resin pre-equilibrated with 0.05 M $MgCl_2$ were poured into a 1−1.5 inch diameter column and subsequently washed with copious (500 mL) deionized H_2O. The rhodium complex was loaded onto the column simply by passing the aqueous Rh solution through the resin (the rhodium complex will 'stick' to the top of the column, forming a thin, dark brown band). The complex was then eluted by slowly increasing the $[MgCl_2]$ in the eluent in 500-mL batches, starting with 0.05 M $MgCl_2$ and increasing in increments of 0.05 M until the red band of the metal complex has passed through the column. The resultant eluted solution was concentrated on a reverse-phase cartridge primed with MeOH and eluted with 1:1:0.001 H_2O/MeCN/TFA (vol/vol/vol). Finally, the solvent was removed by lyophilization to yield the product as a brownish-yellow powder (20 mg,

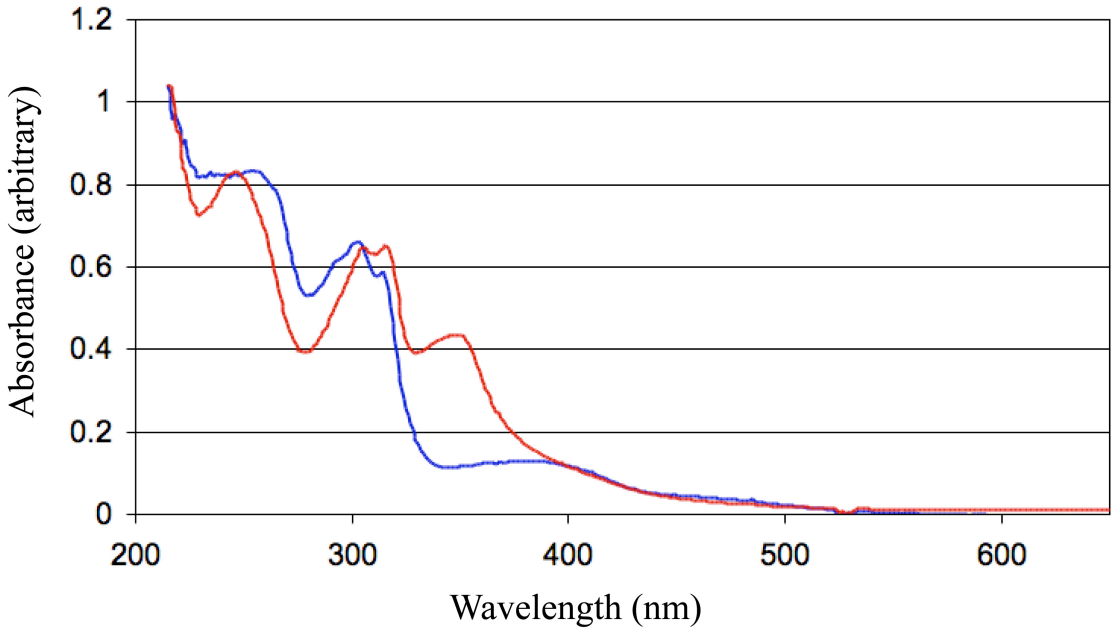

Figure 2.5: UV-Vis spectra of $Rh(bpy)_2(chrysi)^{3+}$ and $Rh(bpy)_2(phzi)^{3+}$. Extinction coefficients for $Rh(bpy)_2(chrysi)^{3+}$ (blue): 302 nm ($\varepsilon = 57{,}000\ M^{-1}$), 315 nm ($\varepsilon = 52{,}200\ M^{-1}$), 391 nm ($\varepsilon = 10{,}600\ M^{-1}$). Extinction coefficients for $Rh(bpy)_2(phzi)^{3+}$ (red): 304 nm ($\varepsilon = 65{,}800\ M^{-1}$), 314 nm ($\varepsilon = 67{,}300\ M^{-1}$), 343 nm ($\varepsilon = 39{,}300\ M^{-1}$). Both spectra were taken in H_2O at pH 7.0.

60%). The complex can be further purified via reverse-phase high-performance liquid chromatography using an HP1100 HPLC system, a Varian DynaMax C18 semipreparative column, and an elution gradient of 85:15 to 40:60 H_2O (0.1% TFA):MeCN (0.1% TFA) over 60 min.

^{1}H-NMR (d_6-DMSO): 14.88 ppm (s, 1H); 14.70 ppm (s, 1H); 9.02 ppm (m, 4H); 9.02 ppm (m, 4H); 8.91 ppm (d, 2H); 8.72 ppm (d, 1H); 8.60 ppm (t, 2H); 8.54 ppm (d, 1H); 8.47 ppm (t, 2H); 8.32 ppm (d, 1H); 8.20 ppm (d, 1H); 8.11 ppm (t, 1H); 8.02 (m, 3H); 7.94 (t, 1H); 7.84 (t, 1H); 7.75 (m, 3H); 7.69 (d, 1H).

ESI-MS: 671 $[M-2H]^+$

UV-Vis (H_2O, pH 7.0, **Figure 2.5**): λ_{max} 304 nm (ε = 65,800 M^{-1}), 314 nm (ε = 67,300 M^{-1}), 343 nm (ε = 39,300 M^{-1}).

2.3.2.7: SYNTHESIS OF $[Rh(bpy)_2(phi)](Cl)_3$

In a 100-mL round-bottom flask, 70 mg $[Rh(bpy)_2(NH_3)_2](Cl)_3$ (0.77 mmol) and 20 mg 9,10-phenanthrenequinone (0.97 mmol) were dissolved in 50 mL MeCN with rapid stirring under ambient conditions.[22] After 10 min, 2 mL aqueous sodium hydroxide (0.4 M) were added, and the reaction vessel was closed to prevent evaporation. After 3 h, the reaction was halted by bringing the pH of the solution to 7.0 by adding a stoichiometric amount of $HCl_{(aq)}$. By this point, the reaction should have changed color dramatically from orange/yellow to dark red; the reaction can also be monitored by TLC using silica F plates in a solvent system of 3:1:1 MeCN/H_2O/MeOH (vol/vol/vol) with 0.1 M KNO_3. After neutralization, the MeCN and H_2O were removed *in vacuo* by rotary evaporation.

The resulting solid was re-dissolved in a minimum volume of water and purified via cation-exchange chromatography using Sephadex SP-C25 ion exchange resin. Four inches of resin pre-equilibrated with 0.05 M $MgCl_2$ were poured into a 1−1.5 inch diameter column and subsequently washed with copious (500 mL) deionized H_2O. The rhodium complex was loaded onto the column simply by passing the aqueous Rh solution through the resin (the rhodium complex will 'stick' to the top of the column, forming a thin, dark orange band). The complex was then eluted by slowly increasing the [$MgCl_2$] in the eluent in 500-mL batches, starting with 0.05 M $MgCl_2$ and increasing in increments of 0.05 M until the red band of the metal complex has passed through the column. The resultant eluted solution was concentrated on a reverse-phase cartridge primed with MeOH and eluted with 1:1:0.001 H_2O/MeCN/TFA (vol/vol/vol). Finally, the solvent was removed by lyophilization to yield the product as a red-orange powder. The complex can be further purified via reverse-phase high-performance liquid chromatography using an HP1100 HPLC system, a Varian DynaMax C18 semipreparative column, and an elution gradient of 85:15 to 40:60 H_2O (0.1% TFA):MeCN (0.1% TFA) over 60 min.

^{1}H-NMR (D_2O): 8.72 ppm (d, 2H); 8.65 ppm (d, 2H); 8.55 ppm (d, 2H); 8.50 ppm (t, 2H); 8.35 ppm (t, 2H); 8.25 ppm (two overlapping t, 4H); 7.75 ppm (two overlapping t, 4H); 7.70 ppm (d, 2H); 7.60 ppm (t, 2H); 7.55 ppm (t, 2H).

ESI-MS: 619 $[M-2H]^+$

UV-Vis (H_2O, pH 7.0): λ_{max} 301 nm, 313 nm, 362 nm (ε = 19,400 M^{-1}).

2.3.3: ENANTIOMERIC SEPARATION OF Δ- AND Λ-RH(BPY)$_2$(CHRYSI)$^{3+}$

Because metalloinsertors bind DNA enantiospecifically, in many cases it has been advantageous to separate the two enantiomers of a complex (**Figure 2.6**). Cation exchange chromatography with a chiral eluent is employed.[23, 24]

In order to separate the enantiomers, one very long column (1.7 m x 1.5 cm) and two smaller columns (0.5 m x 1.5 cm, referred to as guard columns) were filled with Sephadex SP-C25 ion exchange resin equilibrated with water. All three columns were subsequently eluted with 0.15 M (+)-KSb-tartrate. One of the guard columns was then set aside, and the other guard column and the long column were arranged in series with a peristaltic pump as shown in **Figure 2.7**. *Rac*-Rh(bpy)$_2$(chrysi)$^{3+}$ (1 g) dissolved in 5 mL water was then loaded carefully on top of the large column to form a very small band. The pump was turned on and allowed to run continuously, with the chiral eluent in a closed loop. After approximately 1 d, separation became apparent. The fast band is the Λ-enantiomer, while the slower band is the Δ-enantiomer. The first guard column was detached after it 'caught' the first band and was replaced with the second guard column. The second guard column was detached after it 'caught' the second band.

The two guard columns were then washed with 0.05 M $MgCl_2$ to remove the remaining (+)-KSb-tartrate. With careful attention paid to the segregation of the two solutions, the compounds were removed from the guard columns by washing the columns with 0.5 M $MgCl_2$. Each solution was then concentrated on a 5 g C18 cartridge (Waters), washed with copious water, eluted with 1:1:0.001 MeCN/H_2O/TFA (vol/vol/vol), and lyophilized to dryness to yield a red powder (~300 mg for each enantiomer).

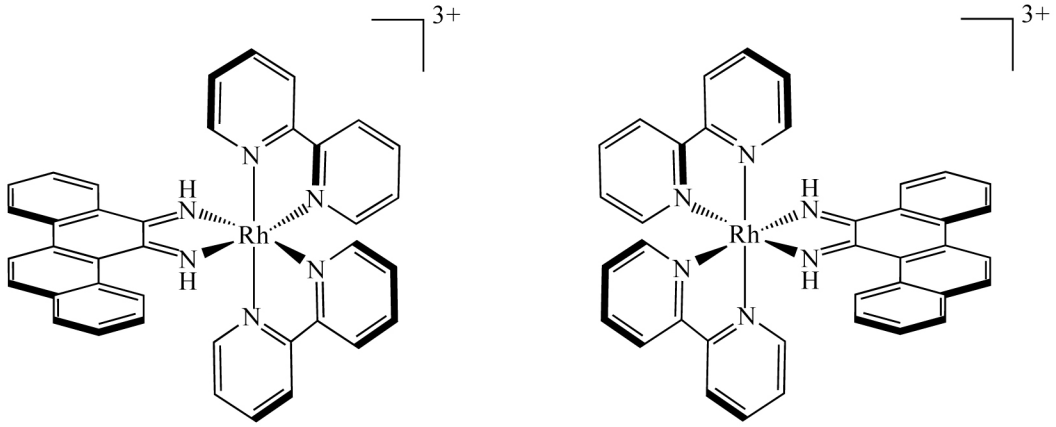

Δ-Rh(bpy)$_2$(chrysi)$^{3+}$ Λ-Rh(bpy)$_2$(chrysi)$^{3+}$

Figure 2.6: Structures of Δ- AND Λ-Rh(bpy)$_2$(chrysi)$^{3+}$

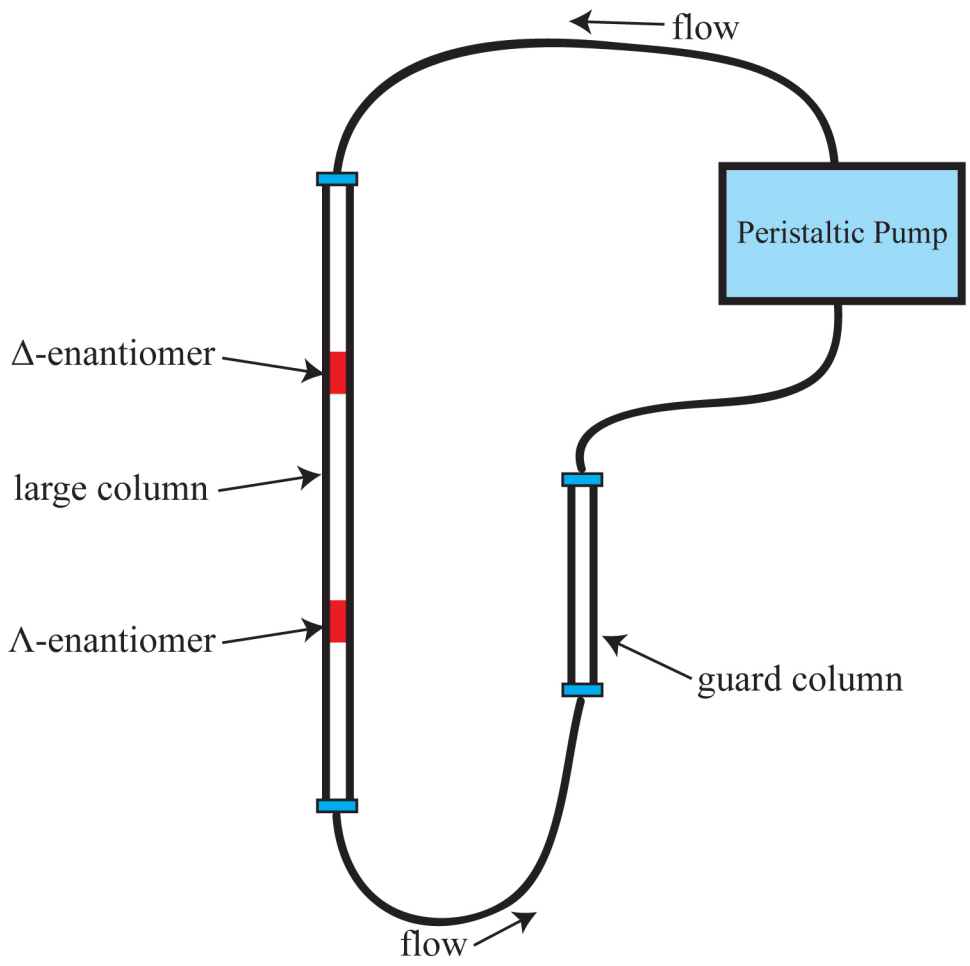

Figure 2.7: Schematic for enantiomer separation procedure. Two columns filled with cation exchange resin and equilibrated with 0.15 M (+)-KSb-tartrate are placed in-line with a peristaltic pump. As the eluent is cycled through the system over the course of a few days, the enantiomers separate, traveling at different speeds through the column due to their diastereomeric interactions with the chiral eluent.

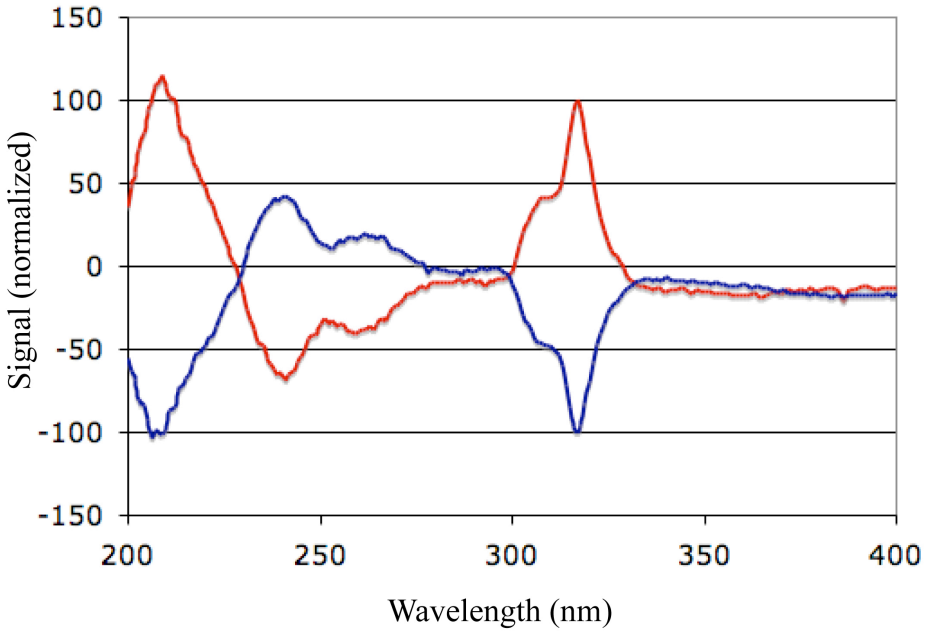

Figure 2.8: Circular dichroism spectra of Δ- and Λ-Rh(bpy)$_2$(chrysi)$^{3+}$. The spectra for the two enantiomers are shown in blue (Δ) and red (Λ). Δε values for Δ-Rh(bpy)$_2$(chrysi)$^{3+}$: 233 (34), 264 (26), 286 (-12), 308 (-42), 318 (-100), 341 (6). Δε values for Λ-Rh(bpy)$_2$(chrysi)$^{3+}$: 233 (-34), 264 (-26), 286 (12), 308 (42), 318 (100), 341 (-6)

Circular dichroism was employed to ascertain the enantiopurity of each solution (**Figure 2.8**). Δε values for Δ-$Rh(bpy)_2(chrysi)^{3+}$: 233 (34), 264 (26), 286 (-12), 308 (-42), 318 (-100), 341 (6). Δε values for Λ-$Rh(bpy)_2(chrysi)^{3+}$: 233 (-34), 264 (-26), 286 (12), 308 (42), 318 (100), 341 (-6).

2.3.4: SYNTHESIS OF TRISHETEROLEPTIC METALLOINSERTORS

2.3.4.1: SYNTHESIS OF $[Rh(phen)Cl_4](HPhen^+)$

The phenanthrolium salt of $[Rh(phen)Cl_4]^-$ was made according to the method of Broomhead and coworkers with minor modifications.[25, 26] Rhodium chloride hydrate (0.6 g) was added to concentrated hydrochloric acid (20 mL) in a 500 mL round-bottom flask. The solid was completely dissolved by refluxing the mixture for 3 h in an oil bath. Phenanthroline hydrate (1 g) was added, and the solution was heated for an additional 20 min during which boiling distilled water (300 mL) was added in 100 mL increments. The resultant solution was chilled at 4 °C overnight to promote crystallization and filtered in the morning to yield the product as a yellow crystalline solid. A synthetic scheme for this reaction and those described in 2.3.4.1−2.3.4.5 are shown in **Figure 2.9**.

2.3.4.2: SYNTHESIS OF $[Rh(phen)Cl_4](H_3O^+)$

The phenanthrolium salt was converted to the hydronium salt according to the method of McKenzie and co-workers.[27] The isolated phenanthrolium crystals (above) were added to fresh, concentrated hydrochloric acid (60 mL in a 100 mL round-bottom flask) and dissolved by refluxing the mixture for 5 h. The resulting solution was chilled

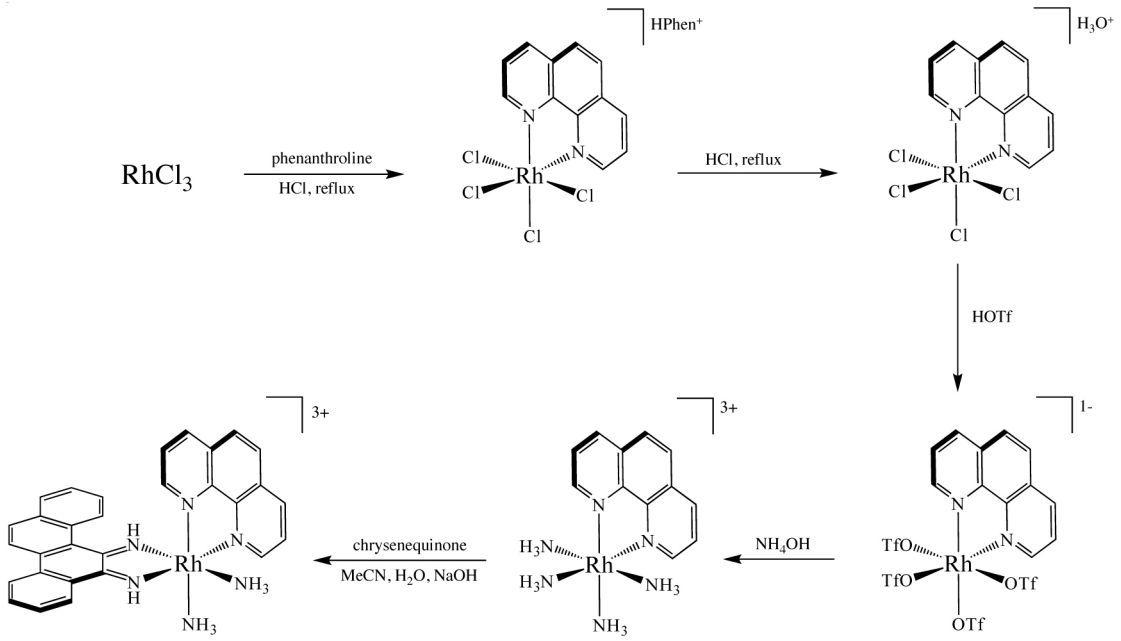

Figure 2.9: Synthetic strategy for trisheteroleptic metalloinsertors. The complexes are assembled sequentially. First, the phenanthroline ligand is added, followed by the stepwise conversion of the chloride ligands to ammines. A single chrysene-5,6-quinone is condensed onto the metal, leaving Rh(phen)(chrysi)$(NH_3)_2^{3+}$, the final intermediate on the way to the trisheteroleptic metalloinsertor molecules

at 4 °C overnight to promote crystallization and filtered in the morning to yield the product as an orange crystalline solid (needles, 0.61 g, 91%).

^{1}H-NMR (d_6-DMSO): 9.2 ppm (d, 2H); 8.83 ppm (d, 2H); 8.29 ppm (s, 2H); 8.15 ppm (d of d, 2H).

2.3.4.3: Synthesis of $[Rh(phen)(OTf)_4](H_3O^+)$

The chloride complex was then converted to the extremely synthetically useful triflate complex.[28–30] A 50 mL Schlenk flask was charged with the hydronium salt (100 mg), evacuated, and filled with $Ar_{(g)}$. Under positive argon pressure, triflic acid (5 g, excess) was added carefully to the reaction vessel using a glass Pasteur pipette (caution: triflic acid is very reactive, pyrophoric, and, to make matters worse, eats through gloves). After the addition of HOTf, the reaction vessel was closed with a rubber septum, the septum was pierced with a 16-gauge needle, and the flask was purged with argon for 60 seconds. The dark red reaction mixture was allowed to stir for 16 h with periodic $Ar_{(g)}$ purges to remove HCl generated by the reaction. After 16 h, the reaction mixture was added dropwise to 300 mL vigorously stirring diethyl either cooled to -78 ºC. The resultant brownish precipitate was collected via filtration on a Buchner funnel, washed with cold diethyl ether, and used as promptly as possible.

2.3.4.4: Synthesis of $[Rh(phen)(NH_3)_4](OTf)_3$

The triflate complex (600 mg) was added to 50 mL concentrated ammonium hydroxide (28−30%) in a round-bottom flask. The reaction was placed in an oil bath and

refluxed for 15 min. The resulting solution was evaporated to dryness, yielding a quantitative recovery of the tetra-ammine product (beige powder).

^{1}H-NMR (d_6-DMSO): 9.23 ppm (d, 2H); 9.02 ppm (d, 2H); 8.39 (s, 2H); 8.26 (d of d, 2H); 5.02 (broad s, 2H); 4.02 (broad s, 2H).

ESI-MS: 349 $[M-2H]^{+}$

This transformation can also be achieved by an alternative method, the reflux of the triflate precursor in condensed liquid ammonia. This method, however, can be somewhat dangerous for obvious reasons.

2.3.4.5: SYNTHESIS OF $[Rh(phen)(chrysi)(X)_2](Cl)_3$

In a 250-mL round-bottom flask, $Rh(phen)(NH_3)_4^{3+}$ (220 mg, 0.276 mmol) was combined with chrysene-5,6-quinone (67 mg, 0.261 mmol) in acetonitrile (100 mL) and an aqueous solution of sodium hydroxide (40 mL, 0.4 M). The reaction was capped to prevent evaporation and stirred overnight. Over the course of the reaction, the mixture changed colors from orange to dark red. After 16 h, the reaction was stopped by neutralization with hydrochloric acid; the reaction mixture was then anion-exchanged on a Sephadex QAE-25 column that had been pre-equilibrated with 0.05 M $MgCl_2$. The solution was concentrated on a reversed phase C-18 cartridge, washed, eluted, and lyophilized to dryness. The resultant red-orange powder was used in subsequent reactions without purification or further characterization.

2.3.4.6: SYNTHESIS OF [RH(PHEN)(CHRYSI)(BPY)](Cl)$_3$

In a 100-mL round-bottom flask, Rh(phen)(chrysi)(X)$_2$ (150 mg, 0.22 mmol) was combined with 2,2'-dipyridyl (150 mg, 0.8 mmol) in a 50/50 mixture of ethanol and deionized water (50 mL total volume) (**Figure 2.10**). The reaction was stirred at reflux overnight in an oil bath. The mixture was then allowed to cool, diluted with 200 mL H_2O, and purified by cation exchange chromatography.

Four inches of resin pre-equilibrated with 0.05 M $MgCl_2$ were poured into a 1−1.5 inch diameter column and subsequently washed with copious (500 mL) deionized H_2O. The rhodium complex was loaded onto the column simply by passing the aqueous Rh solution through the resin (the rhodium complex will 'stick' to the top of the column, forming a thin, dark orange band). The complex was then eluted by slowly increasing the [$MgCl_2$] in the eluent in 500-mL batches, starting with 0.05 M $MgCl_2$ and increasing in increments of 0.05 M until the red band of the metal complex has passed through the column. The resultant eluted solution was concentrated on a reverse-phase cartridge primed with MeOH and eluted with 1:1:0.001 H_2O/MeCN/TFA (vol/vol/vol). Finally, the solvent was removed by lyophilization to yield the product as a red-orange powder. The complex can be further purified via reversed phase high-performance liquid chromatography using an HP1100 HPLC system, a Varian DynaMax C18 semipreparative column, and an elution gradient of 85:15 to 40:60 H_2O (0.1% TFA):MeCN (0.1% TFA) over 60 min.

ESI-MS: 693 $[M-2H]^+$

UV-Vis (H_2O, pH 7.0): λ_{max} 267 nm (ε = 68,000 M^{-1}), 301 nm (ε = 40,000 M^{-1}), 313 nm (ε = 30,400 M^{-1}), 389 nm (ε = 19,400 M^{-1}).

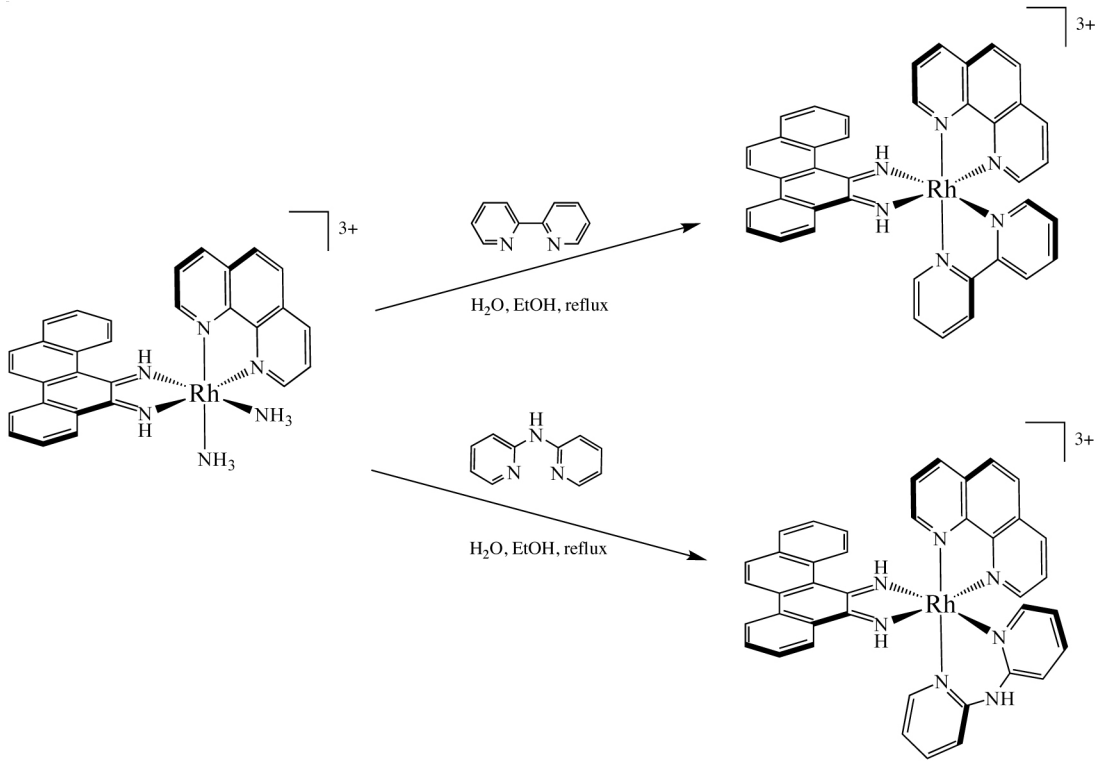

Figure 2.10: Metallation of bpy and HDPA ligands. In the final step of the synthesis of trisheteroleptic metalloinsertors, the dipyridyl ligand [2,2'-bipyridine (bpy) or 2,2'-dipyridylamine (HDPA)] is metallated via reflux in a 1:1 mixture of H_2O:EtOH.

2.3.4.7: SYNTHESIS OF [RH(PHEN)(CHRYSI)(HDPA)](Cl)$_3$

In a 100-mL round-bottom flask, Rh(phen)(chrysi)(X)$_2$ (150 mg, 0.22 mmol) was combined with 2,2'-dipyridylamine (150 mg, 0.75 mmol) in a 50/50 mixture of ethanol and deionized water (50 mL total volume) (**Figure 2.10**). The reaction was stirred at reflux overnight in an oil bath. The mixture was then allowed to cool, diluted with 200 mL H_2O, and purified by cation exchange chromatography.

Four inches of resin pre-equilibrated with 0.05 M $MgCl_2$ were poured into a 1−1.5 inch diameter column and subsequently washed with copious (500 mL) deionized H_2O. The rhodium complex was loaded onto the column simply by passing the aqueous Rh solution through the resin (the rhodium complex will 'stick' to the top of the column, forming a thin, dark orange band). The complex was then eluted by slowly increasing the [$MgCl_2$] in the eluent in 500-mL batches, starting with 0.05 M $MgCl_2$ and increasing in increments of 0..05 M until the red band of the metal complex has passed through the column. The resultant eluted solution was concentrated on a reverse-phase cartridge primed with MeOH and eluted with 1:1:0.001 H_2O/MeCN/TFA (vol/vol/vol). Finally, the solvent was removed by lyophilization to yield the product as a red-orange powder. The complex can be further purified via reverse-phase high-performance liquid chromatography using an HP1100 HPLC system, a Varian DynaMax C18 semipreparative column, and an elution gradient of 85:15 to 40:60 H_2O (0.1% TFA):MeCN (0.1% TFA) over 60 min.

ESI-MS: 708 $[M-2H]^+$, 354 $[M-H]^{2+}$

UV-Vis (H_2O, pH 7.0): λ_{max} 269 nm (ε = 66,400 M^{-1}), 301 nm (ε = 31,100 M^{-1}), 408 nm (ε = 6,500 M^{-1}).

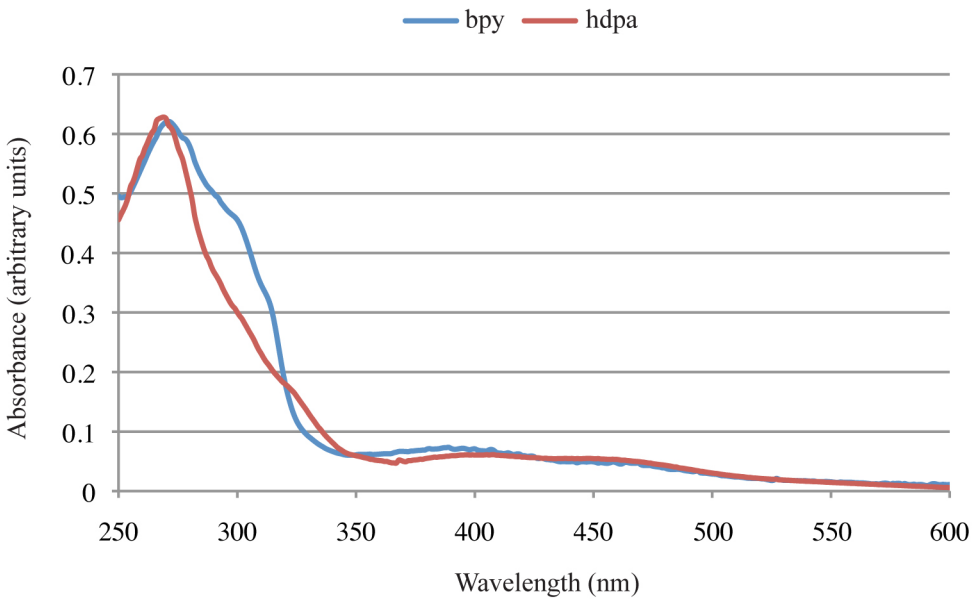

Figure 2.11: UV-Vis spectra of trisheteroleptic Rh(phen)(chrysi)(L)$^{3+}$ complexes. For L = bpy (blue), λ_{max} 267 nm (ε = 68,000 M^{-1}), 301 nm (ε = 40,000 M^{-1}), 313 nm (ε = 30,400 M^{-1}), 389 nm (ε = 19,400 M^{-1}). For L = HDPA (red), λ_{max} 269 nm (ε = 66,400 M^{-1}), 301 nm (ε = 31,100 M^{-1}), 408 nm (ε = 6,500 M^{-1})

2.3.5: SYNTHESIS OF LINKER-MODIFIED DIPYRIDYL LIGANDS

The trisheteroleptic metalloinsertor constructs discussed in Chapter 1 are employed most often in the design of mismatch-specific, bifunctional conjugates. These molecules typically contain two subunits: a mismatch-specific rhodium metalloinsertor and a second, non-specific moiety on which we seek to confer mismatch-specificity. The two subunits, of course, need to be covalently linked in some manner. This duty falls to special linker-modified dipridyl ligands that have been developed in our laboratory over the past five years.[31−33]

The topics of bifunctional conjugates and linker-modified ligands will be addressed in more detail in Chapter 7. However, the synthetic protocols for many of these ligands will be included here in the interest of centralization. It is important to note that in all syntheses involving bipyridine ligands, all glassware should be washed rigorously with a 0.1 M EDTA solution in order to eliminate free iron. Also, it is advisable to soak all silica (for columns and TLC) in a solution of 1:10 NEt_3:hexanes to eliminate smearing during analytical and preparative chromatography

2.3.5.1: SYNTHESIS OF 4-(7-BROMOHEPTYL)-4'-METHYL-2,2'-BIPYRIDINE (^{BR}BPY)

A 50 mL Schlenk flask was flame-dried and subjected to three rounds of evacuation and re-filling with $Ar_{(g)}$. The flask was then charged by syringe with 3.9 mL (28 mmol) diisopropylamine, and 20 mL THF (dry and under argon, Fluka) were transferred into the flask via cannula.[1] The flask was cooled to -78 °C in a dry ice/acetone bath, followed by the dropwise addition of 13.5 mL (27 mmol) M BuLi. The resultant light yellow LDA solution was kept at -78 °C as the second reaction vessel was prepared.

[1] Cannula means “little reed” in Latin.

A 500 mL, three-necked round-bottom flask was flame-dried, charged with 5 g (27 mmol) 4,4'-dimethyl-2,2'-bipyridine, and subjected to three rounds of evacuation and refilling with $Ar_{(g)}$. 200 mL THF (dry and under argon, Fluka) were transferred into the flask via cannula, and the reaction mixture was cooled to -78 °C in a dry ice/acetone bath. The LDA solution was then transferred into the 500 mL round-bottom flask via cannula, and the resultant dark brown reaction mixture was allowed to stir at -78 °C for 1 h. After 1 h, 29.9 mL (40 g, 135 mmol, 5 equiv.) dibromohexane were added to the reaction via syringe. The reaction mixture was immediately transferred to a dry ice bath (i.e. no acetone) and allowed to warm slowly to room temperature over the next 16 h. During this time, the reaction changed colors dramatically from brown to dark green to green to dark yellow and, finally, to light yellow.

Once at room temperature, the reaction vessel was opened to air, and H_2O (150 mL) was added to the reaction mixture to quench any remaining LDA. The pH of the mixture was adjusted to ~10 with saturated $NaHCO_{3(aq)}$. The basified reaction mixture was then extracted once with 50 mL Et_2O and subsequently with 50 mL increments of CH_2Cl_2 until the organic layer no longer stains red when spotted on a TLC plate (silica) and dipped in an Fe(II) solution. At this point (~ 250 mL total volume organic layer), the organic layer was extracted with brine, dried over $MgSO_4$, filtered, and concentrated *in vacuo* to yield the final product as a yellow oil.

The crude product was purified via column chromatography (SiO_2 pretreated with 1:10 NEt_3:hexanes) with a solvent system of 1:1 EtOAc:Hexanes. In this solvent system, the product has an $R_f = .80$, and the unreacted starting material has an $R_f = .60$. The purified product, nicknamed ^{Br}bpy, is a white solid (8.1 g) (**Figure 2.12**).

^{1}H-NMR (CD_2Cl_2): 8.50 ppm (split d, 2H); 8.27 ppm (s, 2H); 7.14 ppm (d, 2H); 3.4 ppm (t, 2H); 2.69 ppm (t, 2H); 2.42 ppm (s, 3H); 1.8 ppm (m, 2H); 1.7 ppm (m, 2H); 1.37 ppm (m, 6H).

ESI-MS: 346, 348 $[M+H]^+$

2.3.5.2: SYNTHESIS OF 4-(7-PHTHALIMIDOHEPTYL)-4'-METHYL-2,2'-BIPYRIDINE (^{PHTH}BPY)

The bromide-terminated linker was converted to an amine-terminated linker by an adapted Gabriel amine synthesis.[34, 35] In a 250 mL round-bottom flask, ^{Br}bpy (0.35 g) was combined with potassium phthalimide (0.225 g) in 20 mL DMF and heated to 130 °C for 12 h. After cooling to room temperature, water (100 mL) was added, and the reaction mixture was brought to ~ pH 10 with saturated $NaHCO_{3(aq)}$. This solution was then extracted 3 times with 75 mL CH_2Cl_2, washed once with brine, dried over $MgSO_4$, and evaporated to dryness to yield a white solid (500 mg, > 95%, ^{Phth}bpy) that was pure by TLC (SiO_2, 1:1 EtOAc:Hex).

^{1}H-NMR ($CDCl_3$): 8.53 ppm (m, 2H); 8.21 ppm (m, 2H); 7.83 ppm (m, 2H); 7.69 ppm (m, 2H); 7.12 ppm (m, 2H); 3.67 ppm (t, 2H); 2.67 ppm (t, 2H); 2.42 ppm (s, 3H); 1.66 ppm (m, 4H); 1.37 ppm (m, 6H).

ESI-MS: 414 $[M+H]^+$

2.3.5.3: SYNTHESIS OF 4-(7-AMINOHEPTYL)-4'-METHYL-2,2'-BIPYRIDINE (^{NH2}BPY)

In a 250 mL round-bottom flask, ^{Phth}bpy (180 mg, 0.44 mmol) was dissolved in EtOH (75 mL) by heating to 70 °C for 1 h. After 1 h, hydrazine monohydrate (0.1 mL, 2.0 mmol) was added, and the reaction mixture was stirred at 70 °C for 16 h. After cooling to room temperature, the solvent was removed *in vacuo*. The residue was taken up in 50 mL 1 M hydrochloric acid. The acid phase was extracted twice with 50 mL $CHCl_3$ to eliminate any residual phthalimide products. The combined organic phases were washed with 50 mL 1 M HCl to prevent inadvertent product loss. The pH of the combined aqueous layers was then adjusted to ~10 with saturated $NaHCO_3$ solution, and the newly basic aqueous layer was extracted 4 times with 50 mL $CHCl_3$, washed with brine, dried over $MgSO_4$, and dried *in vacuo* to yield a white solid that was pure by NMR (150 mg, 90% yield, nicknamed ^{NH2}bpy).

^{1}H-NMR (CD_2Cl_2): 8.51 ppm (m, 2H); 8.25 ppm (m, 2H); 7.12 ppm (m, 2H); 2.70 ppm (m, 4H); 2.43 ppm (s, 3H); 1.85 ppm (m, 4H); 1.39 ppm (m, 6H).

ESI-MS: 284 $[M+H]^+$

2.3.5.4: SYNTHESIS OF 4-(3-(1,3-DIOXOLAN-2-YL)PROPYL)-4'-METHYL-2,2'-BIPYRIDINE (^{DO}BPY)

A 50 mL Schlenk tube was flame-dried and subjected to three rounds of evacuation and re-filling with $Ar_{(g)}$. The flask was then charged by syringe with 7.4 mL (5.35 g, 53 mmol) diisopropylamine, and 25 mL THF (dry and under argon, Fluka) were transferred into the flask via cannula.

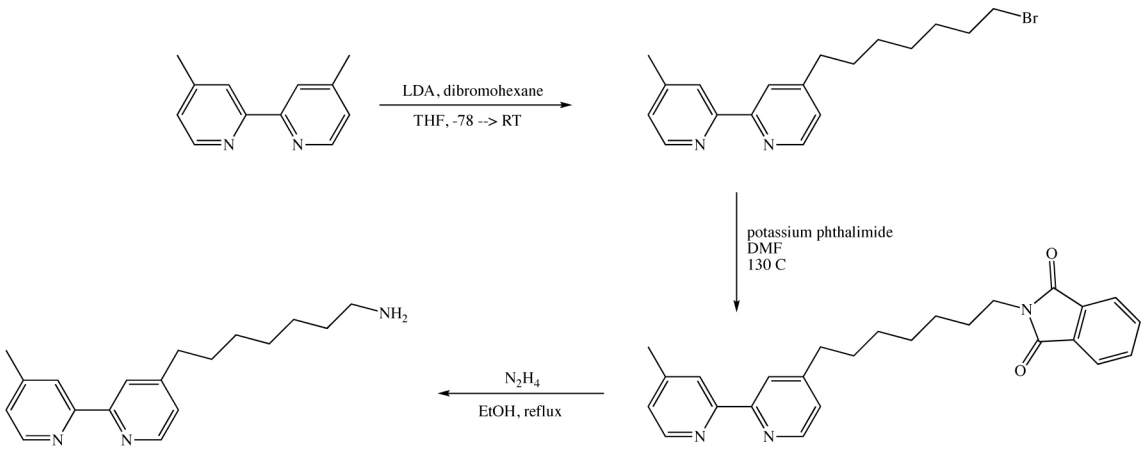

Figure 2.12. Synthetic route to ^{NH2}bpy. 4,4'-Dimethylbipyridine is first mono-alkylated with dibromohexane and LDA. This bromide is then converted to an amine through the via the Gabriel amine synthesis.

The flask was cooled to -78 °C in a dry ice/acetone bath, followed by the dropwise addition of 26 mL (53 mmol) M BuLi. The resultant light yellow LDA solution was kept at -78 °C as the second reaction vessel was prepared.

A 500 mL, three-necked round-bottom flask was flame-dried, charged with 10 g (54 mmol) 4,4'-dimethyl-2,2'-bipyridine, and subjected to three rounds of evacuation and refilling with $Ar_{(g)}$. 200 mL THF (dry and under argon, Fluka) was transferred into the flask via cannula, and the reaction mixture was then cooled to -78 °C in a dry ice/acetone bath. The LDA solution was then transferred into the 500 mL round-bottom flask via cannula, and the resultant dark brown reaction mixture was allowed to stir at -78 °C for 1 h. After 1 h, 30 mL (roughly 5 equiv.) 2-(3-bromopropyl)-1,3-dioxolane were added to the reaction via syringe. The reaction mixture was immediately transferred to a dry ice bath (*i.e.* no acetone) and allowed to warm slowly to room temperature over the next 16 h. During this time, the reaction changed colors dramatically from brown to dark green to green to dark yellow and, finally, to light yellow.

Once at room temperature, the reaction vessel was opened to air, and H_2O (150 mL) was added to the reaction mixture to quench any remaining LDA. The pH of the mixture was adjusted to ~10 with saturated $NaHCO_{3(aq)}$. The basified reaction mixture was then extracted once with 50 mL Et_2O and subsequently with 50 mL increments of CH_2Cl_2 until the organic layer no longer stains red when spotted on a TLC plate (silica) and dipped in an Fe(II) solution. At this point (~ 250 mL total volume organic layer), the organic layer was extracted with brine, dried over $MgSO_4$, filtered, and concentrated *in vacuo* to yield the final product as a yellow oil.

The crude product was purified via column chromatography (SiO_2 pretreated with 1:10 NEt_3:hexanes) with a solvent system of 3:7 EtOAc:Hexanes. In this solvent system, the purified product, nicknamed ^{DO}bpy is a white solid (10.2 g) (**Figure 2.13**).

^{1}H-NMR ($CDCl_3$): 8.50 ppm (m, 2H); 8.20 ppm (m, 2H); 7.11 ppm (m, 2H); 4.87 ppm (t, 1H); 3.8−3.9 (m, 4H); 2.74 ppm (t, 2H); 2.42 ppm (s, 3H); 1.83 ppm (m, 2H); 1.73 (2H).

ESI-MS: 285.0 $[M+H]^+$

2.3.5.5: SYNTHESIS OF 4-(4'-METHYL-2,2'-BIPYRIDIN-4-YL)BUTANOIC ACID (BPY')

In a 250 mL round-bottom flask, combined 1.3 g ^{DO}bpy and 125 mL 1M HCl. Heated the resultant solution to 60 °C for 3 h. After 3 h, the reaction mixture was allowed to cool to room temperature, and its pH was adjusted to ~10 with saturated $NaHCO_{3(aq)}$. The basified reaction mixture was then extracted four times with 100 mL CH_2Cl_2, until the organic layer no longer stains red when spotted on a TLC plate (silica) and dipped in an Fe(II) solution. At this point (~ 400 mL total volume organic layer), the organic layer was extracted with brine, dried over $MgSO_4$, filtered, and concentrated *in vacuo* to yield the aldehyde intermediate as a clear oil (0.95 g, quantitative, **Figure 2.13**). ESI-MS (m/z): 241 $[M+H]^+$.

In a 250 mL round-bottom flask, the aldehyde intermediate (0.95 g, 3.9 mmol) and $KMnO_4$ (616 mg, 3.9 mmol) were dissolved in 100 mL acetone and the solution was stirred for 3 h. After 3 h, the acetone was removed under vacuum, the residue was taken up in H_2O (200 mL), and the resultant solution was heated to 90 °C for 2 more h. After 2

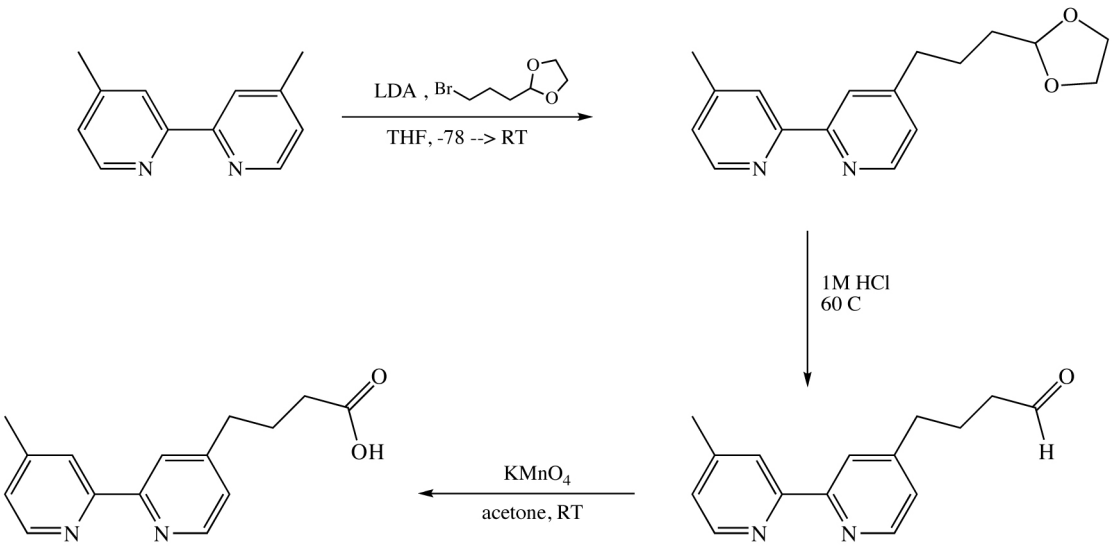

2.13: Synthetic route to bpy'. Dimethylbipyridine is first monoalkylated with 2-(3-bromopropyl)-1,3-dioxolane and LDA. This dioxolane is then deprotected to yield an aldehyde intermediate that is subsequently oxidized with $KMnO_4$ to give the final carboxylic acid product.

h, the solution was filtered through an EDTA-soaked pad (the EDTA is to remove Fe contamination common in Celite). The pH of the solution was adjusted to 4.8 (the isoelectric point of the molecule), and the aqueous layer was extracted with CH_2Cl_2, until the organic layer no longer stained red when spotted on a TLC plate (silica) and dipped in an Fe(II) solution. At this point (~ 400 mL total volume organic layer), the organic layer was extracted with brine, dried over $MgSO_4$, filtered, and concentrated *in vacuo* to yield the carboxylic acid (bpy') as a white solid (0.80 g, 80%).

^{1}H-NMR ($CDCl_3$): 8.55 ppm (m, 2H); 8.24 ppm (d, 2H); 7.2 ppm (m, 2H); 2.80 ppm (t, 2H); 2.42 ppm (m, 2H); 2.05 ppm (m, 2H).

ESI-MS: 257.0 $[M+H]^+$

2.3.5.6: SYNTHESIS OF *N*-(2-(2-(2-AMINOETHOXY)ETHOXY)ETHYL)-4-(4'-METHYL-2,2'-BIPYRIDIN-4-YL)BUTANAMIDE (^{PEG}BPY)

Bpy' (100 mg, 1.9 mmol), DCC (732 mg, 2.8 mmol), and NHS-OH (400 mg, 2.8 mmol) were dissolved in 100 mL CH_2Cl_2 in a 250 mL round-bottom flask and stirred for 2 h at room temperature (**Figure 2.14)**. After 2 h, a precipitate had become apparent; the reaction was then placed in the cold room overnight to facilitate precipitation. In the morning, the solution was filtered and reduced *in vacuo* to yield the pure N-succinimidyl ester product as a clear oil (1 g, 1.8 mmol).

^{1}H-NMR ($CDCl_3$): 8.55 ppm (dd, 2H); 8.26 ppm (d, 2H); 7.21 ppm (d, 2H); 2.86 ppm (m, 6H); 2.68 ppm (t, 2H); 2.46 ppm (s, 3H) ; 2.17 ppm (t, 2H).

ESI-MS: 354.0 $[M+H]^+$

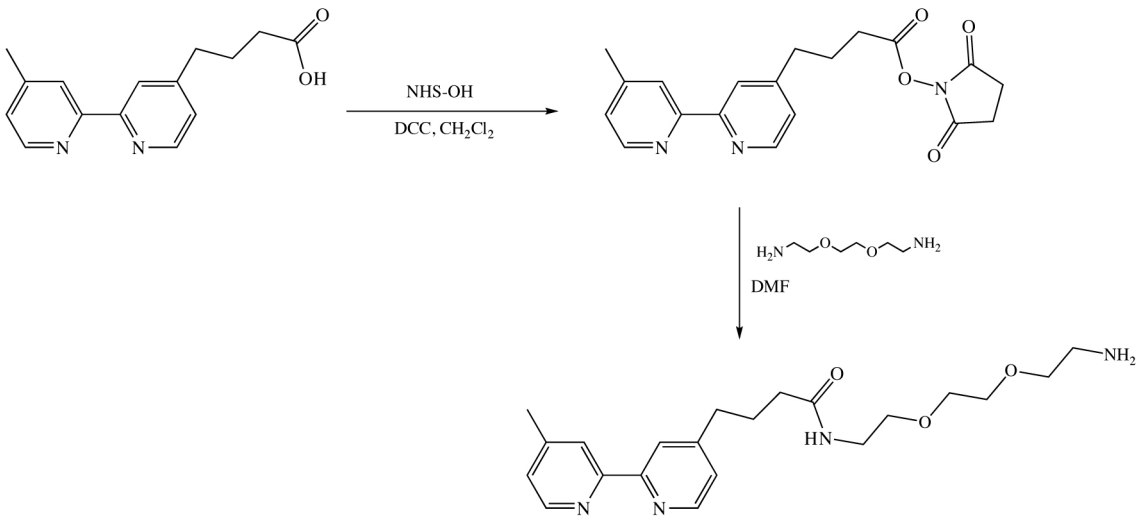

2.14: Synthetic route to ^{PEG}bpy. Bpy' is converted to a ligand bearing an ethylene-glycol-based linker through an N-hydroxysuccinimidyl ester intermediate.

Next, 100 g of the NHS-ester were dissolved in 3 mL DMF and added to a solution of 2 mL (excess) 2,2'-(ethylenedioxy)bis(ethylamine) in 1 mL DMF. After two h, 0.05 mL DIEA were added to ensure reaction. The reaction mixture was stirred for 16 h at room temperature. After 16 h, the reaction mixture was concentrated *in vacuo*, taken up in CH_2Cl_2, extracted twice with a saturated $NaHCO_3$ solution, dried over $MgSO_4$, and re-concentrated *in vacuo*. The final product (^{PEG}bpy) was obtained pure as a clear oil.

^{1}H-NMR ($CDCl_3$): 8.5 ppm (m, 2H); 8.24 ppm (m, 2H); 7.14 ppm (m, 2H); 3.9−3.6 ppm (m, 4H); 3.5−3.3 pm (m, 10H); 2.43 ppm (s, 3H); 2.25−2.15 ppm (m, 2H); 2.15−2.05 (m, 2H).

ESI-MS: 387.0 $[M+H]^+$

2.3.5.7: SYNTHESIS OF *N*-(6-BROMOHEXYL)-*N*-(PYRIDIN-2-YL)PYRIDIN-2-AMINE (^{BR}DPA)

Modified dipyridylamine ligands were synthesized by analogy to the methods of Krasinski and co-workers.[36] In a flame-dried, 250 mL round-bottom flask fitted with a reflux condenser, 2,2'-dipyridylamine (HDPA, 5 g, 29 mmol) was dissolved in THF (50 mL). The solution was purged with $Ar_{(g)}$ for 15 min. After 15 min, NaH (1.08 g, 29 mmol) was added slowly to the reaction mixture, and the solution was again purged with $Ar_{(g)}$ for 15 min. After 15 min, 10 g dibromohexane (42 mmol, 1.3 equiv.) were added. The solution was again purged for 10 min and brought to reflux at 70 °C for 16 h.

The next morning, the solution was allowed to cool to room temperature. Once at room temperature, the reaction vessel was opened to air, and H_2O (150 mL) was added to the reaction mixture to quench any remaining NaH. The pH of the mixture was adjusted

to ~10 with saturated $NaHCO_{3(aq)}$. The basified reaction mixture was then extracted with CH_2Cl_2 (5 x 50 mL). After the extractions, the organic layer was washed with brine, dried over $MgSO_4$, filtered, and concentrated *in vacuo* to yield the final, crude product as a reddish-yellow oil.

The crude product was purified via column chromatography (SiO_2 pre-treated with 1:10 NEt_3:hexanes) with a solvent system of 1:1 EtOAc:Hexanes. Purification yielded the final product (nicknamed ^{Br}DPA) as a white solid (2.5 g, 25%) (**Figure 2.15**).

^{1}H-NMR ($CDCl_3$): 8.3 ppm (d, 2H); 7.4 ppm (d of d, 2H); 7.03 ppm (d, 2H); 6.84 ppm (d, 2H); 4.1 ppm (t, 2H); 3.38 ppm (m, 2H); 1.8 ppm (m, 2H); 1.6 ppm (m, 2H); 1.5−1.4 ppm (m, 6H).

ESI-MS: 334.0 and 336.0 $[M+H]^+$

2.3.5.8: SYNTHESIS OF *N*-(6-PHTHALIMIDOHEXYL)-*N*-(PYRIDIN-2-YL)PYRIDIN-2-AMINE (^{PHTH}DPA)

The bromide-terminated linker was converted to an amine-terminated linker by an adapted Gabriel amine synthesis.[34, 35] In a 250 mL round-bottom flask, ^{Br}DPA (1 g, 3 mmol) was combined with potassium phthalimide (1.53 g, 9 mmol) in 50 mL DMF and heated to 130 °C for 12 h. After cooling to room temperature, water (100 mL) was added, and the reaction mixture was brought to ~ pH 10 with saturated $NaHCO_{3(aq)}$. This solution was then extracted 3 times with 75 mL CH_2Cl_2, washed once with brine, dried over $MgSO_4$, and evaporated to dryness to yield a white solid (500 mg, > 95%, nicknamed ^{Phth}DPA) that was pure by TLC (SiO_2, 1:1 EtOAc:Hex).

^{1}H-NMR ($CDCl_3$): 8.28 ppm (m, 2H); 7.8 ppm (d, 2H); 7.65 ppm (d, 2H); 7.4 ppm (m, 2H); 7.05 ppm (m, 2H); 6.8 ppm (m, 2H); 4.1 ppm (t, 2H); 3.6 ppm (m, 2H); 1.8 ppm (m, 4H); 1.6 ppm (m, 6H).

ESI-MS: 401 $[M+H]^+$

2.3.5.9: SYNTHESIS OF N^1,N^1-DI(PYRIDIN-2-YL)HEXANE-1,6-DIAMINE (^{NH2}DPA)

In a 250 mL round-bottom flask, ^{Phth}DPA (1 g, 2.5 mmol) was dissolved in EtOH (100 mL) by heating to 80 °C for 1 h. After 1 h, hydrazine monohydrate (0.1 mL, 2.0 mmol) was added, and the reaction mixture was stirred at 70 °C for 16 h. After cooling to room temperature, the solvent was removed *in vacuo*. The residue was taken up in 50 mL 1 M hydrochloric acid. The acid phase was extracted twice with 50 mL $CHCl_3$ to eliminate any residual phthalimide products. The combined organic phases were washed with 50 mL 1 M HCl to prevent inadvertent product loss. The pH of the combined aqueous layers was then adjusted to ~10 with saturated $NaHCO_3$ solution, and the newly basic aqueous layer was extracted four times with 50 mL $CHCl_3$, washed with brine, dried over $MgSO_4$, and dried *in vacuo* to yield a white solid that was pure by NMR (650 mg, 90% yield, nicknamed ^{NH2}DPA).

^{1}H-NMR ($CDCl_3$): 8.25 ppm (d, 2H); 7.4 ppm (d of d, 2H); 7.01 ppm (d, 2H); 6.75 ppm (d, 2H); 4.05 ppm (t, 2H); 2.60 ppm (m, 2H); 1.8 ppm (m, 2H); 1.6 ppm (m, 2H); 1.4−1.3 ppm (m, 6H).

ESI-MS: 271 $[M+H]^+$

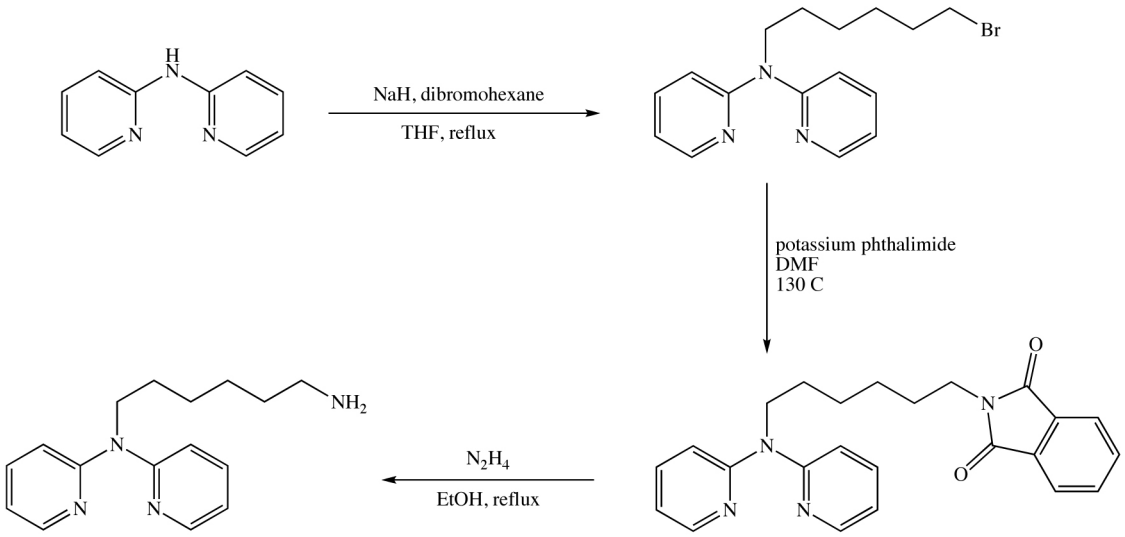

Figure 2.15: Synthetic route to ^{NH2}DPA. 2,2'-dipyridylamine (HDPA) is first monoalkylated with dibromohexane and NaH. This bromide is then converted to an amine through the well-known Gabriel amine synthesis.

2.3.5.10: SYNTHESIS OF 7-(DIPYRIDIN-2-YLAMINO)HEPTANENITRILE (^{CN}DPA)

In a 250 mL round-bottom flask, ^{Br}DPA (1 g, 3 mmol) was combined with potassium cyanide (400 mg, 6 mmol) in 100 mL DMSO and heated to 90 °C for 12 h. After cooling to room temperature, water (100 mL) was added, and the reaction mixture was brought to ~ pH 10 with saturated $NaHCO_{3(aq)}$. This solution was then extracted three times with 75 mL CH_2Cl_2, washed once with brine, dried over $MgSO_4$, and evaporated to dryness to yield a white solid (600 mg, 70%, nicknamed ^{CN}DPA) that was pure by TLC (SiO_2, 1:1 EtOAc:Hex) (**Figure 2.16**).

^{1}H-NMR ($CDCl_3$): 8.25 ppm (d, 2H); 7.5 ppm (d of d, 2H); 7.09 ppm (d, 2H); 6.89 ppm (d, 2H); 4.15 ppm (t, 2H); 3.44 ppm (m, 2H); 1.8 ppm (m, 2H); 1.6 ppm (m, 2H); 1.5−1.4 ppm (m, 6H).

ESI-MS: 281 $[M+H]^+$

2.3.5.11: SYNTHESIS OF 7-(DIPYRIDIN-2-YLAMINO)HEPTANOIC ACID (DPA')

In a 100 mL round-bottom flask, ^{CN}DPA (800 mg, 2.8 mmol) was dissolved in a mixture of 20 mL concentrated HCl and 5 mL concentrated H_2SO_4 and refluxed at 70 °C overnight. After 16 h, H_2O (100 mL) was added to the reaction mixture, and the pH was adjusted to 4.0 with NaOH(s). The aqueous layer was extracted with CH_2Cl_2 (4 x 50 mL). At this point (~ 200 mL total volume CH_2Cl_2), the organic layer was washed with brine, dried over $MgSO_4$, filtered, and concentrated *in vacuo* to yield the carboxylic acid (DPA') as a white solid (600 mg, 80%).

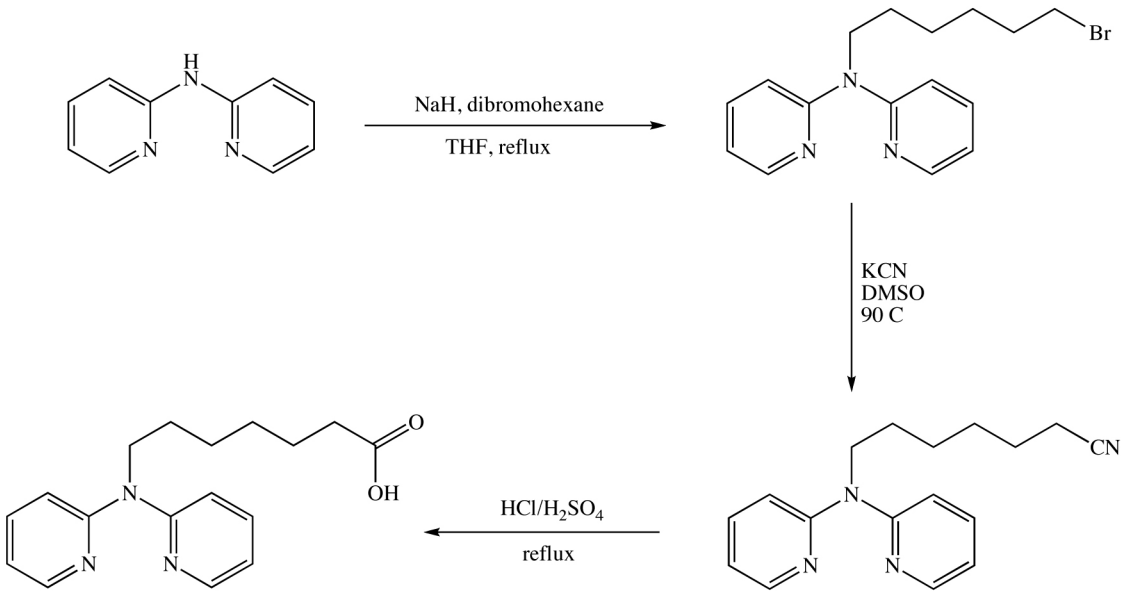

Figure 2.16: Synthetic route to DPA'. 2,2'-dipyridylamine (HDPA) is first monoalkylated with dibromohexane and NaH. This bromide is then converted to the carboxylic acid through a cyano intermediate.

^{1}H-NMR ($CDCl_3$): 8.21 ppm (d, 2H); 7.44 ppm (d of d, 2H); 7.2 ppm (d, 2H); 7.01 ppm (d, 2H); 4.21 ppm (t, 2H); 3.54 ppm (m, 2H); 1.8−1.6 ppm (m, 4H); 1.5−1.4 ppm (m, 6H).

ESI-MS: 300 $[M+H]^+$

2.3.5.12: EXAMPLE METALLATION: SYNTHESIS OF RH(PHEN)(CHRYSI)(BPY')$^{3+}$

In a 100-mL round-bottom flask, Rh(phen)(chrysi)$(X)_2$ (150 mg, 0.22 mmol) was combined with bpy' (150 mg, 0.6 mmol) in a 50/50 mixture of ethanol and deionized water (50 mL total volume) (**Figure 2.17**). The reaction was stirred at reflux overnight in an oil bath. The mixture was then allowed to cool, diluted with 200 mL H_2O, and purified by cation exchange chromatography.

Four inches of resin pre-equilibrated with 0.05 M $MgCl_2$ were poured into a 1−1.5 inch diameter column and subsequently washed with copious (500 mL) deionized H_2O. The rhodium complex was loaded onto the column simply by passing the aqueous Rh solution through the resin (the rhodium complex will 'stick' to the top of the column, forming a thin, dark orange band). The complex was then eluted by slowly increasing the $[MgCl_2]$ in the eluent in 500-mL batches, starting with 0.05 M $MgCl_2$ and increasing in increments of 0.05 M until the red band of the metal complex has passed through the column. The resultant eluted solution was concentrated on a reverse-phase cartridge primed with MeOH and eluted with 1:1:0.001 H_2O/MeCN/TFA (vol/vol/vol). Finally, the solvent was removed by lyophilization to yield the product as a red-orange powder. The complex can be further purified via reverse-phase high-performance liquid chromatography using an HP1100 HPLC system, a Varian DynaMax C18

semipreparative column, and an elution gradient of 85:15 to 40:60 H_2O (0.1% TFA):MeCN (0.1% TFA) over 60 min.

ESI-MS: 793 $[M-2H]^+$

UV-Vis (H_2O, pH 7.0): λ_{max} 267 nm (ε = 68,000 M^{-1}), 301 nm (ε = 40,000 M^{-1}), 313 nm (ε = 30,400 M^{-1}), 389 nm (ε = 19,400 M^{-1}).

2.3.5.13: EXAMPLE METALLATION: SYNTHESIS OF RH(PHEN)(CHRYSI)(DPA')$^{3+}$

In a 100-mL round-bottom flask, Rh(phen)(chrysi)$(X)_2$ (150 mg, 0.22 mmol) was combined with DPA' (150 mg, 0.5 mmol) in a 50/50 mixture of ethanol and deionized water (50 mL total volume) (**Figure 2.17**). The reaction was stirred at reflux overnight in an oil bath. The mixture was then allowed to cool, diluted with 200 mL H_2O, and purified by cation exchange chromatography.

Four inches of resin pre-equilibrated with 0.05 M $MgCl_2$ were poured into a 1−1.5 inch diameter column and subsequently washed with copious (500 mL) deionized H_2O. The rhodium complex was loaded onto the column simply by passing the aqueous Rh solution through the resin (the rhodium complex will 'stick' to the top of the column, forming a thin, dark orange band). The complex was then eluted by slowly increasing the $[MgCl_2]$ in the eluent in 500-mL batches, starting with 0.05 M $MgCl_2$ and increasing in increments of 0.05 M until the red band of the metal complex has passed through the column. The resultant eluted solution was concentrated on a reverse-phase cartridge primed with MeOH and eluted with 1:1:0.001 H_2O/MeCN/TFA (vol/vol/vol). Finally, the

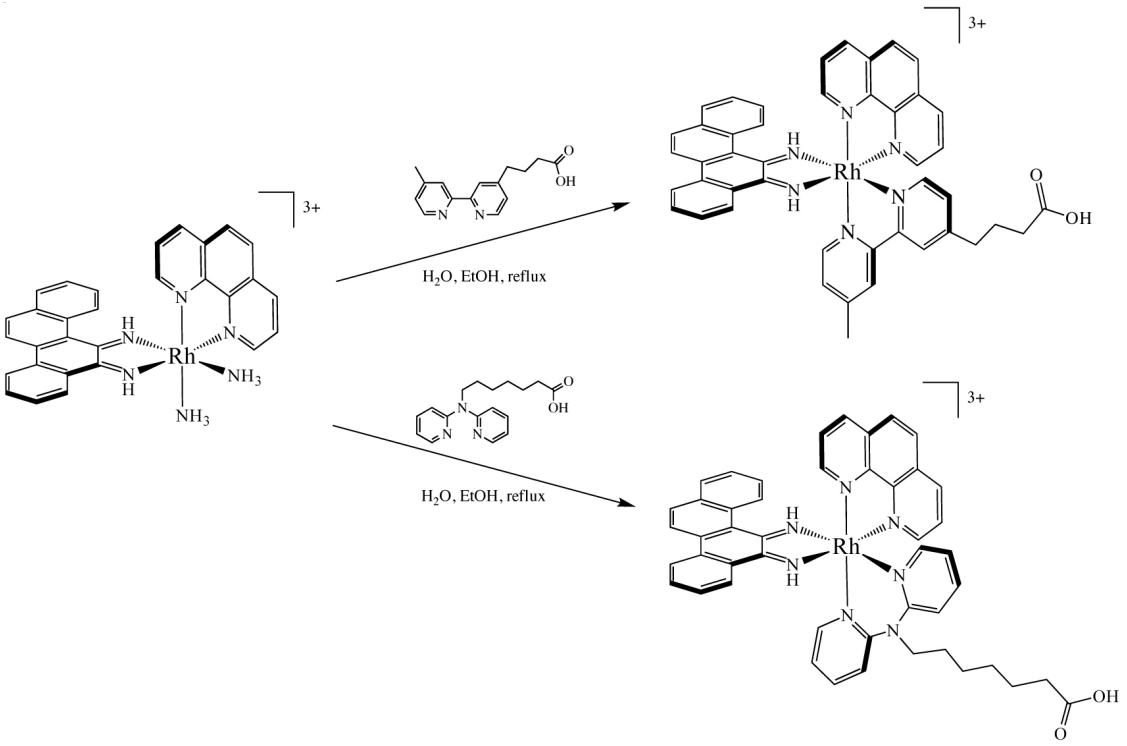

Figure 2.17: Metallation of bpy' and DPA' ligands. In each case, the linker-modified ligand [4-(4'-methyl-2,2'-bipyridin-4-yl)butanoic acid (bpy') or 7-(dipyridin-2-ylamino)heptanoic acid (DPA')] is metallated via reflux in a 1:1 mixture of H_2O:EtOH.

solvent was removed by lyophilization to yield the product as a red-orange powder. The complex can be further purified via reverse-phase high-performance liquid chromatography using an HP1100 HPLC system, a Varian DynaMax C18 semipreparative column, and an elution gradient of 85:15 to 40:60 H_2O (0.1% TFA):MeCN (0.1% TFA) over 60 min.

ESI-MS: 836 $[M-2H]^+$

UV-Vis (H_2O, pH 7.0): λ_{max} 269 nm (ε = 66,400 M^{-1}), 301 nm (ε = 31,100 M^{-1}), 408 nm (ε = 6,500 M^{-1}).

2.3.6: SYNTHESIS OF HDPA-BASED METALLOINSERTORS

2.3.6.1: SYNTHESIS OF $[Rh(chrysi)(NH_3)_4](Cl)_3$

$[Rh(NH_3)_6](PF_6)_3$ (200 mg, 0.3 mmol), chrysene-5,6-quinone (81 mg, 0.3 mmol), MeCN (100 mL) and NaOH (1 mL, 1 M) were combined in a 250-mL round-bottom flask and stirred for 18 h.[6] After 18 h, the reaction was stopped by neutralization with hydrochloric acid. The acetonitrile was removed *in vacuo*, and the residue was re-dissolved in 100 mL H_2O. The product was then anion-exchanged on a Sephadex QAE-25 column that had been pre-equilibrated with 0.05 M $MgCl_2$. Subsequently, the resulting solution was concentrated on a reverse phase C-18 cartridge, washed, eluted, and lyophilized to dryness. The resultant powder was used in subsequent reaction steps without further purification or characterization.

2.3.6.2: SYNTHESIS OF $[Rh(chrysi)(HDPA)_2](Cl)_3$

In a 100-mL round-bottom flask, $[Rh(chrysi)(NH_3)_4](Cl_3)$ (30 mg, 0.002 mmol) was combined with HDPA (7 mg, 0.004 mmol, 2 equiv.) in a 50/50 mixture of ethanol and deionized water (50 mL total volume) (**Figure 2.18**). The reaction was stirred at reflux overnight in an oil bath. The mixture was then allowed to cool, diluted with 200 mL H_2O, and purified by cation exchange chromatography.

Four inches of resin pre-equilibrated with 0.05 M $MgCl_2$ were poured into a 1−1.5 inch diameter column and subsequently washed with copious (500 mL) deionized H_2O. The rhodium complex was loaded onto the column simply by passing the aqueous Rh solution through the resin (the rhodium complex will 'stick' to the top of the column, forming a thin, dark orange band). The complex was then eluted by slowly increasing the $[MgCl_2]$ in the eluent in 500-mL batches, starting with 0.05 M $MgCl_2$ and increasing in increments of 0.05 M until the red band of the metal complex has passed through the column. The resultant eluted solution was concentrated on a reverse-phase cartridge primed with MeOH and eluted with 1:1:0.001 H_2O/MeCN/TFA (vol/vol/vol). Finally, the solvent was removed by lyophilization to yield the product as a red-orange powder. The complex can be further purified via reverse-phase high-performance liquid chromatography using an HP1100 HPLC system, a Varian DynaMax C18 semipreparative column, and an elution gradient of 85:15 to 40:60 H_2O (0.1% TFA):MeCN (0.1% TFA) over 60 min.

ESI-MS: 699 $[M-2H]^+$

UV-Vis (H_2O, pH 7.0): λ_{max} 287 nm (ε = 42,100 M^{-1}), 321 nm (ε = 23,200 M^{-1}), 442 nm (ε = 8,700 M^{-1}) (**Figure 2.19**).

2.3.6.3: SYNTHESIS OF [RH(HDPA)(Cl)$_4$]K

[Rh(HDPA)(Cl)$_4$]K was synthesized according to the method of Lee, et al.[37] $RhCl_3$ (263 mg, 1.1 mmol) and KCl (75 mg, 1.2 mmol) were dissolved in MeOH (10 mL) and heated to reflux for 2 h. After 2 h, a red-orange precipitate had formed in the reaction vessel. At this point, added HDPA (180 mg, 1.1 mmol) and continued reflux for 4 more h. During this time, a yellow precipitate formed. After 4 h, the solution was allowed to cool to room temperature, and the precipitate was collected by vacuum-filtration and dried under vacuum (300 mg, 66%).

ESI-MS (negative ion mode): 452 $[M-H+K]^-$

2.3.6.4: SYNTHESIS OF [RH(HDPA)(OTF)$_4$]K

A 50-mL Schlenk flask was charged with 300 mg [Rh(HDPA)(Cl)$_4$]K and deoxygenated by evacuating it and refilling with $Ar_{(g)}$ three times. Subsequently, 5 g triflic acid (excess) was added carefully to the reaction vessel under positive argon pressure (caution: triflic acid is very reactive and pyrophoric). After the addition of HOTf, the reaction vessel was closed with a rubber septum, the septum was pierced with a 16-gauge needle, and the flask was purged with argon for 60 seconds. The dark red reaction mixture was allowed to stir for 16 h with periodic $Ar_{(g)}$ purges to remove HCl generated by the reaction. After 16 h, the reaction mixture was added dropwise to 300 mL vigorously stirring diethyl either cooled to -78 ºC. The resultant yellowish precipitate was collected via filtration on a Buchner funnel, washed with cold diethyl ether, and used as promptly as possible.

2.3.6.5: SYNTHESIS OF $[Rh(HDPA)(NH_3)_4](X)_3$

In a 250-mL round-bottom flask fitted with a reflux condenser, 400 mg $[Rh(HDPA)(OTf)_4]K$ was suspended in 50 mL concentrated NH_4OH. The suspension was stirred, brought to reflux, and heated until all of the material went into solution (15 min); over the course of heating, the insoluble, singly charged complex is converted to the more soluble, triply-charged complex. Depending on the desired counter-ion, the product can be isolated one of two ways: (a) if the PF_6^- salt is desired, excess NH_4PF_6 should be added to the solution, and the reaction mixture should be cooled overnight to facilitate precipitation; (b) if the OTf^- counter-ion is desired, the NH_4OH should simply be removed by rotary evaporation at room temperature. Recoveries are best using the evaporation method and range from 80−100% depending on mechanical losses.

ESI-MS: 341 $[M-2H]^+$

2.3.6.6: SYNTHESIS OF $[Rh(HDPA)(CHRYSI)(NH_3)_2](Cl)_3$

In a 250-mL round-bottom flask, $Rh(HDPA)(NH_3)_4^{3+}$ (40 mg, 0.02 mmol) was combined with chrysene-5,6-quinone (7 mg, 0.02 mmol) in acetonitrile (30 mL) and an aqueous solution of sodium hydroxide (10 mL, 0.4 M). The reaction was capped to prevent evaporation and stirred overnight. After 16 h, the reaction was stopped by neutralization with hydrochloric acid; the reaction mixture was then anion-exchanged on a Sephadex QAE-25 column that had been pre-equilibrated with 0.05 M $MgCl_2$. The solution was concentrated on a reverse phase C-18 cartridge, washed, eluted, and lyophilized to dryness. The complex was further purified via reverse-phase high-performance liquid chromatography using an HP1100 HPLC system, a Varian DynaMax

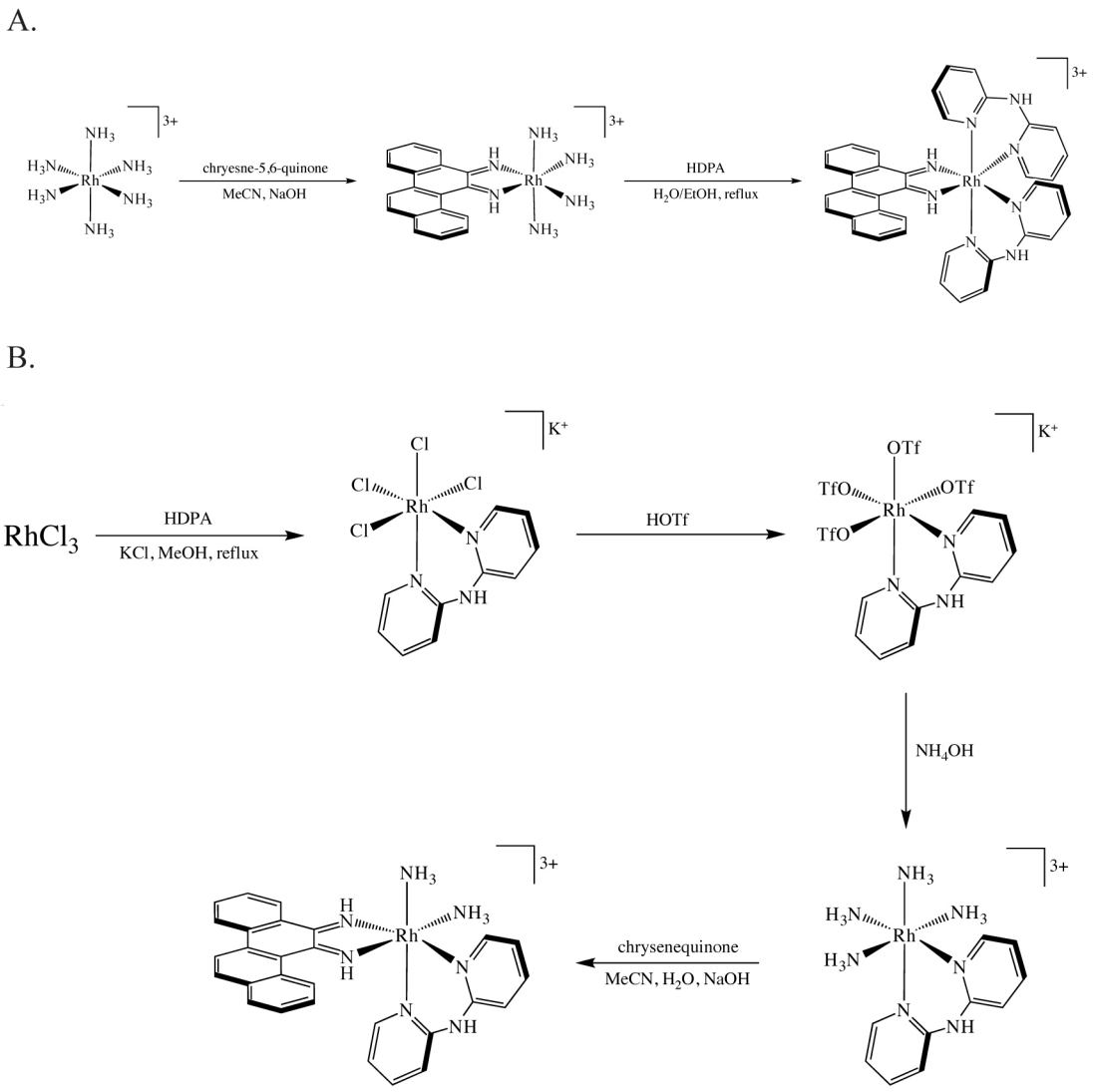

Figure 2.18: Synthesis of HDPA-based metalloinsertors. (A) $Rh(HDPA)_2(chrysi)^{3+}$ is synthesized in two steps from $Rh(NH_3)_6^{3+}$; (B) $Rh(chrysi)(HDPA)(NH_3)_2^{3+}$ is synthesized stepwise from $RhCl_3$.

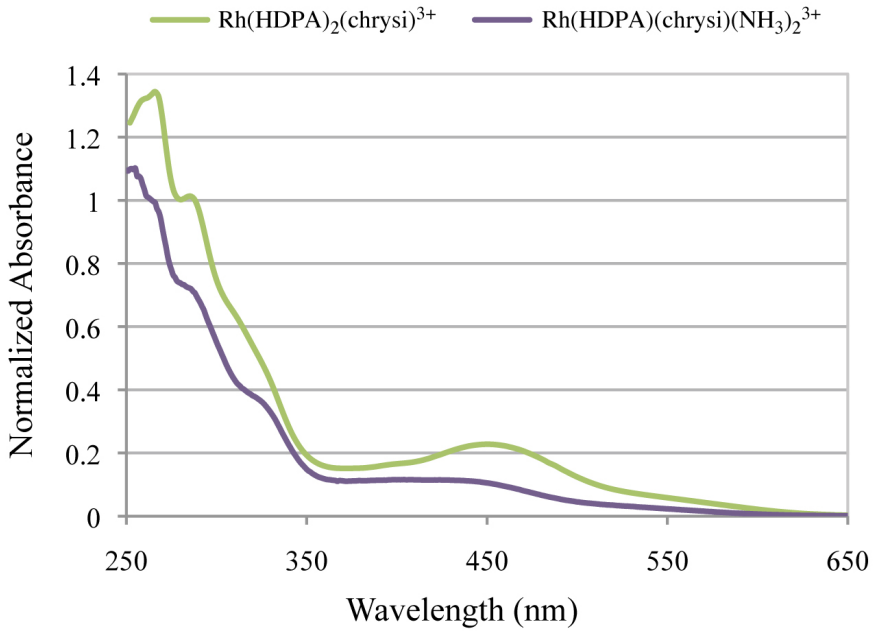

Figure 2.19: UV-Vis spectra of $Rh(HDPA)_2(chrysi)^{3+}$ and $Rh(chrysi)(HDPA)(NH_3)_2^{3+}$. For $Rh(HDPA)_2(chrysi)^{3+}$ (green): λ_{max} 287 nm (ε = 42,100 M^{-1}), 321 nm (ε = 23,200 M^{-1}), 442 nm (ε = 8,700 M^{-1}). For $Rh(HDPA)(chrysi)(NH_3)_2^{3+}$ (purple): λ_{max} 261 nm (ε = 42,645 M^{-1}), 281 nm (ε = 30,850 M^{-1}), 321 nm (ε = 15,900 M^{-1}), 404 nm (ε = 4,800 M^{-1})

C18 semipreparative column, and an elution gradient of 85:15 to 40:60 H_2O (0.1% TFA):MeCN (0.1% TFA) over 60 min.

ESI-MS: 564 $[M-2H]^+$

UV-Vis (H_2O, pH 7.0): λ_{max} 261 nm (ε = 42,645 M^{-1}), 281 nm (ε = 30,850 M^{-1}), 321 nm (ε = 15,900 M^{-1}), 404 nm (ε = 4,800 M^{-1}) (**Figure 2.19**).

2.4: NUCLEIC ACID PROTOCOLS

The nature of synthesis demands the precise reporting of individual reactions as they were performed. This type of writing is not as useful in describing nucleic acid experiments; in this case, the reader is far more likely to be referencing a protocol in order to repeat the *type* of experiment rather than the specific experimental details. Therefore, in this section, generalized protocols will be reported in order to simply the landscape for the future reader.

2.4.1: DNA SYNTHESIS AND PURIFICATION[38]

Oligonucleotides were synthesized using standard phosphoramidites on an ABI 3400 DNA synthesizer (reagents from ABI or Glen Research). The synthesizer was set to leave the DMT protecting group on the DNA and leave the DNA on the beads. After the synthesis run was complete, the columns were taken off the synthesizer and dried on a lyophilizer for 10 min. After 10 min, the columns were opened, and the beads were poured into 1.7 mL microcentrifuge tubes. The beads were suspended in 1.0 mL concentrated NH_4OH and heated to 60 °C for 12 h. After 12 h, the tubes were allowed to cool to room temperature, and the NH_4OH solution was separated from the beads, filtered through a microfilterfuge tube, and evaporated to dryness in a speedvac.

After evaporation, the DMT-protected DNA was taken up in 500 mL H_2O, filtered through a microfilterfuge tube, and purified via reverse phase HPLC with a Varian DynaMax^{TM} C18 semi-preparative column and gradient of 5:95 to 45:55 MeCN:50 mM NH_4OAc (aq) over 30 min. The product-containing fraction was collected in a 15 mL centrifuge tube and lyophilized to dryness. Next, in order to remove the DMT group, the dry DNA was taken up in 300 μL 85% acetic acid, vortexed to ensure complete dissolution, centrifuged, and allowed to sit for 15 min (at this point, the solution may turn a slight orange/pink color if the DNA is concentrated enough). After 15 min, 1.0 mL EtOH is added to precipitate the DNA, and the resultant suspension was moved to a 1.5 mL microcentrifuge tube and centrifuged. The supernatant was then discarded, the solid was further dried in a speedvac.

The dried DMT-off DNA was resuspended in 500 μL H_2O and subjected to a second round of HPLC with a gradient of 2:98 to 17:83 MeCN:50 mM NH_4OAc (aq) over 30 min. The product-containing fraction was collected in a 15 mL centrifuge tube and lyophilized to dryness. After evaporation, the purified DNA was taken up in 200 μL buffer (10 mM Tris·HCl, pH 7.1), quantified by UV-Vis, and stored at -20 °C.

2.4.2: DNA RADIOLABELING AND PURIFICATION[39]

In a 1.7 mL microcentrifuge tube, 15 μL H_2O, 1 μL oligonucleotide (100 μM stock), 2 μL polynucleotide kinase buffer (10X, Roche Biosciences), 1 μL polynucleotide kinase (Roche Biosciences), and 1 μL γ-^{32}P-ATP (MP Biomedicals, 5 mCi stock) were combined. The solutions were then heated at 37 °C for 2 h. After 2 h, 80 μL water was added to the reaction, and the solutions were filtered through Micro Bio-Spin 6

chromatography columns (centrifugation should not exceed 3,000 rpm) and dried *in vacuo*.

After evaporation, the labeling reactions were taken up in 10 μL denaturing formamide loading dye (80% formamide, 10 mM NaOH, 0.025% xylene cyanol, and 0.025% bromophenol blue in 1X TBE buffer), loaded on a 20% denaturing PAGE gel, and electrophoresed for 60−90 min at 90 W with 1X TBE as the running buffer. After electrophoresis, one of the gel plates was removed, leaving the gel affixed to the other plate. The gel was visualized via X-ray, and the parts of the gel that correspond to the full-length, labeled DNA were cut out with a clean razor blade. Using tweezers, the cut out gel pieces were placed into a clean centrifuge tube, 1 mL 100 mM triethylammonium acetate (pH 7.0) was added to the tube, and the tube was incubated overnight at 37 °C.

The next day, the DNA-containing triethylammonium solution was removed and placed in a clean 1.7 mL microcentrifuge tube. The solvent was then removed via speedvac. After evaporation, the samples were re-dissolved in 100 μL water and purified using a Micro Bio-Spin 6 chromatography column (centrifugation should not exceed 3,000 rpm). The solvent was again removed via speedvac. After evaporation, the purified, labeled DNA was taken up in 50 μL buffer (10 mM Tris·HCl, pH 7.1) and stored at 4 °C

2.4.3: MAXAM-GILBERT SEQUENCING REACTIONS[39]

In a small microcentrifuge tube, 32 μL water, 2 μL calf thymus DNA (4 mM stock), and a minimum volume of water containing radiolabeled DNA (corresponding to >1,000,000 counts) were combined. This solution was then divided into two tubes (~18 μL each) for the A+G and C+T sequencing reactions.

For the A+G reaction, 2 μL piperidine formate (formed by mixing 5 μL piperidine, 75 μL formic acid, and 20 μL water) were added to the radiolabeled DNA solution, and the tube was vortexed, centrifuged, and incubated at 37 °C for 30 min. After 30 min, 240 μL hyrdrazine stop solution (0.3 M sodium acetate pH 7.0, 0.1 mM EDTA pH 8.0, 100 μg/mL yeast tRNA) were added to the solution to terminate the reaction.

For the C+T reaction, 30 μL hydrazine monohydrate were added to the radiolabeled DNA solution, and the tube was vortexed, centrifuged, and incubated at 37 °C for 30 min. After 30 min, 200 μL hyrdrazine stop solution (0.3 M sodium acetate pH 7.0, 0.1 mM EDTA pH 8.0, 100 μg/mL yeast tRNA) were added to the solution to terminate the reaction. From this point on, both reaction tubes were treated identically.

Ethanol (750 μL, 200 proof) was added to each reaction, and the tubes were mixed thoroughly and placed in dry ice for 15 min. After 15 min, the tubes were centrifuged for 12 min at 14,000 rpm at 4 °C. After centrifugation, the supernatant was removed carefully to ensure that the radiolabeled pellet (as checked by Geiger counter) was not lost.

A second ethanol precipitation followed the first. Each pellet was taken up in 100 μL H_2O, and 50 μL 7.5 M NH_4OAc was added to each tube, followed by thorough mixing and centrifugation. Ethanol (750 μL, 200 proof) was then added to each reaction, and the tubes were mixed thoroughly and placed in dry ice for 15 min. After 15 min, the tubes were centrifuged for 12 min at 14,000 rpm at 4 °C. After centrifugation, the supernatant was removed carefully to ensure that the radiolabeled pellet (as checked by Geiger counter) was not lost. Samples were dried on a speedvac for 30 min to remove any residual EtOH.

After removing the EtOH, both samples were then dissolved in 100 μL 10% piperidine, vortexed, centrifuged, and heated to 90 °C for 30 min. After allowing the reactions to cool to room temperature, the piperidine was removed *in vacuo*. Once dry, the samples were taken up again in 100 μL water, vortexed, centrifuged, and then dried again *in vacuo.* This cycle was repeated three more times to yield the completed samples.

2.4.4: ELECTROPHORESIS EXPERIMENTS

2.4.4.1: RECOGNITION AND PHOTOCLEAVAGE[24]

Radiolabeled DNA duplexes were prepared to a final concentration of 2 μM by combining 2 μL forward strand (100 μM stock), 2 μL complementary strand (100 μM stock), 4 μL radiolabeled strand (from **2.4.2**, ~50 nM stock), and 92 μL buffer (*e. g.* 40 mM NaCl, 20 mM NaPi, pH 7.1), heating the solution to 90 °C for 5 min, and then allowing the solution to cool to room temperature slowly over the course of 60 min. Duplexes either containing or lacking a central defect (mismatch, abasic site, single base bulge, etc.) were prepared.

For the recognition experiments, 10 μL metalloinsertor stock solution [e. g. 2 μM $Rh(bpy)_2(chrysi)^{3+}$ or $Rh(bpy)_2(phzi)^{3+}$] were combined with 10 μL DNA stock solution in a 1.7 mL microcentrifuge tube. Dark and light control samples were also prepared and, of course, lacked the appropriate solution components. Because metalloinsertor photocleavage is single-stranded, each duplex was interrogated twice, once with each of the two strands radioactively labeled. Samples were irradiated with an Oriel Instruments solar simulator (320−440 nm). Irradiations were performed in open,

Vertically-oriented 1.7 mL microcentrifuge tubes in a Lucite sample holder. After irradiation, samples were incubated at 60 °C for 30 min to degrade any metastable products and then dried under vacuum. Dried samples were redissolved in denaturing formamide loading dye (see above for components) and electrophoresed on a 20% denaturing polyacrylamide gel for 60−90 min at 90 Watts. Images of the gels were obtained via phosphorimagery (Molecular Dynamics) and quantified using ImageQuant software (**Figure 2.20**).

2.4.4.2: BINDING CONSTANT TITRATIONS

Photocleavage titrations are performed to determine the binding constants of metalloinsertors for defect sites of interest.[40] Procedurally, these experiments are very similar to the recognition and photocleavage experiments described above.

In order to perform a binding constant titration, a series of solutions were created in 1.7 mL microcentrifuge tubes, each combining 10 μL radiolabeled duplex DNA stock solution (constant concentration, for example, 1 μM) with 10 μL metalloinsertor stock solution (variable concentrations). The gradient of metalloinsertor concentrations was centered on the approximated dissociation constant of the complex in question; for example, a concentration gradient of 100 nM, 200 nM, 400 nM, 600 nM, 800 nM, 1 μM, 2 μM, 4 μM, 6 μM, 8 μM, 10 μM and 15 μM was employed for a metalloinsertor with an

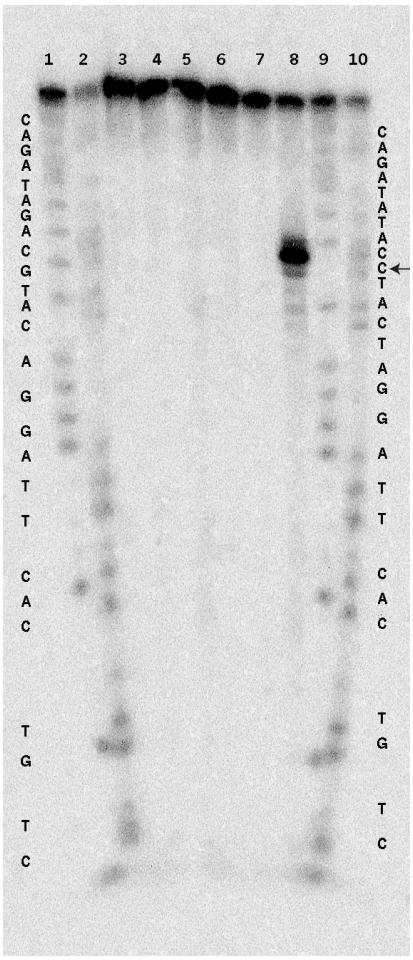

Figure 2.20: Sample mismatch photocleavage gel. 20% polyacrylamide gel showing mismatch-specific photocleavage by Δ-Rh(bpy)$_2$(chrysi)$^{3+}$ of the oligonucleotide 5'-A CTG TCA CTT AGG ATC AT***C*** CAT ATA GAC GCG-3', where *C* denotes the site of a central CC mismatch. Conditions employed: 1 μM duplex DNA, 50 mM NaCl/10mM NaPi pH 7.1 buffer, 1 μM Rh complex when applicable, irradiations performed on an Oriel Instruments solar simulator (320 nm−440 nm) for 15 min. Lanes 1 and 2: matched DNA, sequencing reactions. Lane 3: matched DNA, light control. Lane 4: matched DNA, dark control. Lane 5: matched DNA irradiated with Δ-Rh(bpy)$_2$(chrysi)$^{3+}$. Lane 6: mismatched DNA, light control. Lane 7: mismatched DNA, dark control. Lane 8: mismatched DNA irradiated with Δ-Rh(bpy)$_2$(chrysi)$^{3+}$. Lanes 9 and 10: mismatched DNA, sequencing reactions.

anticipated specific dissociation constant of approximately 1 μM. Dark and light control samples were also prepared and, of course, lacked the appropriate solution components.

Irradiations were performed for 15 min in open, vertically-oriented 1.7 mL microcentrifuge tubes (in Lucite sample holders) using an Oriel Instruments solar simulator (320−440 nm). After irradiation, samples were incubated at 60 °C for 30 min to degrade any metastable products and then dried under vacuum. Dried samples were redissolved in denaturing formamide loading dye and electrophoresed on a 20% denaturing polyacrylamide gel for 60−90 min at 90 Watts. Images of the gels were obtained via phosphorimagery (Molecular Dynamics). The fraction cleaved at the defect site was quantitated using ImageQuant software, expressed as a fraction of the total parent DNA, and fit to a single site, one parameter binding model. The mid-point of the resultant sigmoid (the log of [rhodium complex] at the inflection point of the curve) is the apparent dissociation constant, and the apparent dissociation constant minus half the DNA concentration used in the titration yields the true dissociation constant. The apparent and true binding constants can be determined by taking the inverse of the above values.

2.4.4.3: COMPETITION TITRATIONS

When site recognition via direct methods such as photoactivated strand scission fails, competition titrations provide an alternative means to determine the specificity of a complex. Two types of competition experiments exist: those employing non-specific metallointercalators and those using site-specific metalloinsertors. The former cannot readily provide quantitative data but yields valuable qualitative information on the

relative affinity of the molecule of interest for different sites in the DNA duplex. The latter allows for the interrogation of only a single site in the duplex, but it can provide important quantitative data about the system.[41−43]

For a competition experiment with a non-specific metallointercalator, samples of radiolabeled, duplex DNA (10 μL, 1 μM) in buffer (e. g. 50 mM NaCl, 10 mM NaPi, pH 7.1) were incubated with a saturating amount of a non-specific metallointercalator (for example, 5 μL $Rh(bpy)_2(phi)^{3+}$ solution, with a concentration that provides a saturating amount of 1 rhodium molecule/4 base pairs) and irradiated for 20 min using an Oriel Instruments solar simulator (320−440 nm) in the presence of variable concentrations of the metal complex of interest (5 μL for a total sample volume of 20 μL). Dark, light, and other control samples were also prepared and, of course, lacked the appropriate solution components. After preparation, the samples were dried on a speedvac, taken up in denaturing formamide dye, and electrophoresed on a 20% denaturing polyacrylamide gel for 60−90 min at 90 Watts. Images of the gels were obtained via phosphorimagery (Molecular Dynamics) and quantified using ImageQuant software. In the absence of metalloinsertor, the non-specific metallointercalator will indiscriminately cleave at all base pairs in the duplex, including the mismatch site. If the complex in question specifically binds the mismatch, the intensity of the metallointercalator photocleavage band at that site will decrease upon its addition. This photocleavage attenuation is the indicator of specific binding.

For a competition experiment with a site-specific metalloinsertor, samples of radiolabeled, duplex DNA (10 μL, 1 μM) in buffer (e. g. 50 mM NaCl, 10 mM NaPi, pH 7.1) were incubated with a site-specific metalloinsertor with a known affinity for the site

of interest (for example, 5 μL of a $Rh(bpy)_2(chrysi)^{3+}$ solution, with a concentration that results in 50% of the target site bound) and irradiated for 20 min using an Oriel Instruments solar simulator (320−440 nm) in the presence of variable concentrations of the molecule of interest (5 μL for a total sample volume of 20 μL, with concentrations spread across the relevant concentration regime). Dark, light, and other control samples were also prepared and, of course, lacked the appropriate solution components. After preparation, the samples were dried on a speedvac, taken up in denaturing formamide dye, and electrophoresed on a 20% denaturing polyacrylamide gel for 60−90 min at 90 Watts. Images of the gels were obtained via phosphorimagery (Molecular Dynamics). The fraction cleaved at the defect site was quantitated using ImageQuant software, expressed as a fraction of the total parent DNA, and plotted against the concentration of the metal complex of interest. The binding and dissociation constants of the non-photocleaving complex were calculated by solving simultaneous equilibria involving the DNA, the site-specific metalloinsertor, and the metal complex of interest in Mathematica 6.0.

2.4.5: MALDI-TOF ANALYSIS OF CLEAVAGE FRAGMENTS[44]

For mass spectrometry analysis of photocleavage products, solutions of duplex were incubated with solutions of the molecule of interest and irradiated as described above in section **2.4.4.1**. After irradiation and incubation, the samples were dried *in vacuo*, resuspended in 10 μL water, desalted using 10 μL OMIX C18 tips (Varian), dried *in vacuo* again, and resuspended in 2 μL H_2O. Light and dark controls were also prepared. Mass spectrometry was performed using a Voyager DE-PRO MALDI-TOF

instrument with a 337 nm nitrogen laser source (Applied Biosystems). A 4-hydroxypicolinic acid matrix was employed. All mass spectra were internally calibrated using the mass of the parent oligonucleotide.

2.5: REFERENCES

1. Zeglis, B. M.; Barton, J. K. *Nature Protocols* **2007**, *2(2)*, 357−371.
2. Graebe, C.; Honigsberger, F. *Justus Liebigs Annalen Der Chemie* **1900**, *311* (1/3), 257−275.
3. Junicke, H.; Hart, J. R.; Kisko, J. L.; Glebov, O.; Kirsch, I. R.; Barton, J. K. *Proceedings of the National Academy of Sciences U. S. A.* **2003**, *100*, 3737−3742.
4. Vanallan, J. A.; Reynolds, G. A. *Journal of Organic Chemistry* **1963**, *28* (4), 1019−1022.
5. Gillard, R. D.; Osborn, J. A.; Wilkinson, G. *Journal of the Chemical Society* **1965**, *(JUL)*, 4107−4110.
6. Murner, H.; Jackson, B. A.; Barton, J. K. *Inorganic Chemistry* **1998**, *37* (12), 3007−3012.
7. Gidney, P. M.; Gillard, R. D.; Heaton, B. T. *Journal of the Chemical Society-Dalton Transactions* **1972**, (23), 2621−2628.
8. Creaser, I. I.; Geue, R. J.; Harrowfield, J. M.; Herlt, A. J.; Sargeson, A. M.; Snow, M. R.; Springborg, J. *Journal of the American Chemical Society* **1982**, *104* (22), 6016−6025.

9. Creaser, I. I.; Harrowfield, J. M.; Herlt, A. J.; Sargeson, A. M.; Springborg, J.; Geue, R. J.; Snow, M. R. *Journal of the American Chemical Society* **1977**, *99* (9), 3181−3182.

10. Geue, R. J.; Hohn, A.; Ralph, S. F.; Sargeson, A. M.; Willis, A. C. *Journal of the Chemical Society-Chemical Communications* **1994**, (12), 1513−1515.

11. Geue, R. J.; Korybutdaszkiewicz, B.; Sargeson, A. M. *Journal of the Chemical Society-Chemical Communications* **1993**, (18), 1454−1456.

12. Harrowfield, J. M.; Herlt, A. J.; Lay, P. A.; Sargeson, A. M.; Bond, A. M.; Mulac, W. A.; Sullivan, J. C. *Journal of the American Chemical Society* **1983**, *105* (16), 5503−5505.

13. Harrowfield, J. M.; Robertson, G. B.; Sargeson, A. M.; Whimp, P. O. *Journal of the Chemical Society-Chemical Communications* **1975**, (4), 109−111.

14. Krotz, A. H.; Kuo, L. Y.; Barton, J. K. *Inorganic Chemistry* **1993**, *32* (26), 5963−5974.

15. Pyle, A. M.; Chiang, M. Y.; Barton, J. K. *Inorganic Chemistry* **1990**, *29* (22), 4487−4495.

16. Belser, P.; Vonzelewsky, A.; Zehnder, M. *Inorganic Chemistry* **1981**, *20* (9), 3098−3103.

17. Schlosser, K.; Hoyer, E. *Zeitschrift Fur Anorganische Und Allgemeine Chemie* **1972**, *387* (1), 91−95.

18. Palmer, J. W.; Basolo, F. *Journal of Physical Chemistry* **1960**, *64* (6), 778−780.

19. Palmer, J. W.; Basolo, F. *Journal of Inorganic & Nuclear Chemistry* **1960**, *15* (3−4), 279−286.

20. Jackson, B. A.; Barton, J. K. *Journal of the American Chemical Society* **1997**, *119* (52), 12986−12987.

21. Jackson, B. A.; Henling, L. M.; Barton, J. K. *Inorganic Chemistry* **1999**, *38* (26), 6218−6224.

22. Sitlani, A.; Long, E. C.; Pyle, A. M.; Barton, J. K. *Journal of the American Chemical Society* **1992**, *114* (7), 2303−2312.

23. Keene, F. R. *Coordination Chemistry Reviews* **1997**, *166*, 121−159.

24. Jackson, B. A.; Barton, J. K. *Biochemistry* **2000**, *39* (20), 6176−6182.

25. Broomhead, J. A.; Grumley, W. *Inorganic Chemistry* **1971**, *10* (9), 2002−2009.

26. Broomhead, J. A.; Kane, M. *Inorganic Chemistry* **1971**, *10* (1), 85−87.

27. McKenzie, E. D.; Plowman, R. A. *Journal of Inorganic & Nuclear Chemistry* **1970**, *32* (1), 199−205.

28. Dixon, N. E.; Lawrance, G. A.; Lay, P. A.; Sargeson, A. M. *Inorganic Chemistry* **1984**, *23* (19), 2940−2947.

29. Dixon, N. E.; Lawrance, G. A.; Lay, P. A.; Sargeson, A. M.; Taube, H. *Inorganic Syntheses* **1990**, *28*, 70−76.

30. Dixon, N. E.; Lawrance, G. A.; Lay, P. A.; Sargeson, A. M. *Inorganic Chemistry* **1983**, *22* (5), 846−847.

31. Petitjean, A.; Barton, J. K. *Journal of the American Chemical Society* **2004**, *126* (45), 14728−14729.

32. Schatzschneider, U.; Barton, J. K. *Journal of the American Chemical Society* **2004**, *126* (28), 8630−8631.

33. Lim, M. H.; Lau, I. H.; Barton, J. K. *Inorganic Chemistry* **2007**, *46*, 9528−9530.

34. Gibson, M. S.; Bradshaw, R. W. *Angewandte Chemie−International Edition* **1968**, *7* (12), 919−930.

35. Gabriel, S. *Chemische Berichte* **1887**, *20*, 2224−2237.

36. Krasinski, A.; Radic, Z.; Manetsch, R.; Raushel, J.; Taylor, P.; Sharpless, K. B.; Kolb, H. C. *Journal of the American Chemical Society* **2005**, *127*, 6686−6692.

37. Lee, J. R.; Lung, J. W.; Huang, J. Chinese Chemical Society **2003**, *50* (227−232).

38. Zeglis, B. M.; Pierre, V. C.; Barton, J. K. Chemical Communications **2007**, 4565−4579.

39. Sambrook, J.; Russell, D. Molecular Cloning: A Laboratory Manual. 3rd Edition ed.; Cold Spring Harbor Laboratory Press: Cold Spring Harbor, 2001.

40. Ernst, R. J.; Song, H.; Barton, J. K. Journal of the American Chemical Society **2009**, *131* (6), 2359−2366.

41. Jackson, B. A. California Institute of Technology, Pasadena, 2001.

42. Hart, J. R. Synthesis and applications of bulky rhodium(III) intercalators for the recognition of DNA mismatches. California Institute of Technology, Pasadena, CA, 2006.

43. Garbett, N. C.; Chaires, J. B. Binding: A polemic and rough guide. In Biophysical Tools for Biologists: Vol. 1 in Vitro Techniques, Elsevier Academic Press Inc: San Diego, 2008; Vol. 84, pp 3−23.

44. Brunner, J.; Barton, J. K. Journal of the American Chemical Society **2006**, *128* (21), 6772−6773.

CHAPTER 3: A MISMATCH-SELECTIVE, BIFUNCTIONAL RHODIUM-OREGON GREEN CONJUGATE: A FLUORESCENT PROBE FOR MISMATCHED DNA[ξ]

3.1: INTRODUCTION

Mismatch repair deficiency on the cellular level can have dire consequences on the physiological level: the accumulation of genomic mismatches and their consequent mutations create a high likelihood for cancerous transformations.[1−3] Indeed, mutations in MMR genes have been identified in 80% of hereditary non-polyposis colon cancers (also known as Lynch syndrome), and 15−20% of biopsied solid tumors have shown evidence of somatic mutations associated with MMR genes.[4−10] Moreover, MMR deficiency has also been linked to resistance to common chemotherapeutic and antineoplastic agents such as doxorubicin and cisplatin.[9, 11, 12]

Given these profound links between mismatch repair deficiency and cancer, the development of our unique recognition technology for diagnostic applications has been an important focus of our laboratory.[13−16] Indeed, one can envision two types of metalloinsertor-based diagnostics for mismatch repair deficiency: (1) an *in vitro* probe that could be employed to interrogate the extracted DNA of biopsied cancer cells and (2) an *in vivo* agent that could be used to investigate intact DNA within cultured tumor cells.

In both scenarios, fluorescence is a particularly attractive reporter.[17−20] Consequently, we have previously used a ruthenium-based probe designed to

[ξ] Adapted from Zeglis, B. M.; Barton, J. K. A mismatch-selective bifunctional rhodium-Oregon Green conjugate: A fluorescent probe for mismatched DNA. *J. Am. Chem. Soc.* **2006**, *128*, 5654−5655.

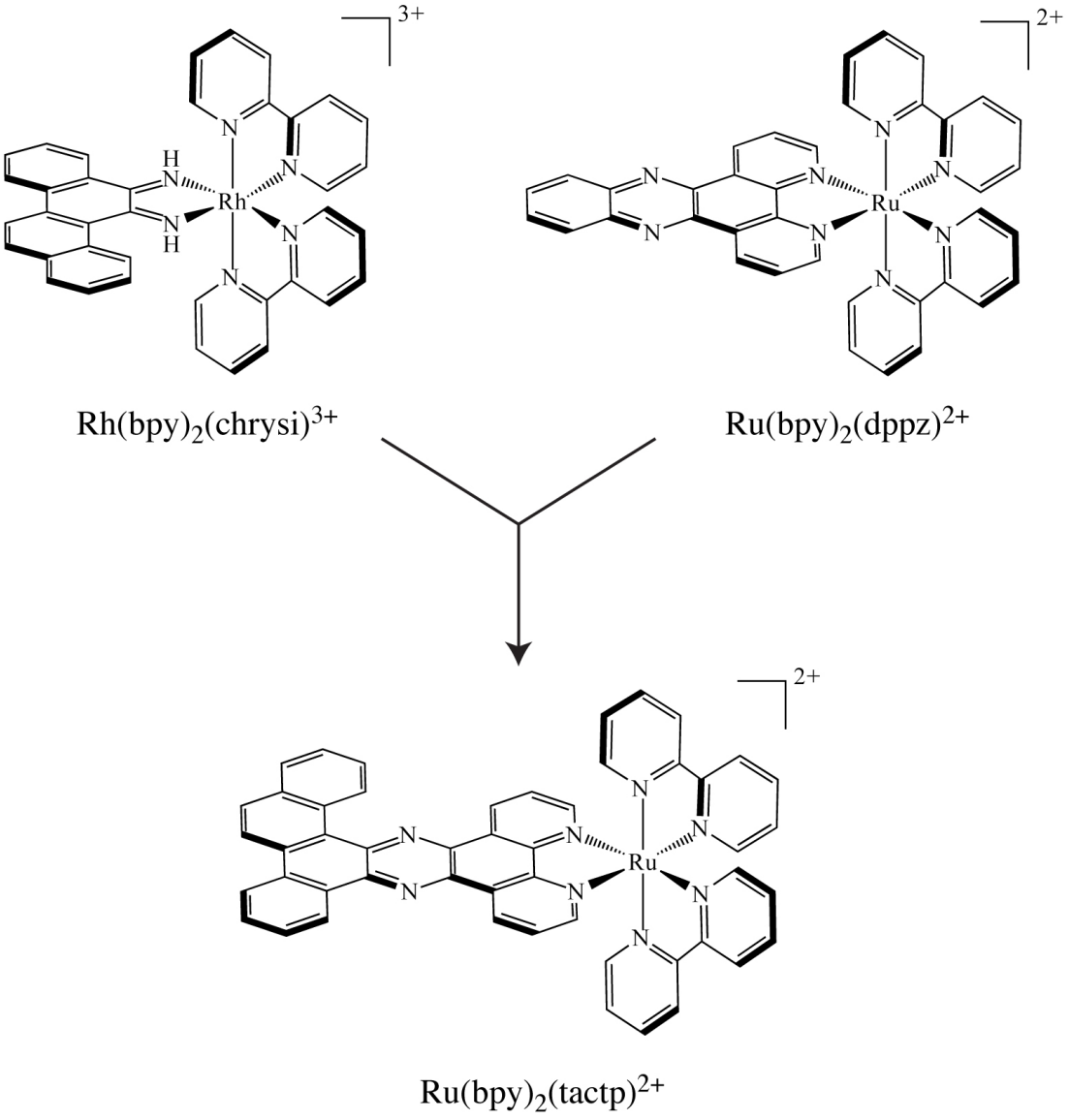

Figure 3.1: Design of $Ru(bpy)_2(tactp)^{2+}$. The ruthenium bisdipyridyl complex bears a sterically expansive, luminescent ligand that is a structural chimera of the chrysi and dppz ligands.

fluoresce specifically in the presence of mismatched DNA (**Figure 3.1**).[21] The metal complex, $Ru(bpy)_2(tactp)^{2+}$, seeks to combine in a single entity the DNA light-switch character of the $Ru(dppz)(L)_2^{2+}$ family of complexes and the mismatch-specificity of the $Rh(chrysi)(L)_2^{3+}$ class of agents. To this end, a chimeric ligand, tactp (4,5,9,18-tetraazachryseno[9,10-b]-triphenyelene), that contains the critical structural features of both chrysene-5,6-quinone (chrysi) and dipyrido[3,2-*a*:2',3'-*c*]phenazine (dppz) was synthesized and metallated onto a ruthenium bisdipyridyl platform. Singlet oxygen sensitization experiments confirm that the complex does, indeed, selectively bind mismatched sites in duplex DNA; however, the avid dimerization of the expansive aromatic ligand leads to high levels of non-specific fluorescence and thus dramatically limits its diagnostic potential.

The significant limitations of the single metal complex $Ru(bpy)_2(tactp)^{2+}$ system led us to pursue a markedly different avenue: bifunctional conjugates. Anatomically, bifunctional conjugates are tripartite, composed of metalloinsertor, linker, and payload subunits.[22–24] In this case, the mismatch-specific metalloinsertor would be covalently tethered to an organic fluorophore, thus conferring mismatch-specificity on the otherwise non-specific fluorescent moiety (**Figure 3.2**). Of course, simply getting the fluorophore in the proximity of mismatched DNA is not good enough. Ideally, a mismatch-specific fluorophore would be inactivated when in free solution or in the presence of matched DNA and selectively activated in the presence of mismatched DNA. Separating the metalloinsertor and fluorophore subunits in a bifunctional conjugate eliminates the possibility of the useful light-switch behavior characteristic of the $Ru(dppz)L_2^{2+}$ complexes. However, the two component, bifunctional system lends itself

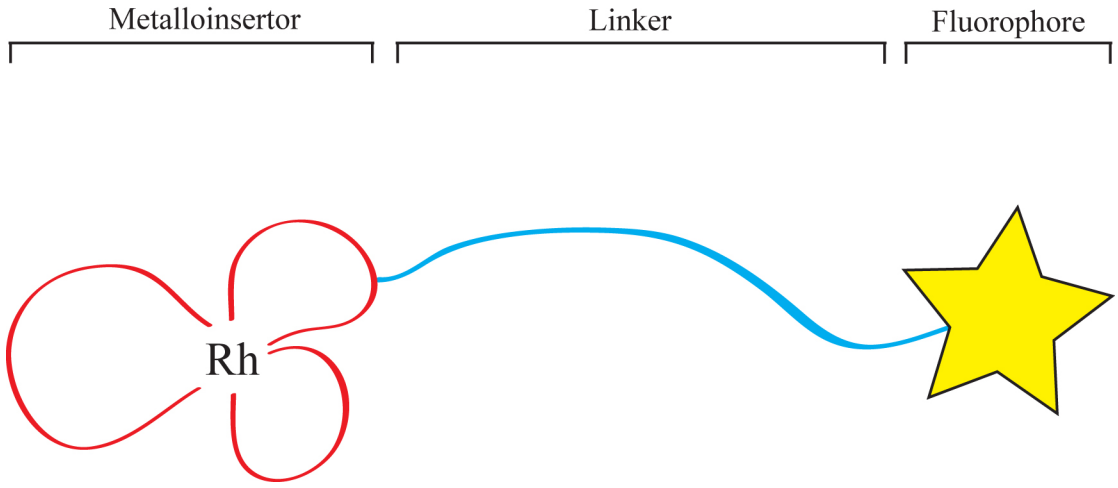

Figure 3.2: The anatomy of a bifunctional conjugate. In the case of a mismatch-specific fluorophore, a metalloinsertor subunit (red) is covalently linked (blue) to an organic fluorophore (yellow).

extremely well to an alternative strategy for achieving fluorescence selectivity: differential intramolecular quenching.

The strategy is quite simple: a flexible linker will covalently attach a positively charged, mismatch-specific metalloinsertor and a negatively charged, organic fluorophore. In the absence of DNA, the positively-charged rhodium complex will ion pair with the negatively charged fluorophore, thus quenching its fluorescence (**Figure 3.3**). The same will be true in the presence of matched DNA, for the mismatch-selective metalloinsertor will not interact with the well-matched oligonucleotide. In the presence of mismatched DNA, in contrast, the metalloinsertor will selectively bind the mismatched sites, and the negatively charged phosphodiester backbone will repel the fluorophore away from the DNA and the rhodium moiety, reducing quenching and increasing fluorescence.

Herein, we report the design, synthesis, and fluorescence testing of bifunctional conjugates for the selective detection of mismatched DNA.

3.2: Results and Discussion

3.2.1: First Generation Conjugate

3.2.1.1: Synthesis and Characterization

The first generation conjugate was assembled sequentially from $RhCl_3$. In order to facilitate conjugation, a trisheteroleptic metalloinsertor, Rh(phen)(chrysi)(^{NH2}bpy)$^{3+}$, was first synthesized according to published protocols (**Figure 3.4**). A dimethyl-bipyridine ligand bearing an aliphatic aminohexyl chain, ^{NH2}bpy, was employed to provide the flexible linker between the metalloinsertor and fluorophore.

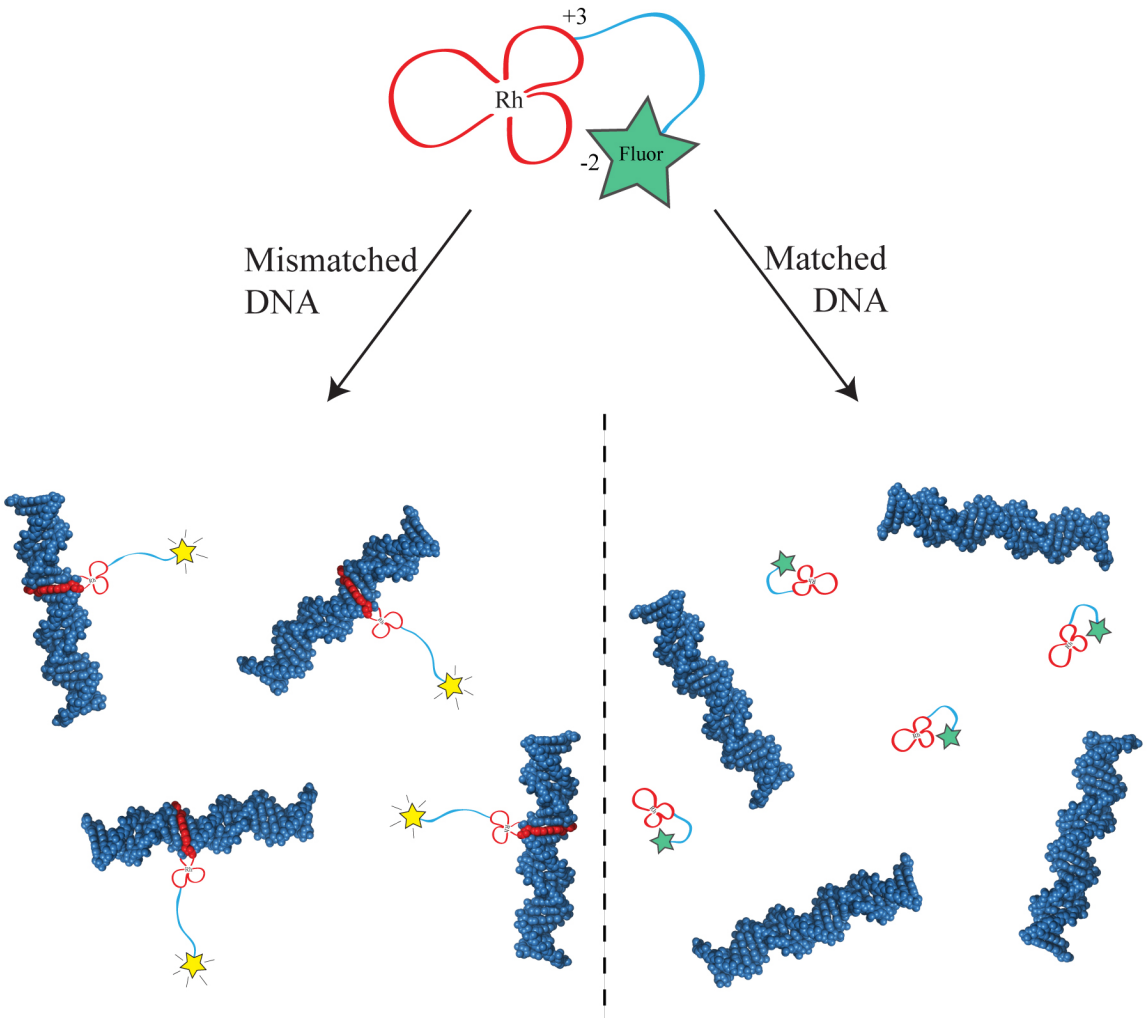

Figure 3.3: Differential intramolecular quenching scheme. In the absence of DNA or presence of matched DNA, the rhodium and fluorophore moieties will ion pair, dramatically quenching the fluorescence of the latter. In the presence of mismatched DNA, the metalloinsertor will bind the oligonucleotide, and the negatively charged phosphate backbone will repel the fluorophore away from the rhodium and the DNA, reducing quenching and increasing fluorescence.

Oregon Green 514™ (Molecular Probes, Invitrogen) was chosen for the fluorophore for three reasons: it is water soluble, it is negatively charged (-2 at pH 7), and it does not interact with DNA. The trisheteroleptic metalloinsertor moiety was easily coupled to the commercially-available succinimidyl ester of Oregon Green 514™ in DMF at room temperature (**Figure 3.5**). The completed conjugate was purified via cation exchange chromatography and reverse-phase HPLC using an HP1100 HPLC system, a Varian DynaMax C18 semipreparative column, and an elution gradient of 85:15 to 40:60 H_2O (0.1% TFA):MeCN (0.1% TFA) over 60 min.

The first generation metalloinsertor-Oregon Green conjugate (RhOG) was characterized via UV-Vis and fluorescence spectroscopy. Not surprisingly, the absorbance spectrum of the conjugate resembles the sum of the spectra of the two subunits, with metalloinsertor bands at 303 nm and 313 nm and a large fluorophore peak at 519 nm (**Figure 3.6a**). Fluorescence studies of RhOG reveal excitation and emission maxima at 519 and 530 nm, respectively, slightly shifted relative to the parent Oregon Green fluorophore (**Figure 3.7b**). As expected, the fluorescence of RhOG is dramatically quenched relative to both free Oregon Green and an equimolar, 1:1 solution of Rh(phen)(chrysi)(^{NH2}bpy)$^{3+}$ and Oregon Green. Further, fluorescence titrations of untethered Oregon Green and untethered Rh(phen)(chrysi)(^{NH2}bpy)$^{3+}$ eliminate the inner filter effect and an energy transfer quenching mechanism and instead support electron transfer as the source of quenching.

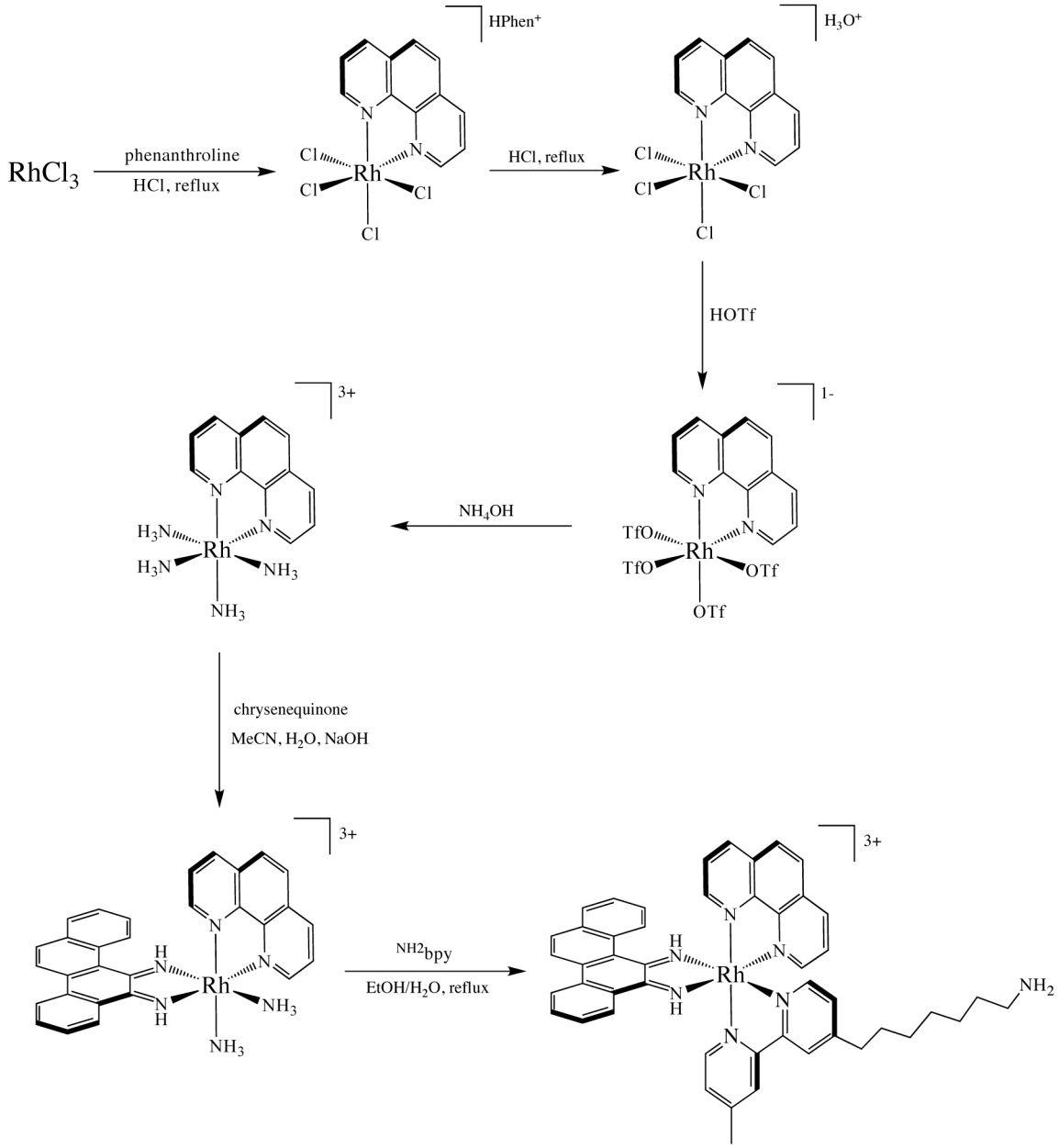

Figure 3.4. **Synthesis of the trisheteroleptic metalloinsertor subunit.** The conjugate's metalloinsertor subunit was synthesized via the sequential addition of phen, chrysi, and ^{NH2}bpy ligands onto a rhodium center.

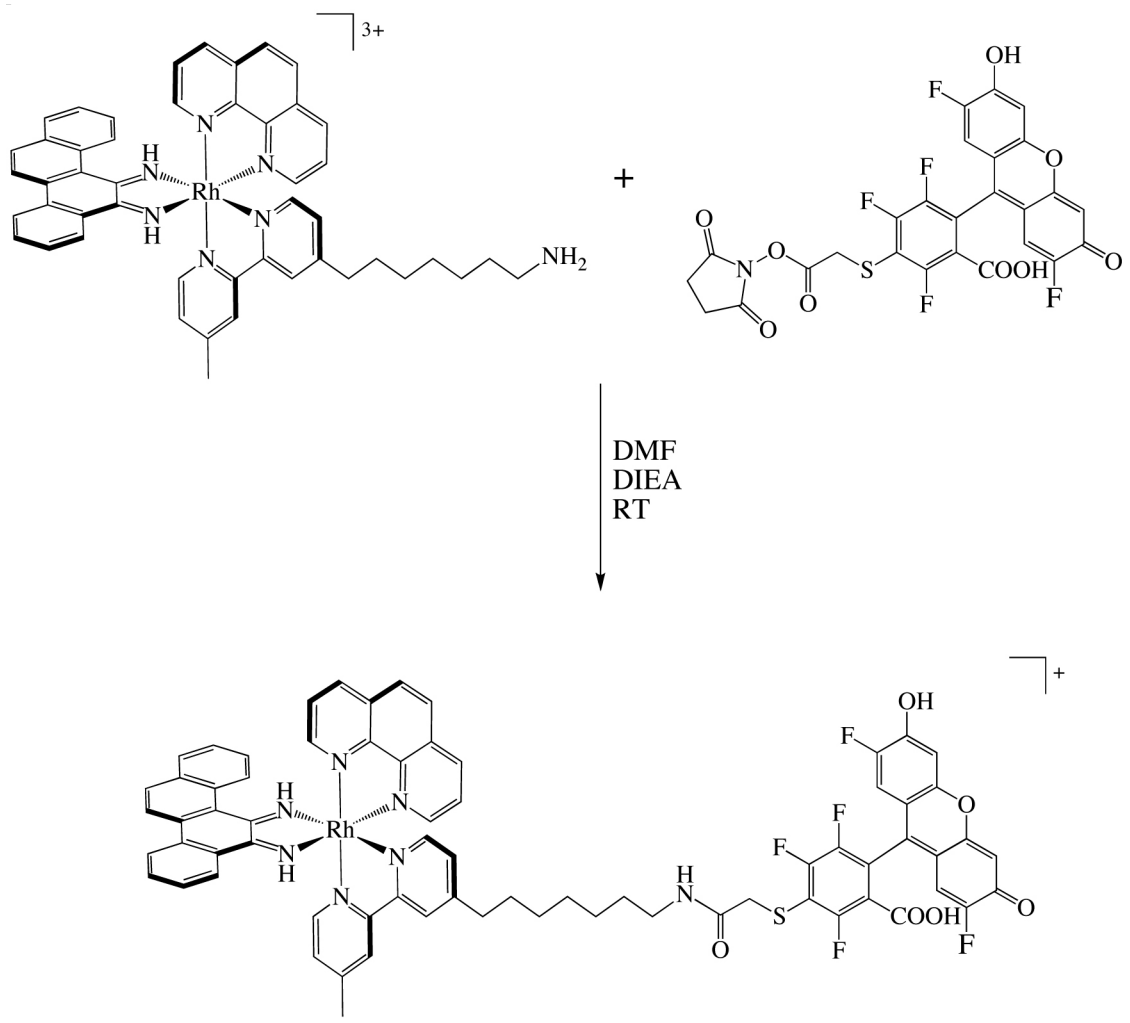

Figure 3.5: Synthesis of RhOG. The metalloinsertor-Oregon Green conjugate was synthesized via the facile coupling of the pendant amine of the rhodium complex to the succinimidyl ester of the commercially available fluorophore starting material.

A.

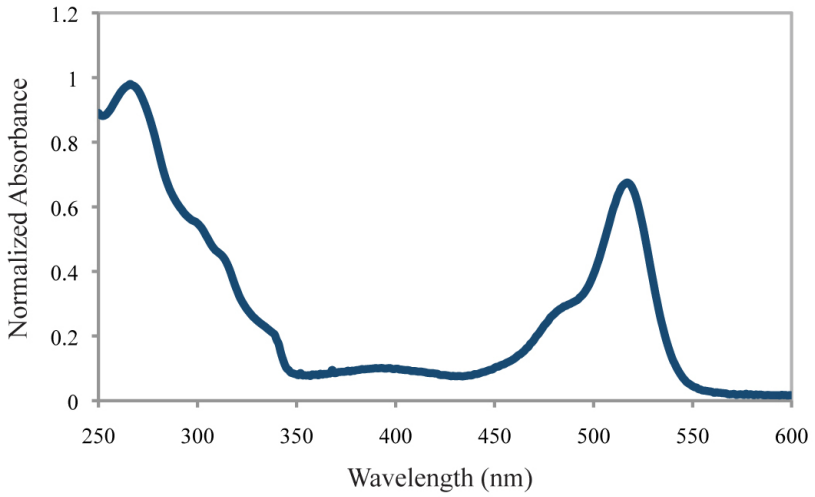

B.

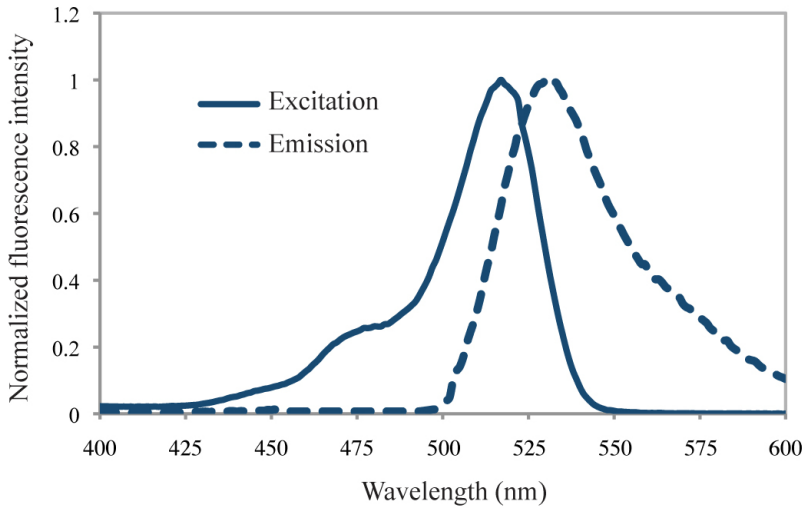

Figure 3.6: Absorbance and fluorescence spectra of RhOG. (A) The UV-Vis spectrum of RhOG: λ_{max} 303 nm (ε = 54,800), 313 (ε = 44,600), 519 (ε = 78,000). (B) The fluorescence excitation (solid line) and emission (dotted line) spectra of RhOG, showing λ_{ex} = 519 nm and λ_{em} = 530 nm.

In order to investigate the intramolecular quenching behavior of RhOG, fluorescence measurements of 1 μM conjugate in the presence of variable salt concentrations (10 mM NaPi, 0−500 mM NaCl, pH 7.1) were taken. A mild dependence of fluorescence on ion strength was revealed. The emission of RhOG, while still significantly quenched relative to Oregon Green, increases almost 5-fold over the range of NaCl concentrations tested. Neither Oregon Green alone nor an untethered 1:1 solution of Rh(phen)(chrysi)(^{NH2}bpy)$^{3+}$ and Oregon Green shows variation in fluorescence with ionic strength. These observations support an intramolecular ion-pair mechanism of quenching; as the salt concentration increases, the Rh•OG ion pair can separate more easily, attenuating quenching and increasing fluorescence (**Figure 3.7**).

3.2.1.2: PHOTOCLEAVAGE EXPERIMENTS

For DNA experiments, two 17-mer oligonucleotides were synthesized and purified, each either containing or lacking a central C•C mispair: 5'-CAC ATG CA**C** GAC GGC GC-3' (in the well-matched oligonucleotide, a guanine is complementary to the bold cytosine; in the mismatched oligonucleotide, a cytosine is complementary at the site).

Mismatch targeting by the bifunctional conjugate was first examined via PAGE experiments using 5'-^{32}P-labeled oligonucleotides. First, a simple photocleavage experiment was employed to determine whether RhOG and its trisheteroleptic metalloinsertor subunit did, indeed, recognize and photocleavage mismatched DNA. In this experiment, matched or mismatched duplex DNA (1 μM) was incubated with 1 μM

A.

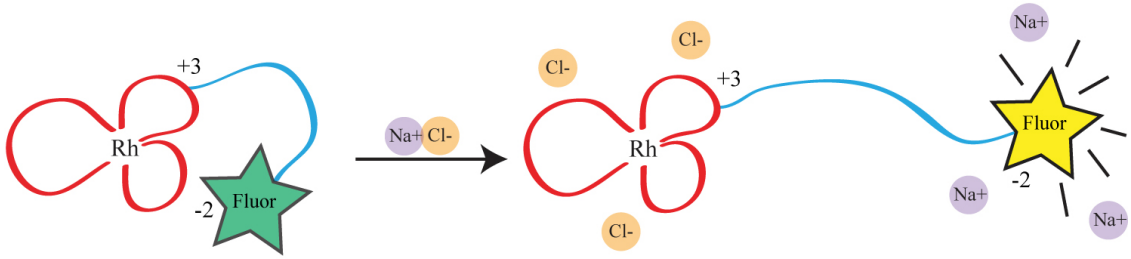

B.

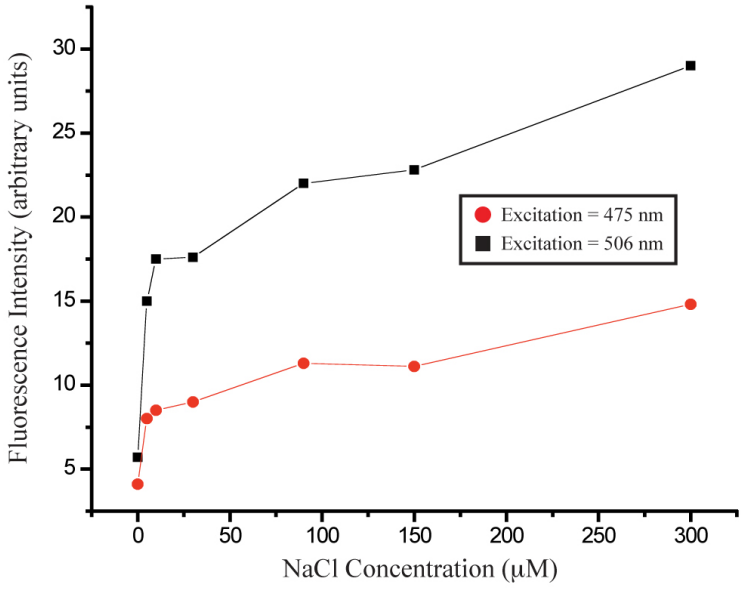

Figure 3.7: Dependence of ionic strength on the fluorescence of RhOG. (A) Schematic showing the hypothesized role of salt in the ion-pairing of RhOG; (B) plot of the fluorescence of RhOG at 530 nm as a function of ionic strength (500 nM RhOG, 10 mM NaPi, pH 7.1)

RhOG and Rh(phen)(chrysi)(^{NH2}bpy)$^{3+}$ and irradiated for 5 min on an Oriel Instruments solar simulator (**Figure 3.8**).

Autoradiography of the gel clearly reveals that both RhOG and Rh(phen)(chrysi)(^{NH2}bpy)$^{3+}$ specifically recognize and cleave mismatched sites in DNA. No photocleavage nor any other evidence for matched site binding is evident. Significantly, it appears that RhOG is a weaker binder than its rhodium subunit alone, likely a consequence of the former's reduced charge.

A photocleavage titration was next used to determine the site-specific binding constant of the conjugate. In this experiment, radiolabeled, mismatched DNA (1 μM) was incubated with variable concentrations of RhOG (100 nM to 10 μM) and irradiated for 10 min on a solar simulator. Autoradiography of the resultant gel and subsequent quantification using ImageQuant software indicate a site-specific binding constant of 4 x 10^5 M^{-1}. This value is consistent with measurements for the parent $Rh(bpy)_2(chrysi)^{3+}$ complex and for other bifunctional conjugates; the affinity of RhOG, however, is slightly reduced compared to previous cases, again possibly a consequence of its reduced charge.[13, 22, 23, 25]

3.2.1.3: FLUORESCENCE MEASUREMENTS

Armed with an understanding of the site-specificity of the conjugate, we next embarked upon fluorescence titrations with matched and mismatched DNA. In these experiments, 1 μM RhOG was added to variable amounts of the matched and mismatched oligonucleotides described above. In all experiments, a wavelength of 475

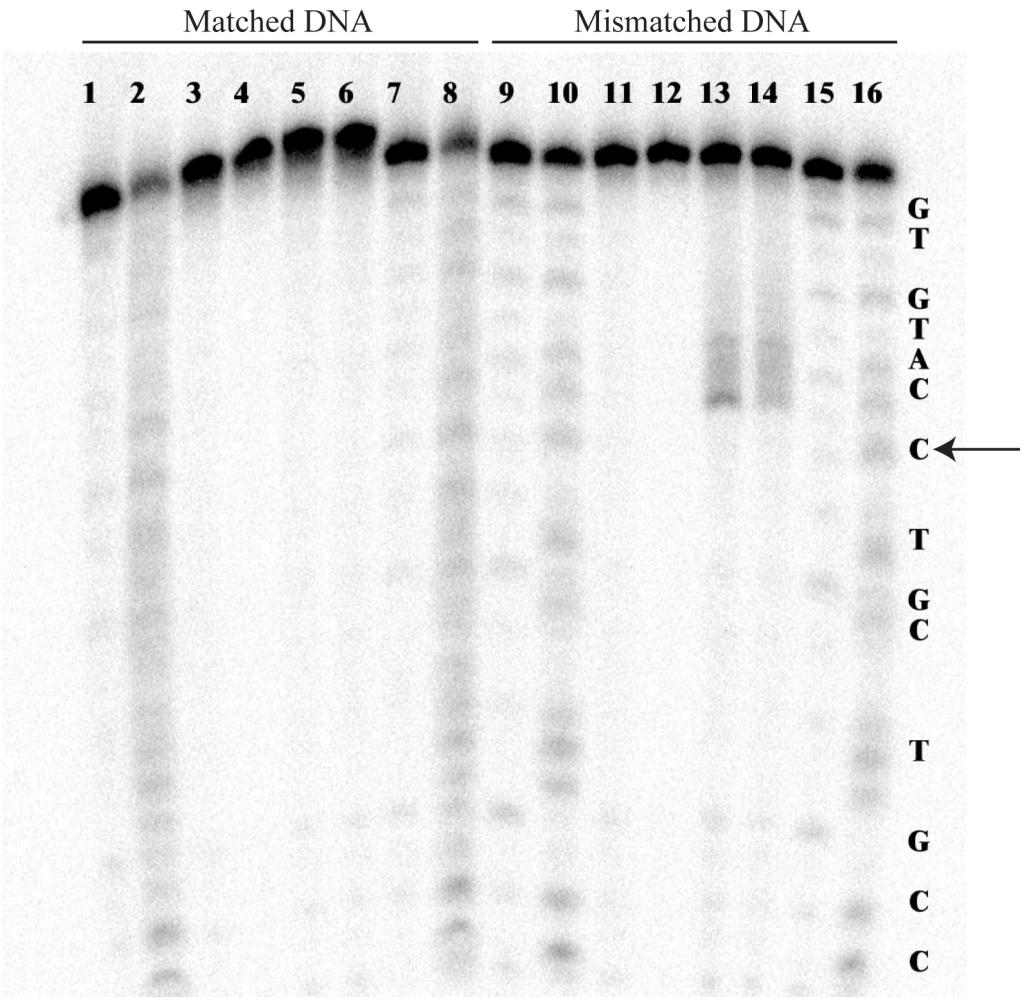

Figure 3.8: RhOG photocleavage gel. Autoradiogram of a denaturing 20% polyacrylamide gel revealing DNA photocleavage for RhOG and its rhodium subunit. Conditions are duplex (1 μM), Rh (1 μM) in 20 mM NaCl, 10 mM NaPi, in pH 7.1 followed by irradiation for 5 min with a solar simulator. Lanes 1, 2, 7, 8, 9, 10, 15, and 16 show Maxam Gilbert sequence reactions for matched (1, 2, 7, 8) and mismatched (9, 10, 15, 16) DNA. For matched and mismatched DNA, respectively: lanes 3 and 11 show light controls (irradiation, no RhOG); lanes 4 and 12 show dark controls (RhOG with no irradiation); lanes 5, 6, 13, and 14 show DNA after irradiation in the presence of Rh(phen)(chrysi)(^{NH2}bpy)$^{3+}$ (5, 13) and RhOG (6, 14). The DNA sequence is 5'-^{32}P-GCGCCGTCGT**X**CATGTG-3' where X = C or G. The complement contains a matched or mismatched C complementary to the bold X site. The arrow marks the mismatched site.

nm was employed for excitation (to avoid emission interference from scattered light), and the emission was monitored at 530 nm.

Despite the known binding selectivity of the conjugate, only a slight increase in fluorescence is observed with mismatched DNA when compared to matched DNA; at saturating DNA concentrations, the relative intensity with mismatched versus matched DNA is 1.3 ± 0.1 (**Figure 3.9**). Significantly, the fluorescence of the conjugate remains very quenched in the presence of both types of oligonucleotide. Further, in control experiments, no mismatch-dependent differences in fluorescence are found for Oregon Green alone or for a 1:1 solution of Rh(phen)(chrysi)(^{NH2}bpy)$^{3+}$ and Oregon Green. Further still, RhOG shows no increased fluorescence with single stranded DNA. Taken together, these data indicate that the bifunctional conjugate does, indeed, display enhanced fluorescence with mismatched DNA. Granted, the differential is slight; however, the success, though limited, paved the way for the optimization of the system.

3.2.2: SECOND GENERATION CONJUGATES

3.2.2.1: SYNTHESIS AND CHARACTERIZATION

The limited success of RhOG prompted a reevaluation of the conjugate's design. The ionic strength dependence and DNA titration data clearly indicate that RhOG is capable of the intramolecular quenching mechanism envisioned for the system. However, the ultimately meager differential fluorescence displayed by the conjugate suggests that while an "closed" to "open" (quenched to unquenched) conformational shift is possible in the presence of salt or mismatched DNA, the "open" configuration simply remains too quenched for the molecule to display any dramatically differential fluorescence. It was

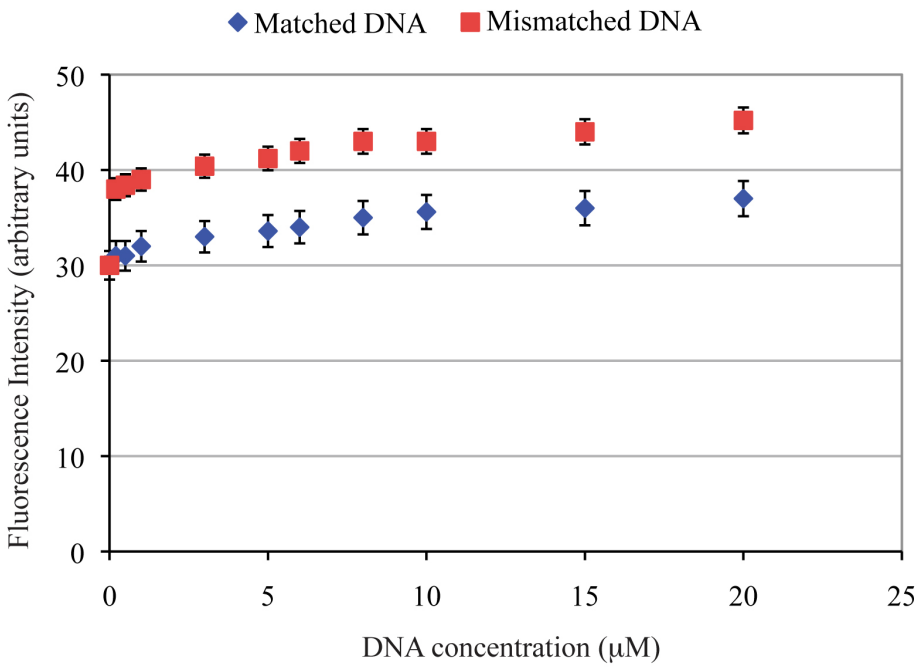

Figure 3.9: Fluorescence of RhOG with matched and mismatched DNA. The DNA titration shows a slight (25%) increase in the fluorescence of the conjugate in the presence of mismatched DNA when compared to matched DNA. Conditions: 1 μM RhOG, 20 mM NaCl, 10 mM NaPi, pH 7.1

hypothesized that this behavior arises simply because the metalloinsertor quencher and fluorophore are too close together. Put simply, the conjugate remains too quenched in the "open" state.

To counter this problem, three new conjugates with elongated linkers were designed and synthesized. Of course, the first step in this process was the synthesis of the three novel linker-modified bipyridine ligands. The first, nicknamed ^{el}bpy, bears a 11 carbon aliphatic linker similar to that in the aforementioned ^{NH2}bpy. Not surprisingly, ^{el}bpy was synthesized in a similar manner. 4,4'-dimethylbipyridine is first monoalkylated with LDA and 1,10-dibromodecane. Then, the bromide-terminated chain of the alkylation product was converted to an amine-terminated linker through a phthalimide intermediate via the Gabriel synthesis (**Figure 3.10**, see EXPERIMENTAL).

During the synthesis of ^{el}bpy, it became evident that any aliphatic linker longer than ten carbons would present serious solubility problems. Therefore, two additional new ligands were synthesized to contain an ethylene glycol (more rigorously, dioxyethane) unit within the linker. The first, ^{peg}bpy, contains a 14 atom linker and can be synthesized in five steps from 4,4'-dimethylbipyridine by analogy to the methods of Della Ciana *et al*.[28] First, the starting material is monoalkylated with LDA and 2-(3-bromopropyl)-1,3-dioxolane. The dioxolane is then deprotected under acidic conditions to yield the corresponding aldehyde, which is then oxidized with potassium permanganate to a carboxylic acid. This carboxylic acid is converted to a succinimidyl ester with N-hydroxysuccinimide and DCC. Finally, the NHS ester is coupled to 2,2'-(ethylenedioxy)bis(ethylamine) to yield the final ^{peg}bpy product (**Figure 3.11**).

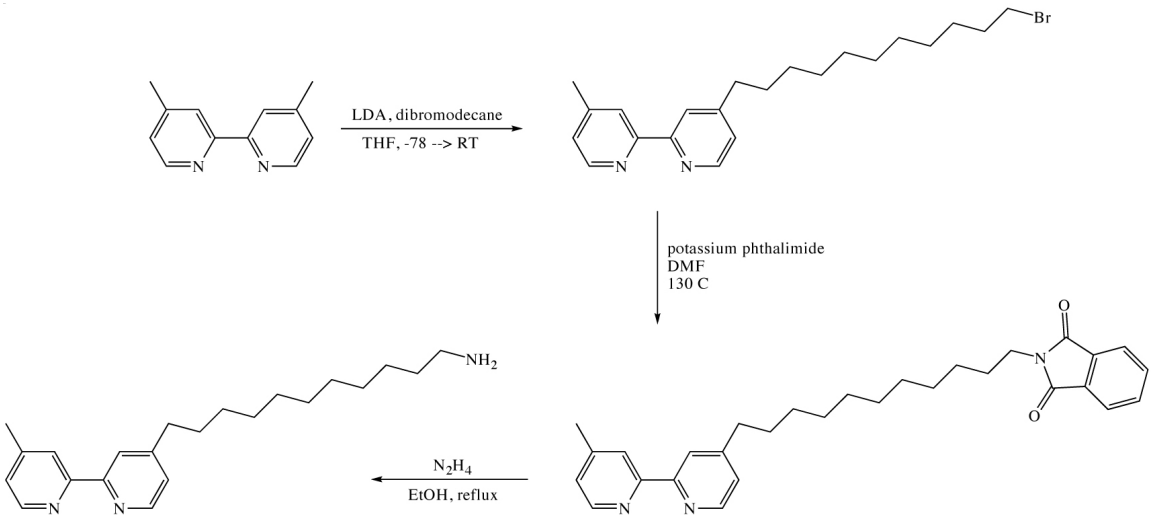

Figure 3.10: Synthesis of ^{el}bpy. The modified bipyridine with an amine-terminated, eleven carbon aliphatic linker was synthesized in three steps from 4,4'-dimethylbipyridine via the Gabriel amine synthesis.[26, 27]

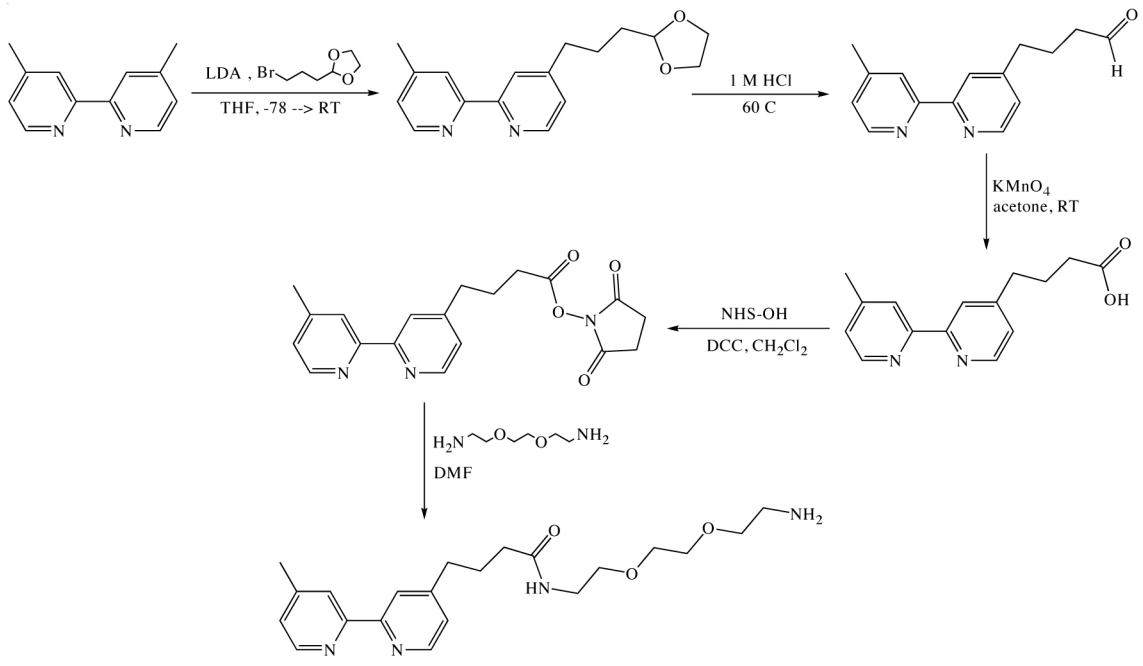

Figure 3.11: Synthesis of ^{peg}bpy. The ligand bears an 14 atom linker and is synthesized in five steps from 4,4'-dimethylbipyridine via sequential alkylation, deprotection, oxidation, and coupling reactions.

The third ligand, ^{lpeg}bpy, contains a 17 atom linker and was also synthesized in five steps from 4,4'-dimethylbipyridine, though by a different strategy. First, the aliphatic linker was installed onto 4,4'-dimethylbipyridine via monoalkylation with LDA and dibromohexane. The bromide group terminating the linker was then converted to a carboxylic in two steps through a cyanide intermediate. Finally, this carboxylic acid was converted to the final ^{lpeg}bpy ligand through a succinimidyl ester intermediate (**Figure 3.12**).

With the linker-modified ligands complete, the trisheteroleptic metalloinsertor subunits were assembled sequentially from $RhCl_3$ as described above. As with RhOG, each metalloinsertor was then coupled to the succinimidyl ester of Oregon Green 514 to yield three new bifunctional conjugates: ^{el}RhOG, ^{peg}RhOG, and ^{lpeg}RhOG (**Figure 3.13**). All three conjugates were purified via reverse phase HPLC (see EXPERIMENTAL).

The three new conjugates — ^{el}RhOG, ^{peg}RhOG, and ^{lpeg}RhOG — were characterized via UV-Vis and fluorescence spectroscopy. As with RhOG, the absorbance spectrum of each conjugate resembles the additive combination of the spectra of the two subunits, with metalloinsertor bands at 303 nm and 313 nm and a large fluorophore peak at 519 nm (**Figure 3.14**). Not surprisingly, fluorescence studies of the second generation conjugates revealed more similarities to the first generation version. Each conjugate is characterized by excitation and emission maxima at 519 and 530 nm, respectively, again red-shifted relative to the parent Oregon Green fluorophore (**Figure 3.15**). Further, like RhOG, the fluorescence of each conjugate is significantly quenched relative to both free Oregon Green and an equimolar, 1:1 solution of Oregon Green and either Rh(phen)(chrysi)(^{el}bpy)$^{3+}$, Rh(phen)(chrysi)(^{peg}bpy)$^{3+}$, Rh(phen)(chrysi)(^{lpeg}bpy)$^{3+}$.

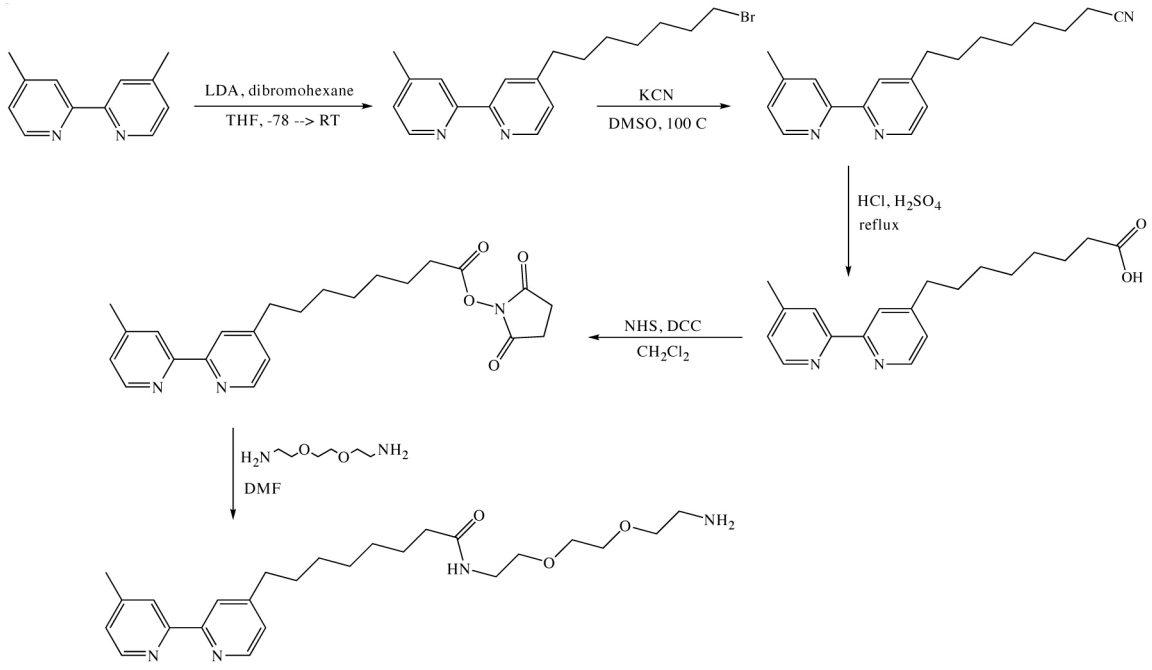

Figure 3.12: Synthesis of ^{lpeg}bpy. The ligand is synthesized in five steps from 4,4'-dmethylbipyridine via monoalkylation, cyanide substitution, hydrolysis, and coupling steps.

^{el}RhOG:

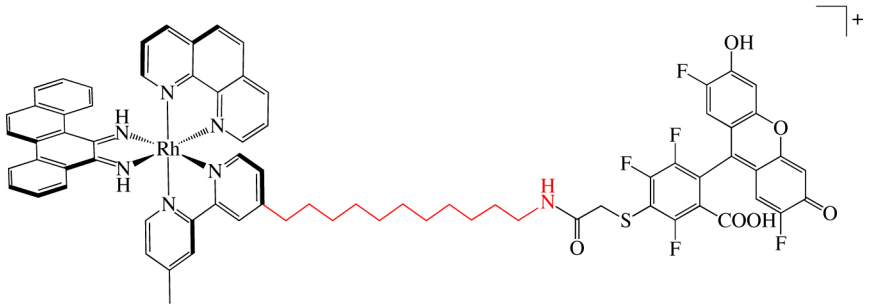

^{peg}RhOG:

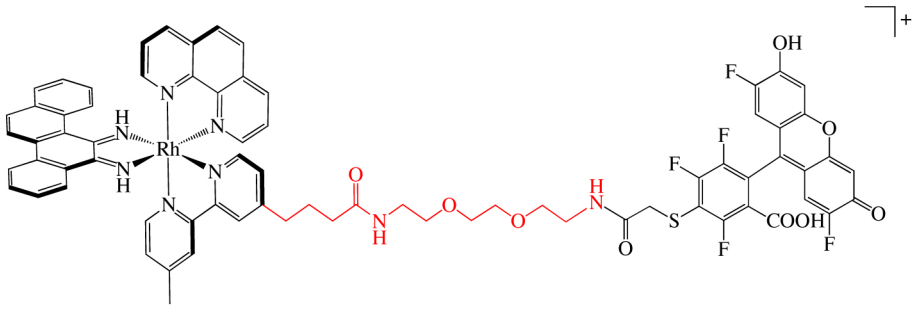

^{lpeg}RhOG:

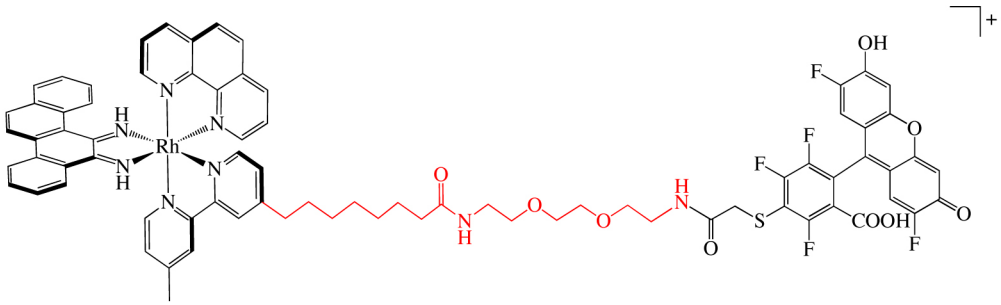

Figure 3.13: Structures of ^{el}RhOG, ^{peg}RhOG, and ^{lpeg}RhOG. The new, elongated linkers are displayed in red.

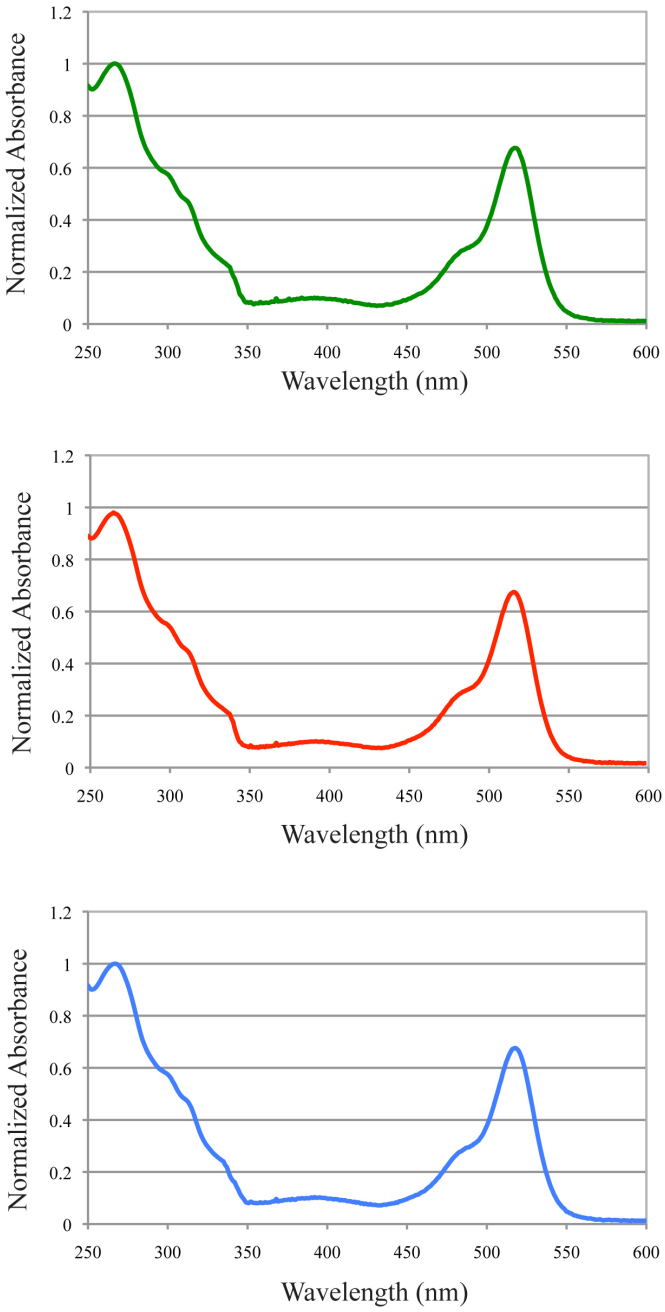

Figure 3.14: The UV-Vis spectra of the second generation ^{x}RhOG conjugates. The absorption spectra of ^{el}RhOG (green), ^{peg}RhOG (red), and ^{lpeg}RhOG (blue) are shown. The extinction coefficients for the conjugates in question are identical: λ_{max} 303 nm (ε = 54,800), 313 (ε = 44,600), and 519 (ε = 78,000).

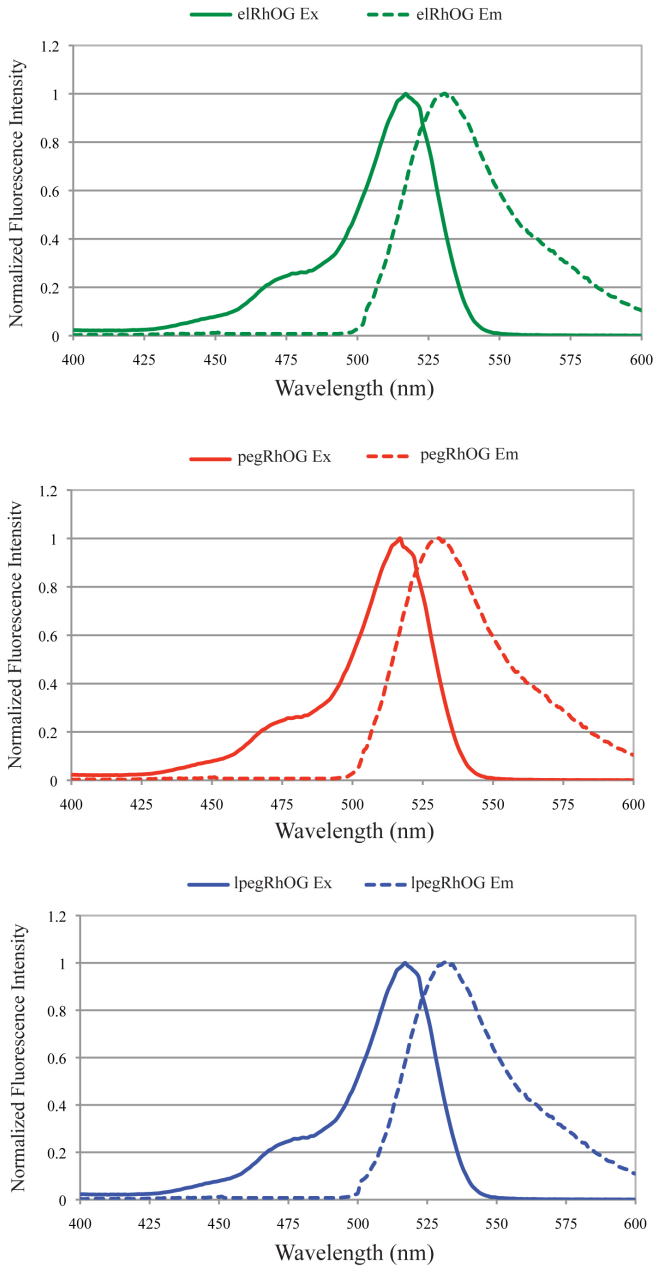

Figure 3.15: The fluorescence spectra of the second generation ^{x}RhOG conjugates. The excitation (solid line) and emission (dotted line) fluorescence spectra of ^{el}RhOG (green), ^{peg}RhOG (red), and ^{lpeg}RhOG (blue) are shown. The three spectra are virtually identical, with excitation maxima of 519 nm and emission maxima of 530 nm.

For example, for ^{peg}RhOG, the ratio of the fluorescence intensity of conjugate : equimolar untethered subunits : free Oregon Green is 1 : 73 : 100.

Fluorescence measurements were taken at variable ionic strengths in order to investigate the intramolecular quenching behavior of the new conjugates. For each conjugate, emission measurements (excitation = 475 nm, emission = 530 nm) of 1 μM ^{x}RhOG in the presence of variable concentrations of salt (10 mM NaPi, 0−500 mM NaCl, pH 7.1) were taken. For ^{peg}RhOG and ^{lpeg}RhOG, a strong dependence of fluorescence on ionic strength is observed. In both cases, the fluorescence emission of the conjugate increases over 15-fold as the sodium chloride concentration is increased from 0 to 500 mM. These data strongly support an intramolecular ion-pair mechanism of quenching for these conjugates. Perhaps more importantly, these values reveal that the longer, more flexible linkers of ^{peg}RhOG and ^{lpeg}RhOG confer a greater dynamic range of fluorescence intensities on these conjugates compared to the first generation RhOG molecule. Put more simply, these linkers allow the rhodium and fluorophore subunits to separate more fully in the "open" state, attenuating quenching even further and leading to a larger fluorescence increase.

^{el}RhOG, in contrast, exhibits far different behavior. The fluorescence of this conjugate displays no dependence on the ionic strength of the solution. It thus becomes apparent that this conjugate cannot perform the conformational shift necessary for intramolecular quenching, likely a consequence of the hydrophobicity of the eleven carbon aliphatic linker. It is possible that the alkyl chain contracts on itself in aqueous solution to avoid interaction with water, thus preventing the "open" vs. "closed" transition necessary for differential and ionic strength-responsive quenching.

3.2.2.2: PHOTOCLEAVAGE EXPERIMENTS

For DNA experiments, two 17-mer oligonucleotides were employed, each either containing or lacking a central C•C mispair: 5'-CAC ATG CA**C** GAC GGC GC-3' (in the well-matched oligonucleotide, a guanine is complementary to the bold cytosine; in the mismatched oligonucleotide, a cytosine is complementary at the site). As with RhOG, mismatch targeting was first examined via PAGE experiments. Initially, simple photocleavage experiments were employed to determine whether ^{el}RhOG, ^{peg}RhOG, and ^{lpeg}RhOG were capable of the selective recognition and photoactivated scission of mismatched DNA. In the experiment, matched and mismatched duplex DNA (1 μM) were incubated with 1 μM of either ^{el}RhOG, ^{peg}RhOG, or ^{lpeg}RhOG and irradiated for 5 min on an Oriel Instruments solar simulator. Autoradiography of the resultant gel (**Figure 3.16**) reveals that all three conjugates recognize and photocleave mismatched DNA. Not surprisingly, no photocleavage at matched sites is apparent for any of the conjugates.

Subsequently, photocleavage titrations were employed to determine the specific binding constant of the conjugates to the mismatched site. In these experiments, radiolabeled, mismatched DNA (1 μM) was incubated with variable concentrations of either ^{el}RhOG, ^{peg}RhOG, or ^{lpeg}RhOG (100 nM to 10 μM) and irradiated for 10 min on a solar simulator. Autoradiography of the gels and subsequent quantification using ImageQuant software revealed a site-specific binding constants of 2×10^5 M^{-1} (^{el}RhOG), 6×10^5 M^{-1} (^{peg}RhOG), and 7×10^5 M^{-1} (^{lpeg}RhOG). These values are consistent with measurements for RhOG, $Rh(bpy)_2(chrysi)^{3+}$, and other bifunctional conjugates.

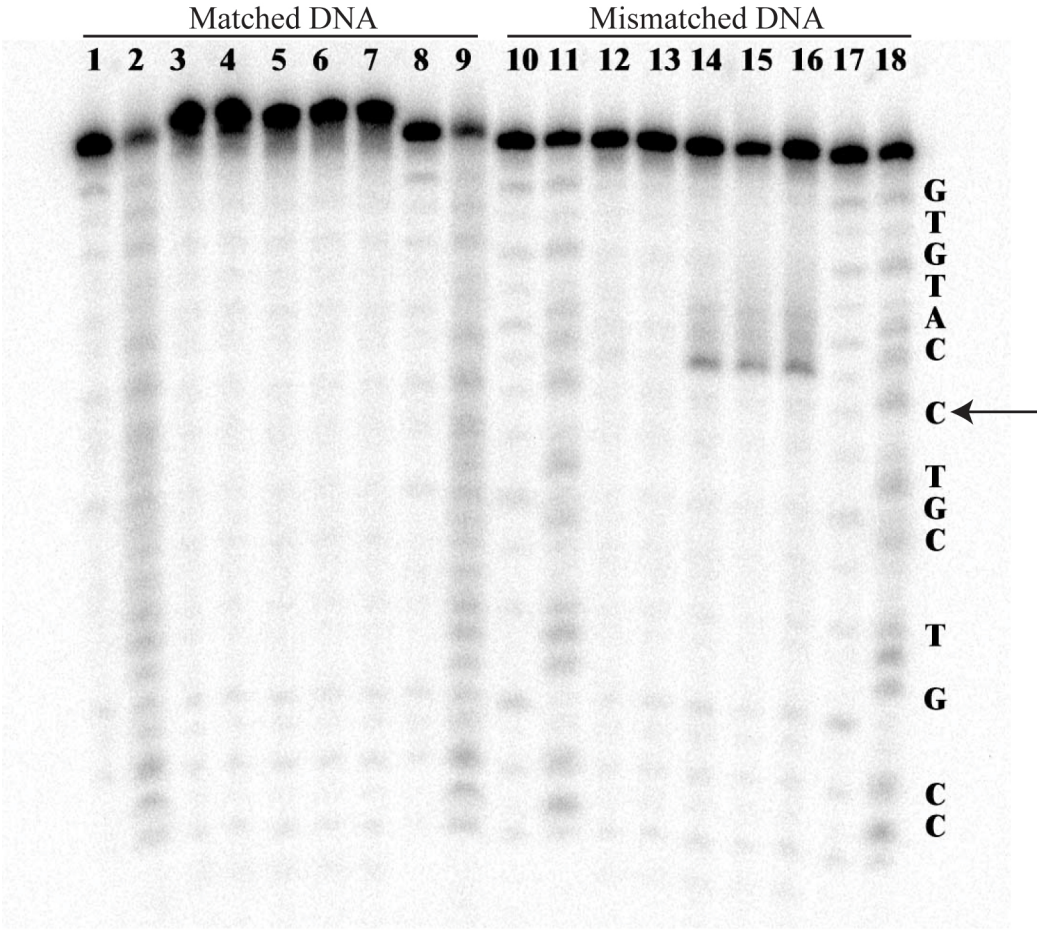

Figure 3.16: ^{x}RhOG photocleavage gel. Autoradiogram of a denaturing 20% polyacrylamide gel revealing mismatch recognition and photocleavage by ^{el}RhOG, ^{peg}RhOG, and ^{lpeg}RhOG. Conditions are duplex (1 μM), Rh (1 μM) in 20 mM NaCl, 10 mM NaPi, in pH 7.1 followed by irradiation for 5 min with a solar simulator. Lanes 1, 2, 8, 9, 10, 11, 17, and 18 show Maxam Gilbert sequence reactions for matched (1, 2, 8, 9) and mismatched (10, 11, 17, 18) DNA. For matched and mismatched DNA, respectively: lanes 3 and 12 show light controls (irradiation, no Rh); lanes 4 and 13 show dark controls (no irradiation); lanes 5, 6, 7, 14, 15, and 16 show DNA after irradiation in the presence of ^{el}RhOG (5, 14), ^{peg}RhOG (6, 15), and ^{lpeg}RhOG (7, 16). The DNA sequence is 5'-^{32}P-GCGCCGTCGT**X**CATGTG-3' where X = C or G. The complement contains a matched or mismatched C complementary to the bold X site. The arrow marks the mismatched site.

Further, these affinities, like that of RhOG, are slightly reduced compared to the parent complexes, again possibly a consequence of the reduced charge of the conjugates.

3.2.2.3: FLUORESCENCE MEASUREMENTS

Fluorescence measurements with matched and mismatched DNA were able to provide insight into the potential of these second generation conjugates as mismatch-specific fluorophores. In these experiments, 1 μM ^{x}RhOG was added to variable concentrations of the matched and mismatched oligonucleotides (described above) in buffer (20 mM NaCl, 10 mM NaPi, pH 7.1). A wavelength of 475 nm was employed for excitation (to avoid emission interference from scattered light), and the emission was monitored at 530 nm.

This line of investigation first revealed that ^{el}RhOG shows very little, if any, enhanced fluorescence with mismatched DNA compared to matched DNA ($F_{mm}/F_m = 1.1 \pm 0.1$). This is not a surprise, especially given the apparent inability of ^{el}RhOG to perform the differential intramolecular quenching desired for the system.

However, over the range of DNA concentrations studied, ^{peg}RhOG and ^{lpeg}RhOG show *significantly* greater fluorescence with mismatched DNA than with matched DNA. Indeed, at saturating DNA concentrations, the relative fluorescence intensities of the two conjugates with mismatched versus matched DNA are 3.2 ± 0.2 and 3.3 ± 0.1 for ^{peg}RhOG and ^{lpeg}RhOG, respectively (**Figure 3.17** and **3.18**). Control experiments with Oregon Green alone and 1:1 mixtures of Oregon Green:Rh(phen)(chrysi)(^{peg}bpy)$^{3+}$ and Oregon Green:Rh(phen)(chrysi)(^{lpeg}bpy)$^{3+}$ display no mismatch-dependent differences in fluorescence. Likewise, neither ^{peg}RhOG nor ^{lpeg}RhOG show any fluorescence

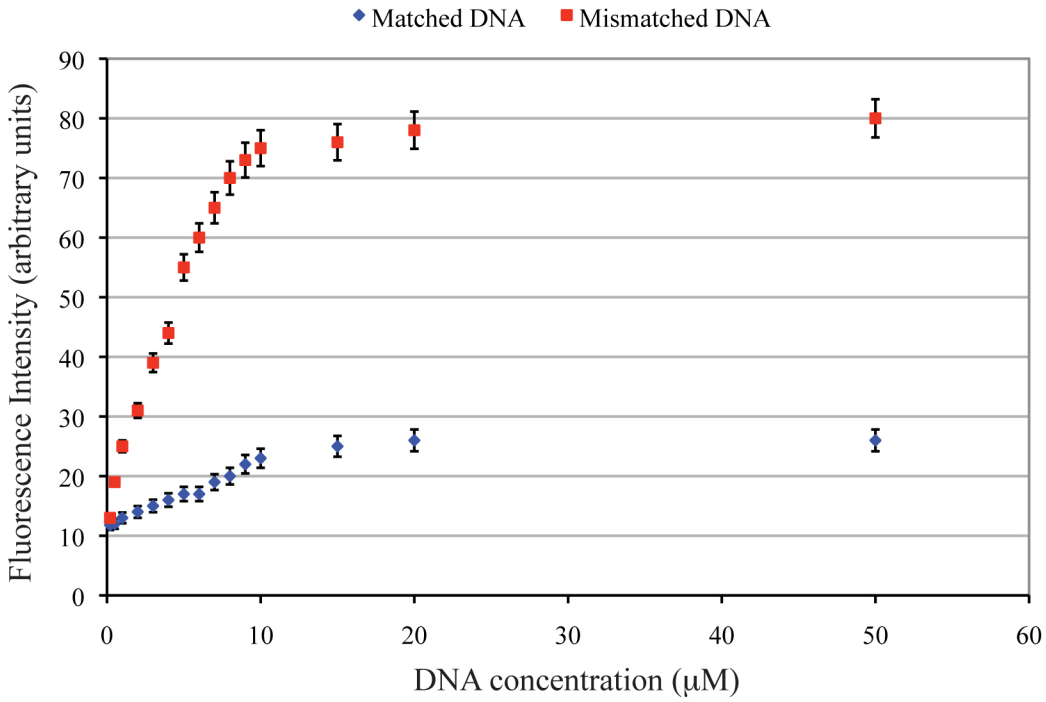

Figure 3.17: Fluorescence of ^{peg}RhOG with matched and mismatched DNA. At saturating DNA concentrations, ^{peg}RhOG shows a relative intensity with mismatched versus matched DNA of 3.2 ± 0.2.

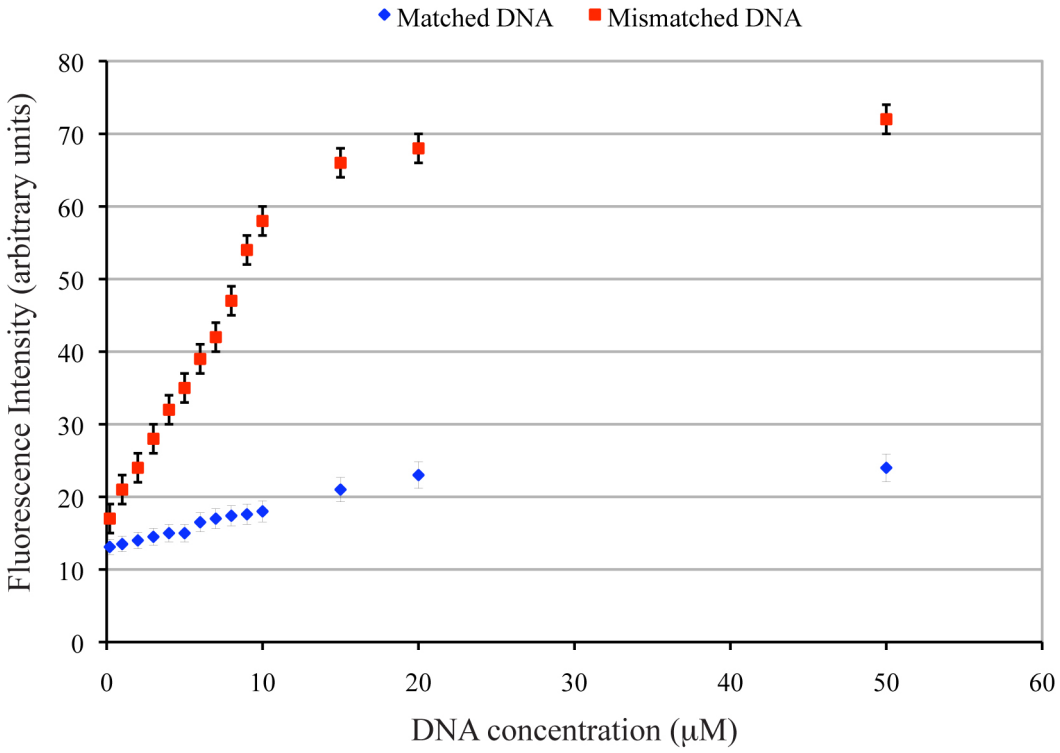

Figure 3.18: Fluorescence of ^{lpeg}RhOG with matched and mismatched DNA. At saturating DNA concentrations, ^{lpeg}RhOG shows a relative intensity with mismatched versus matched DNA of 3.3 ± 0.1.

enhancement with single stranded DNA. Interestingly, no DNA-dependent (mismatched or matched) changes in fluorescence anisotropy are observed for either conjugate, suggesting that the fluorophore moiety is exceedingly mobile in the DNA-bound form.

Taken together, the data for ^{peg}RhOG and ^{lpeg}RhOG represent a significant success in the optimization of the initial bifunctional conjugate system. By employing a longer, more flexible linkers, the ratios of the fluorescence intensities of the conjugates with mismatched to matched DNA increase almost threefold. However, it would be remiss not to note one important caveat: even in the presence of mismatched DNA, the conjugates are significantly quenched, with only 6% of the fluorescence intensity of an equimolar, 1:1 solution of free fluorophore and metalloinsertor and 3% compared to that of the free fluorophore alone.

3.3: CONCLUSIONS

This work establishes a simple yet effective strategy for the design of a bifunctional metalloinsertor-fluorophore conjugate that serves as a fluorescent probe for mismatched DNA. All four of the conjugates synthesized selectively bind and photocleave DNA, while the two with the longest and most flexible linkers show significantly enhanced fluorescence with mismatched DNA compared to matched DNA. Thus, it becomes clear that this work stands not only as a proof-of-concept for a novel mismatch-specific fluorophore but also as an instructive study on the importance of linker optimization in the design of bifunctional conjugates.

3.4: EXPERIMENTAL PROTOCOLS

Many of the procedural details for this investigation are included in Chapter 2 of this text. These include the following: the syntheses of $Rh(phen)(chrysi)(NH_3)_2^{3+}$ (2.3.4.1−2.3.4.5), ^{NH2}bpy (2.3.5.1−2.3.5.3), and ^{peg}bpy (2.3.5.4−2.3.5.6); the synthesis, purification, and radiolabeling of oligonucleotides (2.4.1−2.4.2); the Maxam-Gilbert sequencing of radiolabeled DNA (2.4.3); and the performance of recognition and binding titration experiments via PAGE (2.4.4.1−2.4.4.2). Experimental details of the fluorimetry measurements discussed herein are included above in Section 3.2.

3.4.1: MATERIALS AND INSTRUMENTATION

All reagents were obtained from commercial sources and used as received without further purification. $RhCl_3$ was purchased from Pressure Chemicals. Oregon Green 514™ succinimidyl ester was purchased from Molecular Probes (Invitrogen) and stored at -20 °C. All non-aqueous solvents were purchased from Fluka and stored under argon and over molecular sieves. All water used was purified using a MilliQ water purification system. Unless otherwise noted, all reactions were performed under ambient conditions.

^{1}H-NMR spectra were recorded on a Varian 300 MHz spectrometer at room temperature using solvent residual signal as a reference to TMS. Mass spectrometry was performed at either the Caltech mass spectrometry facility or in the Beckman Institute Protein/Peptide Micro Analytical Laboratory (PPMAL). Absorption spectra were recorded on a Beckman DU 7400 spectrophotometer. Extinction coefficients were determined using inductively coupled plasma mass spectrometry. All fluorescence measurements were taken on an ISS K2 fluorimeter (5 mm path length) equipped with a

250 W xenon lamp as an excitation source. Unless otherwise noted, an excitation wavelength of 475 nm was employed, and fluorescence experiments were performed using 1 μM fluorophore of interest in a buffer of 20 mM NaCl, 10 mM NaPi, pH 7.1. All experiments were performed in triplicate.

Oligonucleotides were synthesized on an ABI 3400 DNA synthesize and purified via HPLC in duplicate (DMT-off and DMT-on) before use. All reverse-phase HPLC purifications were performed on an HP1100 high-pressure liquid chromatography system equipped with diode array detector using a Varian DynaMax C18 semipreparative column (see Chapter 2, Section 2.4.1). Irradiations were performed using an Oriel Instruments solar simulator (320-440 nm). All PAGE experiments described employed denaturing 20% polyacrylamide gels (SequaGel, National Diagnostics) and were performed according to published procedures. Further, gels were developed using Molecular Dynamics phosphorimaging screens and a Molecular Dynamics Storm 820 phosphorimager and were subsequently visualized and quantified with Molecular Dynamics ImageQuant software.

3.4.2: SYNTHESIS OF 11-(4'-METHYL-2,2'-BIPYRIDIN-4-YL)UNDECAN-1-AMINE (^{EL}BPY)

3.4.2.1: ALKYLATION

A 50 mL Schlenk flask was flame-dried and subjected to three rounds of evacuation and re-filling with $Ar_{(g)}$. The flask was then charged by syringe with 3.9 mL (28 mmol) diisopropylamine, and 20 mL THF (dry and under argon, Fluka) were transferred into the flask via cannula. The flask was cooled to -78 °C in a dry ice/acetone

bath, followed by the dropwise addition of 13.5 mL (27 mmol) 2 M BuLi. The resultant light yellow LDA solution was kept at -78 °C as the reaction vessel was prepared.

A 500 mL, three-necked round-bottom flask was flame-dried, charged with 5 g (27 mmol) 4,4'-dimethyl-2,2'-bipyridine, and subjected to three rounds of evacuation and refilling with $Ar_{(g)}$. 200 mL THF (dry and under argon, Fluka) were transferred into the flask via cannula, and the reaction mixture was cooled to -78 °C in a dry ice/acetone bath. The LDA solution was then transferred into the 500 mL round-bottom flask via cannula, and the resultant dark brown reaction mixture was allowed to stir at -78 °C for 1 h. After 1 h, 40 g (5 equiv.) dibromohexane were added to the reaction via syringe. The reaction mixture was immediately transferred to a dry ice bath (i.e. no acetone) and allowed to warm slowly to room temperature over the next 16 h. During this time, the reaction changed colors dramatically from brown to dark green to green to dark yellow and, finally, to light yellow.

Once at room temperature, the reaction vessel was opened to air, and H_2O (150 mL) was added to the reaction mixture to quench any remaining LDA. The pH of the mixture was adjusted to ~10 with saturated $NaHCO_{3(aq)}$. The basified reaction mixture was then extracted once with 50 mL Et_2O and subsequently with 50 mL increments of CH_2Cl_2 until the organic layer no longer stains red when spotted on a TLC plate (silica) and dipped in an Fe(II) solution. At this point (~ 250 mL total volume organic layer), the organic layer was washed with brine, dried over $MgSO_4$, filtered, and concentrated *in vacuo* to yield the final product as a yellow oil.

The crude product was purified via column chromatography (SiO_2 pretreated with 1:10 NEt_3:hexanes) with a solvent system of 1:1 EtOAc:Hexanes. The purified product, nicknamed ^{elBr}bpy, is a white solid (7.3 g).

^{1}H-NMR (CD_2Cl_2): 8.53 ppm (split d, 2H); 8.28 ppm (s, 2H); 7.16 ppm (d, 2H); 3.42 ppm (t, 2H); 2.70 ppm (t, 2H); 2.44 ppm (s, 3H); 1.87 ppm (m, 2H); 1.7 ppm (m, 2H); 1.5−1.1 ppm (m, 14H).

ESI-MS (m/z): 403, 405 $[M+H]^+$

3.4.2.2: PHTHALIMIDE SUBSTITUTION

The bromide-terminated linker was converted to an amine-terminated linker by an adapted Gabriel amine synthesis. In a 250 mL round-bottom flask, ^{elBr}bpy (0.35 g) was combined with potassium phthalamide (0.240 g) in 35 mL DMF and heated to 130 °C for 12 h. After cooling to room temperature, water (100 mL) was added, and the reaction mixture was brought to ~ pH 10 with saturated $NaHCO_{3(aq)}$. This solution was then extracted three times with 75 mL CH_2Cl_2, washed once with brine, dried over $MgSO_4$, and evaporated to dryness to yield a white solid (515 mg, > 95%, ^{elphth}bpy) that was pure by TLC (SiO_2, 1:1 EtOAc:Hex).

ESI-MS (m/z): 470 $[M+H]^+$, 492 $[M+Na]^+$

3.4.2.3: HYDROLYSIS

In a 250 mL round-bottom flask, ^{elphth}bpy (250 mg, 0.53 mmol) was dissolved in EtOH (50 mL) by heating to 60 °C for 30 min. After 30 min, hydrazine monohydrate (0.2 mL, 4.1 mmol, 8 equiv.) was added, and the reaction mixture was stirred at 70 °C for 16

h. After cooling to room temperature, the solvent was removed *in vacuo*. The residue was taken up in 50 mL chloroform and extracted five times with 50 mL 1 M hydrochloric acid. The acid phase was then extracted twice with 50 mL $CHCl_3$ to eliminate any residual phthalimide products. The pH of the combined aqueous layers was then adjusted to ~10 with saturated $NaHCO_3$ solution, and the newly basic aqueous layer was extracted four times with 50 mL $CHCl_3$, washed with brine, dried over $MgSO_4$, and dried *in vacuo* to yield a white solid that was pure by NMR (100 mg, 70%, nicknamed ^{el}bpy).

^{1}H-NMR (CD_2Cl_2): 8.47 ppm (m, 2H); 8.20 ppm (m, 2H); 7.10 ppm (m, 2H); 2.85 ppm (m, 2H); 2.65 ppm (m, 2H); 2.41 ppm (s, 3H); 1.6 ppm (m, 4H); 1.4−1.2 ppm (m, 18H).

ESI-MS (m/z): 340 $[M+H]^+$, 380 $[M+K]^+$

3.4.3: SYNTHESIS OF *N*-(2-(2-(2-AMINOETHOXY)ETHOXY)ETHYL)-8-(4'-METHYL-2,2'-BIPYRIDIN-4-YL)OCTANAMIDE (^{LPEG}BPY)

The first step in the synthesis of ^{lpeg}bpy is the monoalkylation of 4,4'-dimethylbipyridine to make ^{Br}bpy. This procedure is detailed in Chapter 2 of this work under 2.3.5.1.

3.4.3.1: CYANIDE SUBSTITUTION

In a 250 mL round-bottom flask, ^{Br}bpy (500 g, 1.4 mmol) was combined with potassium cyanide (200 mg, 3.125 mmol) in 100 mL DMSO and heated to 90 °C for 12 h. After cooling to room temperature, water (100 mL) was added, and the reaction mixture was brought to pH ~ 10 with saturated $NaHCO_{3(aq)}$. This solution was then

extracted three times with 75 mL CH_2Cl_2, washed once with brine, dried over $MgSO_4$, and evaporated to dryness to yield a white solid (300 mg, 71%, nicknamed ^{CN}bpy) that was pure by TLC (SiO_2, 1:1 EtOAc:Hex).

ESI-MS (m/z): 294 $[M+H]^+$

3.4.3.2: HYDROLYSIS

In a 100 mL round-bottom flask, ^{CN}bpy (300 mg, 1.2 mmol) was dissolved in a mixture of 20 mL concentrated HCl and 5 mL concentrated H_2SO_4 and refluxed at 70 °C overnight. After 16 h, H_2O (100 mL) was added to the reaction mixture, and the pH was adjusted to 4.0 with NaOH(s). The aqueous layer was extracted with CH_2Cl_2 (4 x 50 mL). At this point (~ 200 mL total volume CH_2Cl_2), the organic layer was washed with brine, dried over $MgSO_4$, filtered, and concentrated *in vacuo* to yield the carboxylic acid as a white solid (bpy'', 250 mg, 80%).

ESI-MS (m/z): 312.3 $[M+H]^+$

3.4.3.3: FORMATION OF THE SUCCINIMIDYL ESTER

In a 250 mL round-bottom flask, 210 mg bpy'' (0.67 mmol), 86 mg N-hydroxysuccinimide (0.75 mmol), and 150 mg DCC (0.75 mmol) were dissolved in 100 mL CH_2Cl_2. The solution was stirred for 2 h at room temperature. After 2 h, a precipitate had become apparent, and the reaction was placed in the cold room overnight to facilitate precipitation. In the morning, the solution was filtered, and the filtrate was reduced *in vacuo* to reveal the pure N-succinimidyl ester product as a clear oil (250 mg, 0.6 mmol, 90%).

ESI-MS (m/z): 410 $[M+H]^+$, 432 $[M+Na]^+$

3.4.3.4: COUPLING

In a 25 mL pear-shaped flask, 100 g of the NHS-ester were dissolved in 3 mL DMF, and a solution of 2 mL (excess) of 2,2'-(ethylenedioxy)bis(ethylamine) in 1 mL DMF was added. After two h of stirring, 0.05 mL DIEA were added to ensure deprotonation of the amines. The reaction mixture was stirred for 15 h at room temperature. After 16 h, the reaction mixture was concentrated *in vacuo*, taken up in CH_2Cl_2, extracted twice with a saturated $NaHCO_3$ solution, dried over $MgSO_4$, and re-concentrated *in vacuo*. The final product (^{PEG}bpy) was obtained pure as a clear oil.

ESI-MS (m/z): 443.2 $[M+H]^+$

3.4.4: METALLATION OF ^{X}BPY LIGANDS

In a 100-mL round-bottom flask, Rh(phen)(chrysi)$(X)_2$ (150 mg, 0.22 mmol) was combined with ^{x}bpy (150 mg, approximately 0.6 mmol) in a 50/50 mixture of ethanol and deionized water (50 mL total volume). The reaction was stirred at reflux overnight in an oil bath. The mixture was then allowed to cool, diluted with 200 mL H_2O, and purified by cation exchange chromatography.

Four inches of resin pre-equilibrated with 0.05 M $MgCl_2$ were poured into a 1−1.5 inch diameter column and subsequently washed with copious (500 mL) deionized H_2O. The rhodium complex was loaded onto the column simply by passing the aqueous Rh solution through the resin (the rhodium complex will 'stick' to the top of the column, forming a thin, dark orange band). The complex was then eluted by slowly increasing the

[$MgCl_2$] in the eluent in 500-mL batches, starting with 0.05 M $MgCl_2$ and increasing in increments of 0.05 M until the red band of the metal complex has passed through the column. The resultant eluted solution was concentrated on a reverse-phase cartridge primed with MeOH, eluted with 1:1:0.001 H_2O/MeCN/TFA (vol/vol/vol), and lyophilized to yield the product as a red-orange powder.

ESI-MS [Rh(phen)(chrysi)(^{NH2}bpy)$^{3+}$]: 820 $[M+H]^+$, 410 $[M+2H]^{2+}$

ESI-MS [Rh(phen)(chrysi)(^{el}bpy)$^{3+}$]: 873 $[M+H]^+$, 436 $[M+2H]^{2+}$

ESI-MS [Rh(phen)(chrysi)(^{peg}bpy)$^{3+}$]: 923 $[M+H]^+$, 462 $[M+2H]^{2+}$

ESI-MS [Rh(phen)(chrysi)(^{lpeg}bpy)$^{3+}$]: 979 $[M+H]^+$, 490 $[M+2H]^{2+}$

3.4.5: COUPLING THE METALLOINSERTOR AND FLUOROPHORE SUBUNITS

In a flame-dried, Argon-filled 10 mL Schlenk flask, Oregon Green 514 succinimidyl ester (5 mg) and Rh(phen)(chrysi)(^{x}bpy)$^{3+}$ (5 mg) were dissolved in 2 mL DMF. The resultant vessel was purged with $Ar_{(g)}$ for 5 min and then stirred for 2 h at room temperature. After 2 h, 0.5 mL DIEA were added, and the resultant reaction mixture was allowed to stir overnight under argon. After 16 h, H_2O (4 mL) was added to the reaction mixture, and the aqueous solution was loaded onto a C18 reverse-phase cartridge (Waters Sep-Pak), washed with water, and eluted with 1:1:0.001 (H_2O:MeCN:TFA). The purified product was frozen and lyophilized to dryness. Each conjugate was further purified via reverse-phase high-performance liquid chromatography using an HP1100 HPLC system, a Varian DynaMax C18 semipreparative column, and an elution gradient of 85:15 to 40:60 H_2O (0.1% TFA):MeCN (0.1% TFA) over 60 min.

UV-Vis (all complexes, H_2O, pH 7.0): λ_{max} 302 nm (ε = 54,800), 313 (ε = 44,600), and 519 (ε = 78,000).

ESI-MS (RhOG): 1316 $[M+H]^+$, 659 $[M+2H]^{2+}$

ESI-MS (^{el}RhOG): 1370 $[M+H]^+$, 685 $[M+2H]^{2+}$

ESI-MS (^{peg}RhOG): 1417 $[M+H]^+$, 709 $[M+2H]^{2+}$

ESI-MS (^{lpeg}RhOG): 1473 $[M+H]^+$, 737 $[M+2H]^{2+}$

3.5: REFERENCES

1. Kolodner, R. D. *Trends in Biochemical Science* **1995,** *20*, 397−401.
2. Hsieh, P.; Yamane, K. *Mechanisms of Ageing and Development* **2008,** *129* (7−8), 391−407.
3. Hoffmann, J. S.; Cazaux, C. *International Journal of Oncology* **1998,** *12* (2), 377−382.
4. Scott, R. J. *Onkologie* **1997,** *20* (1), 42−47.
5. Toft, N. J.; Arends, M. J. *Journal of Pathology* **1998,** *185* (2), 123−129.
6. Bocker, T.; Ruschoff, J.; Fishel, R. *Biochimica Et Biophysica Acta−Reviews on Cancer* **1999,** *1423* (3), O1−O10.
7. Wheeler, J. M. D.; Bodmer, W. F.; Mortensen, N. J. M. *Gut* **2000,** *47* (1), 148−153.
8. Jacob, S.; Praz, F. *Biochemie* **2002,** *84*, 27−47.
9. Valentini, A. M.; Armentano, R.; Pirrelli, M.; Caruso, M. L. *Cancer Treatment Reviews* **2006,** *32* (8), 607−618.
10. Muller, A.; Korabiowska, M.; Brinck, U. *In Vivo* **2003,** *17* (1), 55−59.

11. Pors, K.; Patterson, L. H. *Current Topics in Medicinal Chemistry* **2005,** *5* (12), 1133−1149.

12. Fink, D.; Aebi, S.; Howell, S. B. *Clinical Cancer Research* **1998,** *4* (1), 1−6.

13. Jackson, B. A.; Barton, J. K. *Journal of the American Chemical Society* **1997,** *119* (52), 12986−12987.

14. Jackson, B. A.; Alekseyev, V. Y.; Barton, J. K. *Biochemistry* **1999,** *38* (15), 4655−4662.

15. Zeglis, B. M.; Barton, J. K. *Nature Protocols* **2007,** *2* (2), 357−371.

16. Zeglis, B. M.; Pierre, V. C.; Barton, J. K. *Chemical Communications* **2007**, 4565−4579.

17. Baumstark, D.; Wagenknecht, H. A. *Angewandte Chemie−International Edition* **2008,** *47* (14), 2612−2614.

18. Cho, M.; Chung, S.; Heo, S. D.; Ku, J.; Ban, C. *Biosensors & Bioelectronics* **2007,** *22* (7), 1376−1381.

19. Takei, F.; Suda, H.; Hagihara, M.; Zhang, J. H.; Kobori, A.; Nakatani, K. *Chemistry−a European Journal* **2007,** *13* (16), 4452−4457.

20. Nesterova, I. V.; Erdem, S. S.; Pakhomov, S.; Hammer, R. P.; Soper, S. A. *Journal of the American Chemical Society* **2009,** *131* (7), 2432−+.

21. Ruba, E.; Hart, J. R.; Barton, J. K. *Inorganic Chemistry* **2004,** *43* (15), 4570−4578.

22. Petitjean, A.; Barton, J. K. *Journal of the American Chemical Society* **2004,** *126* (45), 14728−14729.

23. Schatzschneider, U.; Barton, J. K. *Journal of the American Chemical Society* **2004,** *126* (28), 8630−8631.

24. Lim, M. H.; Lau, I. H.; Barton, J. K. *Inorganic Chemistry* **2007,** *46*, 9528−9530.

25. Jackson, B. A.; Barton, J. K. *Biochemistry* **2000,** *39* (20), 6176−6182.

26. Gabriel, S. *Chemische Berichte* **1887,** *20*, 2224−.

27. Gibson, M. S.; Bradshaw, R. W. *Angewandte Chemie−International Edition* **1968,** *7* (12), 919−925.

28. Della Ciana, L.; Hamachi, I.; Meyer, T. J. *Journal of Organic Chemistry* **1989,** *54* (7), 1731−1735.

CHAPTER 4: THE BINDING OF RU(BPY)$_2$(EILATIN)$^{2+}$ TO MATCHED AND MISMATCHED DNA[ψ]

4.1: INTRODUCTION

The success and potential of the first generations of metalloinsertors have spurred considerable efforts to expand the family of compounds.[1, 2] To this end, over the past ten years, our laboratory has developed mismatch-specific complexes featuring different metal centers[3], inserting ligands[4], and ancillary ligands.[5–9] Importantly, this variation provides an opportunity to exploit both the structure and reactivity of new molecular components. Further, the inherent modularity of metal complexes has made many of these alterations, especially those involving ancillary ligands, relatively facile.

The recent revelation of the detailed structure of metalloinsertion at a single base mismatch has further informed the drive for innovation.[10, 11] Traditional metallointercalators such as Rh(bpy)$_2$(phi)$^{3+}$ bind DNA from the major groove, stacking a planar, aromatic ligand between adjacent base pairs and thus doubling the helical rise.[12–17] In contrast, Rh(bpy)$_2$(chrysi)$^{3+}$ and other metalloinsertors bind their target sites from the minor groove by extruding the mismatched bases into the major groove and replacing the displaced bases in the helical π-stack with their sterically expansive ligand (**Figure 4.1**). This binding is accommodated by a slight widening of the phosphate backbone at the mismatched site.

Prior to elucidating this structure, we had reported a direct correlation between the specific binding affinity of a metalloinsertor and the thermodynamic destabilization of its

---

[ψ] Adapted from Zeglis, B. M.; Barton, J. K. Binding of Ru(bpy)$_2$(eilatin)$^{2+}$ to matched and mismatched DNA. *Inorg. Chem.* **2008**, *47*, 6452−5457.

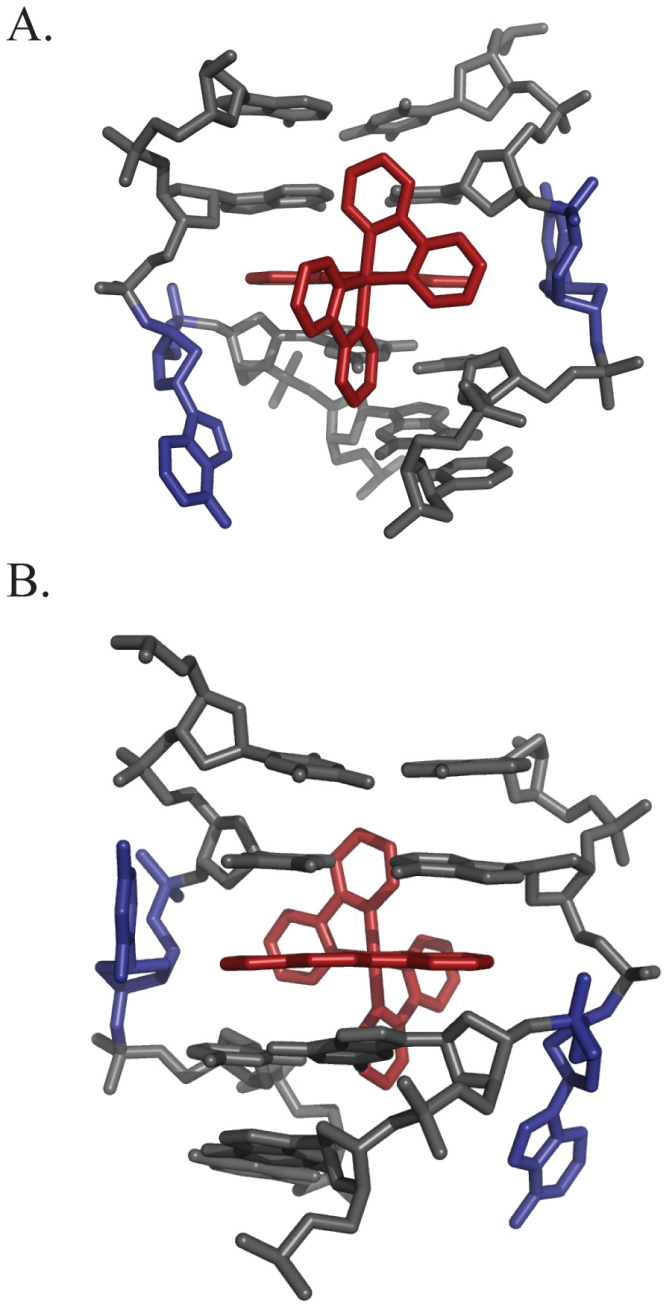

Figure 4.1: Structure of metalloinsertion at a C•A mismatch.[11] Views of metalloinsertion from the minor (A) and major (B) groove sides of the target site.

target site (see Chapter 1).[18–21] More destabilized mismatches are bound more tightly than less destabilized sites, with highly stable, G-containing sites escaping recognition altogether. The extrusion of the mispaired bases by a metalloinsertor provides a clear explanation for this behavior: the less stable the mismatch, the more easily it is extruded from the helix by a metalloinsertor.

One of the primary objectives in the synthesis and study of novel metalloinsertors is the development of mismatch-specific complexes that target the elusive, more stable mismatches. In pursuit of this goal, we considered that augmenting the size of the bulky aromatic ligand might provide this increase in the range of mismatches targeted, an idea predicated on the notion that greater surface area for π-stacking might yield the boost in binding affinity needed for the recognition of more thermodynamically stable mismatched sites. Herein, we report investigations into the DNA-binding properties of $Ru(bpy)_2(eilatin)^{2+}$, a complex bearing an exceptionally expansive ligand (**Figure 4.2**).[22]

Eilatin is a highly symmetric, heptacylic natural product from the pyrido[2,3,4-kl]acridine family of marine alkaloids. It was first isolated in 1988 from the tunicate *Eudistoma sp.* in the Gulf of Eilat in the Red Sea.[23] While the molecule itself has proven of significant interest both to synthetic[24, 25] and biological[26–30] chemists, it is, however, eilatin as a ligand in an octahedral metal complex that offers the possibility of high-affinity metalloinsertion.[22, 31] Indeed, the maximum width of the coordinated eilatin ligand is 13.3 Å, compared to 11.8 Å for the mismatch-specific chrysene-5,6-quinone diimine (chrysi) ligand and 9.2 Å for the non-specific 9,10-phenanthrenequinone diimine (phi) ligand (**Figure 4.3**).[32] Moreover, the eilatin ligand contains seven aromatic rings

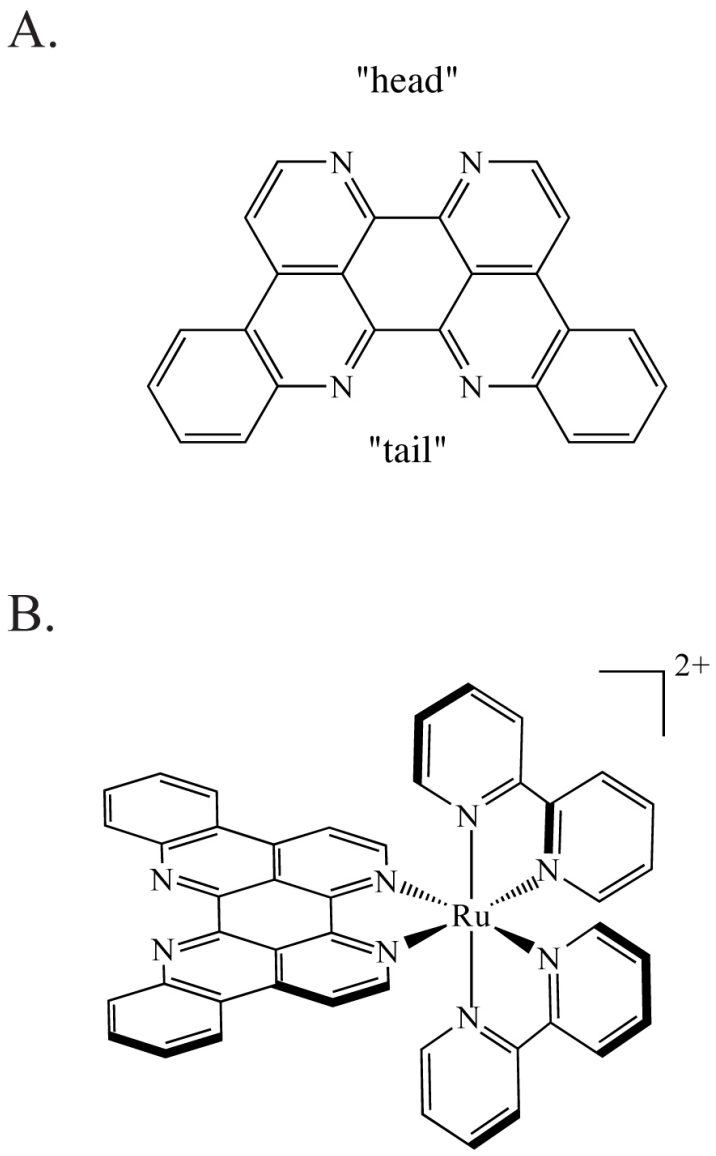

Figure 4.2: Eilatin and $Ru(bpy)_2(eilatin)^{2+}$. The structures of (A) eilatin and (B) $Ru(bpy)_2(eilatin)^{2+}$

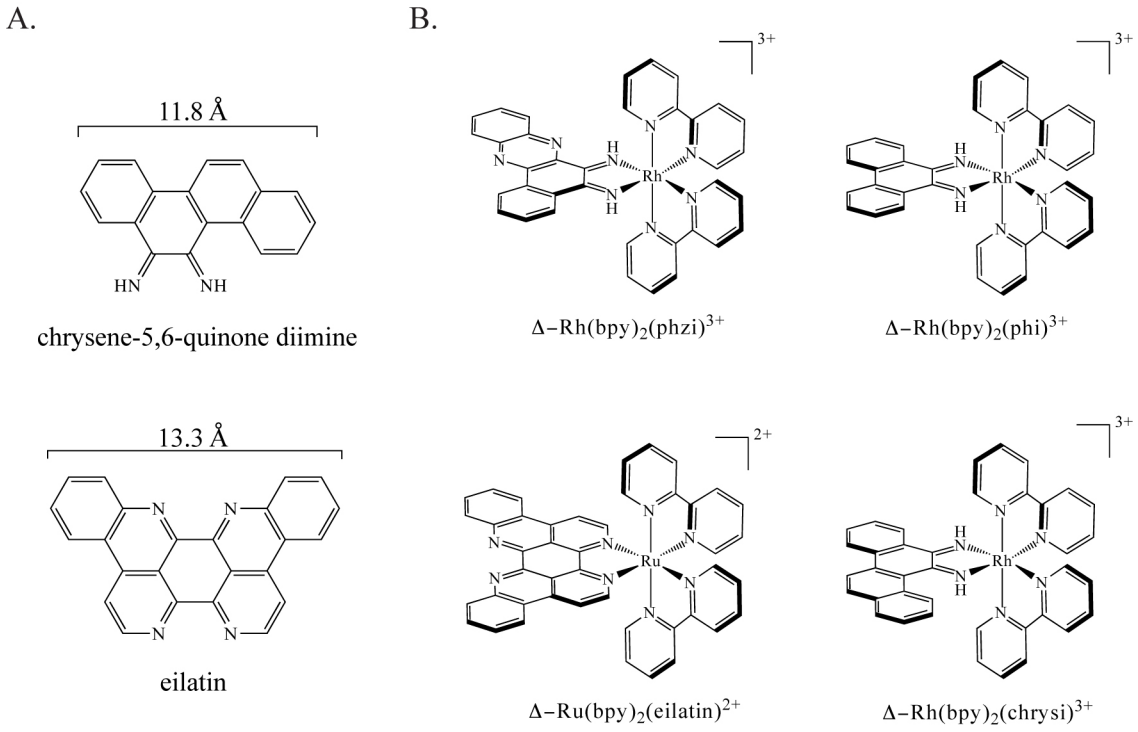

Figure 4.3: Comparison of eilatin to other DNA-binding ligands. (A) The widths of chrysene-5,6-quinone diimine and eilatin, as approximated using ChemDraw3D with energy-minimized structures. (B) The structures of four DNA-binding metal complexes: a metallointercalator, $Rh(bpy)_2(phi)^{3+}$; two metalloinsertors, $Rh(bpy)_2(chrysi)^{3+}$ and $Rh(bpy)_2(phzi)^{3+}$; and the complex under investigation, $Ru(bpy)_2(eilatin)^{2+}$.

available for π-stacking upon insertion into the DNA helix; the chrysi ligand, for comparison, has only four. It is our hypothesis that the singular expanse of the eilatin ligand makes $Ru(bpy)_2(eilatin)^{2+}$ a tremendously attractive candidate for a high affinity, mismatch-specific metalloinsertor.

$Ru(bpy)_2(eilatin)^{2+}$ has been previously prepared and characterized spectroscopically by Kol and coworkers.[22, 31, 33–35] Moreover, studies with nucleic acids by Tor and coworkers have revealed binding to folded RNAs and non-specific association with calf thymus DNA.[36–38] It is of note here that in investigating the DNA-binding properties of $Ru(bpy)_2(eilatin)^{2+}$, we are departing from the well-studied $Rh(bpy)_2(chrysi)^{3+}$ system on two fronts, both the metal and the inserting ligand. Our laboratory has previously examined the binding of luminescent ruthenium complexes to DNA and RNA, most notably the light-switch compound $Ru(phen)_2(dppz)^{2+}$.[39, 40] Yet here, our interest is primarily derived from the shape characteristics of the ligand and its potential applications as a specific probe for mismatched DNA. Our studies show, however, that steric bulk alone is insufficient to achieve site-specificity.

4.2: Results and Discussion

4.2.1: Synthesis and Characterization

Eilatin was synthesized according to the biomimetic route published by Gellerman and coworkers (**Figure 4.4a**).[41–43] Kynuramine, a natural product in its own right, was first protected via trifluoroacetylation using ethyl trifluoroacetate in methanol. The protected product was then reacted with catechol under oxidative conditions (EtOH, $NaIO_3$) to form a 1,2-acridinedione derivative intermediate. This intermediate was

purified via column chromatography (9:1 $CHCl_3$:MeOH, SiO_2) and then treated with base to catalyze the cyclization reaction that yields a yellow fluorescent product: eilatin. While the synthetic transformations may seem somewhat convoluted, an alignment of the precursors makes quite clear the origins of the molecule's carbon and nitrogen skeleton (**Figure 4.4b**).

The metallation of the eilatin ligand onto ruthenium was also performed according to published procedures. A solution of $Ru(bpy)_2(Cl)_2$ and eilatin in 1:1 MeOH:H_2O was refluxed for five hours to yield the desired product: $Ru(bpy)_2(eilatin)^{2+}$.[22] The complex was isolated from the reaction mixture via precipitation with NH_4PF_6, and the hexafluorophosphate anions were subsequently exchanged for chlorides via anion exchange chromatography. The final product was purified via reverse-phase HPLC using an HP1100 HPLC system, a Varian DynaMax C18 semipreparative column, and an elution gradient of 85:15 to 40:60 H_2O (0.1% TFA):MeCN (0.1% TFA) over 60 min. It is important to note that the metallation of eilatin is face-selective; only the sterically congested "head" of the ligand readily binds metals under most conditions. Far more forcing reactions are required to make 2:1 metal:eilatin complexes.[33]

The spectroscopic properties of $Ru(bpy)_2(eilatin)^{2+}$ are particularly interesting. Easily the most notable feature of the complex is its beautiful dark green color, a consequence of a broad ligand π-π^* absorption band centered around 520 nm and an extremely low energy $d_\pi(M)$-$\pi^*(L)$ MLCT centered at 600 nm (**Figure 4.6**).

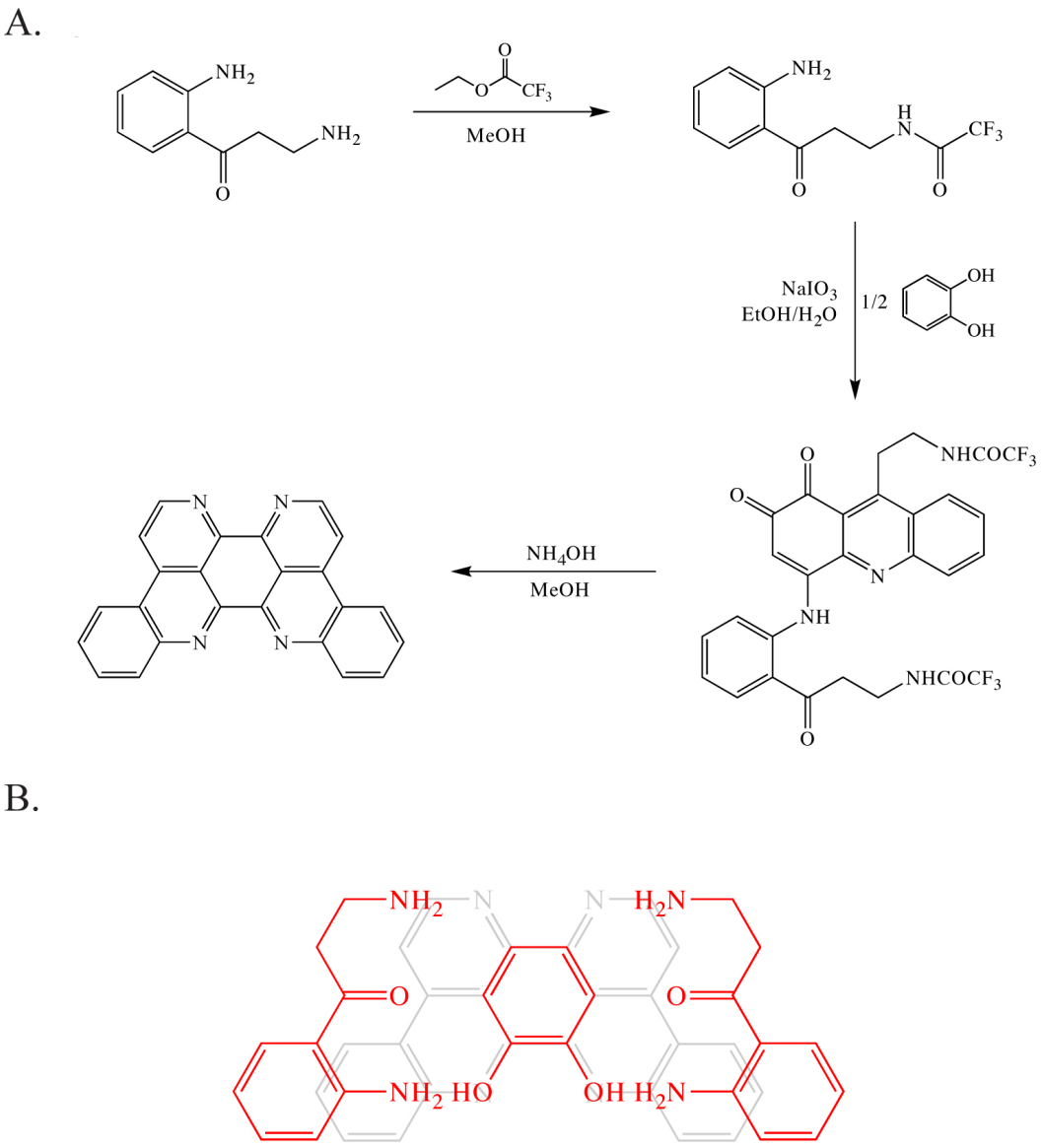

Figure 4.4: The synthesis of eilatin. (A) Eilatin can be synthesized via a biomimetic pathway in three steps from the natural product kynuramine. (B) An overlay of the starting materials and the product makes clear the origins of the carbon and nitrogen atoms in the molecule.

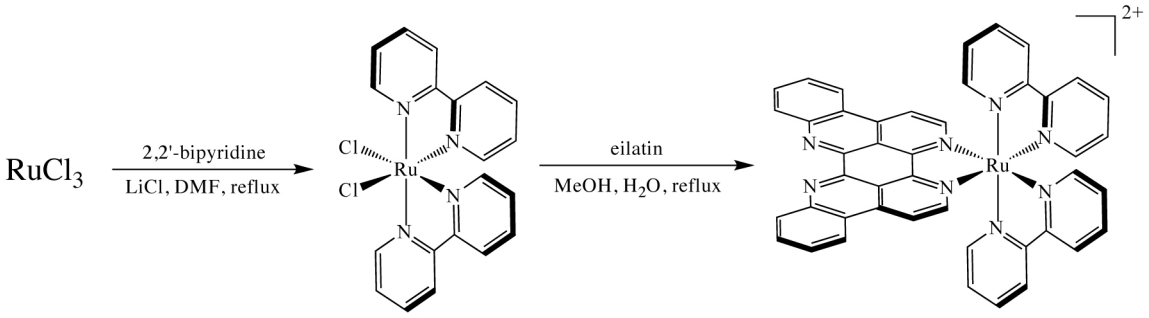

Figure 4.5: The synthesis of $Ru(bpy)_2(eilatin)^{2+}$. The metallation of the eilatin ligand is face-selective. Far harsher reaction conditions are required to prompt a metal to bind to the more sterically constrictive "tail" of the molecule.

Perhaps not surprisingly given the expanse of the ligand, dimerization, in particular homochiral association, of $Ru(bpy)_2(eilatin)^{2+}$ has been observed by other groups.[34, 35, 44, 45] As a consequence, UV-Vis spectroscopy was also used to probe this phenomenon in the concentration regimes relevant to the investigation. Fortunately, spectrophotometric titrations of the complex over the salient range of concentrations reveal no deviations from Beer's Law, indicating that dimer- and oligomerization are of little import in the study at hand.

4.2.2: INVESTIGATING THE SITE-SPECIFICTY OF $RU(BPY)_2(EILATIN)^{2+}$

Owing to the short excited state lifetime of $Ru(bpy)_2(eilatin)^{2+}$, direct methods such as DNA photocleavage or singlet oxygen sensitization could not be used to characterize the sites targeted by the Ru complex within the DNA duplex.[46] Instead, competition experiments were employed. We first utilized $Rh(bpy)_2(phi)^{3+}$, which binds duplex DNA with little site-selectivity[47], in order to probe the binding sites of the Ru complex through competitive inhibition. A synthetic 33-mer oligonucleotide was synthesized with complements featuring a guanine (EL-M) or a cytosine (EL-MM) across from a central cytosine (bold) to form matched and mismatched strands: 5'-CGC TAC GTC TAT ATG **C**AT GAT CCT AAG TGA CAG TAC-3'. After synthesis and purification, the forward strand (shown) was radioactively labeled with ^{32}P at its 5'-terminus via standard protocols. Then, samples (1 μM) of radiolabeled EL-M and EL-MM DNA in buffer (50 mM NaCl, 10 mM NaPi, pH 7.1) were incubated with 8 μM

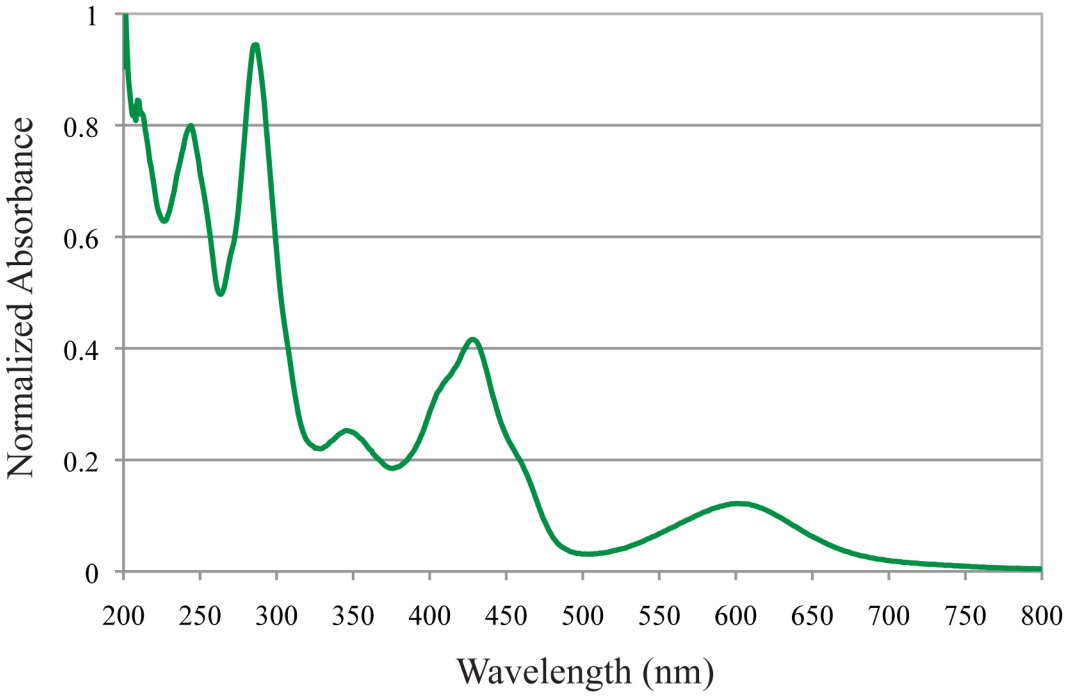

Figure 4.6: UV-Vis spectrum of $Ru(bpy)_2(eilatin)^{2+}$. Extinction coefficients (H_2O, pH 7.0): λ_{max} 244 nm (ε = 64,000), 287 nm (ε = 68,000), 426 nm (ε = 38,000).

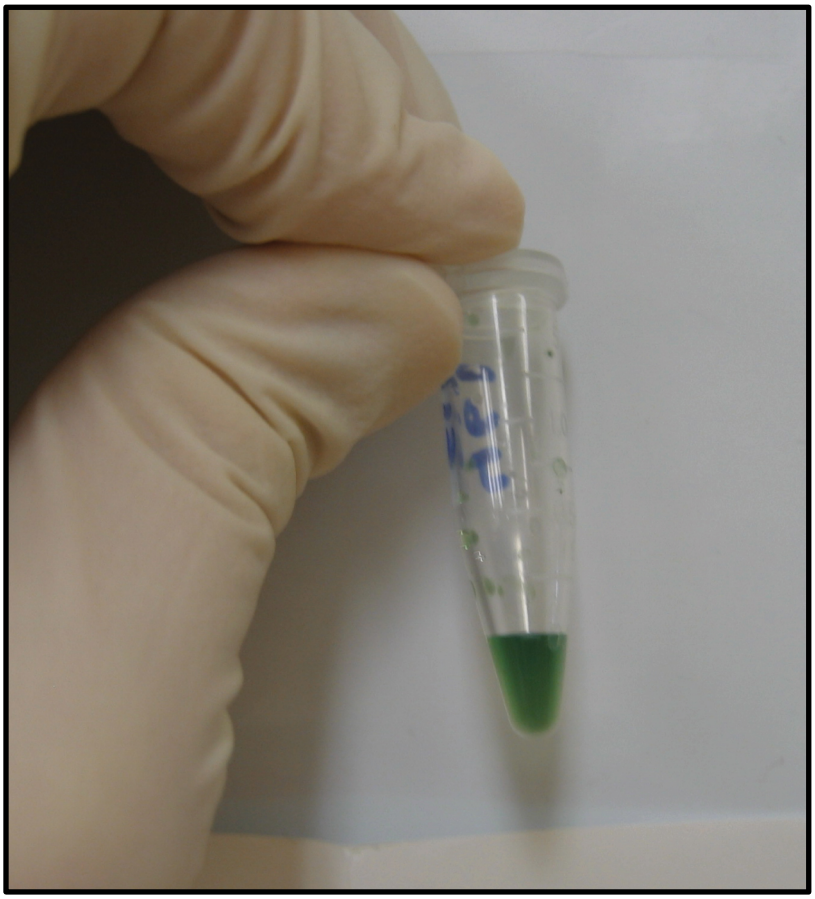

Figure 4.7: The distinctive green color of $Ru(bpy)_2(eilatin)^{2+}$. The solution shown is approximately 200 μM.

$Rh(bpy)_2(phi)^{3+}$ and irradiated for 20 minutes in the presence of variable amounts of $Ru(bpy)_2(eilatin)^{2+}$ using a solar simulator. A concentration of 8 μM $Rh(bpy)_2(phi)^{3+}$ provides 1 rhodium molecule per 4 base pairs, enough to saturate the entire oligonucleotide with rhodium complexes. Because previously published reports revealed few enantiomeric trends in the binding of $Ru(bpy)_2(eilatin)^{2+}$ to well-matched oligonucleotides, a racemic mixture of the Δ- and Λ-isomers was employed in all experiments. Moreover, while the dimerization of $Ru(bpy)_2(eilatin)^{2+}$ in solution has been observed, spectrophotometric titrations of the complex over the relevant range of concentrations reveal no deviations from Beer's Law, indicating that dimer- and oligomerization are of little import in the study at hand.

Autoradiography of the resultant gel reveals that $Rh(bpy)_2(phi)^{3+}$ promotes photocleavage on the EL-M DNA at six discrete sites (with base numbers from the 3'-end): C19, G22, C27, C29, T32, and C33 (**Figure 4.8**). Interestingly, EL-MM DNA is cleaved at the same locations by $Rh(bpy)_2(phi)^{3+}$ but also displays two more cleavage bands: T13 and C16. The C16 position is the mismatched site. The somewhat curious cleavage at T13 may result from local conformational changes created by the nearby mismatch in the EL-MM sequence, leading to hyper-reactivity.[48]

The effect of increasing $Ru(bpy)_2(eilatin)^{2+}$ concentrations on $Rh(bpy)_2(phi)^{3+}$ photocleavage are also manifest in the gel (**Figures 4.8−4.10**). With increasing concentrations of $Ru(bpy)_2(eilatin)^{2+}$, all of the $Rh(bpy)_2(phi)^{3+}$ cleavage bands lessen in intensity on both the matched and mismatched duplexes, indicating that $Ru(bpy)_2(eilatin)^{2+}$ is competing with, and eventually inhibiting, rhodium binding at all sites.

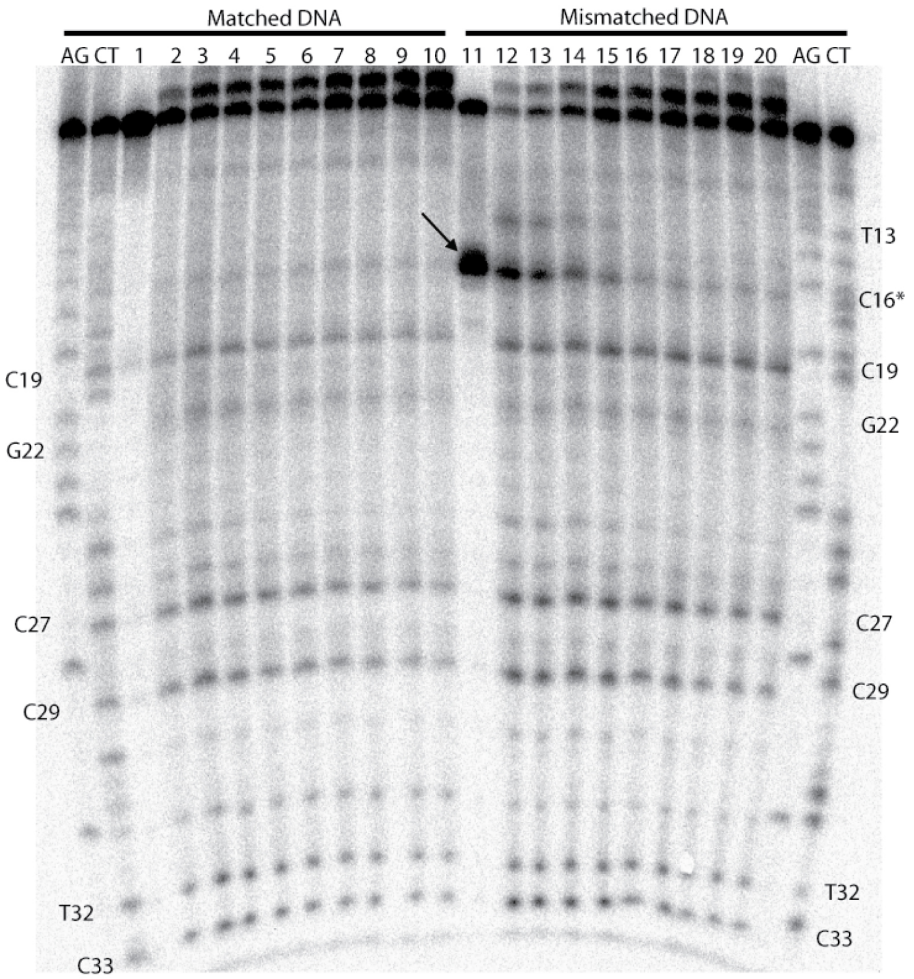

Figure 4.8: $Rh(bpy)_2(phi)^{3+}$ vs. $Ru(bpy)_2(eilatin)^{2+}$ competition gel. Denaturing polyacrylamide gel showing the competition of $Rh(bpy)_2(phi)^{3+}$ and $Ru(bpy)_2(eilatin)^{2+}$ for matched and mismatched DNA of the sequence 3'-GCGATGCAGATATAC***C***TACTAGGATTCACTGTCATG-^{32}P-5' (the italicized C is opposite a G in the matched duplex, in the mismatched sequence a C). All samples were prepared with 1 μM DNA, 50 mM NaCl, 10 mM NaPi, pH 7.1 and, unless otherwise stated, irradiated for 20 minutes on a solar simulator. Left and right AG and CT lanes are Maxam-Gilbert sequencing reactions for matched and mismatched DNA, respectively. Lanes 1−10 employ matched DNA, lanes 11−20 mismatched DNA. Sample conditions: lanes 1 and 11, 1 μM $Rh(bpy)_2(chrysi)$; lanes 2−10 and 12−20, 8 μM $Rh(bpy)_2(phi)^{3+}$. Lanes 3−10 and 13−20 also contain increasing amounts of $Ru(bpy)_2(eilatin)^{2+}$, beginning with 2.5 μM $Ru(bpy)_2(eilatin)^{2+}$ in lanes 3 and 13 and increasing in increments of 2.5 μM to 22.5 μM in lanes 10 and 20. The arrow marks the mismatched site.

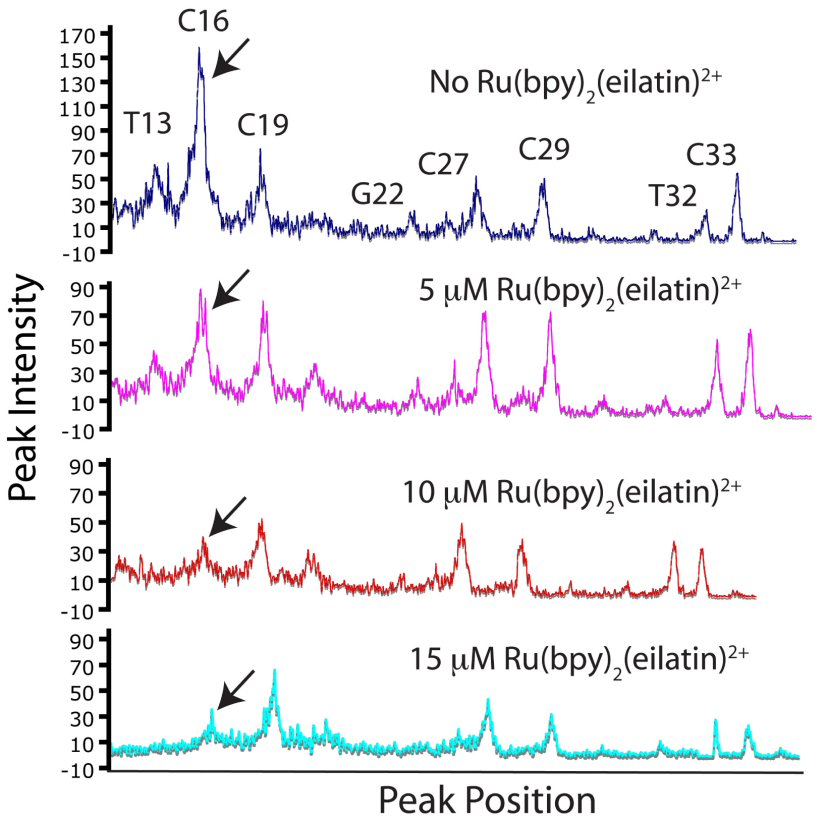

Figure 4.9: $Rh(bpy)_2(phi)^{3+}$ vs. $Ru(bpy)_2(eilatin)^{2+}$ competition experiment. Line plots of lanes 14, 16, 18, and 20 in the competition gel. The arrow marks the mismatched site.

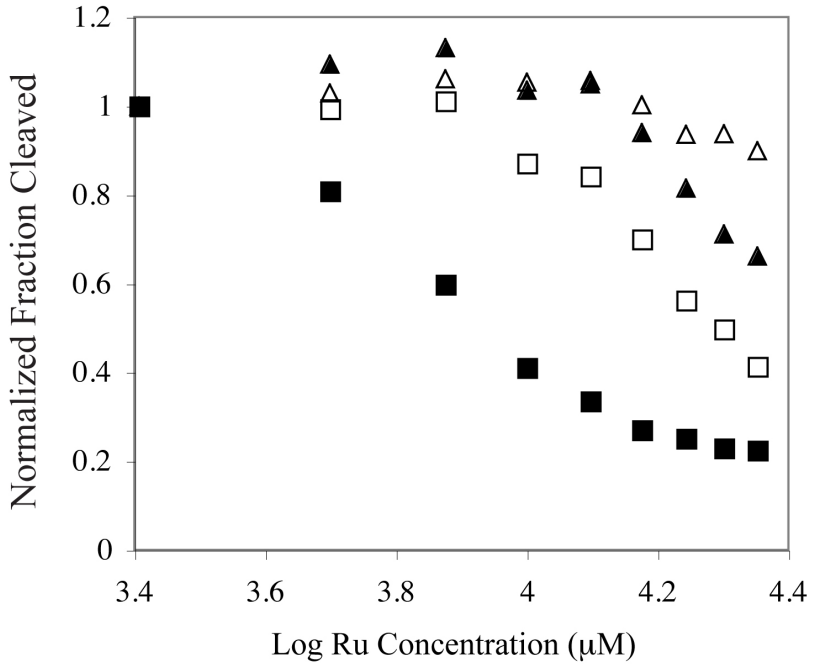

Figure 4.10: $Rh(bpy)_2(phi)^{3+}$ vs. $Ru(bpy)_2(eilatin)^{2+}$ competition experiment. Quantitation of $Rh(bpy)_2(phi)^{3+}$ cleavage band intensity is shown as a function of $Ru(bpy)_2(eilatin)^{2+}$ concentration. Filled square represents C16; empty square, C29; filled triangle, C27; empty triangle, C19.

At these Ru concentrations, this non-specific inhibition of Rh photocleavage cannot be accounted for primarily through light absorption by the Ru complex but instead must reflect competitive binding of the Ru complex to well-matched DNA sites. Increasing concentrations of $Ru(bpy)_3^{2+}$, a metal complex that binds DNA very weakly and has extinction coefficients similar to $Ru(bpy)_2(eilatin)^{2+}$ over the spectral range of interest, have no effect on the photocleavage intensities of $Rh(bpy)_2(phi)^{3+}$ and $Rh(bpy)_2(chrysi)^{3+}$ in the salient concentration range (**Figure 4.11**). Importantly, this $Ru(bpy)_3^{2+}$ control also helps to exclude the possibility that $Ru(bpy)_2(eilatin)^{2+}$ reduces metallointercalator and metalloinsertor photocleavage via quenching of the rhodium excited state. For the well-matched duplex, photocleavage with 8 mM $Rh(bpy)_2(phi)^{3+}$ is fully inhibited at ~15 mM $Ru(bpy)_2(eilatin)^{2+}$. Non-specific duplex binding occurring in the micromolar range is thus comparable for the two complexes.

Interestingly, however, site preferences for both $Rh(bpy)_2(phi)^{3+}$ and $Ru(bpy)_2(eilatin)^{2+}$ are evident on the mismatched duplex. In the absence of Ru, Rh photocleavage on the mismatched duplex is most intense at the mismatched site, C16. However, with increasing Ru, it is photocleavage at this mismatched site that is preferentially inhibited; cleavage at the mismatched site is competed out at noticeably lower concentrations of $Ru(bpy)_2(eilatin)^{2+}$ (~5 μM) than at the other matched sites. This differential inhibition is most evident in the line plot and gel quantitation graph of the titration (**Figures 4.9** and **4.10**). The higher photocleavage for $Rh(bpy)_2(phi)^{3+}$ in the absence of Ru actually reflects a slightly higher affinity for the mismatched site versus matched sites, a common characteristic of classical intercalators.[49]

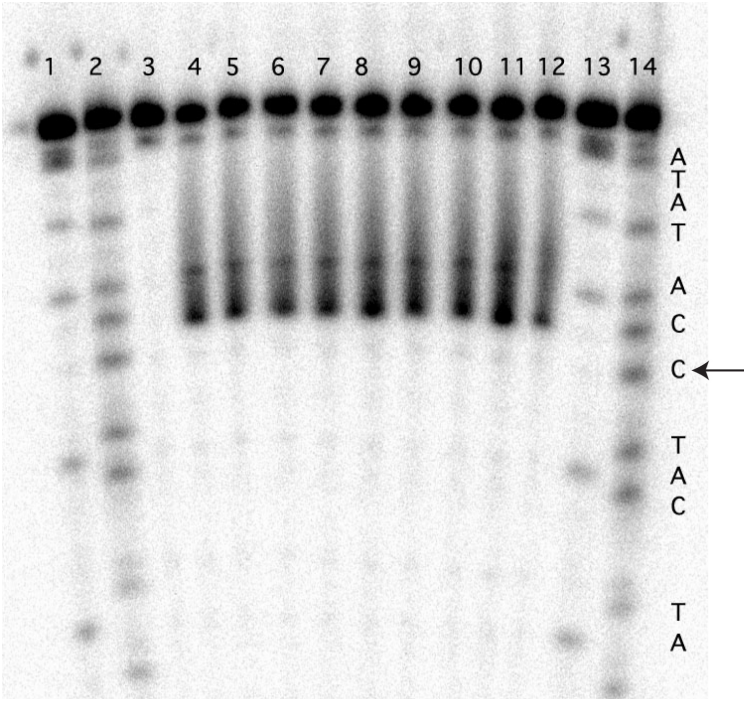

Figure 4.11: $Rh(bpy)_2(chrysi)^{3+}$ vs. $Ru(bpy)_3^{2+}$ competition experiment. Denaturing polyacrylamide gel showing the competition of $Rh(bpy)_2(chrysi)^{3+}$ and $Ru(bpy)_2(eilatin)^{2+}$ for mismatched DNA of the sequence 3'-GCGATGCAGATATAC***C***TACTAGGATTCACTGTCATG-^{32}P-5' (the italicized *C* is complementary to another C). All samples were prepared with 0.66 μM DNA, 50 mM NaCl, 10 mM NaPi, pH 7.1 and, unless otherwise stated, irradiated for 6 minutes on a solar simulator. Lanes 1, 2, 13, and 14 are Maxam-Gilbert sequencing reactions for A+G and C+T, respectively. Lane 3 is a light control showing DNA irradiated in the absence of metal complex. Lanes 4−12 contain 0.66 μM $Rh(bpy)_2(chrysi)^{3+}$ and increasing concentrations of $Ru(bpy)_3^{2+}$: 0, 0.1, 0.33, 0.66, 1, 2, 3.3, 5, 15, and 33 μM respectively. Wide photocleavage bands do not reflect non-specific photocleavage at more than one site but rather the multiple products produced by hydrogen abstraction upon photo-activated cleavage at the mismatched site. The arrow marks the mismatched site.

Preferential inhibition of Rh photocleavage by $Ru(bpy)_2(eilatin)^{2+}$ may similarly reflect this preferential stacking with a mismatched site. Indeed, the gel quantitation shows that binding to the mismatch is less than an order of magnitude tighter than to matched sites. Curiously, the T13 cleavage site is also competed out by the Ru complex well before the other matched locations. Since hyper-reactivity of $Rh(bpy)_2(phi)^{3+}$ at T13 likely depends on the nearby C16 mismatch, it appears it is similarly affected by competition with $Ru(bpy)_2(eilatin)^{2+}$.

4.2.3: DETERMINING THE MISMATCH-SPECIFIC BINDING AFFINITY OF $RU(BPY)_2(EILATIN)^{2+}$

While competition experiments with a non-specific intercalator provides qualitative information about site preference, quantitative data regarding site-specific affinity can be determined by competition with a mismatch-specific metalloinsertor, $Rh(bpy)_2(chrysi)^{3+}$. For this second competition experiment, a similar but shorter 5'-^{32}P-labeled oligonucleotide was synthesized to minimize non-specific binding to matched DNA. Complements containing a guanine and cytosine across from a central cytosine (bold) were also synthesized to afford matched (ES-M) and mismatched (ES-MM) duplexes: 5'-^{32}P-TTAGGATCAT**C**CATATA -3'. A titration employing 1 μM mismatched DNA in buffer (50 mM NaCl, 10 mM NaPi, pH 7.1) and variable $Rh(bpy)_2(chrysi)^{3+}$ was first used to obtain a mismatch-specific binding constant for the rhodium complex of 1.7(2) x 10^6 M^{-1} (**Figure 4.12**).

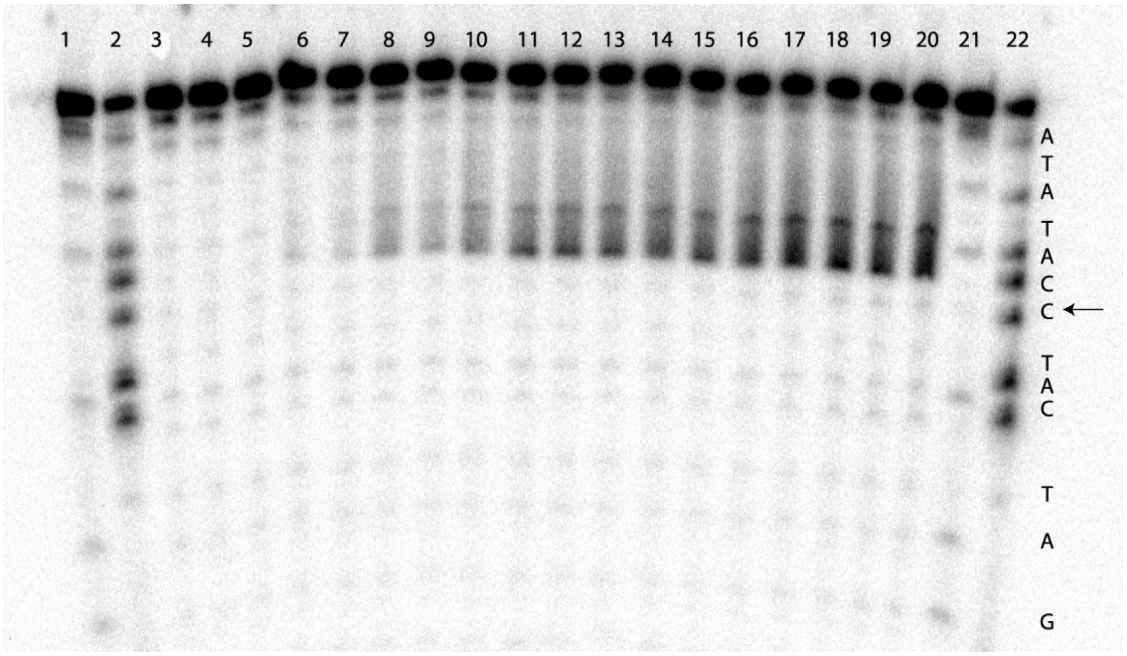

Figure 4.12: $Rh(bpy)_2(chrysi)^{3+}$ binding constant gel. Denaturing polyacrylamide gel showing the photocleavage titration of $Rh(bpy)_2(chrysi)^{3+}$ and the oligonucleotide 5'-^{32}P-TTAGGATCAT*C*CATATA-3' (the italicized C marks the site of the C•C mismatch). All samples were prepared with 1 μM DNA, 50 mM NaCl, 10 mM NaPi, pH 7.1 and, unless otherwise stated, irradiated for 5 minutes on a solar simulator. Lanes 1, 2, 21, and 22 are Maxam-Gilbert sequencing reactions for A+G and C+T, respectively. Lane 3 is a light control displaying DNA irradiated in the absence of metal complex. Lane 4 is a dark control displaying DNA incubated with metal complex without irradiation. Lanes 5−20 contain increasing concentrations of $Rh(bpy)_2(chrysi)^{3+}$: 0, 0.1, 0.2, 0.3, 0.4, 0.5, 0.6, 0.7, 0.8, 0.9, 1, 2, 3, 4, 5 μM, respectively. Wide photocleavage bands do not reflect non-specific photocleavage at more than one site but rather the multiple products produced by hydrogen abstraction upon photo-activated cleavage at the mismatched site. The arrow marks the mismatched site.

Given a known specific binding constant for $Rh(bpy)_2(chrysi)^{3+}$, a competition experiment with $Ru(bpy)_2(eilatin)^{2+}$ can yield the quantitative binding affinity of the Ru complex for the mismatched site.[50, 51] The competition experiment was performed using 3 μM ES-MM DNA and 3 μM $Rh(bpy)_2(chrysi)^{3+}$ in 50 mM NaCl, 10 mM NaPi, pH 7.1 along with increasing concentrations of $Ru(bpy)_2(eilatin)^{2+}$ (0−20 μM). The samples were then irradiated for 15 minutes on a solar simulator and subsequently eluted through a denaturing polyacrylamide gel. The resultant gel clearly shows initially strong $Rh(bpy)_2(chrysi)^{3+}$ photocleavage at the mismatch site that is inhibited by increasing concentrations of $Ru(bpy)_2(eilatin)^{2+}$ (**Figures 4.13** and **4.14**). From these titration data we can extract a C•C mismatch-specific binding constant for $Ru(bpy)_2(eilatin)^{2+}$ of 2.2(2) x 10^6 M^{-1}.[50, 51] It is interesting that the Ru affinity for this mismatched site is comparable to that of $Rh(bpy)_2(chrysi)^{3+}$. Note that this value reflects binding to a 15-mer that contains additional matched sites to which the Ru complex may also bind (albeit likely at higher Ru concentrations). As a result, the binding affinity for the mismatched site must be considered in the context of competition also with matched sites.

4.2.4: IMPLICATIONS FOR METALLOINSERTOR DESIGN

Taken together, the two competition experiments clearly indicate that while $Ru(bpy)_2(eilatin)^{2+}$ does show some preference for binding the C•C mismatch, the bulky complex also displays significant binding to well-matched B-form DNA sites. The site-specificity of the Ru complex for a mismatch is therefore significantly less than that of $Rh(bpy)_2(chrysi)^{3+}$. A comparison of the measured mismatched-site dissociation constant (K_D = 460(9) nM) to those reported for matched sites supports this assertion;

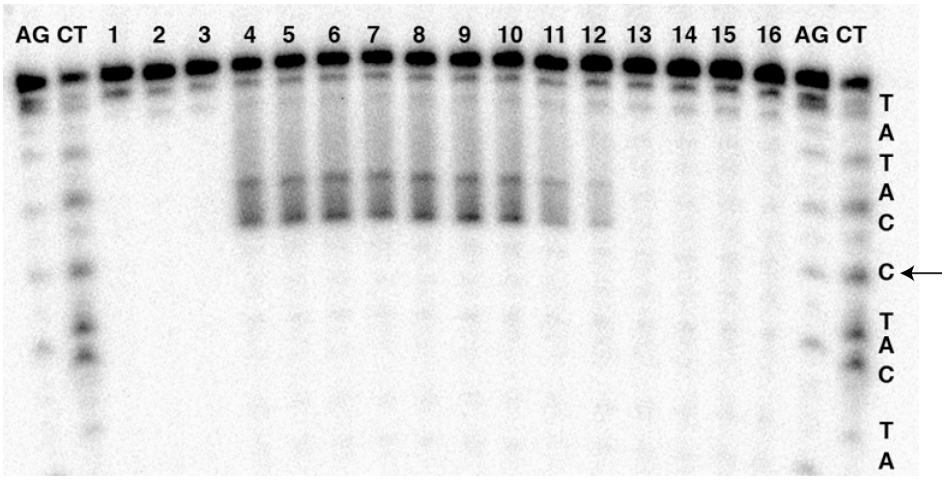

Figure 4.13: $Rh(bpy)_2(chrysi)^{3+}$ vs. $Ru(bpy)_2(eilatin)^{2+}$ competition experiment. Denaturing polyacrylamide gel of a competition experiment between $Rh(bpy)_2(chrysi)^{3+}$ and $Ru(bpy)_2(eilatin)^{2+}$ for a CC mismatch in the oligonucleotide 5'-^{32}P-TTAGGATCAT*C*CATATA-3'. AG and CT lanes are Maxam Gilbert sequencing reactions. All samples contained 3 μM mismatched duplex in a buffer of 50 mM NaCl, 10 mM NaPi, pH 7.1 and were irradiated for 10 minutes using a solar simulator unless otherwise stated. Sample conditions: lane 1, DNA only irradiated without Rh; lane 2, 3 μM $Rh(bpy)_2(chrysi)^{3+}$ without irradiation; lane 3, 3 μM $Ru(bpy)_2(eilatin)^{2+}$ irradiated without Rh; lanes 4−16, 3 μM $Rh(bpy)_2(chrysi)^{3+}$ and increasing concentrations of $Ru(bpy)_2(eilatin)^{2+}$, 0, 0.1, 0.33, 0.66, 1, 2, 3, 5, 10, 20, 33, 66, 100 μM, respectively. Wide photocleavage bands do not reflect non-specific photocleavage at more than one site but rather the multiple products produced by hydrogen abstraction upon photo-activated cleavage at the mismatched site. The arrow marks the mismatched site.

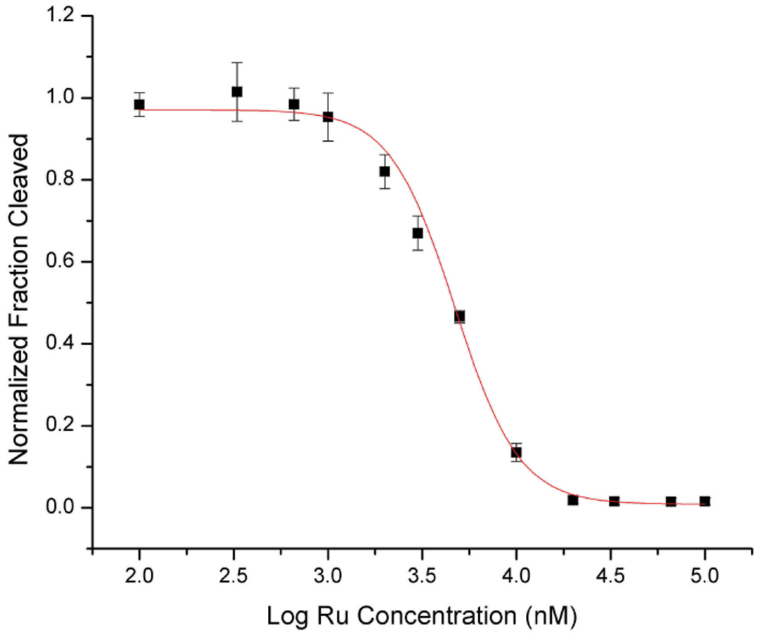

Figure 4.14: $Rh(bpy)_2(chrysi)^{3+}$ vs. $Ru(bpy)_2(eilatin)^{2+}$ competition experiment. Competitive binding of $Ru(bpy)_2(eilatin)^{2+}$ to mismatched DNA monitored using $Rh(bpy)_2(chrysi)^{3+}$ photocleavage. The plot shows fraction DNA cleaved against $Ru(bpy)_2(eilatin)^{2+}$ concentration for four trials of the competition experiment.

with matched DNA, binding is in the low micromolar range.[36–38] Thus the selectivity of the complex for mismatched sites is modest (ratio of binding mismatched versus matched ≤ 10) . It is noteworthy that earlier it was suggested that $Ru(bpy)_2(eilatin)^{2+}$ may bind preferentially to large structural motifs in folded RNAs. Indeed, binding of the hydrophobic and cationic Ru complex may arise with a range of nucleic acid structures.

The ability of $Ru(bpy)_2(eilatin)^{2+}$ to bind both matched and mismatched DNA prompts the consideration of how the Ru complex may interact structurally with matched and mismatched sites. **Figure 4.15** shows schematic illustrations of $Ru(bpy)_2(eilatin)^{2+}$ bound to mismatched DNA in comparison to $Rh(bpy)_2(chrysi)^{3+}$ and to matched DNA in comparison to $Rh(bpy)_2(phi)^{3+}$. Binding of the Rh complexes to their target sites are based upon crystal structures and show access from the minor groove side for metalloinsertion into a mismatched site and from the major groove side for access by metallointercalation.[11, 16] For the Rh complexes, it is apparent that these binding modes permit complete stacking of the inserting ligand between the base pairs. Moreover, the ancillary ligands of the octahedral complexes provide a barrier both to deeper insertion and significant rotation in the pocket. The complexes are bound so that the dyad axis of the base pairs bisects the immine-Rh-immine angle. In this mode, binding of the complexes is optimized for stacking, both at the mismatched and matched site. As illustrated in **Figure 4.15**, the Ru complex is also well situated within a mismatched site for substantial stacking overlap. Overlap with the base pairs is quite comparable for the chrysi and eilatin ligands, consistent with their similar binding affinity for the C•C mismatch. Significantly for $Ru(bpy)_2(eilatin)^{2+}$, however, the complex can still stack well within a matched site, although rotated relative to the bound Rh complex.

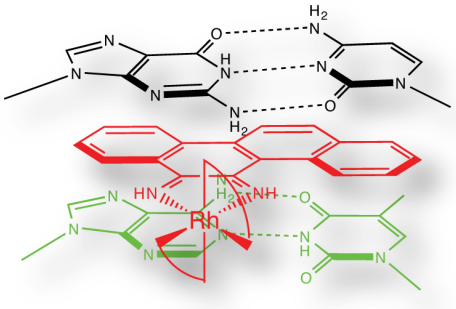

Chrysi Mismatched Site Binding: Insertion from Minor Groove
(bases extruded by inserting ligand not shown)

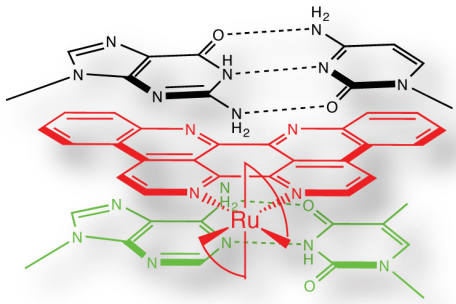

Eilatin Mismatched Site Binding: Insertion from Minor Groove
(bases extruded by inserting ligand not shown)

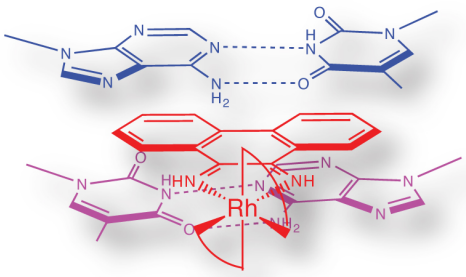

Phi Matched Site Binding: Intercalation from Major Groove

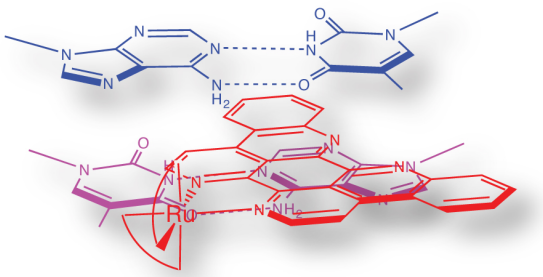

Eilatin Matched Site Binding: Intercalation from Major Groove

Figure 4.15: Proposed binding model for $Ru(bpy)_2(eilatin)^{2+}$ with matched and mismatched DNA. Schematic illustrations of $Ru(bpy)_2(eilatin)^{2+}$ (right) bound to mismatched (top) and matched (bottom) DNA sites based on the crystal structures of a chrysi (top left) and phi complex (bottom left) of Rh bound to mismatched and matched DNA, respectively. For binding to the mismatched site, the metal complexes are oriented from the minor groove side, whereas for binding to the matched site, the association is from the major groove side.

The eilatin ligand is sufficiently expansive that substantial stacking is available between the base pairs without a straight-on orientation of the complex. It is noteworthy that we have seen previously for $Ru(bpy)_2dppz^{2+}$ (dppz = dipyridophenazine) fluorescence and NMR results that are consistent with a mixture of straight-on and side-on orientations in matched duplex DNA.[52] Here, at the matched site, the eilatin complex can easily rotate within the intercalation site and maintain significant overlap with the bases above and below. Indeed, the stacking area appears comparable to that of the phi complex, just as their binding affinities for matched sites are similar. The great expanse of the eilatin ligand permits this significant stacking without the axial ligands serving as a barrier to rotation. Thus, while binding to a mismatched site by $Ru(bpy)_2(eilatin)^{2+}$ is preferred, binding to matched sites is not precluded.

4.3: CONCLUSIONS

These studies show that simply increasing the expanse of a metalloinsertor is not sufficient to gain an increase in specific binding to a mismatched site in duplex DNA. While binding to a mismatched site is still preferred by a complex with a bulkier ligand, the increased expanse also provides stacking area for the complex at a matched site if the ligand is particularly large. In comparing the family of bulky metal complexes, similar affinities in binding mismatched DNA are observed for those bearing the phzi and chrysi ligands versus that containing the even more expansive eilatin ligand. With $Ru(bpy)_2(eilatin)^{2+}$, however, we see that specificity for a single base pair mismatch is lost. That the eilatin ligand extends considerably from the metal center in two directions is likely responsible for this loss in specificity for mismatched sites and gain in affinity

for matched DNA. Clearly, the structural characteristics of $Ru(bpy)_2(eilatin)^{2+}$ allow the complex to bind matched DNA in a manner that $Rh(bpy)_2(chrysi)^{3+}$ and $Rh(bpy)_2(phzi)^{3+}$ cannot. As a consequence, then, these experiments teach us something simple about the design of mismatch-recognition ligands: bulky is good, but bulkier is not necessarily better.

4.4: EXPERIMENTAL PROTOCOLS

Many of the procedural details for this investigation are included in Chapter 2 of this text. These include the following: the synthesis of $Rh(bpy)_2(chrysi)^{3+}$ (2.3.2.5); the synthesis of $Rh(bpy)_2(phi)^{3+}$ (2.3.2.7); the synthesis, purification, and radiolabeling of oligonucleotides (2.4.1−2.4.2); the Maxam-Gilbert sequencing of radiolabeled DNA (2.4.3); the execution of binding constant titrations (2.4.4.2); the performance of competition experiments with non-specific metallointercalators (2.4.4.3); and the performance of competition experiments with site-specific metalloinsertors (2.4.4.3). Further experimental details of the competition experiments can be found in their corresponding figure captions.

4.4.1: MATERIALS AND INSTRUMENTATION

All reagents were obtained from commercial sources and used as received without further purification. $RhCl_3$ and $RuCl_3$ were purchased from Pressure Chemicals. $Rh(bpy)_2(phi)^{3+}$ and $Rh(bpy)_2(chrysi)^{3+}$ were synthesized according to published protocols.[32] All non-aqueous solvents were purchased from Fluka and stored under argon

and over molecular sieves. All water used was purified using a MilliQ water purification system. Unless otherwise noted, all reactions were performed under ambient conditions.

^{1}H-NMR spectra were recorded on a Varian 300 MHz spectrometer at room temperature using solvent residual signal as a reference to TMS. Mass spectrometry was performed at either the Caltech mass spectrometry facility or in the Beckman Institute Protein/Peptide Micro Analytical Laboratory (PPMAL). Absorption spectra were recorded on a Beckman DU 7400 spectrophotometer. Extinction coefficients for $Ru(bpy)_2(eilatin)^{2+}$ were determined using inductively coupled plasma mass spectrometry.

Oligonucleotides were synthesized on an ABI 3400 DNA synthesizer and purified via HPLC in duplicate (DMT-OFF and DMT-ON) before use. All reverse-phase HPLC purifications were performed on an HP1100 high-pressure liquid chromatography system equipped with a diode array detector using a Varian DynaMax C18 semipreparative column (see Chapter 2, section 2.4.1). Irradiations were performed using an Oriel Instruments solar simulator (320−440 nm). All PAGE experiments described employed denaturing 20% polyacrylamide gels (SequaGel, National Diagnostics) and were performed according to published procedures. Gels were developed using Molecular Dynamics phosphorimaging screens and a Molecular Dynamics Storm 820 phosphorimager and were subsequently visualized and quantified with Molecular Dynamics ImageQuant software.

4.4.2: SYNTHESIS OF EILATIN

Eilatin was synthesized according to the biomimetic synthesis published by Gellerman, et al. (see **Figure 4.4**).[41–43]

4.4.2.1: SYNTHESIS OF KYNURAMINE TRIFLUOROACETAMIDE

In a 25 mL round-bottom flask, kynuramine (250 mg, 1.5 mmol) and ethyl trifluoroacetate (710 mg, 5 mmol) were dissolved in 6 mL MeOH. The resultant solution was stirred at room temperature for 4 h. After 4 h, the solution was dried via rotary evaporation. The residue was then taken up in 98:2 CH_2Cl_2:H_2O, washed 3 times with 50 mL $NaHCO_{3(aq)}$, dried with $MgSO_4$, and filtered. The organic phase was then dried *in vacuo* to yield the product as a yellow oil (300 mg, 77%).

ESI-MS: 260 $[M+H]^+$, 282 $[M+Na]^+$

4.4.2.2: SYNTHESIS OF 1,2-ACRIDINEDIONE INTERMEDIATE

In a 100 mL round-bottom flask, kynuramine trifluoroacetamide (200 mg, 0.76 mmol), catechol (37 mg, 0.34 mmol, 0.5 equiv.), and $NaIO_3$ (1.5 g, 7.7 mmol, 10 equiv.) were dissolved in 50 mL 9.5:1 EtOH:H_2O. The reaction mixture was cloudy at first and was stirred for 48 h. Over the course of the reaction, the mixture turned dark brown. After 48 h, the solvent was removed via rotary evaporation. The residue was taken up in CH_2Cl_2 and purified via column chromatography (SiO_2, 4:1 EtOAc:Hex). After purification, the product was isolated as an orange oil (350 mg, 0.57 mmol, 76%).

ESI-MS: 606 $[M+H]^+$, 628 $[M+Na]^+$

4.4.2.3: SYNTHESIS OF EILATIN

In a 25 mL round-bottom flask, the 1,2-acridinedione intermediate (50 mg, 0.08 mmol) was dissolved in 10 mL MeOH and 2 mL NH_4OH. The reaction mixture was stirred at room temperature for 24 hours. After 24 hours, the solution was concentrated *in vacuo*, and the residue was taken up in a minimum volume of MeOH. The reaction mixture was then purified via preparative TLC (SiO_2, 96:4 $CHCl_3$:MeOH) to yield the desired product as a yellow oil (20 mg, 0.05 mmol, 63%).

ESI-MS: 356 $[M+H]^+$, 369 $[M+Na]^+$

^{1}H-NMR (d_6-DMSO): 9.32 ppm (d, 2H); 8.70 ppm (d, 2H); 8.68 ppm (d, 2H); 8.57 ppm (d, 2H); 8.00 ppm (d, 2H); 7.87 ppm (d, 2H);

UV-Vis (MeOH, **Figure 4.16**): λ_{max} 242 nm (ε = 48,200), 286 (ε = 36,700), 366 (ε = 11,500), 388 (ε = 21,000), 408 (ε = 30,400), and 434 (ε = 27,000).

4.4.3: SYNTHESIS OF RU(BPY)$_2$(EILATIN)$^{2+}$

4.4.3.1: SYNTHESIS OF RU(BPY)$_2$Cl$_2$

In a 50 mL round-bottom flask, $RuCl_3$ (0.52 g, 2.5 mmol), 2,2'-bipyridine (0.8 g, 5.0 mmol), LiCl (0.85 g, excess) were suspended in 10 mL and DMF. Reflux the reaction mixture for 8 h at 180 °C. After 8 h, the suspension was allowed to cool to room temperature and poured into 80 mL of stirring acetone. The reaction vessel was washed 2 times with 10 mL acetone. The combined acetone fractions were cooled to 4 °C overnight to prompt crystallization. After 16 h, the solution was vacuum filtered to isolate the dark purple precipitate, which was subsequently washed with water (3 x 10 mL) and diethyl ether (3 x 10 mL).

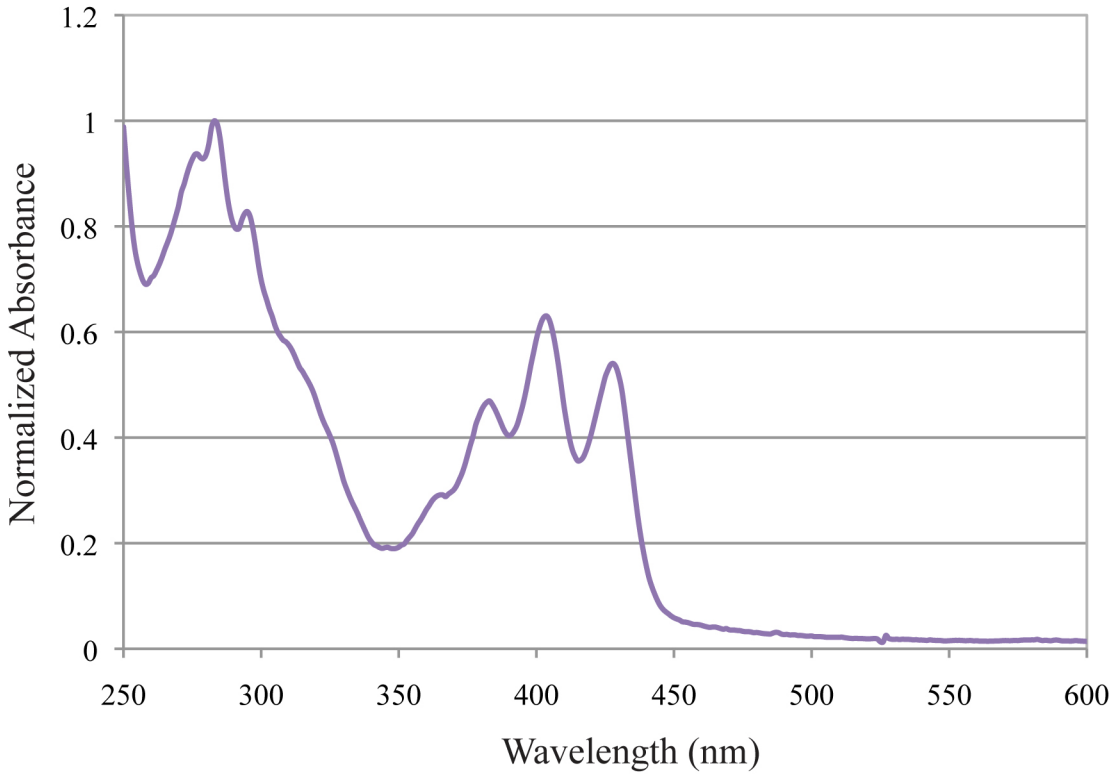

Figure 4.16: UV-Vis spectrum of eilatin. Extinction coefficients: λ_{max} 286 (ε = 36,700), 366 (ε = 11,500), 388 (ε = 21,000), 408 (ε = 30,400), and 434 (ε = 27,000)

ESI-MS: 478 $[M+H]^+$, 450 $[M-Cl]^+$

^{1}H-NMR (d_6-DMSO): 9.95 ppm (d, 2H); 8.60 ppm (d, 2H); 8.48 ppm (d, 2H); 8.05 ppm (t, 2H); 7.75 ppm (t, 2H); 7.65 ppm (t, 2H); 7.50 ppm (d, 2H); 7.08 ppm (t, 2H).

4.4.3.2: SYNTHESIS OF $RU(BPY)_2(EILATIN)^{2+}$

In a 100 mL round-bottom flask, $Ru(bpy)_2(Cl)_2$ (10 mg, 0.02 mmol) and eilatin (10 mg, 0.03 mmol) were dissolved in 20 mL MeOH and 5 mL H_2O. The resultant solution was refluxed at 100 °C for 4 h. After 4 h, the solvent was removed via rotary evaporation, the residue was re-dissolved in H_2O to form a greenish solution, and the product was precipitated via addition of excess NH_4PF_6. The suspension was vacuum filtered, and the dark green precipitate was washed with copious water.

The product precipitate was taken up in acetonitrile and anion exchanged on a Sephadex QAE-25 column that had been pre-equilibrated with 0.05 M $MgCl_2$. The resultant green solution was concentrated on a reverse phase C-18 cartridge, washed, eluted, and lyophilized to dryness. Finally, the green solid was taken up in H_2O and purified via reverse-phase high-performance liquid chromatography using an HP1100 HPLC system, a Varian DynaMax C18 semipreparative column, and an elution gradient of 85:15 to 40:60 H_2O (0.1% TFA):MeCN (0.1% TFA) over 60 min.

ESI-MS (m/z): 768 $[M-2H]^+$, 385 $[M-H]^{2+}$

^{1}H-NMR (d_6-DMSO): 8.93 ppm (d, 2H); 8.77 ppm (d, 2H); 8.74 (d, 2H); 8.29 (m, 2H); 8.17 ppm (d, 2H); 8.14 ppm (d, 2H); 8.08 (m, 2H); 7.96 (m, 2H); 7.88 (d, 2H); 7.69 (m, 2H).

UV-Vis (H_2O, pH 7.0): λ_{max} 244 nm (ε = 64,000), 287 nm (ε = 68,000), 426 nm (ε = 38,000).

4.5: REFERENCES

1. Erkkila, K. E.; Odom, D. T.; Barton, J. K. *Chemical Reviews* **1999**, *99* (9), 2777−2795.
2. Zeglis, B. M.; Pierre, V. C.; Barton, J. K. *Chemical Communications* **2007**, 4565−4579.
3. Ruba, E.; Hart, J. R.; Barton, J. K. *Inorganic Chemistry* **2004**, *43* (15), 4570−4578.
4. Junicke, H.; Hart, J. R.; Kisko, J. L.; Glebov, O.; Kirsch, I. R.; Barton, J. K. *Proceedings of the National Academy of Sciences U. S. A.* **2003**, *100*, 3737−3742.
5. Schatzschneider, U.; Barton, J. K. *Journal of the American Chemical Society* **2004**, *126* (28), 8630−8631.
6. Petitjean, A.; Barton, J. K. *Journal of the American Chemical Society* **2004**, *126* (45), 14728−14729.
7. Brunner, J.; Barton, J. K. *Biochemistry* **2006**, *45* (40), 12295−12302.
8. Zeglis, B. M.; Barton, J. K. *Journal of the American Chemical Society* **2006**, *128* (17), 5654−5655.
9. Ernst, R. J.; Song, H.; Barton, J. K. *Journal of the American Chemical Society* **2009**, *131* (6), 2359−2366.
10. Cordier, C.; Pierre, V. C.; Barton, J. K. *Journal of the American Chemical Society* **2007**, *129*, 12287−12295.

11. Pierre, V. C.; Kaiser, J. T.; Barton, J. K. *Proceedings of the National Academy of Sciences U. S. A.* **2007**, *103*, 429−434.

12. Collins, J. G.; Shields, T. P.; Barton, J. K. *Journal of the American Chemical Society* **1994**, *116* (22), 9840−9846.

13. Franklin, S. J.; Barton, J. K. *Biochemistry* **1998**, *37* (46), 16093−16105.

14. Hudson, B. P.; Barton, J. K. *Journal of the American Chemical Society* **1998**, *120* (28), 6877−6888.

15. Hudson, B. P.; Dupureur, C. M.; Barton, J. K. *Journal of the American Chemical Society* **1995**, *117* (36), 9379−9380.

16. Kielkopf, C. L.; Erkkila, K. E.; Hudson, B. P.; Barton, J. K.; Rees, D. C. *Nature Structural Biology* **2000**, *7* (2), 117−121.

17. Krotz, A. H.; Kuo, L. Y.; Barton, J. K. *Inorganic Chemistry* **1993**, *32* (26), 5963−5974.

18. Jackson, B. A.; Alekseyev, V. Y.; Barton, J. K. *Biochemistry* **1999**, *38* (15), 4655−4662.

19. Jackson, B. A.; Barton, J. K. *Journal of the American Chemical Society* **1997**, *119* (52), 12986−12987.

20. Jackson, B. A.; Barton, J. K. *Biochemistry* **2000**, *39* (20), 6176−6182.

21. Jackson, B. A.; Henling, L. M.; Barton, J. K. *Inorganic Chemistry* **1999**, *38* (26), 6218−6224.

22. Rudi, A.; Kashman, Y.; Gut, D.; Lellouche, F.; Kol, M. *Chemical Communications* **1997**, (1), 17−18.

23. Rudi, A.; Benayahu, Y.; Goldberg, I.; Kashman, Y. *Tetrahedron Letters* **1988**, *29* (50), 6655−6656.

24. Nakahara, S.; Tanaka, Y.; Kubo, A. *Heterocycles* **1993**, *36* (5), 1139−1144.

25. Blanco, M. D.; Avendano, C.; Menendez, J. C. *Tetrahedron* **1999**, *55* (43), 12637−12646.

26. Einat, M.; Lishner, M.; Amiel, A.; Nagler, A.; Rudi, A.; Kashman, Y.; Fabian, I. *Experimental Hematology* **1994**, *22* (8), 797−797.

27. Einat, M.; Lishner, M.; Amiel, A.; Nagler, A.; Yarkorli, S.; Rudi, A.; Kashman, Y.; Markel, D.; Fabian, I. *Experimental Hematology* **1995**, *23* (14), 1439−1444.

28. Ding, Q. Z.; Chichak, K.; Lown, J. W. *Current Medicinal Chemistry* **1999**, *6* (1), 1−27.

29. Lishner, M.; Shur, I.; Bleiberg, I.; Rudi, A.; Kashman, Y.; Fabian, I. *Leukemia* **1995**, *9* (9), 1543−1548.

30. McDonald, L. A.; Eldredge, G. S.; Barrows, L. R.; Ireland, C. M. *Journal of Medicinal Chemistry* **1994**, *37* (22), 3819−3827.

31. Bergman, S. D.; Gut, D.; Kol, M.; Sabatini, C.; Barbieri, A.; Barigelletti, F. *Inorganic Chemistry* **2005**, *44* (22), 7943−7950.

32. Zeglis, B. M.; Barton, J. K. *Nature Protocols* **2007**, *2* (2), 357−371.

33. Gut, D.; Goldberg, I.; Kol, M. *Inorganic Chemistry* **2003**, *42* (11), 3483−3491.

34. Gut, D.; Rudi, A.; Kopilov, J.; Goldberg, I.; Kol, M. *Journal of the American Chemical Society* **2002**, *124* (19), 5449−5456.

35. Bergman, S. D.; Frantz, R.; Gut, D.; Kol, M.; Lacour, J. *Chemical Communications* **2006**, (8), 850−852.

36. Leudtke, N. W.; Hwang, J. S.; Glazer, E. C.; Gut, D.; Kol, M.; Tor, Y. *Chembiochem* **2002**, *3* (8), 766−771.

37. Luedtke, N. W.; Hwang, J. S.; Nava, E.; Gut, D.; Kol, M.; Tor, Y. *Nucleic Acids Research* **2003**, *31* (19), 5732−5740.

38. Chouai, A.; Wicke, S. E.; Turro, C.; Bacsa, J.; Dunbar, K. R.; Wang, D.; Thummel, R. P. *Inorganic Chemistry* **2005**, *44* (17), 5996−6003.

39. Friedman, A. E.; Chambron, J. C.; Sauvage, J. P.; Turro, N. J.; Barton, J. K. *Journal of the American Chemical Society* **1990**, *112* (12), 4960−4962.

40. Jenkins, Y.; Friedman, A. E.; Turro, N. J.; Barton, J. K. *Biochemistry* **1992**, *31* (44), 10809−10816.

41. Gellerman, G.; Babad, M.; Kashman, Y. *Tetrahedron Letters* **1993**, *34* (11), 1827−1830.

42. Gellerman, G.; Rudi, A.; Kashman, Y. *Tetrahedron Letters* **1993**, *34* (11), 1823−1826.

43. Gellerman, G.; Rudi, A.; Kashman, Y. *Tetrahedron* **1994**, *50* (45), 12959−12972.

44. Bergman, S. D.; Kol, M. *Inorganic Chemistry* **2005**, *44* (6), 1647−1654.

45. Bergman, S. D.; Reshef, D.; Frish, L.; Cohen, Y.; Goldberg, I.; Kol, M. *Inorganic Chemistry* **2004**, *43* (13), 3792−3794.

46. Chow, C. S.; Barton, J. K. *Methods in Enzymology* 1992, *212*, 219−242.

47. Pyle, A. M.; Long, E. C.; Barton, J. K. *Journal of the American Chemical Society* **1989**, *111* (12), 4520−4522.

48. Lim, M. H.; Lau, I. H.; Barton, J. K. *Inorganic Chemistry* **2007**, *46*, 9528−9530.

49. Jackson, B. A. Thesis, California Institute of Technology, Pasadena, CA, **2001**.

50. Hart, J. R. Thesis, California Institute of Technology, Pasadena, CA, **2006**.

51. Garbett, N. C.; Chaires, J. B. Binding: A polemic and rough guide. In *Biophysical Tools for Biologists: Vol 1 in Vitro Techniques*, Elsevier Academic Press Inc: San Diego, **2008**, Vol. 84, 3−23.

52. Dupureur, C. M.; Barton, J. K. *Journal of the American Chemical Society* **1994**, *116* (22), 10286−10287.

CHAPTER 5: METALLOINSERTION AT ABASIC SITES AND SINGLE BASE BULGES IN DNA[Φ]

5.1: INTRODUCTION

The maintenance of genomic integrity is critical to cellular health. However, a wide variety of agents, ranging from genotoxic chemicals to error-prone cellular polymerases, render DNA dangerously susceptible to damage and mutation.[1] The types of DNA defects are as varied as their causative agents, yet the most common forms are single base mismatches, abasic sites, single base bulges, and oxidized bases. Left unrepaired, all of these defects can lead to deleterious mutations, often in the form of single nucleotide polymorphisms.[2] To counter these threats, the cell has evolved complex DNA repair machineries, most notably the mismatch repair (MMR)[3−5] and base excision repair (BER)[6] pathways. Under normal conditions, the MMR (mismatches and single base bulges) and BER (abasic sites and oxidized bases) machineries will quickly and efficiently repair their target defects, thereby preventing any lasting damage to the cell or its genome. However, the suppression or disabling of these pathways is often met with dire consequences: mismatch repair deficiency, for example, has been implicated in 80% of hereditary non-polyposis colon cancers in addition to significant percentages of breast, ovarian, and skin cancers.[3, 7−10] It thus becomes clear that the synthesis and study of molecules able to specifically target these defects may aid in the development of new cancer diagnostics and therapeutics.

[Φ]Adapted from Zeglis, B. M.; Boland, J. A.; Barton, J. K. Targeting abasic sites and single base bulges in DNA with metalloinsertors. *J. Am. Chem. Soc.* **2008**, *130*, 7530−7531 and Zeglis, B. M.; Boland, J. A.; Barton, J. K. Recognition of abasic sites and single base bulges in DNA by a metalloinsertor. *Biochemistry* **2009**, *48*, 839−849.

As we have discussed in the preceding chapters, the design and application of metal complexes capable of specifically targeting one such defect, single base mismatches, have been focuses of our laboratory for over a decade.[11] These metal complexes, most notably $Rh(bpy)_2(chrysi)^{3+}$ (chrysi = chrysene-5,6-quinone diimine) and $Rh(bpy)_2(phzi)^{3+}$ (phzi = benzo[a]phenazine-5,6-quinone diimine) (**Figure 5.1**), bear sterically bulky ligands that are too wide to fit between matched base pairs and thus instead preferentially target thermodynamically destabilized mismatched sites.[12, 13] The compounds are highly specific ($\geq$ 1000-fold) for mispaired sites over matched base pairs and recognize over 80% of mismatches in all possible sequence contexts, with only thermodynamically stable, G-containing mismatches escaping binding altogether.[14–16] Furthermore, the complexes can, upon irradiation with ultraviolet light, promote direct cleavage of the DNA backbone at the binding site.

More recently, crystallography and NMR studies have revealed that these complexes do not bind their target sites via classical intercalation, in which the complex binds from the major groove and increases the base pair rise by stacking an aromatic ligand between intact base pairs. Rather, they employ a unique binding mode that we have termed metalloinsertion, in which the complex binds from the minor groove, ejecting the mismatched bases into the major groove and replacing them in the base stack with the sterically expansive aromatic ligand (**Figure 5.2**).[17, 18] These structural data make quite clear the origin of the correlation between recognition and thermodynamic destabilization: the less stable the mismatch, the easier the ejection of the mismatched bases.

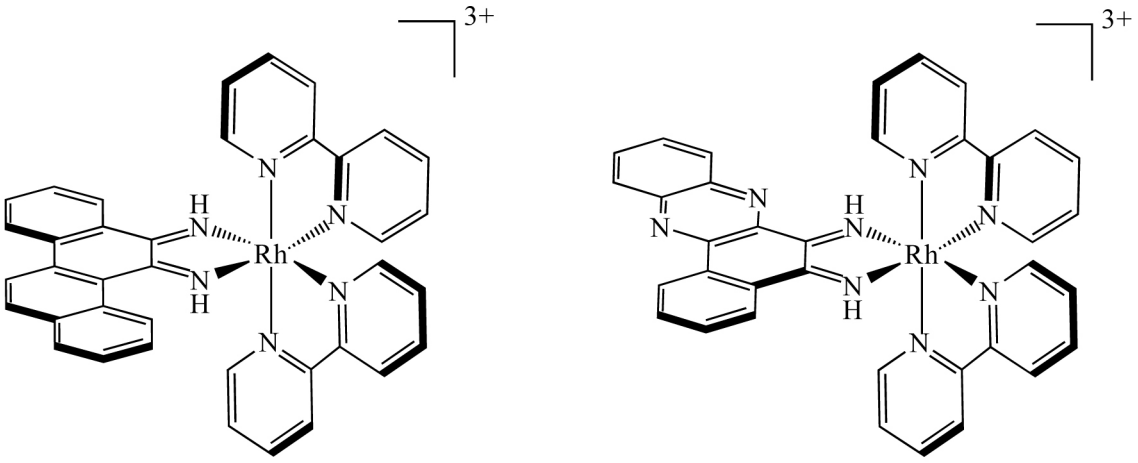

Δ-Rh(bpy)$_2$(chrysi)$^{3+}$ Δ-Rh(bpy)$_2$(phzi)$^{3+}$

Figure 5.1: Structures of two mismatch-specific metalloinsertors. The Δ-enantiomers of Rh(bpy)$_2$(chrysi)$^{3+}$ (left) and Rh(bpy)$_2$(phzi)$^{3+}$ (right) are shown; each complex bears two 2,2'-dipyridine ligands and a sterically expansive inserting ligand.

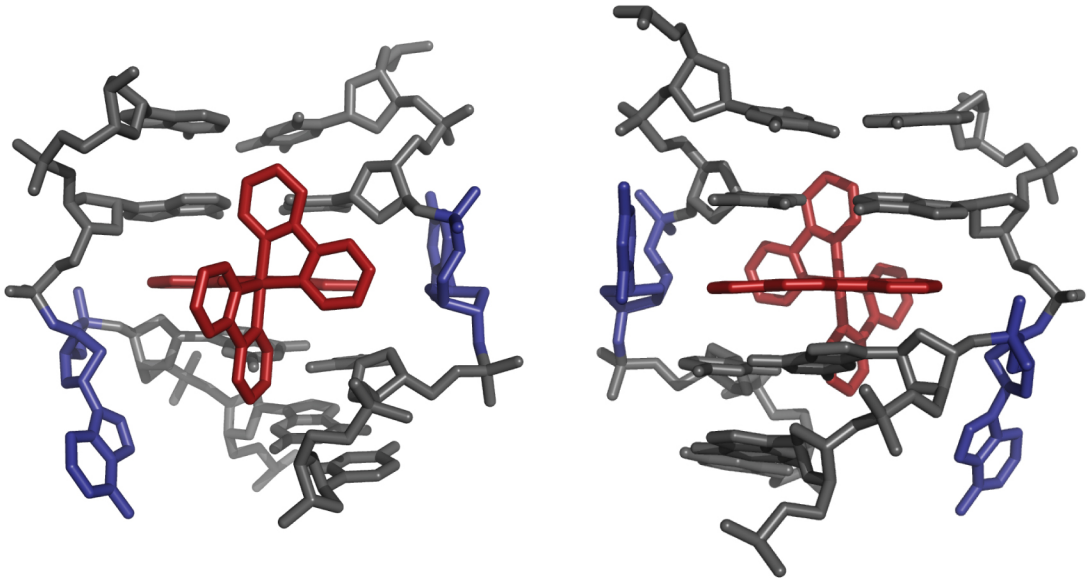

Figure 5.2: Crystal structure of metalloinsertion at a C•A mismatch.[18]
Metalloinsertion of $Rh(bpy)_2(chrysi)^{3+}$ at a C•A mispair as viewed from the minor (left) and major (right) sides of the duplex; the metal complex approaches the DNA from the minor groove, ejects the mispaired bases, and replaces them in the π-stack with the sterically expansive chrysi ligand.

Yet mismatches are not the only destabilizing DNA defect. Indeed, far from it. Consequently, the relationship between thermodynamic instability and metalloinsertor binding has led our laboratory to investigate the recognition of two different DNA defects: abasic sites and single base bulges.

Abasic sites arise from the cleavage of the glycosidic bond between the ribose and the nucleobase. This can occur spontaneously, as a result of exogenous agents, or as an intermediate in the BER pathway (**Figure 5.3**).[19, 20] Regardless of their source, abasic sites are among the most common DNA defects *in vivo*. Understandably, the exact numbers have proven difficult to predict and even harder to determine experimentally; however, data from *in vitro* studies have suggested that in human cells, as many as 10,000 abasic sites per cell cycle can be formed by spontaneous depurination *alone*.[21]

In the cell, abasic sites exist as a 40:60 mixture of α- and β-hemiacetal anomers in equilibrium with a minor ring-opened aldehylic form that represents less than 1% of total sites (**Figure 5.4a**).[22] Just as important to the structure of the defect site, however, is the unpaired base complementary to the abasic ribose. Numerous structural studies have shown that the conformation of this unpaired base can be extra- or intrahelical depending upon its identity and that of the surrounding bases (**Figure 5.5a**).[23−28] Unpaired purines are almost always intrahelical, whereas unpaired pyrimidines likely exist in equilibrium between extrahelical and intrahelical forms, with the extrahelical form favored when the base is flanked by other pyrimidines. Relative to intact duplex DNA, duplexes containing abasic sites are thermodynamically destabilized by 3−11 kcal/mol.[29, 30] Both the sequence context and the identity of the unpaired base play roles in the magnitude of the

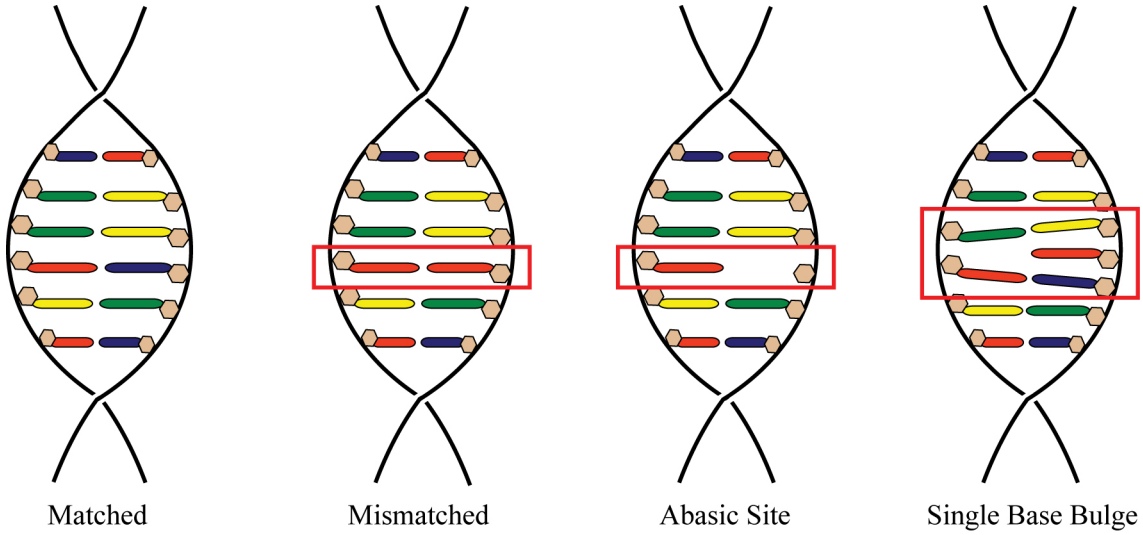

Figure 5.3: Schematic illustration of DNA defect sites. While both abasic sites and single base bulges are characterized by an unpaired base, the local environment of said base differs considerably in each case.

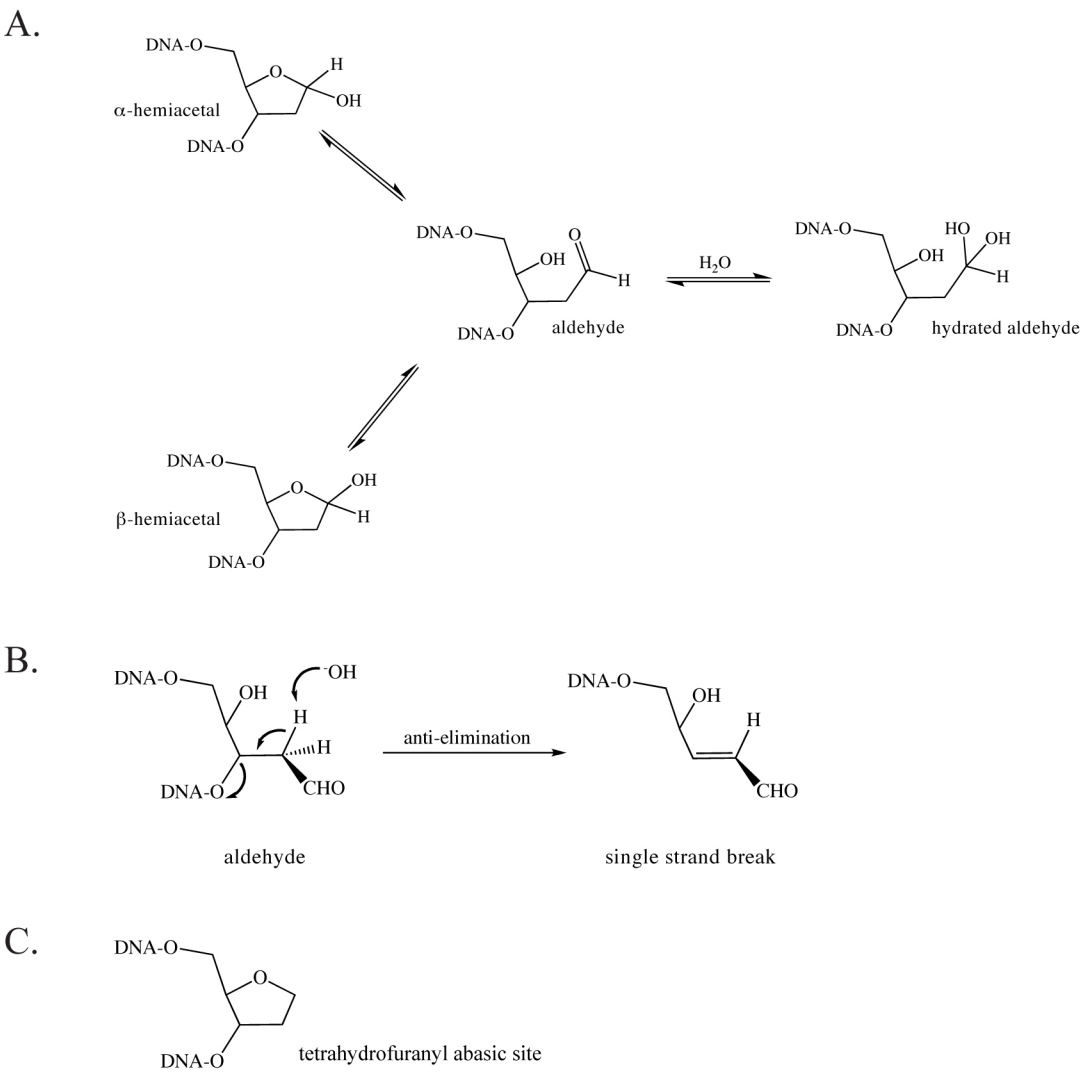

Figure 5.4: The structure and chemistry of abasic sites. (A) Illustration of the equilibrium of abasic sites between the two major hemiacetal anomers and the minor aldehylic and hydrated aldehylic forms. (B) The anti-elimination mechanism of single strand break formation at an aldehylic abasic site. (C) The synthetic tetrahydrofuranyl abasic site

destabilization. Sites in which the abasic ribose is flanked by purines are more stable than those flanked by pyrimidines, and, to a lesser degree, sites with unpaired purines are more stable than those with unpaired pyrimidines.

Single base bulges are defects in which a nucleotide is inserted in one strand of an otherwise well matched duplex (**Figure 5.3**). Caused by errors in recombination and replication, these sites are more thermodynamically stable than abasic sites, with destabilizations ranging from 0−3 kcal/mol.[31] Recent computational and spectroscopic studies have shown that while bulged base identity and sequence context certainly influence the destabilization of the site, reliable patterns such as those for abasic sites do not exist.[32, 33] Several structural studies have shown that the unpaired base may be intra- or extrahelical (**Figure 5.5b**).[34−41] Similar to the case for abasic sites, unpaired purines are almost always intrahelical, whereas an equilibrium between intra- and extrahelical conformations is likely for unpaired pyrimidines. Further, unpaired bases flanked by purines are more likely to remain intrahelical than those surrounded by pyrimidines. Regardless of unpaired base helicity, all duplexes with single base bulges are bent relative to well-matched DNA.

Under normal conditions, abasic sites and single base bulges are repaired through the BER and MMR pathways, respectively. However, if left unrepaired, both lesions represent significant threats to cell viability. Abasic sites can lead to single nucleotide polymorphisms, block transcription, inhibit DNA replication, and act as potent topoisomerase poisons.[19, 20, 42] Single base bulges, in contrast, are a very common source of frame-shift mutations.[43] Indeed, deficiency in the repair of both types of defects has been associated with several different cancers. MMR-deficiency (*vide supra*) has been

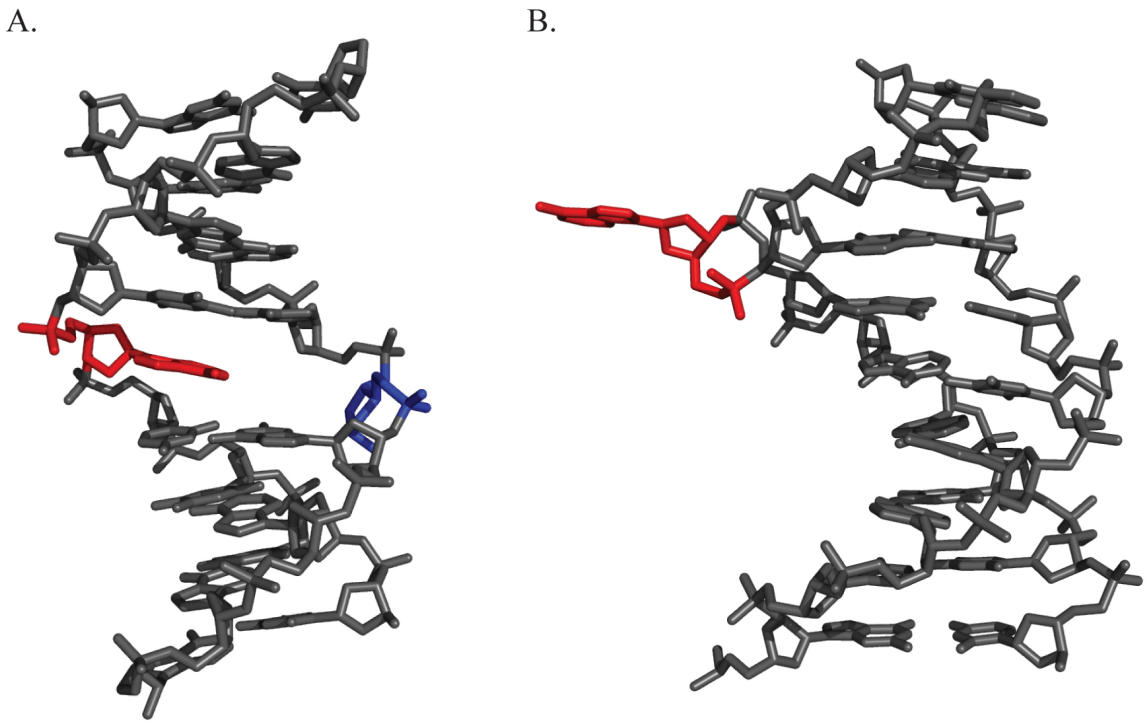

Figure 5.5: Structures of an abasic site and a single base bulge. (A) The NMR solution structure of an intrahelical adenosine opposite an abasic site.[27] (B) The X-ray crystal structure of an extrahelical adenosine single base bulge[36]; it is important to note that while this bulged adenosine adopts an extrahelical conformation, most solution evidence suggests that bulged purines adopt intrahelical conformations.

linked to hereditary non-polyposis colon, ovarian, breast, and skin cancers, while BER-deficiency has been implicated in types of colorectal and gastric cancers.[6, 44, 45]

Given these well-established links to cancer, it is not surprising that agents that recognize these lesions have already been designed and studied (**Figure 5.6**). Methodologies for the targeting of abasic sites include organic base substitute-intercalator conjugates[46] and nucleophilic amines that react with the minor aldehylic form of the natural abasic site.[47] Bulge recognition agents present a more diverse picture: naphthyridine derivatives[48–50], octahedral cobalt complexes[51], and dinuclear ruthenium compounds[52, 53] have all been shown to bind single or multiple base bulges along with DNA hairpins. Of particular interest here is the anti-tumor drug neocarzinostatin chromophore (NCS-Chrom, **Figure 5.6e)**, a member of the enediyne family of molecules.[54–57] NCS-Chrom binds single base bulges in duplex DNA via the minor groove with promising specificity and, upon activation with thiol, undergoes a transformation to a reactive biradical species that can cleave the DNA at the binding site. The success of NCS-Chrom not withstanding, almost all of these recognition agents exhibit affinities, specificities, or reactivities that are less than ideal for diagnostic or therapeutic applications.

Our investigation of metalloinsertors for abasic site and single base bulge recognition is thus motivated both by the desire to augment our understanding of the recognition of DNA lesions by metal complexes and by the opportunity to create useful diagnostic agents for the detection of these two deleterious defects.

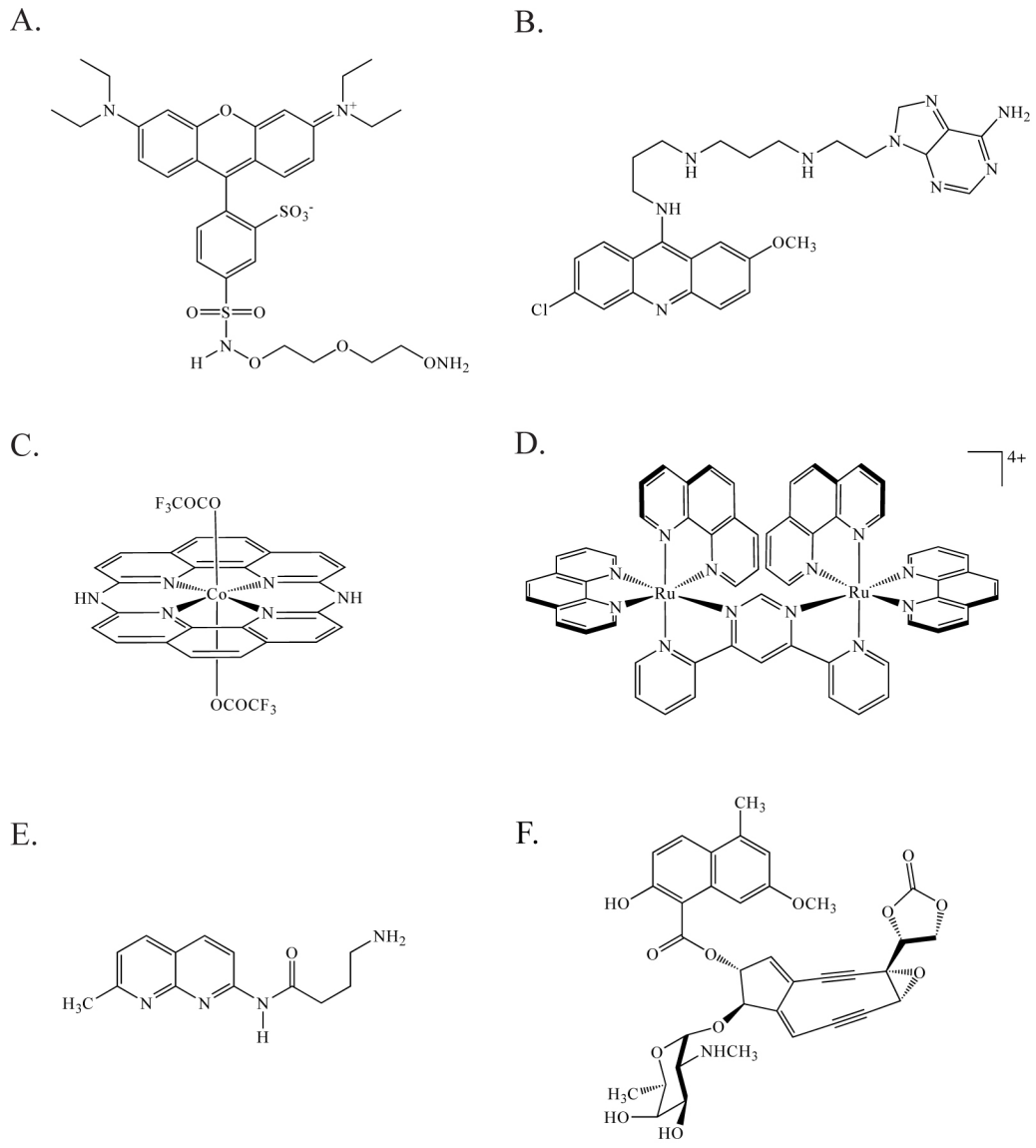

Figure 5.6: Abasic site and bulge recognition agents. For abasic sites: (A) fluorophore-conjugated nucleophilic amine[47]; (B) base analogue-intercalator conjugate[46]. For bulges: (C) octahedral cobalt complex[51]; (D) dinuclear ruthenium polypyridyl complex[52]; (E) naphthyridine derivative[49]; (F) neocarzinostatin chromophore[56]

5.2: RESULTS

5.2.1: SEQUENCE DESIGN AND MELTING TEMPERATURE ANALYSIS

A series of oligonucleotides was synthesized and purified to allow for the interrogation of abasic sites and single base bulges in variable sequence contexts and with all possible unpaired bases. The 27-mer single strands are identical except for a central six base region in which the sequence variation occurs. Four different oligonucleotides containing synthetic abasic sites were designed, each placing the abasic site in a different sequence context: 5'-GΦT-3' (AB1), 5'-GΦA-3' (AB2), 5'-AΦG-3' (AB3), and 5'-TΦC-3' (AB4) (**Table 5.1**). For each abasic strand, four complements were prepared. Each positions a different base complementary to the abasic site: for example, 3'-C*A*A-5' (AB1-A), 3'-C*C*T-5' (AB2-C), 3'-T*G*C-5' (AB3-G), and 3'-A*T*G-5' (AB4-T). These oligonucleotides, taken together, allow us to examine the recognition of abasic sites in the three major sequence context types (5'-PurΦPur-3', 5'-PyrΦPur-3', 5'-PyrΦPyr-3') with all possible opposing unpaired bases. For purposes of comparison, matched and mismatched strands were also created for each sequence context; complementary in each case to the AB#-C strand, these oligonucleotides create either a fully matched duplex or one containing a central C•C mismatch.

Four additional oligonucleotides were synthesized to facilitate the study of single base bulges (**Table 5.2**). These, termed B1−B4, are identical to the AB# strands in all respects except that they lack the tetrahydrofuranyl abasic site. Thus, when these 26-mers are annealed to the 27-mer complements of the abasic oligonucleotides, duplexes with single base bulges are formed. In each case, the nucleotide formerly complementary to the abasic site is now the bulged base: for example, 3'-C*T*A-5' (B1-T), 3'-C*A*T-5' (B2-

A), 3’-T*C*C-5’ (B3-C), and 3’-A*G*G-5’ (B4-G). The same sets of matched and mismatched duplexes were employed as controls. In all, 32 oligonucleotides forming 28 unique duplexes were created.

Melting temperature analysis of the DNA allows us to determine the relative thermodynamic destabilization to the duplex created by each lesion. All four matched duplexes have melting temperatures around 64 °C. Relative to these, the mismatched duplexes are destabilized by 7−8 °C. Duplexes containing single base bulges are similarly destabilized, if not slightly more stable, with melting temperatures 6−8 °C lower than that of the corresponding matched duplex. In contrast, duplexes containing abasic sites are even less stable than their mismatched counterparts, with melting temperatures reduced by 8−11 °C. Taken together, these ΔT_m values are in agreement with the published literature It is somewhat surprising, however, that within the family of abasic duplexes, we do not see significant variation in ΔT_m based upon sequence context or unpaired base identity. This result is more likely a product of instrument sensitivity than an indicator of the absence of such influences on site stability. Nonetheless, these measurements plainly illustrate the relative stabilities of the sites at hand: abasic site < mismatched base pair < single base bulge << matched base pair.

Sequence	Seq. Variation[a]	Context	Recognition[b]	$K_B(10^6\ M^{-1})$[c]	T_m(°C)[d]
AB1-M	GGGTGA CCCACT	–	–	–	64.5
AB1-MM	GGCTGA CCCACT	5′-PurCPyr-3′ 3′-PyrCPur-5′	Yes	2.2(2)	57.0
AB1-X	GGΦTGA[e] CCXACT[f]	5′-PurΦPyr-3′ 3′-PyrXPur-5′	X = A: Yes, C: Yes, G: Yes, T: Yes	A: 1.3(1) C: 2.3(5) G: 1.4(2) T: 3.9(6)	A: 56.0 C: 56.0 G: 57.0 T: 55.5
AB2-M	GGATGA CCTACG	–	–	–	64.0
AB2-MM	GCATGA CCTACT	5′-PurCPur-3′ 3′-PyrCPyr-5′	Yes	1.7(2)	56.5
AB2-X	GΦATGA CXTACT	5′-PurΦPur-3′ 3′-PyrXPyr-5′	X = A: Yes, C: Yes, G: Yes, T: Yes	A: 2.1(1) C: 2.6(5) G: 1.4(5) T: 3.5(3)	A: 54.0 C: 53.5 G: 55.0 T: 54.5
AB3-M	GGAGGA CCTCCT	–	–	–	64.0
AB3-MM	GGACGA CCTCCT	5′-PurCPur-3′ 3′-PyrCPyr-5′	No	–	56.0
AB3-X	GGAΦGA CCTXCT	5′-PurΦPur-3′ 3′-PyrXPyr-5′	X = A: No, C: No, G: No, T: No	–	A: 55.5 C: 55.0 G: 56.0 T: 56.0
AB4-M	TGCTGA ACGACT	–	–	–	64.0
AB4-MM	TCCTGA ACGACT	5′-PyrCPyr-3′ 3′-PurCPur-5′	Yes	2.5(3)	56.0
AB4-X	TΦCTGA AXGACT	5′-PyrΦPyr-3′ 3′-PurXPur-5′	X = A: Yes, C: Yes, G: Yes, T: Yes	A: 1.2(3) C: 2.9(4) G: 1.7(1) T: 3.1(5)	A: 54.5 C: 53.5 G: 54.5 T: 53.0

a. Sequence within variable region of 5′-GAC TTA TCT AG*N NNN NN*T AAG CTG GTC-3′ (top) and complement (bottom).
b. Determined by photocleavage assay employing 1 μM $Rh(bpy)_2(chrysi)^{3+}$ and 1μM duplex DNA in buffer (50 mM NaCl, 10 mM NaPi, pH 7.1).
c. Measured via binding titration experiment using 1 μM duplex DNA and variable concentrations (0-20 μM) of $Rh(bpy)_2(chrysi)^{3+}$ in buffer.
d. Determined with UV-Visible spectrophotometry employing 1 μM duplex DNA in buffer. Accurate within 1 °C.
e. Φ denotes tetrahydrofuranyl abasic site.
f. X denotes base complementary to abasic site.

Table 5.1: Sequence and recognition information for abasic assemblies

Sequence[a]	Seq. Variation[b]	Context	Recognition[c]	T_m (°C)[d]
B1-X	GG TGA CC X ACT[e]	5′-Pur Pyr-3′ 3′-Pyr Pur-5′ X	X = A: No C: Yes G: Yes T: Yes	A: 58.0 C: 59.0 G: 59.0 T: 59.0
B2-X	G ATGA C X TACT	5′-Pur Pur-3′ 3′-Pyr Pyr-5′ X	X = A: Yes C: Yes G: Yes T: Yes	A: 56.0 C: 57.0 G: 57.5 T: 57.5
B3-X	GGA GA CCT X CT	5′-Pur Pur-3′ 3′-Pyr Pyr-5′ X	X = A: No C: No G: No T: No	A: 55.5 C: 55.0 G: 56.0 T: 56.0
B4-X	T CTGA A X GACT	5′-Pyr Pyr-3′ 3′-Pur Pur-5′ X	X = A: No C: No G: No T: No	A: 57.0 C: 56.4 G: 57.0 T: 57.0

a. Data for the corresponding matched and mismatched strands (e.g. AB1-M and AB1-MM for B1-X) can be found in Table 1.
b. Sequence within variable region of 5′-GAC TTA TCT AG*N NNN NN*T AAG CTG GTC-3′ (top) and complement (bottom). The complement contains the bulged base.
c. Determined by photocleavage assay employing 5 μM $Rh(bpy)_2(chrysi)^{3+}$ and 1μM duplex DNA in buffer (50 mM NaCl, 10 mM NaPi, pH 7.1).
d. Determined with UV-Visible spectrophotometry employing 1 μM duplex DNA in buffer. Accurate within 1 °C.
e. X denotes the bulged base.

Table 5.2: Sequence and recognition information for single base bulge assemblies

5.2.2: Recognition of abasic sites by $Rh(bpy)_2(chrysi)^{3+}$

Polyacrylamide gel electrophoresis experiments clearly indicate that $Rh(bpy)_2(chrysi)^{3+}$ specifically recognizes and photocleaves abasic sites in DNA (**Figure 5.7**). Indeed, the metalloinsertor binds and promotes strand scission at lesion sites in all sequence context types (5'-PurΦPur-3', 5'-PurΦPyr-3', and 5'-PyrΦPyr-3') and with all possible unpaired bases. No photocleavage is observed in the absence of metalloinsertor or with well-matched DNA. In total, twelve of the sixteen abasic sites are bound and cleaved. Specifically, the abasic sites in duplexes AB1, AB2, and AB4 are recognized and cleaved regardless of unpaired base identity; surprisingly, however, no photocleavage is observed for the AB3 duplexes. This pattern corresponds precisely to that observed for the strands bearing a central C•C mismatch: AB1-MM, AB2-MM and AB4-MM are all bound and cleaved, while AB3-MM escapes binding and scission. That the AB3 duplexes are not bound and cleaved is certainly not a consequence of the sequence context type; the AB2 duplexes, like the AB3 assembles, place the abasic site in a 5'-PurΦPur-3' sequence context and are, in fact, cleaved quite readily. The answer likely lies in the sensitivity of metalloinsertors to specific sequence contexts. Similar effects of sequence context have been seen previously for the family of complexes with mismatched duplexes.[11] Indeed, experiments employing higher rhodium concentrations and longer irradiation times suggest that $Rh(bpy)_2(chrysi)^{3+}$ does bind and cleave the abasic sites in the AB3 duplexes, just not nearly as strongly or efficiently as those in the other sequence contexts.

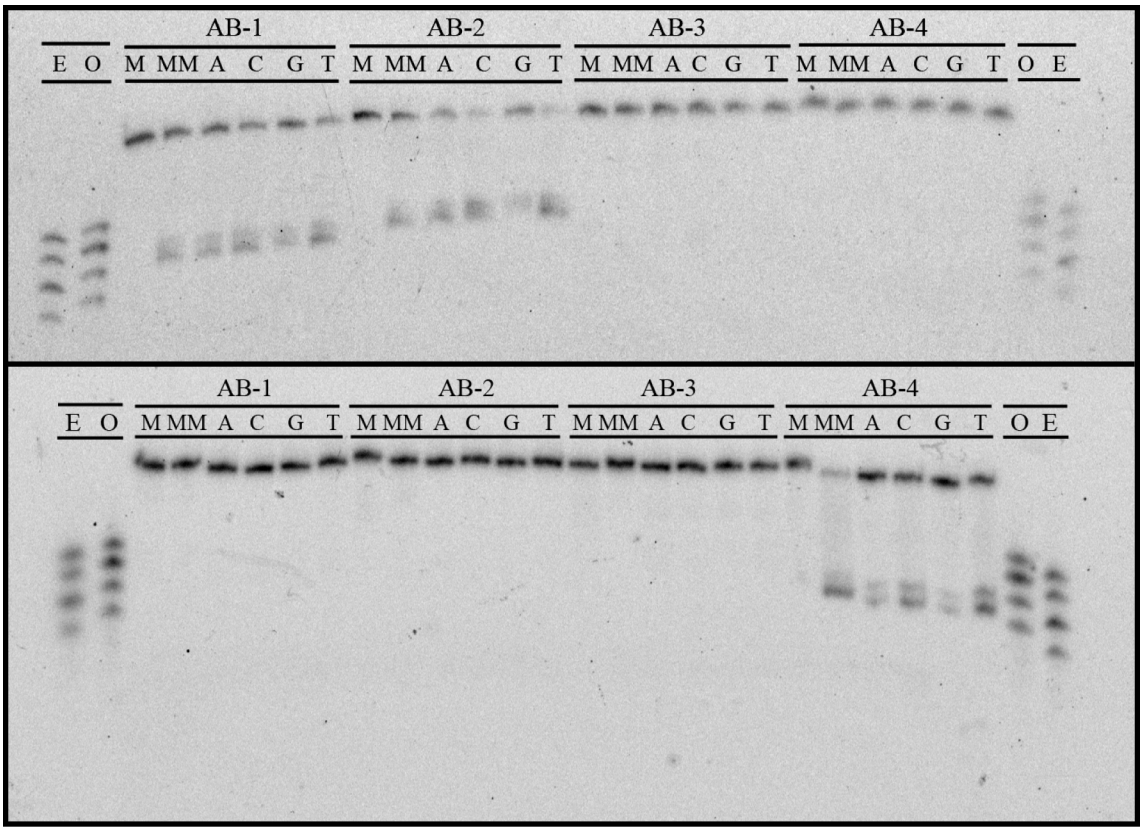

Figure 5.7: Abasic site recognition and photocleavage gel. PAGE assay illustrating the recognition and photocleavage of mismatch and abasic site recognition. Sequence contexts are listed along top line of each gel, and individual duplexes are indicated in the second line (M = matched, MM = mismatched, A = unpaired adenine, C = cytosine, G = guanine, and T = thymine). In the top gel, the single strand beginning 5'-GAC CAG … (that containing the unpaired base in the abasic assemblies) is 5'-^{32}P-labeled. In the bottom gel, the single strand beginning 5'-GAC TTA … (that containing the abasic site) is 5'-^{32}P-labeled. In both experiments, 1 μM duplex was incubated with $Rh(bpy)_2(chrysi)^{3+}$ in 50 mM NaCl, 10 mM NaPi, pH 7.1. Samples were irradiated for 10 min on an Oriel Instruments solar simulator (320−440 nm emission) and incubated for 30 min at 60 °C prior to electrophoresis. "E" and "O" denote lanes containing even (10, 12, 14, 16) and odd (11, 13, 15, 17) standardization fragments.

Photocleavage experiments also reveal interesting patterns in the strand asymmetry of scission. Regardless of the identity of the unpaired base, duplexes AB1 and AB2 are cleaved on the strand containing the unpaired nucleotide. Interestingly, however, duplex AB4 is cleaved instead on the strand containing the tetrahydrofuranyl abasic site, again irrespective of the unpaired base. This behavior exactly mirrors the photocleavage observed in the analogous mismatched duplexes. While, of course, the mismatched duplexes contain no unpaired bases or abasic sites, the AB1-MM and AB2-MM assemblies are cleaved on the strand corresponding to that containing an unpaired base in the abasic duplexes, and the AB4-MM assembly is cleaved on the strand corresponding to that containing the abasic site in the abasic duplex. This observation must reflect the binding architecture of the complex in the abasic site (see Discussion).

Another important similarity between photocleavage at mismatch and abasic sites is the length of the scission products. Regardless of unpaired base identity, AB1 cleavage fragments are 14 base pairs long, AB2 fragments 15 base pairs long, and AB4 fragments 13 base pairs long. These fragments correspond to cleavage at the ribose 3' to the unpaired base in duplexes AB1 and AB2 and at the ribose 3' to the abasic site in the AB4 duplexes. Importantly, photocleavage at the C•C mismatch in each duplex produces fragments of analogous lengths.

5.2.3: Recognition of abasic sites by $Rh(bpy)_2(phzi)^{3+}$

In order to probe the generality of metalloinsertor recognition of abasic sites, photocleavage experiments were also performed using $Rh(bpy)_2(phzi)^{3+}$, a second generation complex with a heterocyclic bulky ligand (**Figure 5.1**). $Rh(bpy)_2(phzi)^{3+}$ is

clearly able to both recognize and, upon irradiation, cleave the representative abasic sites (**Figure 5.8**). Again, no recognition or photocleavage is observed in the absence of metalloinsertor or DNA defect. Significantly, photocleavage with $Rh(bpy)_2(phzi)^{3+}$ is observed at much lower concentrations (100 nM) than with $Rh(bpy)_2(chrysi)^{3+}$, a characteristic also observed for mismatch photocleavage and attributed to the added π-stacking capabilities of the heterocyclic inserting ligand.

5.2.4: BINDING AFFINITIES OF $RH(BPY)_2(CHRYSI)^{3+}$ FOR ABASIC SITES

Photocleavage titration experiments were employed to determine site-specific binding constants for the twelve abasic sites and three mismatches for which photocleavage was observed (**Figure 5.9** shows a representative titration, see also **Table 5.1**). The binding constants for the mismatched sites, 2.2(2) x 10^6 M^{-1} (AB1-MM), 1.7(2) x 10^6 M^{-1} (AB2-MM), 2.5(3) x 10^6 M^{-1} (AB4-MM), are comparable to those previously reported for C•C mismatches.[11] Since metalloinsertor binding affinity correlates directly to site destabilization, it is not surprising that the binding constants of $Rh(bpy)_2(chrysi)^{3+}$ for abasic sites are similar to if not somewhat greater than those for the most destabilizing (e.g., C•C) mismatches.

Despite probable differences in site destabilization between the three different sequence contexts, little variation is observed in the affinity values, a result that suggests a threshold behavior in the relationship between destabilization and binding affinity. Such behavior has previously been suggested for mismatch binding.[11] Small differences, however, do appear based on the identity of the unpaired base within a single sequence

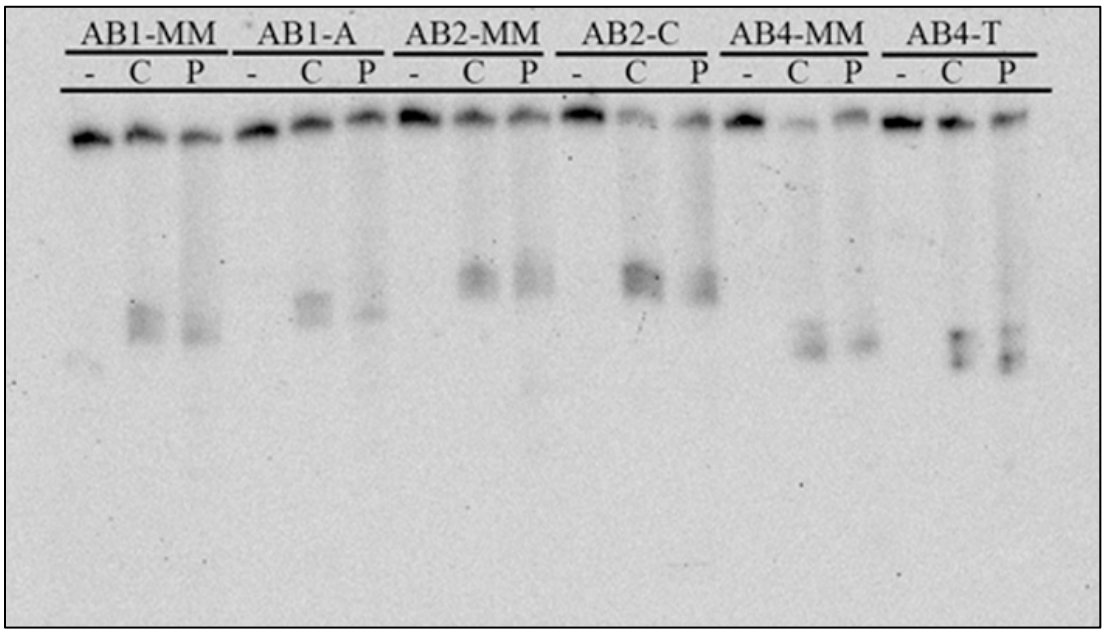

Figure 5.8: Recognition of abasic sites with $Rh(bpy)_2(phzi)^{3+}$. PAGE assay illustrating the recognition and photocleavage of mismatches and abasic sites by $Rh(bpy)_2(chrysi)^{3+}$ and $Rh(bpy)_2(phzi)^{3+}$. 1 μM duplex was incubated without metal complex (lanes marked "–") , with 1 μM $Rh(bpy)_2(chrysi)^{3+}$ (lanes marked "C"), or with 100 nM $Rh(bpy)_2(phzi)^{3+}$ (lanes marked "P") in 50 mM NaCl, 10 mM NaPi, pH 7.1. Duplex identity is indicated at the top of the gel. Samples were irradiated for 10 min on an Oriel Instruments solar simulator (320−440 nm emission) and incubated for 30 min at 60 °C prior to electrophoresis.

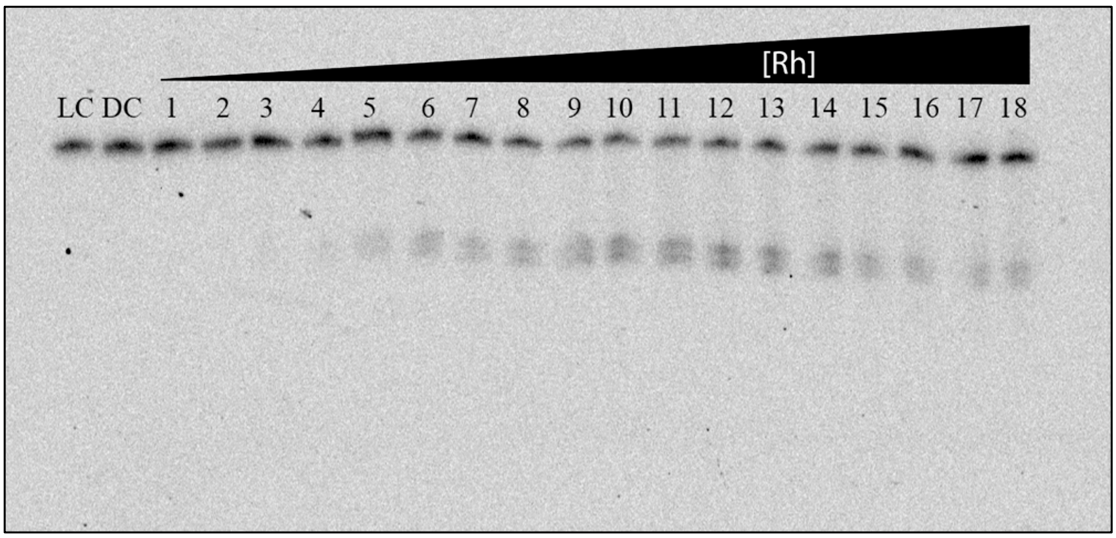

Figure 5.9: Determining the binding constant of $Rh(bpy)_2(chrysi)^{3+}$ for an abasic site. PAGE assay illustrating a typical photocleavage assay for binding constant determination. 1 μM duplex was incubated with increasing concentrations of $Rh(bpy)_2(chrysi)^{3+}$ in 50 mM NaCl, 10 mM NaPi, pH 7.1. The AB1-C duplex was employed for this particular titration. Samples were irradiated for 10 min on an Oriel Instruments solar simulator (320−440 nm emission) and incubated for 30 min at 60 °C prior to gel electrophoresis. LC and DC represent light (no rhodium, 10 min irradiation) and dark (1 μM Rh, no irradiation) controls. Lanes 1−18 contain 50 nM, 100 nM, 200 nM, 300 nM, 400 nM, 500 nM, 600 nM, 700 nM, 800 nM, 1 μM, 2 μM, 3 μM, 4 μM, 5 μM, 7 μM, 9 μM, 13 μM, 15μM, 17.5 μM, 20 μM $Rh(bpy)_2(chrysi)^{3+}$.

context. For example, the values for the AB2 assemblies are 1.4(5) x 10^6 M^{-1} (G), 2.1(1) x 10^6 M^{-1} (A), 2.6(5) x 10^6 M^{-1} (C), and 3.5(3) x 10^6 M^{-1} (T). The metalloinsertor seems to bind abasic sites with unpaired pyrimidines slightly tighter than sites with unpaired purines. These differences are admittedly minor; however, the trend is consistent among the three sequence contexts. An explanation based on the dynamic motions and helicity of the unpaired base in each case is perhaps most likely.

5.2.5: ENANTIOSPECIFICITY OF $Rh(bpy)_2(chrysi)^{3+}$ FOR ABASIC SITES

Photocleavage assays employing Δ-$Rh(bpy)_2(chrysi)^{3+}$ and Λ-$Rh(bpy)_2(chrysi)^{3+}$ clearly indicate that abasic recognition is enantiospecific for the right-handed isomer of the metalloinsertor (**Figure 5.10**). PAGE experiments reveal that concentrations of 1 μM Δ-$Rh(bpy)_2(chrysi)^{3+}$ bind and cleave all abasic sites interrogated, while incubation and irradiation with 1 μM Λ-$Rh(bpy)_2(chrysi)^{3+}$ produces no photocleavage bands. This chiral specificity has been well-documented for the recognition of mismatched sites by metalloinsertors.[62] Recent structural studies of $Rh(bpy)_2(chrysi)^{3+}$ bound to a C•A mismatch have shed light on the question; because the metalloinsertor binds the mismatch site from the narrow, sterically constrictive minor groove, the chirality of complex must match that of the helix to prevent steric clash between the ancillary ligands and the DNA backbone. In short, the right-handed helix can only accommodate the right-handed enantiomer. The observation that the recognition of abasic sites by metalloinsertors is also enantiospecific argues strongly for site binding via the minor groove.

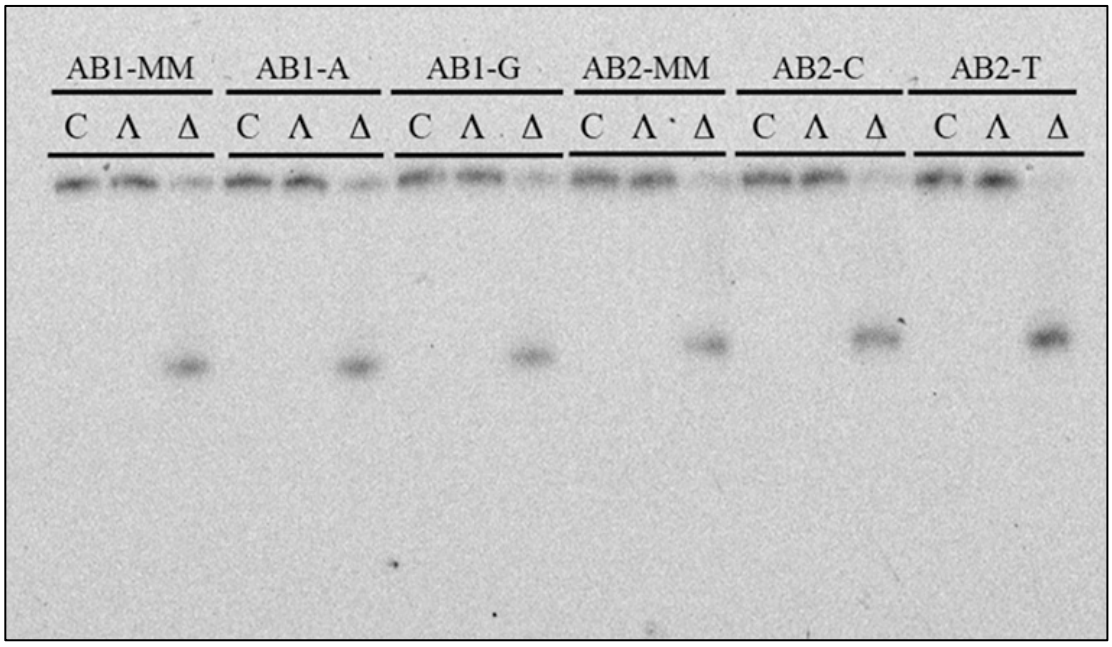

Figure 5.10: The enantiospecificity of abasic site recognition. PAGE assay illustrating the enantioselectivity of mismatch and abasic site recognition. 1 μM duplex was incubated with either Δ-$Rh(bpy)_2(chrysi)^{3+}$, Λ-$Rh(bpy)_2(chrysi)^{3+}$, or no Rh complex at all in 50 mM NaCl, 10 mM NaPi, pH 7.1. Samples were irradiated for 10 min on an Oriel Instruments solar simulator (320−440 nm emission) and incubated for 30 min at 60 °C prior to electrophoresis.

5.2.6: MALDI-TOF analysis of abasic site photocleavage products

While we have predominantly employed gel electrophoresis in our study of the recognition of abasic sites, MALDI-TOF mass spectrometry affords a unique opportunity to investigate not only the site specificity of recognition but also the identity of the individual photocleavage products.[63] A similar investigation has been previously reported for the recognition of mismatched sites. Here, the photocleavage of all 12 cleaved abasic duplexes and their mismatched analogues was investigated. The MALDI-TOF analysis of AB1-C photocleavage provides a suitable example (**Figure 5.11**). In light (no Rh, with irradiation) and dark (Rh, no irradiation) controls, only peaks corresponding to the singly (DNA^{1+}) and doubly (DNA^{2+}) charged parent single strands are observed, m/z = 8198.7 and 4100.3 for AB1 and 8213.2 and 4106.9 for AB1-C. Photocleavage samples reveal three new masses in addition to the parent strands at m/z = 3733.7, 4286.8, and 4475.9. These fragments are consistent with the DNA being cleaved only on the AB1-C strand. We assign the cleavage fragment at m/z = 3733.7 as a 12-mer with a 5'-phosphate group and the product at m/z = 4286.8 as a 14-mer with a 3'-phosphate group. These fragments correspond to common DNA cleavage products and clearly indicate scission on the 3'-side of the unpaired base. The final cleavage fragment, appearing at m/z = 4475.9, corresponds to the aforementioned 14-mer with a 3'-2,3-dehydronucleotide in place of a phosphate. Upon sample incubation for 24 h at 23 °C, however, complete conversion of the dehydronucleotide product to the 3'-phosphate fragment is observed, suggesting that the former is a metastable intermediate.

Analogous results are obtained for all abasic sites that are cleaved on the strand containing the unpaired base. The situation changes only slightly for the AB4 assemblies,

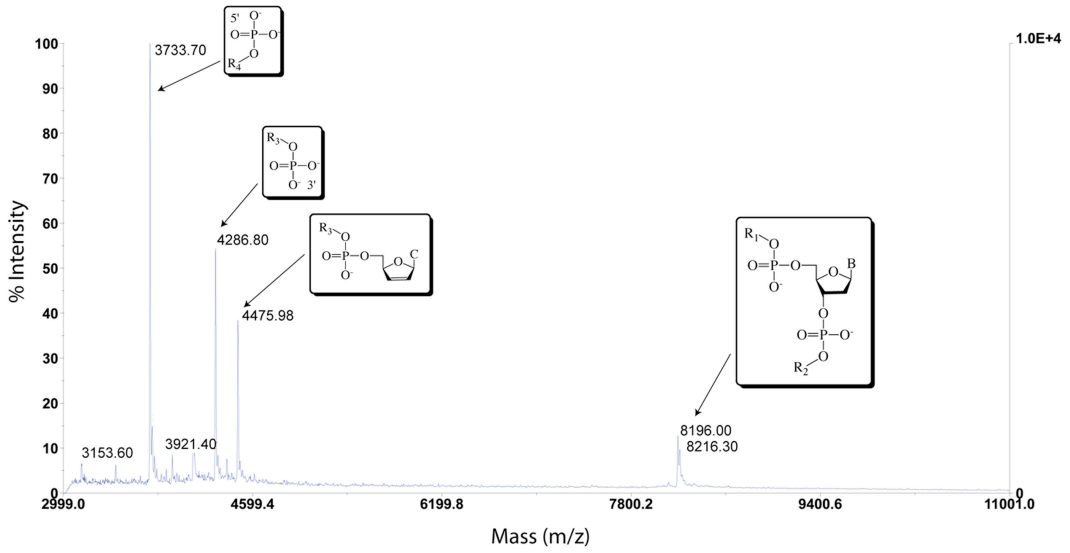

Figure 5.11: Mass spectrometry of abasic site photocleavage products. MALDI-TOF mass spectrograph of photocleavage products of duplex AB1-C, 5'- GAC CAG CTT ATC A*C*C CCT AGA TAA GCG -3' in which the underlined, italicized cytosine is the unpaired complement of an abasic site. The rightmost peaks correspond to the full, uncleaved parent strands. Assigned scission products can be viewed on the left-hand side of the plot and correspond to 5'-PO_4-CCT AGA TAA GCG-3', 5'-GAC CAG CCT ATC A*C*-PO_4-3', and 5'-GAC CAG CCT ATC A*C*-dehydroC-3'. R_1 = GAC CAG CTT ATC A; R_2 = CCC TAG ATA AGC G; R_3 = GAC CAG CCT ATC A*C*; R_4 = CCT AGA TAA GCG; B = cytosine.

in which scission occurs on the strand containing the abasic site; for these duplexes, all of the same cleavage products are observed, but strand scission occurs on the 3' side of the abasic site. Importantly, analogous products are also seen for photocleavage of the mismatched strands. Indeed, exactly the same products are seen for the AB1-C and AB1-MM assemblies (**Figure 5.12)**: strand scission occurs on the 3'-sides of the unpaired cytosine in AB1-C and the corresponding mispaired cytosine in AB1-MM, resulting in identical fragments. Interestingly, unlike previous MALDI-TOF experiments with mismatched sites[18, 63], no furanose products were observed. The same is true for the MALDI-TOF analysis of the abasic assemblies.

Taken together, these mass spectrometry experiments provide a number of key insights. First, the data confirm observations made via gel electrophoresis regarding site specificity, strand asymmetry of scission, and cleavage product length. More important, however, is the light shed on the relationship between the recognition of abasic sites and that of mismatches. As stated above, analogous, and in some cases indistinguishable, products are observed for mismatch and abasic site photocleavage. This result strongly suggests a similar, if not identical, binding mode for metalloinsertors at abasic sites. Furthermore, cleavage product analysis and structural information have indicated that mismatch photocleavage proceeds via an H1'-abstraction mechanism. The results at hand indicate that abasic site strand scission occurs via the same pathway.

5.2.7: Recognition of single base bulges by $Rh(bpy)_2(chrysi)^{3+}$

Compared to abasic sites, single base bulges are recognized less effectively and, when bound, cleaved less efficiently. In fact, out of the sixteen possible single base

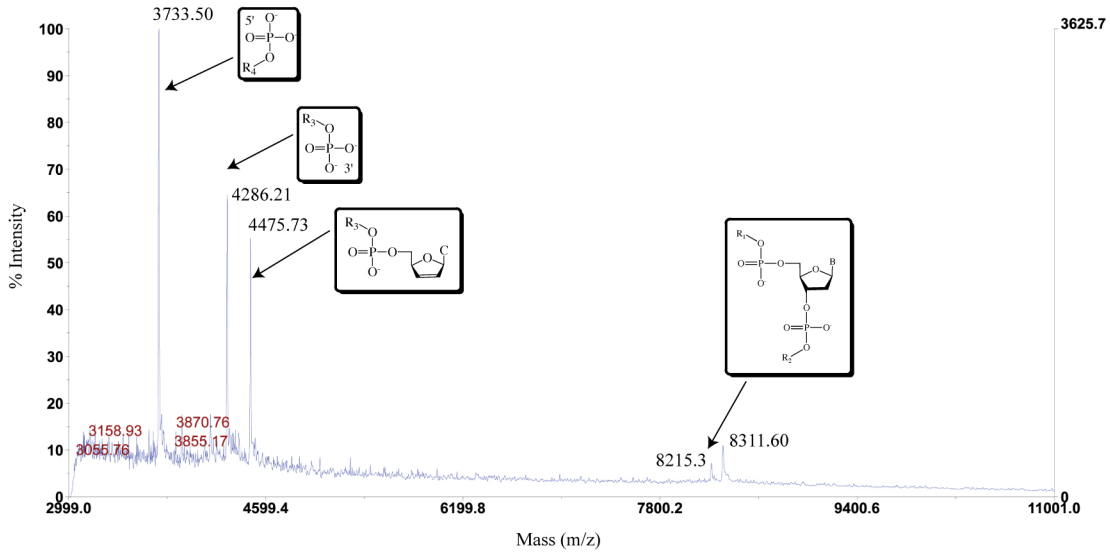

Figure 5.12: Mass spectrometry of mismatch site photocleavage products. MALDI-TOF mass spectrograph of photocleavage products of duplex AB1-MM, 5'- GAC CAG CTT ATC A*C*C CCT AGA TAA GCG -3' in which the underlined, italicized cytosine is the complement of a mismatched C. The rightmost peaks correspond to the full, uncleaved parent strands. Assigned scission products can be viewed on the left-hand side of the plot and correspond to 5'-PO_4-CCT AGA TAA GCG-3', 5'-GAC CAG CCT ATC A*C*-PO_4-3', and 5'-GAC CAG CCT ATC A*C*-dehydroC-3'. R_1 = GAC CAG CTT ATC A; R_2 = CCC TAG ATA AGC G; R_3 = GAC CAG CCT ATC A*C*; R_4 = CCT AGA TAA GCG; B = cytosine.

bulges in this investigation, only seven were recognized and cleaved: B1-C, B1-G, B1-T, B2-A, B2-C, B2-G, and B2-T (**Figure 5.13**). Furthermore, in some cases, even faint bulge photocleavage bands required longer irradiation times (20−30 min, compared to 10 min for substantial abasic site cleavage). Based on comparison to shorter labeled oligonucleotides, the bulge photocleavage fragments appear to be 14 bases long for the B1 duplexes and 15 bases long for the B2 duplexes, indicating strand scission on the 3'-side of the bulged base. However, the low photocleavage efficiency at single base bulges precludes the accurate determination of binding affinities. Based on photocleavage titrations and qualitative observations, however, it is evident that in each case the metalloinsertor binding affinity is ~10^5 M^{-1}.

Both sequence context and bulged base identity appear to play roles in recognition. Single base bulges in the B3 and B4 sequence contexts escape binding and photocleavage *in toto*, whereas all of the bulges in the B2 sequence context are recognized and cleaved to some extent. The recognition of single base bulges in the B1 sequence context seems to be dependent upon the identity of the bulged base; the bulged cytosine, guanine, and thymine are cleaved, whereas the bulged adenine is not. Proffering an explanation for this behavior proves difficult, especially without the aid of simple trends for the thermodynamic destabilization of singe base bulge sites (see DISCUSSION).

Despite the lack of generality in the recognition of single base bulges, the initial photocleavage assays and subsequent experimentation do provide some insight into how the metalloinsertor may bind these sites. First, the strand asymmetry and cleavage product length of single base bulge scission match those of photocleavage at mismatched

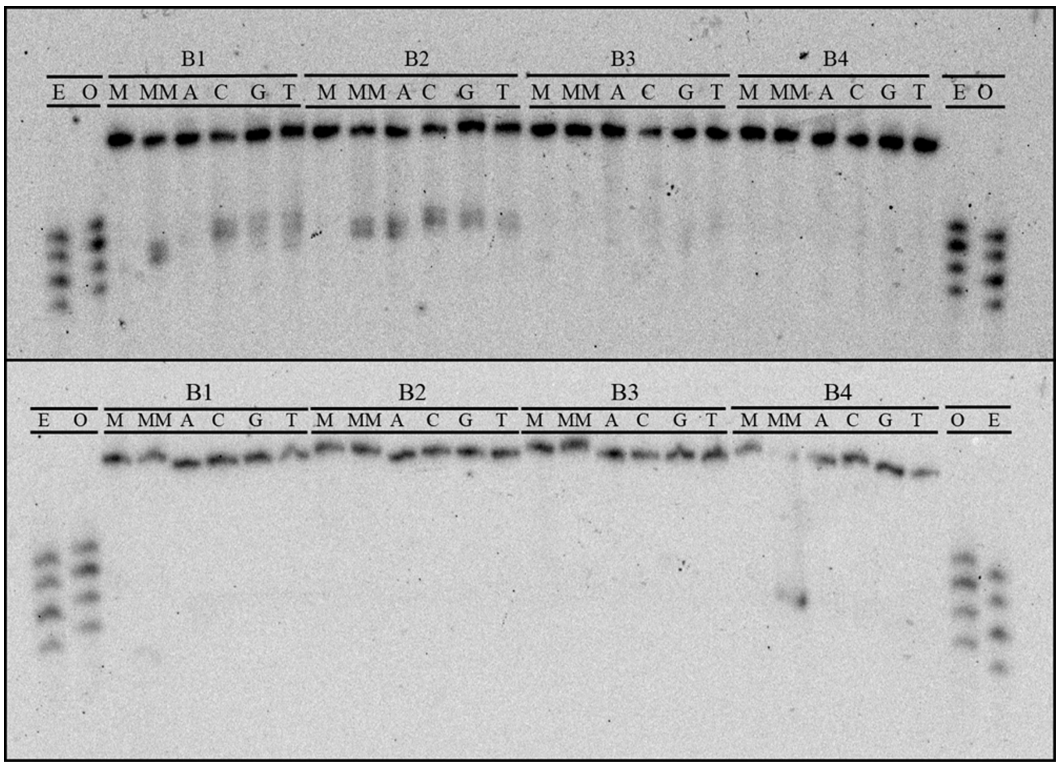

Figure 5.13: Single base bulge recognition and photocleavage gel. PAGE assay illustrating the recognition and photocleavage of mismatch and single base bulge recognition. Sequence contexts are listed along top line of each gel, and individual duplexes are indicated in the second line (M = matched, MM = mismatched, A = bulged adenine, C = cytosine, G = guanine, and T = thymine). In the top gel, the single strand beginning 5'-GAC CAG … (that containing the bulged base in SBB assemblies) is 5'-^{32}P-labeled. In the bottom gel, the single strand beginning 5'-GAC TTA … is 5'-^{32}P-labeled. In both experiments, 1 μM duplex was incubated with $Rh(bpy)_2(chrysi)^{3+}$ in 50 mM NaCl, 10 mM NaPi, pH 7.1. Samples were irradiated for 30 min on an Oriel Instruments solar simulator (320−440 nm emission) and incubated for 30 min at 60 °C prior to electrophoresis. "E" and "O" denote lanes containing even (10, 12, 14, 16) and odd (11, 13, 15, 17) standardization fragments.

sites. Second, photocleavage assays employing Δ- and Λ-$Rh(bpy)_2(chrysi)^{3+}$ clearly indicate that bulge recognition is enantiospecific for the right-handed isomer of the metalloinsertors. Third, MALDI-TOF analysis of bulge photocleavage products reveal fragments analogous to those produced in mismatch and abasic site recognition and scission (**Figure 4.14)**.[1] For example, $Rh(bpy)_2(chrysi)^{3+}$ photocleavage of the B2-A duplex produces fragments of m/z = 7999.9, 8251.1, 3442.7, 4614.8, and 4802.3. The first two values correspond to the parent single strands of the duplex. The peak at m/z = 3442.7 corresponds to an 11-mer fragment with a 5'-phosphate, the fragment at m/z = 4614.8 to a 15-mer with a 3'-phosphate, and that at m/z = 4798.7 to the same 15-mer fragment but with a 3'-2,3-dehydronucleotide instead of a 3'-phosphate. These products are, in fact, almost identical to those produced via cleavage of the AB2-A abasic site. Thus the data clearly suggest that even though $Rh(bpy)_2(chrysi)^{3+}$ only recognizes single base bulges in a minority of cases, lesion binding, when it does happen, likely occurs in a mode analogous to that of the metalloinsertor at mismatches and abasic sites.

5.3: DISCUSSION

$Rh(bpy)_2(chrysi)^{3+}$ recognizes abasic sites with high affinity and specificity and with little regard for sequence context or the identity of the opposing unpaired base. The targeting of single base bulges, however, appears to be more complicated, with only seven of sixteen possible single base bulge sites bound and cleaved by the metal

[1] The low photocleavage efficiency associated with single base bulge photocleavage renders MALDI-TOF analysis difficult owing to the low amounts of product fragments produced; however, all relevant peaks can be easily identified above baseline.

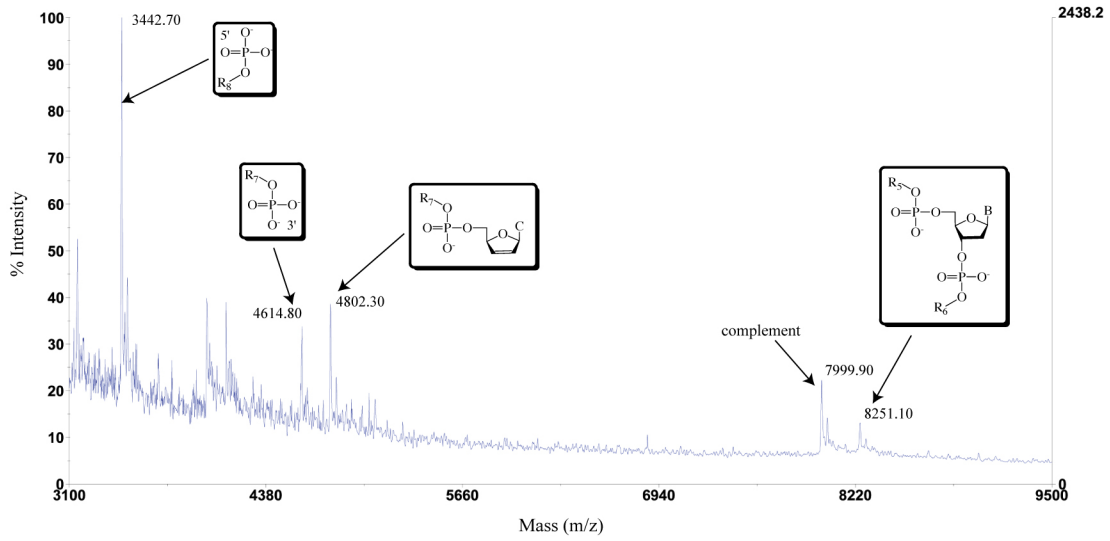

Figure 5.14: Mass spectrometry of single base bulge photocleavage products. MALDI-TOF mass spectrograph of photocleavage products of duplex B2-A, 5'-GAC CAG CTT ATC AT*A* CCT AGA TAA GCG -3' in which the underlined, italicized adenine is the unpaired, bulged base. The rightmost peaks correspond to the full, uncleaved parent strands. Assigned scission products can be viewed on the left-hand side of the plot and correspond to 5'-PO_4-CTA GAT AAG CG-3', 5'-GAC CAG CCT ATC AT*A*-PO_4-3', and 5'-GAC CAG CCT ATC AT*A*-dehydroC-3'. R_5 = GAC CAG CTT ATC AT; R_6 = CCT AGA TAA GCG; R_7 = GAC CAG CCT ATC AT*A*; R_8 = CTA GAT AAG CG; B = Adenine

complex. Yet, now that we have shown that $Rh(bpy)_2(chrysi)^{3+}$ can, indeed, bind both types of site, two simple questions follow: (1) how does the complex bind each lesion and (2) what are the constraints upon the recognition of these defects?

5.3.1: $Rh(bpy)_2(chrysi)^{3+}$ binds abasic sites via metalloinsertion

NMR and X-ray crystallographic evidence has revealed that $Rh(bpy)_2(chrysi)^{3+}$ binds mismatched sites not by classical major groove intercalation but rather via a previously unseen binding mode: insertion. The complex approaches the DNA from the minor groove, ejects the mismatched bases into the major groove, and replaces the extruded bases in the π-stack with its own aromatic ligand (**Figure 5.2**).

In the absence of concrete structural information for the binding mode at abasic sites, we must rely on comparisons to mismatch recognition when considering how $Rh(bpy)_2(chrysi)^{3+}$ targets abasic sites. The similarities are striking. First, photocleavage at mismatches and abasic sites exhibits identical strand asymmetry. In the AB1 and AB2 duplexes, the metal complex cleaves the strand containing the unpaired bases; in the AB4 duplexes, the strand containing the abasic site is cut. Mismatch photocleavage mirrors this behavior, with the corresponding strands of the mismatched duplexes being photocleaved. Second, the enantiospecificity of recognition is revealing. While bis-dipyridyl complexes intercalate into B-DNA with very little enantioselectivity[64], Δ-$Rh(bpy)_2(chrysi)^{3+}$ is able to target and cleave mismatched sites enantiospecifically, a consequence of metalloinsertion occurring from the sterically constrictive minor groove. The same high specificity is observed for the recognition of abasic sites: only the right-handed enantiomer targets and cleaves the abasic lesion. This clearly argues strongly for

involvement of the minor groove. Third, analysis of photocleavage products by mass spectrometry provides still more evidence for similarity. This technique reveals that both abasic sites and mismatches are cleaved on the 3'-side of the defects, producing three products: (1) a fragment containing a 5'-phosphate, (2) a fragment containing a 3'-phosphate, and (3) a metastable fragment identical to (2) but with a 3'-2,3-dehydronucleotide. Indeed, when the unpaired base in the abasic assembly is a cytosine and thus contains the same sequence as the mismatched assembly, identical photocleavage fragments are formed. These products are consistent with H1'-hydrogen abstraction by the photoactivated ligand, a mechanistic pathway accessible only via the minor groove. Finally, a variety of other, more minor similarities between abasic site and mismatch recognition exist, including the failure of $Rh(bpy)_2(chrysi)^{3+}$ to target either type of defect in the AB3 sequence context and the similarity of the site-specific binding affinities of the complex for both types of lesion. These observations also argue for similar binding modes. In sum, this study clearly indicates that the recognition and photocleavage of abasic sites by metalloinsertors occur in a manner almost, if not precisely, identical to mismatch targeting. Thus, these data are fully consistent with $Rh(bpy)_2(chrysi)^{3+}$ targeting abasic sites via metalloinsertion from the minor groove (**Figure 5.15)**. It should be noted that this conclusion fits well with an intuitive and teleological approach to the situation: to a metalloinsertor, an abasic site looks like a mismatch with half the extrusion work already accomplished.

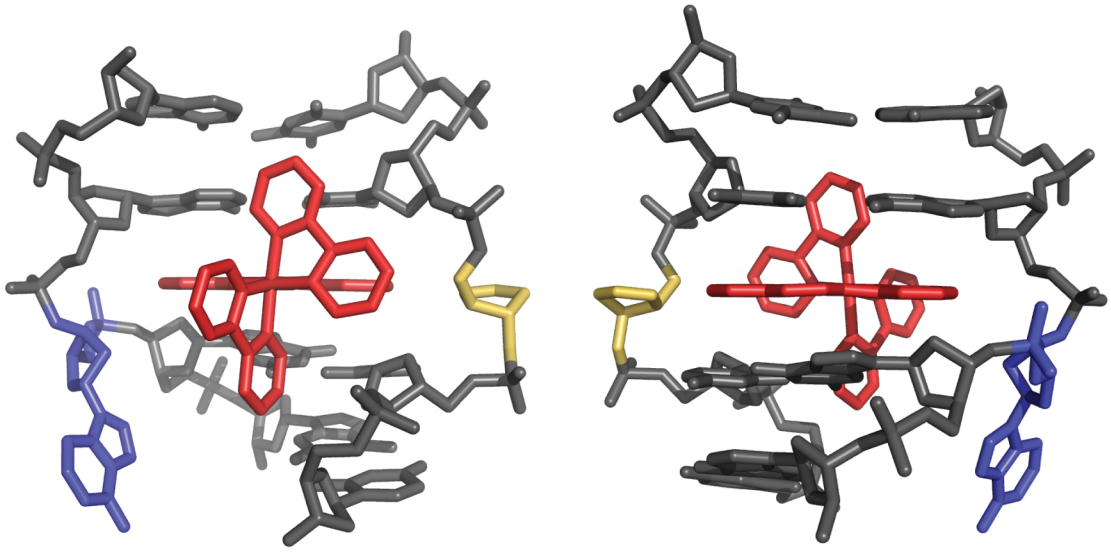

Figure 5.15. Model for metalloinsertion at an abasic site. The metalloinsertor, $Rh(bpy)_2(chrysi)^{3+}$ approaches the abasic site from the minor groove, ejects the unpaired base, and replaces it in the π-stack with the sterically expansive chrysi ligand. Views from the minor (left) and major (right) grooves are shown. The model is based on the crystal structure of $Rh(bpy)_2(chrysi)^{3+}$ inserted at a C•A mismatch.[8]

5.3.2: FACTORS AFFECTING THE RECOGNITION OF ABASIC SITES BY METALLOINSERTORS

Certainly the most puzzling aspect of the investigation into the recognition of abasic sites is the absence of photocleavage for the abasic AB3 duplexes. Neither sequence context nor thermodynamic stabilization provide satisfying explanations; the AB2 duplexes, which also house the abasic site in a 5'-PurΦPur-3' sequence context, are cleaved, and melting temperature measurements suggest that the AB3 duplexes are as destabilized as the other abasic assemblies. The failure of $Rh(bpy)_2(chrysi)^{3+}$ to cleave the AB3 duplex containing a central C•C mismatch is equally, if not more, surprising. Cytosine-cytosine mismatches are among the most destabilizing mispairs and are readily recognized and cleaved by metalloinsertors in almost any sequence context. It follows that the most likely, if slightly unsatisfying, explanation is based purely on sequence: the particular 5'-AΦG-3' sequence context in the AB3 duplexes simply does not allow for efficient binding and photocleavage. Such anomalies, though poorly understood at present, have been reported for mismatch targeting and constitute only a very small percentage of cases.[65]

5.3.3: FACTORS AFFECTING RECOGNITION OF SINGLE BASE BULGES BY METALLOINSERTORS

The somewhat sporadic recognition and cleavage of single base bulges by $Rh(bpy)_2(chrysi)^{3+}$ also merit some attention. As we have noted, only seven of sixteen possible bulges were recognized and cleaved. A thermodynamic rationale is not available, principally due to the lack of reliable, reported patterns between bulge

sequence and destabilization. Sequence context surely plays a role, but it cannot be the sole determining factor. Both the B2 and B3 assemblies place the bulged base in a 5'-PyrXPyr-3' context, but one set of duplexes (B2) exhibits cleavage regardless of bulged base identity, while the other (B3) escapes recognition entirely. The selective cleavage of three bulged bases in the B1 assemblies suggests that the identity of the bulged base may be a determining factor, but the recognition of the B2 sequence bulges regardless of base identity suggests a slightly more complicated rationale.

One possible explanation may be found in the likely conformation of the bulged base. In the B2 duplexes, all of which are photocleaved by $Rh(bpy)_2(chrysi)^{3+}$, each bulged base is in a 5'-PyrXPyr-3' sequence context and is therefore likely to spend at least some time in a extrahelical conformation. In contrast, the B4 duplexes house the bulged base in a 5'-PurXPur-3' conformation, with the better-stacking purines shifting the likely position of the bulged base from extra- to intrahelical; in this case, none of the single base bulges is bound and cleaved. The B1 duplexes provide an intermediate case. Here, the bulged bases are in a 5'-PyrXPur-3' sequence context. In this case, the bulged bases likely in an extrahelical conformation, the pyrimidines C and T, are bound and cleaved, while one of those more likely to prefer an intrahelical orientation, the purine A, escapes recognition. In sum, the data suggest that the more likely a base is to exist in an extrahelical conformation, the more easily it will be targeted by our metalloinsertors. It should be noted, however, that this hypothesis fails to explain the successful targeting of the bulged guanine in the B1-G assembly.

Disregarding the specifics, a more satisfying, if not more vague, explanation for the sporadic recognition of single base bulges can be found in the structure of the sites

themselves. While single base bulges are structurally related to abasic sites, they are not, of course, identical. In the former, the unpaired base lies across from an abasic ribose, and it follows that the bases flanking this sugar are separated by a ribophosphate unit. In the latter, the unpaired base is simply an extra nucleotide inserted into an otherwise well-matched helix: there is no ribophosphate 'space' complementary to the bulge site. These differences take on extra weight when a metalloinsertor binds. At a mismatch, $Rh(bpy)_2(chrysi)^{3+}$ ejects the mispaired bases and replaces them in the DNA π-stack with its sterically expansive ligand; in the end, the chrysi ligand is stacked between two non-adjacent base pairs that are separated on each strand by ribophosphate units connected to the once-mismatched, now-extruded base pairs. The same structure minus one of the extruded nucleobases is adopted during metalloinsertion at an abasic site. However, this type of binding is not possible at a single base bulge. Because there is no empty ribophosphate 'space' across from the bulged base, a metal complex must bind the site via a hybrid metallointercalation/metalloinsertion binding mode. One half of the sterically expansive ligand must bind via intercalation, stacking between adjacent base pairs, while the other half must bind via insertion, extruding the bulged base and taking its place in the π-stack (**Figure 4.16**). Logically, it follows that if the binding mode for the metalloinsertor changes, the rules for recognition and affinity must likewise change. In the end, we believe that this altered binding geometry is responsible for the failure of $Rh(bpy)_2(chrysi)^{3+}$ to reliably recognize and photocleave single base bulges.

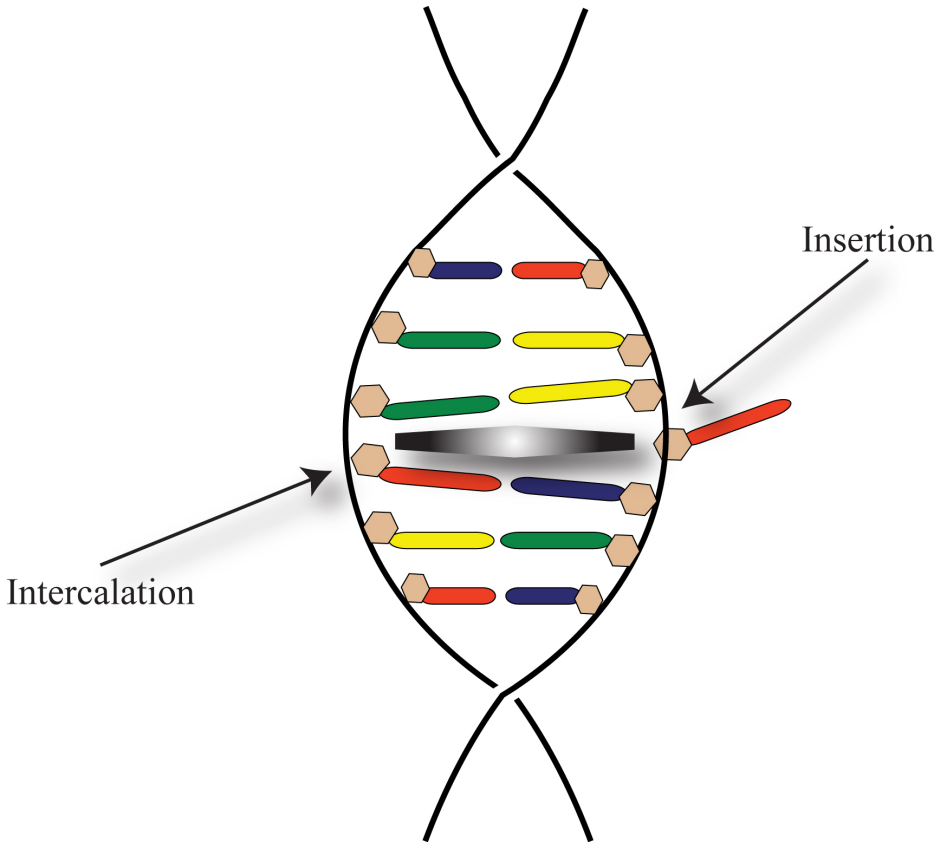

Figure 5.16: The hybrid binding mode required by single base bulges. Because there is no empty ribophosphate 'space' across from the bulged base, a metal complex must bind the site via a hybrid metallointercalation/metalloinsertion binding mode. The left side of the sterically expansive ligand (silver) must bind via intercalation, stacking between adjacent base pairs, while the right half binds must bind via insertion, extruding the bulged base and taking its place in the π-stack

5.4: CONCLUSIONS

This investigation clearly illustrates that both abasic sites and single base bulges are targeted by $Rh(bpy)_2(chrysi)^{3+}$, a sterically bulky metalloinsertor. Abasic sites are targeted with high specificity and affinity in all sequence contexts and with all unpaired bases, and a wide variety of evidence points to metalloinsertion as the binding mode of the complex at these defects. The recognition of single base bulges is less reliable, though the available data suggest an insertion-type binding mode is likely in this case as well.

The broader implications of this study are threefold. The revelation that specific metalloinsertion is not a phenomenon unique to mismatches certainly is important in the development of recognition agents for DNA defects. Perhaps this and subsequent investigations will enable us to expand the utility of these complexes beyond mismatch recognition into applications involving the *in vivo* detection of abasic sites or other thermodynamically destabilized DNA defects. Second, the ability of $Rh(bpy)_2(chrysi)^{3+}$ to specifically target abasic sites represents an exciting diagnostic possibility. A reliable probe for these lesions, especially one with the specificity, affinity, and reactivity of $Rh(bpy)(chrysi)^{3+}$ or $Rh(bpy)_2(phzi)^{3+}$, could prove an invaluable clinical and diagnostic tool. And third, these results dictate that abasic sites and single base bulges may, in addition to mismatches, be *in vivo* targets for metalloinsertors. Experiments with mismatch repair proficient and deficient cell lines have illuminated the substantial therapeutic potential of metalloinsertors and, furthermore, have strongly suggested that $Rh(bpy)_2(chrysi)^{3+}$ and $Rh(bpy)_2(phzi)^{3+}$ target mismatches in the cell. Similar studies employing cells deficient in abasic site repair pathways may further expose the potential therapeutic value of these complexes. Looking forward, the discovery that

metalloinsertors specifically target and photocleave abasic sites creates a variety of new and exciting opportunities in the study and development of metal complexes that target DNA lesions.

5.5: EXPERIMENTAL PROTOCOLS

Many of the procedural details for this investigation are included in CHAPTER 2 of this text. These include the following: the synthesis of $Rh(bpy)_2(chrysi)^{3+}$ and $Rh(bpy)_2(phzi)^{3+}$ (2.3.2.5−2.3.2.6); and the synthesis, purification, and radiolabeling of oligonucleotides (2.4.1−2.4.2). Although general methods for photocleavage gel experiments and MALDI-TOF mass spectrometry are also described in CHAPTER 2, the critical nature of these procedures in this investigation dictates that detailed protocols be presented here as well.

5.5.1: MATERIALS AND INSTRUMENTATION

All reagents were obtained from commercial sources and used as received without further purification. $RhCl_3$ was purchased from Pressure Chemicals. $Rh(bpy)_2(phi)^{3+}$ and $Rh(bpy)_2(chrysi)^{3+}$ were synthesized according to published protocols.[58] The enantiomers of $Rh(bpy)_2(chrysi)^{3+}$ were likewise resolved as described earlier.[58] All non-aqueous solvents were purchased from Fluka and stored under argon and over molecular sieves. All water used was purified using a MilliQ water purification system.

Analytical mass spectrometry was performed at either the Caltech mass spectrometry facility or in the Beckman Institute Protein/Peptide Micro Analytical

Laboratory (PPMAL). Absorption spectra were recorded on a Beckman DU 7400 spectrophotometer.

Standard oligonucleotides were synthesized on an ABI 3400 DNA synthesizer. Abasic site-containing oligonucleotides were ordered from Integrated DNA technologies; given the instability of the natural hemiacetal abasic lesion[59], the often employed tetrahydrofuranyl abasic site analogue was used instead (**Figure 5.4c**).[60, 61] In all text, the symbol Φ denotes the abasic site. Following synthesis or delivery, the oligonucleotides were purified both with and without dimethoxytrityl (DMT) protecting groups via reverse phase HPLC (see Chapter 2, Section 2.4.1).

Concentrations of metal complexes were determined using UV-visible spectrophotometry with extinction coefficients of ε_{302} = 57,000 $cm^{-1}M^{-1}$ and ε_{315} = 52,200 $cm^{-1}M^{-1}$ for $Rh(bpy)_2(chrysi)^{3+}$ and ε_{304} = 65,800 $cm^{-1}M^{-1}$ and ε_{314} = 67,300 $cm^{-1}M^{-1}$ for $Rh(bpy)_2(phzi)^{3+}$. DNA strand concentrations were also determined spectrophotometrically using base extinction coefficients of ε_{260} = 15,400 $cm^{-1}M^{-1}$ (A), ε_{260} = 7,400 $cm^{-1}M^{-1}$ (C), ε_{260} = 11,500 $cm^{-1}M^{-1}$ (G), and ε_{260} = 8,700 $cm^{-1}M^{-1}$ (T). DNA concentrations are presented per strand. Duplex melting temperatures were determined by following hypochromicity at 260 nm for 1 μM duplex in a buffer of 50 mM NaCl, 10 mM NaPi, pH 7.1, via variable temperature UV-Vis.

All oligonucleoties were 5'-radioactively labeled with ^{32}P using [γ-^{32}P]ATP (MP Biomedicals) and polynucleotide kinase (Roche) employing standard methodologies and purified via 20% polyacrylamide gel electrophoresis (SequaGel, National Diagnostics) (see Chapter 2, Section 2.4.2). All photocleavage experiments were performed using end-labeled DNA with identical sequence, unlabeled carrier DNA in a buffer of 50 mM NaCl,

10 mM NaPi, pH 7.1. Duplexes were annealed by incubation at 90 °C for 15 min followed by slow cooling to room temperature.

Irradiations were performed using an Oriel Instruments solar simulator (320−440 nm). All PAGE experiments described employed denaturing 20% polyacrylamide gels (SequaGel, National Diagnostics) and were performed according to published procedures. Gels were developed using Molecular Dynamics phosphorimaging screens and a Molecular Dynamics Storm 820 phosphorimager and were subsequently visualized and quantified with Molecular Dynamics ImageQuant software.

MALDI-TOF mass spectrometry was performed using a Voyager DE-PRO MALDI-TOF mass spectrometer with a 337 nm nitrogen laser source (Applied Biosystems). A 4-hydroxypicolinic acid matrix was employed. All mass spectra were internally calibrated using the mass of the parent oligonucleotide.

5.5.2: RECOGNITION AND PHOTOCLEAVAGE EXPERIMENTS.

Solutions of $Rh(bpy)_2(chrysi)^{3+}$ or $Rh(bpy)_2(phzi)^{3+}$ were incubated with 5'-^{32}P-labeled oligonucleotides either containing or lacking a central DNA lesion (see section 5.3.1 for further details). Unless otherwise noted, final solutions were prepared 20 min prior to irradiation, contained 1 μM duplex and 1 μM metalloinsertor, and were 20 μL in volume. Dark and light control samples, of course, lacked the appropriate solution components. Because metalloinsertor photocleavage is single-stranded, each duplex was interrogated twice, once with each of the two strands radioactively labeled. Samples were irradiated with an Oriel Instruments solar simulator (320−440 nm). Irradiations were performed in open, vertically oriented 1.7 mL microcentrifuge tubes. After irradiation,

samples were incubated at 60 °C for 30 min and then dried under vacuum. Dried samples were redissolved in denaturing formamide loading dye and electrophoresed on 20% denaturing polyacrylamide gels. Images of the gels were obtained via phosphorimagery (Molecular Dynamics) and quantified using ImageQuant software.

5.5.3: DETERMINATION OF SITE-SPECIFIC BINDING CONSTANTS.

Photocleavage titrations were performed to determine the thermodynamic binding constants for $Rh(bpy)_2(chrysi)^{3+}$ with lesion sites of interest. Solutions of DNA (1 μM) were incubated with variable concentrations of $Rh(bpy)_2(chrysi)^{3+}$ (0−20 μM) and subsequently irradiated on an Oriel Instruments solar simulator for 10 min. After irradiation, the samples were incubated at 60 °C for 30 min and then dried under vacuum. Dried samples were redissolved in denaturing formamide loading dye and electrophoresed on 20% denaturing polyacrylamide gels. Images of the gels were obtained via phosphorimagery (Molecular Dynamics). The fraction cleaved at the lesion site was quantitated using ImageQuant software, expressed as a fraction of the total parent DNA, and fit to a single site, one parameter binding model.

5.5.4: MALDI-TOF ANALYIS OF CLEAVAGE PRODUCT

For mass spectrometry analysis of photocleavage products, 2 μM solutions of duplex were incubated with 2 μM $Rh(bpy)_2(chrysi)^{3+}$ and irradiated as described above. After irradiation and incubation, the samples were dried under vacuum, resuspended in 10 μL water, and desalted using 10 μL OMIX C18 tips (Varian). The resultant desalted solution was dried *in vacuo* and resuspended in 2 μL deionized H_2O. Appropriate light and dark controls were also prepared. Experiments were performed using a Voyager DE-

PRO MALDI-TOF mass spectrometer with a 337 nm nitrogen laser source (Applied Biosystems). A 4-hydroxypicolinic acid matrix was employed. All mass spectra were internally calibrated using the mass of the parent oligonucleotide. In the interest of thoroughness, the full data sets for the MALDI-TOF analysis of the photocleavage of abasic sites and single base bulges are included in **Tables 5.3−5.7**.

Duplex	[Rh]	Irradiation	Fragment	Fragment Description	Predicted Mass	Obs. Mass
1MM-1C	-	15 min	5'-CGC TTA TCT AGG GCT GAT AAG CTG GTC	1MM-full	8306.5	8306.2
			5'-GAC CAG CTT ATC ACC CCT AGA TAA GCG	1C-full	8213.4	8213.5
1MM-1C	2 μM	15 min	5'-CGC TTA TCT AGG GCT GAT AAG CTG GTC	1MM-full	8306.5	8311.6
			5'-GAC CAG CTT ATC ACC CCT AGA TAA GCG	1C-full	8213.4	8215.25
			5'-PO_4-CCT AGA TAA GCG	5'-phos-frag	3734.5	3733.5
			GAC CAG CTT ATC AC-PO_4-3'	3'-phos-frag	4287.8	4286.8
			GAC CAG CTT ATC AC-PO_4-dehydroC-3'	3'-DHC-frag	4477.8	4475.7
1ϕ-1A	-	15 min	5'- CGC TTA TCT AGG GϕT GAT AAG CTG GTC	1ϕ-full	8197.5	8196.5
			5'-GAC CAG CTT ATC AAC CCT AGA TAA GCG	1A-full	8237.4	8237.3
1ϕ-1A	2 μM	15 min	5'- CGC TTA TCT AGG GϕT GAT AAG CTG GTC	1ϕ-full	8197.5	8195.5
			5'-GAC CAG CTT ATC AAC CCT AGA TAA GCG	1A-full	8237.4	8233.6
			5'-PO_4-CCT AGA TAA GCG	5'-phos-frag	3734.5	3732.6
			GAC CAG CTT ATC AA-PO_4-3'	3'-phos-frag	4311.8	4309.9
			GAC CAG CTT ATC AA-PO_4-dehydroC-3'	3'-DHC-frag	4501.8	4498.2
1ϕ-1C	-	15 min	5'- CGC TTA TCT AGG GϕT GAT AAG CTG GTC	1ϕ-full	8197.5	8196.0
			5'-GAC CAG CTT ATC ACC CCT AGA TAA GCG	1C-full	8213.4	8213.8
1ϕ-1C	2 μM	15 min	5'- CGC TTA TCT AGG GϕT GAT AAG CTG GTC	1ϕ-full	8197.5	8200.2
			5'-GAC CAG CTT ATC ACC CCT AGA TAA GCG	1C-full	8213.4	8216.3
			5'-PO_4-CCT AGA TAA GCG	5'-phos-frag	3734.5	3733.7
			GAC CAG CTT ATC AC-PO_4-3'	3'-phos-frag	4287.8	4286.8
			GAC CAG CTT ATC AC-PO_4-dehydroC-3'	3'-DHC-frag	4477.8	4475.8
1ϕ-1G	-	15 min	5'- CGC TTA TCT AGG GϕT GAT AAG CTG GTC	1ϕ-full	8197.5	8195.2
			5'-GAC CAG CTT ATC AGC CCT AGA TAA GCG	1G-full	8253.4	8250.6
1ϕ-1G	2 μM	15 min	5'- CGC TTA TCT AGG GϕT GAT AAG CTG GTC	1ϕ-full	8197.5	8194.8
			5'-GAC CAG CTT ATC AGC CCT AGA TAA GCG	1G-full	8253.4	8252.4
			5'-PO_4-CCT AGA TAA GCG	5'-phos-frag	3734.5	3732.9
			GAC CAG CTT ATC AG-PO_4-3'	3'-phos-frag	4327.8	4325.9
			GAC CAG CTT ATC AG-PO_4-dehydroC-3'	3'-DHC-frag	4517.8	4514.8
1ϕ-1T	-	15 min	5'- CGC TTA TCT AGG GϕT GAT AAG CTG GTC	1ϕ-full	8197.5	8198.1
			5'-GAC CAG CTT ATC ATC CCT AGA TAA GCG	1T-full	8228.4	8231.2
1ϕ-1T	2 μM	15 min	5'- CGC TTA TCT AGG GϕT GAT AAG CTG GTC	1ϕ-full	8197.5	8199.4
			5'-GAC CAG CTT ATC ATC CCT AGA TAA GCG	1T-full	8228.4	8230.5
			5'-PO_4-CCT AGA TAA GCG	5'-phos-frag	3734.5	3732.5
			GAC CAG CTT ATC AT-PO_4-3'	3'-phos-frag	4302.8	4300.0
			GAC CAG CTT ATC AT-PO_4-dehydroC-3'	3'-DHC-frag	4492.8	4489.9

Table 5.3: MALDI-TOF data for sequence 1 mismatched and abasic assemblies

Duplex	[Rh]	Irradiation	Fragment	Fragment Description	Predicted Mass	Obs. Mass
2MM-2C	-	15 min	5'-CGC TTA TCT AGG CAT GAT AAG CTG GTC	2MM-full	8290.5	8287.3
			5'-GAC CAG CTT ATC ATC CCT AGA TAA GCG	2C-full	8228.4	8225.3
2MM-2C	2 μM	15 min	5'-CGC TTA TCT AGG CAT GAT AAG CTG GTC	2MM-full	8306.5	8311.6
			5'-GAC CAG CTT ATC ATC CCT AGA TAA GCG	2C-full	8213.4	8215.25
			5'-PO_4-CTA GAT AAG CG	5'-phos-frag	3445.3	3443.5
			GAC CAG CTT ATC ATC-PO_4-3'	3'-phos-frag	4592.0	4288.3
			GAC CAG CTT ATC ATC-PO_4-dehydroC-3'	3'-DHC-frag	4782.0	4777.3
2ϕ-2A	2 μM	15 min	5'-CGC TTA TCT AGG ϕAT GAT AAG CTG GTC	2ϕ-full	8181.5	8183.5
			5'-GAC CAG CTT ATC ATA CCT AGA TAA GCG	2A-full	8252.4	8255.3
2ϕ-2A	2 μM	15 min	5'-CGC TTA TCT AGG ϕAT GAT AAG CTG GTC	2ϕ-full	8181.5	8180.9
			5'-GAC CAG CTT ATC ATA CCT AGA TAA GCG	2A-full	8252.4	8251.6
			5'-PO_4-CTA GAT AAG CG	5'-phos-frag	3445.3	3443.9
			GAC CAG CTT ATC ATA-PO_4-3'	3'-phos-frag	4616.0	4612.8
			GAC CAG CTT ATC ATA-PO_4-dehydroC-3'	3'-DHC-frag	4806.0	4603.7
2ϕ-2C	-	15 min	5'-CGC TTA TCT AGG ϕAT GAT AAG CTG GTC	2ϕ-full	8181.5	8181.0
			5'-GAC CAG CTT ATC ATC CCT AGA TAA GCG	2C-full	8228.4	8227.9
2ϕ-2C	2 μM	15 min	5'-CGC TTA TCT AGG ϕAT GAT AAG CTG GTC	2ϕ-full	8181.5	8182.0
			5'-GAC CAG CTT ATC ATC CCT AGA TAA GCG	2C-full	8228.4	8227.1
			5'-PO_4-CTA GAT AAG CG	5'-phos-frag	3445.3	3443.7
			GAC CAG CTT ATC ATC-PO_4-3'	3'-phos-frag	4592.0	4590.9
			GAC CAG CTT ATC ATC-PO_4-dehydroC-3'	3'-DHC-frag	4782.0	4779.0
2ϕ-2G	-	15 min	5'-CGC TTA TCT AGG ϕAT GAT AAG CTG GTC	2ϕ-full	8181.5	8181.0
			5'-GAC CAG CTT ATC ATG CCT AGA TAA GCG	2G-full	8268.4	8271.7
2ϕ-2G	2 μM	15 min	5'-CGC TTA TCT AGG ϕAT GAT AAG CTG GTC	2ϕ-full	8181.5	8186.7
			5'-GAC CAG CTT ATC ATG CCT AGA TAA GCG	2G-full	8268.4	8274.1
			5'-PO_4-CTA GAT AAG CG	5'-phos-frag	3445.3	3447.9
			GAC CAG CTT ATC ATG-PO_4-3'	3'-phos-frag	4632.0	4635.8
			GAC CAG CTT ATC ATG-PO_4-dehydroC-3'	3'-DHC-frag	4822.0	4825.3
2ϕ-2T	-	15 min	5'-CGC TTA TCT AGG ϕAT GAT AAG CTG GTC	2ϕ-full	8181.5	8184.5
			5'-GAC CAG CTT ATC ATT CCT AGA TAA GCG	2T-full	8243.4	8246.3
2ϕ-2T	2 μM	15 min	5'-CGC TTA TCT AGG ϕAT GAT AAG CTG GTC	2ϕ-full	8181.5	8182.7
			5'-GAC CAG CTT ATC ATT CCT AGA TAA GCG	2T-full	8243.4	8242.0
			5'-PO_4-CTA GAT AAG CG	5'-phos-frag	3445.3	3444.2
			GAC CAG CTT ATC ATT-PO_4-3'	3'-phos-frag	4607.0	4605.3
			GAC CAG CTT ATC ATT-PO_4-dehydroC-3'	3'-DHC-frag	4797.0	4794.6

Table 5.4: MALDI-TOF data for sequence 2 mismatched and abasic assemblies

Duplex	[Rh]	Irradiation	Fragment	Fragment Description	Predicted Mass	Obs. Mass
4MM-4C	-	15 min	5'-CGC TTA TCT AGT CCT GAT AAG CTG GTC	4MM-full	8241.1	8233.9
			5'-GAC CAG CTT ATC AGC ACT AGA TAA GCG	4C-full	8277.5	8272.7
4MM-4C	2 μM	15 min	5'-CGC TTA TCT AGT CCT GAT AAG CTG GTC	4MM-full	8241.1	8244.9
			5'-GAC CAG CTT ATC AGC ACT AGA TAA GCG	4C-full	8277.5	8275.7
			5'-PO_4-TGA TAA GCT GGT C	5'-phos-frag	4069.7	4067.1
			CGC TTA TCT AGT C-PO_4-3'	3'-phos-frag	3980.6	3978.9
			CGC TTA TCT AGT C-PO_4-dehydroC-3'	3'-DHC-frag	4170.6	4166.0
4ϕ-4A	2 μM	15 min	5'-CGC TTA TCT AGT ϕCT GAT AAG CTG GTC	4ϕ-full	8132.3	8130.8
			5'-GAC CAG CTT ATC AGA ACT AGA TAA GCG	4A-full	8302.5	8299.8
4ϕ-4A	2 μM	15 min	5'-CGC TTA TCT AGT ϕCT GAT AAG CTG GTC	4ϕ-full	8132.3	8130.5
			5'-GAC CAG CTT ATC AGA ACT AGA TAA GCG	4A-full	8302.5	8300.2
			5'-PO_4-TGA TAA GCT GGT C	5'-phos-frag	4069.7	4064.1
			CGC TTA TCT AGT ϕ-PO_4-3'	3'-phos-frag	3871.4	3869.0
			CGC TTA TCT AGT ϕ-PO_4-dehydroC-3'	3'-DHC-frag	4061.6	*Buried*
4ϕ-4C	-	15 min	5'-CGC TTA TCT AGT ϕCT GAT AAG CTG GTC	4ϕ-full	8132.3	8129.5
			5'-GAC CAG CTT ATC AGC ACT AGA TAA GCG	4C-full	8277.5	8274.8
4ϕ-4C	2 μM	15 min	5'-CGC TTA TCT AGT ϕCT GAT AAG CTG GTC	4ϕ-full	8132.3	8133.7
			5'-GAC CAG CTT ATC AGC ACT AGA TAA GCG	4C-full	8277.5	8278.3
			5'-PO_4-TGA TAA GCT GGT C	5'-phos-frag	4069.7	4065.1
			CGC TTA TCT AGT ϕ-PO_4-3'	3'-phos-frag	3871.4	3867.9
			CGC TTA TCT AGT ϕ-PO_4-dehydroC-3'	3'-DHC-frag	4061.6	*Buried*
4ϕ-4G	-	15 min	5'-CGC TTA TCT AGT ϕCT GAT AAG CTG GTC	4ϕ-full	8132.3	8131.9
			5'-GAC CAG CTT ATC AGG ACT AGA TAA GCG	4G-full	8317.5	8318.9
4ϕ-4G	2 μM	15 min	5'-CGC TTA TCT AGT ϕCT GAT AAG CTG GTC	4ϕ-full	8132.3	8132.1
			5'-GAC CAG CTT ATC AGG ACT AGA TAA GCG	4G-full	8317.5	8317.0
			5'-PO_4-TGA TAA GCT GGT C	5'-phos-frag	4069.7	4066.2
			CGC TTA TCT AGT ϕ-PO_4-3'	3'-phos-frag	3871.4	3868.3
			CGC TTA TCT AGT ϕ-PO_4-dehydroC-3'	3'-DHC-frag	4061.6	*Buried*
4ϕ-4T	-	15 min	5'-CGC TTA TCT AGT ϕCT GAT AAG CTG GTC	4ϕ-full	8132.3	8131.9
			5'-GAC CAG CTT ATC AGT ACT AGA TAA GCG	4T-full	8292.4	8291.6
4ϕ-4T	2 μM	15 min	5'-CGC TTA TCT AGT ϕCT GAT AAG CTG GTC	4ϕ-full	8132.3	8132.1
			5'-GAC CAG CTT ATC AGT ACT AGA TAA GCG	4T-full	8292.4	8291.1
			5'-PO_4-TGA TAA GCT GGT C	5'-phos-frag	4069.7	4065.5
			CGC TTA TCT AGT ϕ-PO_4-3'	3'-phos-frag	3871.4	3869.4
			CGC TTA TCT AGT ϕ-PO_4-dehydroC-3'	3'-DHC-frag	4061.6	*Buried*

Table 5.5: MALDI-TOF data for sequence 4 mismatched and abasic assemblies

Duplex	[Rh]	Irradiation	Fragment	Fragment Description	Predicted Mass	Obs. Mass
1B-1C	-	15 min	5'-CGC TTA TCT AGG G T GAT AAG CTG GTC	1B-full	8017.5	8019.9
			5'-GAC CAG CTT ATC ACC CCT AGA TAA GCG	1C-full	8213.4	8215.5
1B-1C	2 μM	15 min	5'- CGC TTA TCT AGG G T GAT AAG CTG GTC	1B-full	8017.5	8020.5
			5'-GAC CAG CTT ATC ACC CCT AGA TAA GCG	1C-full	8213.4	8216.6
			5'-PO_4-T AGA TAA GCG	5'-phos-frag1	3156.4	3152.9
			5'-PO_4-CT AGA TAA GCG	5'-phos-frag2	3445.1	3440.7
			GAC CAG CTT ATC ACC C-PO_4-3'	3'-phos-frag	4866.0	4862.4
			GAC CAG CTT ATC ACC C-PO_4-dehydroC-3'	3'-DHC-frag	4058.0	5050.1
2B-2A	2 μM	15 min	5'-CGC TTA TCT AGG AT GAT AAG CTG GTC	2B-full	8000.1	7999.6
			5'-GAC CAG CTT ATC ATA CCT AGA TAA GCG	2A-full	8252.4	8247.9
2B-2A	2 μM	15 min	5'-CGC TTA TCT AGG AT GAT AAG CTG GTC	2B-full	8000.1	7999.9
			5'-GAC CAG CTT ATC ATA CCT AGA TAA GCG	2A-full	8252.4	8251.1
			5'-PO_4-CTA GAT AAG CG	5'-phos-frag	3445.3	3442.7
			GAC CAG CTT ATC ATA-PO_4-3'	3'-phos-frag	4616.0	4614.8
			GAC CAG CTT ATC ATA-PO_4-dehydroC-3'	3'-DHC-frag	4806.0	4798.7
2B-2C	-	15 min	5'-CGC TTA TCT AGG AT GAT AAG CTG GTC	2B-full	8000.1	7998.5
			5'-GAC CAG CTT ATC ATC CCT AGA TAA GCG	2C-full	8228.4	8225.8
2B-2C	2 μM	15 min	5'-CGC TTA TCT AGG AT GAT AAG CTG GTC	2B-full	8000.1	7996.1
			5'-GAC CAG CTT ATC ATC CCT AGA TAA GCG	2C-full	8228.4	8222.7
			5'-PO_4-TAG ATA AGC G	5'-phos-frag1	3156.4	3156.5
			5'-PO_4-C TAG ATA AGC G	5'-phos-frag2	3445.3	3445.8
			GAC CAG CTT ATC ATC C-PO_4-3'	3'-phos-frag	4881.0	4876.9
			GAC CAG CTT ATC ATC C-PO_4-dehydroC-3'	3'-DHC-frag	5073.0	5068.0
2B-2G	-	15 min	5'-CGC TTA TCT AGG AT GAT AAG CTG GTC	2B-full	8000.1	7997.3
			5'-GAC CAG CTT ATC ATG CCT AGA TAA GCG	2G-full	8268.4	8263.4
2B-2G	2 μM	15 min	5'-CGC TTA TCT AGG AT GAT AAG CTG GTC	2B-full	8000.1	7999.7
			5'-GAC CAG CTT ATC ATG CCT AGA TAA GCG	2G-full	8268.4	8266.6
			5'-PO_4-CTA GAT AAG CG	5'-phos-frag	3445.3	3447.2
			GAC CAG CTT ATC ATG-PO_4-3'	3'-phos-frag	4632.0	4632.8
			GAC CAG CTT ATC ATG-PO_4-dehydroC-3'	3'-DHC-frag	4822.0	4820.6
2B-2T	-	15 min	5'-CGC TTA TCT AGG AT GAT AAG CTG GTC	2B-full	8000.1	8002.5
			5'-GAC CAG CTT ATC ATT CCT AGA TAA GCG	2T-full	8243.4	8244.8
2B-2T	2 μM	15 min	5'-CGC TTA TCT AGG AT GAT AAG CTG GTC	2B-full	8000.1	7999.8
			5'-GAC CAG CTT ATC ATT CCT AGA TAA GCG	2T-full	8243.4	8241.5
			5'-PO_4-CTA GAT AAG CG	5'-phos-frag	3445.3	3442.8
			GAC CAG CTT ATC ATT-PO_4-3'	3'-phos-frag	4607.0	4602.3
			GAC CAG CTT ATC ATT-PO_4-dehydroC-3'	3'-DHC-frag	4797.0	4795.6

Figure 5.6: MALDI-TOF data for single base bulge assemblies. Note the evidence for cleavage at "slipped" bulges in 1B-1C and 2B-2C

5.6: REFERENCES

1. Marnett, L. J.; Plastaras, J. P. *Trends in Genetics* **2001**, *17*, 214−221.
2. Loeb, L. A.; Loeb, K. R. *Proceedings of the National Academy of Sciences U. S. A.* **2003**, *100*, 776−781.
3. Li, G. M. *Frotiers in Bioscience* **2003**, *8*, D997−U1.
4. Lyer, R. R.; Pluciennik, A.; Burdett, V.; Modrich, P. L. *Chemical Reviews* **2006**, *106* (2), 302−323.
5. Modrich, P. *Journal of Biological Chemistry* **2006**, *281* (41), 30305−30309.
6. David, S. S.; O'Shea, V. L.; Kundu, S. *Nature* **2007**, *447*, 941−950.
7. Jacob, S.; Praz, F. *Biochemie* **2002**, *84*, 27−47.
8. Kolodner, R. D. *Trends in Biochemical Science* **1995**, *20*, 397−401.
9. Kolodner, R. *Genes & Development* **1996**, *10* (12), 1433−1442.
10. Jiricny, J. *Cancer Surveys* **1996**, *28*, 47−68.
11. Zeglis, B. M.; Pierre, V. C.; Barton, J. K. *Chemical Communications* **2007**, 4565−4579.
12. Jackson, B. A.; Barton, J. K. *Journal of the American Chemical Society* **1997**, *119* (52), 12986−12987.
13. Junicke, H.; Hart, J. R.; Kisko, J. L.; Glebov, O.; Kirsch, I. R.; Barton, J. K. *Proceedings of the National Academy of Sciences U. S. A.* **2003**, *100*, 3737−3742.
14. Jackson, B. A.; Alekseyev, V. Y.; Barton, J. K. *Biochemistry* **1999**, *38* (15), 4655−4662.
15. Jackson, B. A.; Barton, J. K. *Biochemistry* **2000**, *39* (20), 6176−6182.

16. Jackson, B. A.; Henling, L. M.; Barton, J. K. *Inorganic Chemistry* **1999**, *38* (26), 6218−6224.

17. Cordier, C.; Pierre, V. C.; Barton, J. K. *Journal of the American Chemical Society* **2007**, *129*, 12287−12295.

18. Pierre, V. C.; Kaiser, J. T.; Barton, J. K. *Proceedings of the National Academy of Sciences U. S. A.* **2007**, *103*, 429−434.

19. Lhomme, J.; Constant, J. F.; Demeunynck, M. *Biopolymers* **1999**, *52* (2), 65−83.

20. Boiteux, S.; Guillet, M. *DNA Repair* **2004**, *3*, 1−12.

21. Lindahl, T.; Nyberg, B. *Biochemistry* **1972**, *11* (19), 3610−3518.

22. Wilde, J. A.; Bolton, P. H.; Mazumder, A.; Manoharan, M.; Gerlt, J. A. *Journal of the American Chemical Society* **1989**, *111* (5), 1894−1896.

23. Goljer, I.; Kumar, S.; Bolton, P. H. *Journal of Biological Chemistry* **1995**, *270*, 22980−22987.

24. Coppel, Y.; Berthet, N.; Coulombeau, C.; Garcia, J.; Lhomme, J. *Biochemistry* **1997**, *36*, 4817−4830.

25. Feig, M.; Zacharias, M.; Pettitt, B. M. *Biophysical Journal* **2001**, *81*, 351−370.

26. Chen, J.; Dupradeau, F.−Y.; Case, D. A.; Turner, C. J.; Stubbe, J. *Nucleic Acids Research* **2008**, *36* (1), 253−262.

27. Hoehn, S. T.; Turner, C. J.; Stubbe, J. *Nucleic Acids Research* **2001**, *29* (16), 3413−3423.

28. Kalnik, M. W.; Chang, C. N.; Johnson, F.; Grollman, A. P.; Patel, D. J. *Biochemistry* **1989**, *28*, 3373−3383.

29. Vesnaver, G.; Chang, C. N.; Eisenberg, M.; Grollman, A. P.; Breslauer, K. J. *Proceedings of the National Academy of Sciences U. S. A.* **1989**, *86*, 3614−3618.

30. Gelfand, C. A.; Plum, G. E.; Grollman, A. P.; Johnson, F.; Breslauer, K. J. *Biochemistry* **1998**, *37*, 7321−7327.

31. Alani, E.; Chi, N. W.; Kolodner, R. D. *Genes and Development* **1995**, *9*, 234−247.

32. Tanaka, F.; Kameda, A.; Tamamoto, M.; Ohuchi, A. *Biochemistry* **2004**, *43*, 7143−7150.

33. LeBlanc, D. A.; Morden, K. M. *Biochemistry* **1991**, *30*, 4042−4047.

34. Nikonowicz, E. P.; Meadows, R. P.; Gorenstein, D. G. *Biochemistry* **1990**, *25*, 7456−7464.

35. Hare, D.; Shapiro, L.; Patel, D. J. *Biochemistry* **1987**, *25*, 7456−7464.

36. Joshua−Tor, L.; Frolow, F.; Appella, E.; Hope, H.; Rabinovich, D.; Sussman, J. L. *Journal of Molecular Biology* 1992, *225* (2), 397−431.

37. Joshua−Tor, L.; Rabinovich, D.; Hope, H.; Frolow, F.; Appella, E.; Sussman, J. L. *Nature* **1988**, *334*, 82−84.

38. Patel, D. J.; Kozlowski, S. A.; Marky, L. A.; Rice, J. A.; Broka, C.; Itakura, K.; Breslauer, K. J. *Biochemistry* **1982**, *21*, 445−451.

39. Kalnik, M. W.; Norman, D. G.; Swann, P. F.; Patel, D. J. *Journal of Biological Chemistry* **1989**, *264* (7), 3702−3712.

40. Kalnik, M. W.; Norman, D. G.; Zagorski, M. G.; Swann, P. F.; Patel, D. J. *Biochemistry* **1989**, *28*, 294−303.

41. Miller, M.; Harrison, R. W.; Wlodawer, A.; Appella, E.; Sussman, J. L. *Nature* **1988**, *334*, 85−86.

42. Cline, S. D.; Jones, W.; Stone, M. P.; Osheroff, N. *Biochemistry* **1999**, *38*, 15500−15507.

43. Streisinger, G.; Owen, J. *Genetics* **1985**, *109*, 633−659.

44. Shinmura, K.; Tao, H.; Goto, M.; Igarashi, H.; Taniguchi, T.; Maekawa, M.; Takezaki, T.; Sugimura, H. *Carcinogenesis* **2004**, *25* (12), 2311−2317.

45. WIlson, D. M.; Bohr, V. A. *DNA Repair* **2007**, *6*, 544−559.

46. Fkyerat, A.; Demeunynck, M.; Constant, J. F.; Michon, P.; Lhomme, J. *Journal of the American Chemical Society* **1993**, *115*, 9952−9959.

47. Boturyn, D.; Boudali, A.; Constant, J. F.; Defrancq, E.; Lhomme, J. *Tetrahedron* **1997**, *53* (15), 5485−5492.

48. Kobori, A.; Murase, T.; Suda, H.; Saito, I.; Nakatani, K. *Bioorganic & Medicinal Chemistry Letters* **2004**, *14* (13), 3431−3433.

49. Nakatani, K.; Sando, S.; Saito, I. *Journal of the American Chemical Society* 2000, *122*, 2172−2177.

50. Takei, F.; Suda, H.; Hagihara, M.; Zhang, J. H.; Kobori, A.; Nakatani, K. *Chemistry−a European Journal* **2007**, *13* (16), 4452−4457.

51. Cheng, C. C.; Kuo, Y. N.; Chuang, K. S.; Luo, C. F.; WAng, W. J. *Angewandte Chemie−International Edition* **1999**, *38*, 1255−1257.

52. Morgan, J. L.; Buck, D. P.; Turley, A. G.; Collins, J. G.; Keene, F. R. *Journal of Biological Inorganic Chemistry* **2006**, *11* (7), 824−834.

53. Morgan, J. L.; Buck, D. P.; Turley, A. G.; Collins, J. G.; Keene, F. R. *Inorganica Chimica Acta* **2006**, *359* (3), 888−898.

54. Jones, G. B.; Lin, Y. Q.; Ma, D.; Xiao, Z. W.; Hwang, G. S.; Kappen, L.; Goldberg, I. H. *Current Topics in Medicinal Chemistry* **2008**, *8* (6), 436−447.

55. Kappen, L. S.; Goldberg, I. H. *Biochemistry* **1997**, *36* (48), 14861−14867.

56. Kappen, L. S.; Xi, Z.; Goldberg, I. H. *Biochemistry* **2001**, *40* (50), 15378−15383.

57. Xiao, Z.; Kappen, L. S.; Goldberg, I. H. *Bioorganic & Medicinal Chemistry Letters* **2006**, *16* (11), 2895−2899.

58. Zeglis, B. M.; Barton, J. K. *Nature Protocols* **2007**, *2* (2), 357−371.

59. Lindahl, T.; Andersson, A. *Biochemistry* **1972**, *11* (19), 3618−3623.

60. Takeshita, M.; Chang, C. N.; Johnson, F.; Will, S.; Grollman, A. P. *Journal of Biological Chemistry* **1987**, *262*, 10171−10179.

61. Sagi, J.; Hang, B.; Singer, B. *Chemical Research in Toxicology* **1999**, *22*, 917−923.

62. Barton, J. K. *Science* **1986**, *233*, 727−732.

63. Brunner, J.; Barton, J. K. *Journal of the American Chemical Society* **2006**, *128* (21), 6772−6773.

64. Erkkila, K. E.; Odom, D. T.; Barton, J. K. *Chemical Reviews* **1999**, *99* (9), 2777−2795.

65. Jackson, B. A. California Institute of Technology, Pasadena, **2001**.

CHAPTER 6: THE STRUCTURE OF $Rh(bpy)_2(chrysi)^{3+}$ BOUND TO AN ADENOSINE-ADENOSINE MISMATCH: GENERAL ARCHITECTURE OF THE METALLOINSERTION BINDING MODE[δ]

6.1: INTRODUCTION

Almost fifty years ago, L.S. Lerman proposed four different non-covalent binding modes for small molecules with DNA: (1) electrostatic binding to the sugar phosphate backbone, (2) hydrophobic association with the minor groove, (3) intercalation into the helix by π-stacking between adjacent base pairs, and (4) insertion into the helix by separation and displacement of a base pair.[1] The first three are frequently observed and have been extensively characterized both in solution and in the solid state.[2–6] In contrast, the fourth binding mode, insertion, has eluded researchers almost completely.[7] Recently, however, we have structurally characterized both by crystallography[8] and NMR[9] first examples of insertion into DNA by a small molecule: the mismatch-specific, octahedral metal complex $Rh(bpy)_2(chrysi)^{3+}$ (chrysi = chrysene-5,6-quinone diimine) (**Figure 6.1**).

Because insertion requires the separation of a base pair and the ejection of the bases from the double helix, it follows logically that this binding mode would occur more readily at thermodynamically destabilized sites in DNA. Indeed, to date, insertion has only been definitively observed with octahedral, coordinatively inert metal complexes bearing sterically expansive ligands, such as chrysi or phzi (benzo[a]phenanzine-5,6-quinone diimine)[10]; in both cases, the bulky ligands are 0.5 Å wider than the 10.85 Å

[δ] Adapted from Zeglis, B. M.; Pierre, V. C.; Kaiser, J. R.; Barton, J. K. A bulky rhodium complex bound to an adenosine-adenosine DNA mismatch: general architecture of the metalloinsertion binding mode. *Biochemistry* **2009**, *48(20)*, 4247−4253.

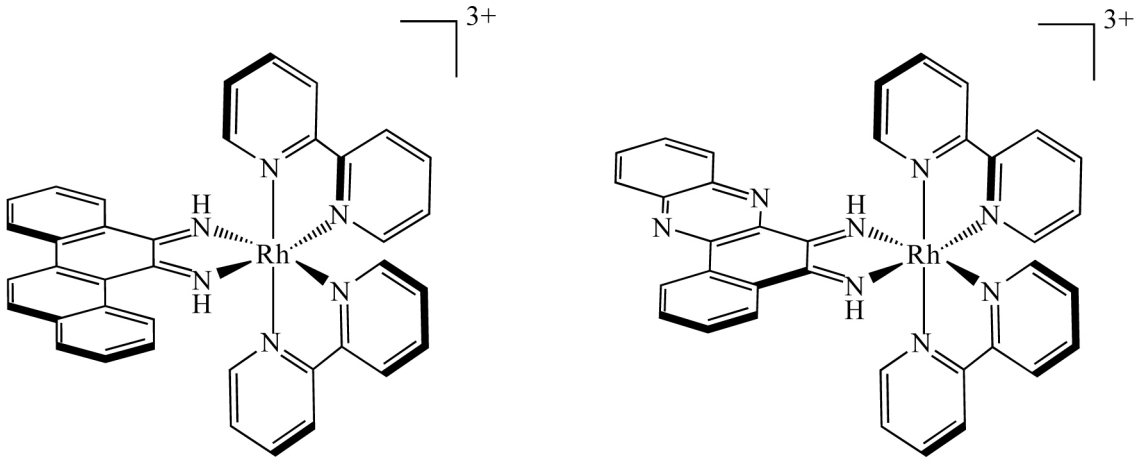

Δ-Rh(bpy)$_2$(chrysi)$^{3+}$ Δ-Rh(bpy)$_2$(phzi)$^{3+}$

Figure 6.1: Structures of Δ-Rh(bpy)$_2$(chrysi)$^{3+}$ and Δ-Rh(bpy)$_2$(phzi)$^{3+}$

span of a matched A•T or G•C base pair. This difference in width precludes the intercalation of the complex at matched sites and thus confers specificity for binding at thermodynamically destabilized mismatched sites.[11]

As we have discussed, rhodium metalloinsertors – most notably $Rh(bpy)_2(chrysi)^{3+}$ and $Rh(bpy)_2(phzi)^{3+}$ – bind single base mismatches with high selectivity and with binding affinities that correlate directly with the local destabilization created by the mismatch.[12–15] Importantly, upon irradiation with UV light, the complexes can photocleave the backbone of a single strand of the mismatched duplex at the binding site. Further still, mismatch binding by this family of complexes is enantiospecific, with only the right-handed, Δ-enantiomer capable of mismatch recognition and binding. Not surprisingly, the remarkable selectivity of these complexes has spurred investigations into their diagnostic and therapeutic applicability. Indeed, in the years since their discovery, metalloinsertors have shown significant promise not only in the detection of single base mismatches[16–18], abasic sites[19, 20], and single nucleotide polymorphisms[21] but also as chemotherapeutic agents.[22–25]

The crystallographic structure of Δ-$Rh(bpy)_2(chrysi)^{3+}$ bound to a palindromic oligonucleotide containing two C•A mismatches has recently been determined (**Figure 6.2**).[8] This structure first revealed that the mismatch-specific rhodium complex does not bind DNA through classical metallointercalation but rather by metalloinsertion: the complex approaches the DNA from the minor groove side and inserts the bulky chrysi ligand at the mismatch site, extruding the mismatched base pairs into the major groove and replacing them in the DNA π-stack. The sugar-phosphate backbone of the DNA opens slightly to accommodate the sterically expansive ligand at the mismatch site.

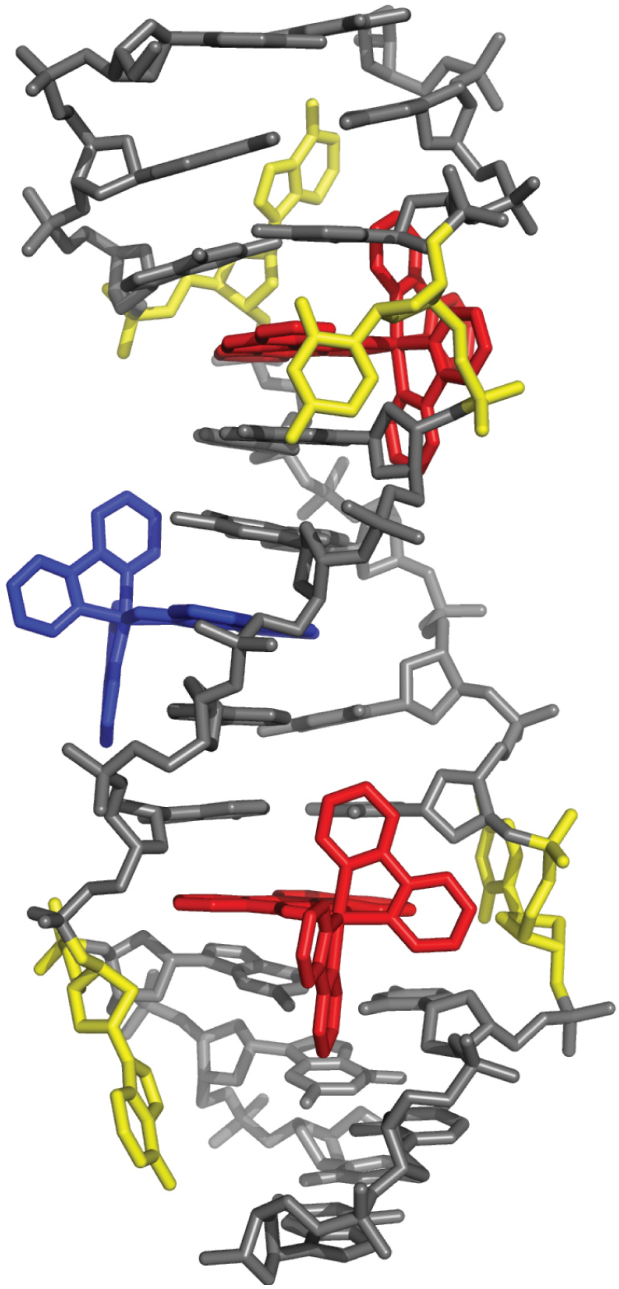

Figure 6.2: Crystal structure of $Rh(bpy)_2(chrysi)^{3+}$ bound to a C•A mismatch.[8] The metal complexes (red) approach the DNA (grey) from the minor groove, ejecting the mismatched bases (yellow) into the major groove and replacing them in the helix. Surprisingly, an intercalated rhodium complex (blue) is also present in the structure.

Overall, the DNA is disturbed very little beyond the insertion site, for all sugars remain in the C2'-endo conformation, and all bases retain an *anti* configuration. Somewhat surprising, however, was the presence of a third rhodium complex in the structure that is bound not through insertion at the mismatched sites but through intercalation at a central 5'-AT-3' step. Given that no detectable binding to a matched site has been observed for these bulky complexes in solution, we considered that this intercalation was the result of crystal packing forces. Subsequent NMR studies of Δ-$Rh(bpy)_2(chrysi)^{3+}$ bound to a similar oligonucleotide containing a C•C mismatch confirmed the insertion binding mode in solution and, significantly, showed no evidence of an intercalated rhodium moiety.[9]

The revelation that these compounds bind mismatches via metalloinsertion rather than metallointercalation provides explanations for two long-standing empirical observations: (1) the correlation between the binding affinity of the metal complex and the thermodynamic destabilization of the mismatched site and (2) the enantiospecificity of the metalloinsertors for the binding and recognition of their target sites. The relationship between binding strength and destabilization stems from the unique base extrusion characteristic of the binding mode: the less stable the mispair, the easier its separation and the more readily the metal complex can bind. The origin of the enantiospecificity lies in the groove-selectivity of metalloinsertion. Unlike metallointercalators, metalloinsertors bind via the narrow and sterically-constrictive minor groove. Simply put, in order to avoid steric clash between the ancillary ligands and the DNA backbone, the right-handed helix can only accommodate the right-handed (Δ) enantiomer.

Yet this structural knowledge can do far more than simply help us explain past observations. A thorough understanding of the detailed structure of metalloinsertion can help us design better recognition agents. However, one structure alone will not suffice. Additional structural information is necessary to shed light on the origin of the intercalated rhodium complex in the first structure and, more importantly, to illustrate the generality of the binding mode.

Here, we describe two crystal structures of Δ-$Rh(bpy)_2(chrysi)^{3+}$ bound to an A•A mismatch. Both structures provide examples of metalloinsertion at a new mismatch, but the two structures differ principally in the presence or absence of a third, intercalated rhodium. The comparison of these structures with studies of the metalloinsertor bound to a C•A and a C•C mismatch illuminates the general architecture of the metalloinsertion binding mode at destabilized sites in DNA.

6.2: EXPERIMENTAL PROTOCOLS

6.2.1: SYNTHESIS AND PURIFICATION

The metalloinsertor Δ-$Rh(bpy)_2(chrysi)^{3+}$ was co-crystallized with a self-complementary oligonucleotide containing two A•A mismatches (5'-$C_1G_2G_3\mathit{A}_4A_5A_6T_7T_8\mathit{A}_9C_{10}C_{11}G_{12}$-3'). The enantiopure rhodium complex was synthesized, purified, and isolated as described previously (see Chapter 2).[16] Standard oligonucleotides were synthesized from phosphoramidites on an ABI 3400 DNA synthesizer and purified both with and without the dimethoxytrityl protecting group via two rounds of reverse-phase HPLC (HP1100 HPLC system with Varian DynaMax™ C18 semi-preparative column, gradient of 5:95 to 45:55 MeCN:50 mM NH_4OAc (aq) over 30

min for DMT-on purification and 2:98 to 17:83 MeCN:50 mM NH_4OAc (aq) over 30 min for DMT-off purification).

6.2.2: CRYSTAL PREPARATION AND DATA COLLECTION

Annealed oligonucleotides were incubated with the rhodium complex before crystallization. Subsequent manipulations were performed with minimal exposure of the complex to light. Two different sets of bright orange crystals, henceforth referred to as **1** and **2**, were obtained, each under a distinct set of conditions. In both cases, thirteen different sequences were screened before crystals were obtained with the sequence described above. Crystal set **1** was grown from a solution of 1 mM double-stranded duplex, 3 mM enantiomerically pure Δ−$Rh(bpy)_2(chrysi)^{3+}$, 20 mM sodium cacodylate (pH 7.0), 6 mM spermine·4HCl, 40 mM NaCl, and 5% 2-methyl-2,4-pentanediol (MPD) equilibrated in sitting drops versus a reservoir of 35% MPD at ambient temperature. The crystals grew in space group $P3_221$ with unit cell dimensions a = b = 48.34 Å, c = 69.50 Å, $\alpha = \beta = 90°$, $\gamma = 120°$, with one biomolecule per asymmetric unit (**Table 6.1**).

Crystal set **2** was grown from a solution of 1 mM double-stranded duplex, 2 mM enantiomerically pure Δ−$Rh(bpy)_2(chrysi)^{3+}$, 20 mM sodium cacodylate (pH 7.0), 6 mM spermine·4HCl, 40 mM KCl, and 5% MPD equilibrated in sitting drop versus a reservoir of 35% MPD at ambient temperature. The crystals grew in space group $P4_32_12$ with unit cell dimensions a = b = 39.02 Å, c = 57.42 Å, $\alpha = \beta = \gamma = 90°$, with half of a biomolecule per asymmetric unit (**Table 6.1**).

	Structure 1	Structure 2
Data Collection		
Space group	$P3_121$	$P4_32_12$
Cell dimensions: a, b, c α, β, γ	 48.3, 48.3, 69.5 90.0, 90.0, 120.0	 39.0, 39.0, 57.4 90.0, 90.0, 90.0
Wavelength	1.0046	1.5418
Resolution	35.0−1.60 (1.69−1.60)	28.71−1.80 (1.90−1.80)
R_{merge}	0.035 (0.499)	0.061 (0.782)
R_{pim}	0.013 (0.288)	0.031 (0.342)
I/σI	26.7 (2.0)	19.1 (2.3)
Completeness, %	99.5 (98.9)	98.7 (97.4)
Redundancy	7.9 (4.2)	6.5 (6.6)
Refinement		
No. of Reflections	22677	4469
R_{work}/R_{free}	0.184/0.227	0.183/0.213
No. of atoms (DNA)	524	262
No. of atoms (RhL_6)	120	90
No. of atoms (water)	89	63
B-factors (DNA)	43.44	25.7
B-factors (complex)	43.44	22.1
B-factors (water)	48.86	41.4
RMS dev. (lengths)	0.013	0.032
RMS dev. (angles)	2.450	4.281

Table 6.1: Data collection and refinement statistics

The data for crystal **1** were collected on beamline 11−1 at the Stanford Synchrotron Radiation Laboratory (Menlo Park, CA; λ = 1.00 Å, 100 K, Marresearch 325 CCD detector). The data for crystal **2** were collected from a flash-cooled crystal at 100 K on an R-axis IV image plate using CuKα radiation produced by a Rigaku (Tokyo, Japan) RU-H3RHB rotating-anode generator with double-focusing mirrors and an Ni filter. Both sets of data were processed with MOSFLM and SCALA from the CCP4 suite of programs.[26]

6.2.3: CRYSTAL STRUCTURE DETERMINATION AND REFINEMENT

Both structures were solved by single anomalous dispersion using the anomalous scattering of rhodium (f" = 3.6 electrons for Rh at λ = 1.54 Å, and f" = 1.7 electrons for Rh at λ = 1.00 Å) with the CCP4 suite of programs. For crystal **1**, 2 heavy atoms were located per asymmetric unit; for crystal **2**, 1.5 heavy atoms were located per asymmetric unit, with one on a special position. Structure **1** was refined with PHENIX v. 1.3 against 1.6 Å data taking into account the anomalous contribution of rhodium; for non-hydrogen atoms, anisotropic temperature factors were refined.[27] The final R_{cryst} and R_{free} were 0.18 and 0.23, respectively. Structure **2** was refined using REFMAC5 v. 5.5.0066 against 1.8 Å data to a final R_{cryst} = 0.18 and R_{free} = 0.21.[a, 28]

In crystal **2**, the rhodium complex located near the crystallographic twofold axis perpendicular to the helical axis of the DNA intercalates in two different orientations linked by symmetry. In crystal **1**, residual density with anomalous contribution was also present near a crystallographic two-fold axis at the end of the duplex, most likely the

[a] The two structures were solved with different but widely employed refinement programs.

result of a disordered cacodylate or chloride ion. In the later stages of refinement for both crystals, riding hydrogens were included. Figures were drawn with Pymol.[29]

6.3: Results and Discussion

6.3.1: Two types of crystals

The palindromic oligonucleotide 5'-$C_1G_2G_3\mathit{A}_4A_5A_6T_7T_8\mathit{A}_9C_{10}C_{11}G_{12}$-3' contains two adenosine-adenosine mismatches, each situated three bases from the end of the strand and separated from one another by a central 5'-AATT-3' tetrad. Here, the duplex was co-crystallized with Δ-$Rh(bpy)_2(chrysi)^{3+}$ for high-resolution x-ray structure determination in order to improve our understanding of metalloinsertion at DNA single base mismatches. Interestingly, diffraction quality crystals with two different space groups ($P3_221$ and $P4_32_12$) were obtained under very similar crystallization conditions. Indeed, both crystals were grown with the same temperature, buffer, pH, type and concentration of precipitant, concentration of DNA, and concentration of spermine. The only differences are the concentration of metalloinsertor and the identity of salt employed: crystal **1** ($P3_221$), containing 2 rhodiums per duplex, was obtained using 3 mM complex and 40 mM NaCl, and crystal **2** ($P4_32_12$), containing 3 rhodiums per duplex, was obtained using 2 mM metalloinsertor and 40 mM KCl. Taken together, the structures of crystal **1** (1.6 Å) and **2** (1.8 Å) provide insights into the structure and generality of metalloinsertion.

6.3.2: STRUCTURE 1

In crystal **1**, the oligonucleotide co-crystallizes with the metalloinsertor in the space group $P3_221$, with six asymmetric units per unit cell. The asymmetric unit contains one DNA duplex complexed with two metalloinsertors (**Figure 6.3**). Significantly, crystallization breaks the C_2 symmetry of the DNA-metalloinsertor palindromic assembly, rendering the two mismatch sites inequivalent and providing two independent views of the mismatched site. Inspection of the unit cell reveals that the duplexes do not stack head-to-tail to form a longer double helix, as is frequently observed with DNA.[3] Instead, it is the inter-duplex π-stacking of the ejected adenosines — either interwoven with the ancillary bipyridine ligand of a nearby rhodium complex or stacked with an adjacent, ejected adenosine — that determines the overall crystal packing and thus the space group (**Figure 6.4**).

At both mismatched sites, the metal complex inserts from the minor groove by separating and ejecting the mismatched bases, and the sterically expansive chrysi ligand of the metalloinsertor replaces the destabilized bases in the helical π-stack (**Figures 6.5** and **6.6**). The two ejected purines are pushed outward into the major groove. One of them remains close and perpendicular to the base stack, while the other folds back to the minor groove in a position stabilized by crystal packing. In both cases, deep insertion in the double helix is not inhibited by the increased steric hindrance of the minor groove; the distance between the rhodium center and the helical axis is 4.8 Å, approximately half the radius of the duplex.

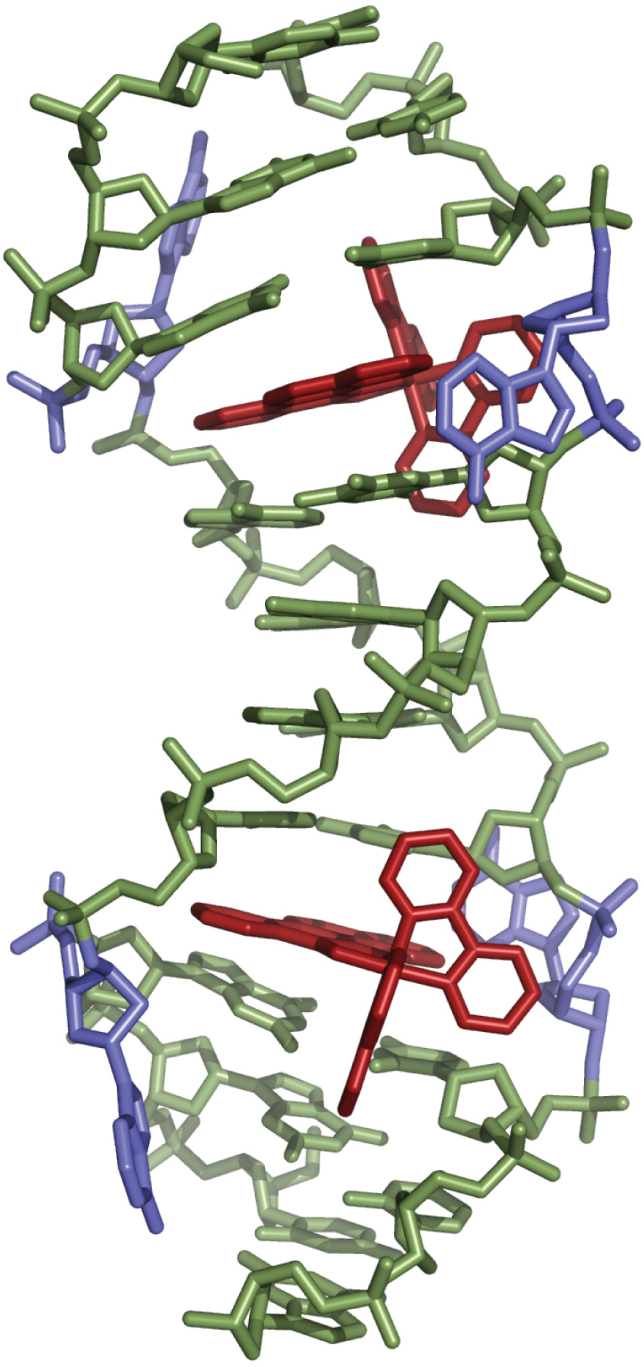

Figure 6.3: Structure 1. Two Δ-Rh(bpy)$_2$(chrysi)$^{3+}$ (red) are inserted, one in each A•A mismatch of the oligonucleotide 5'-CGG*A*AATT*A*CCG-3' (green). The ejected adenosines are shown in blue.

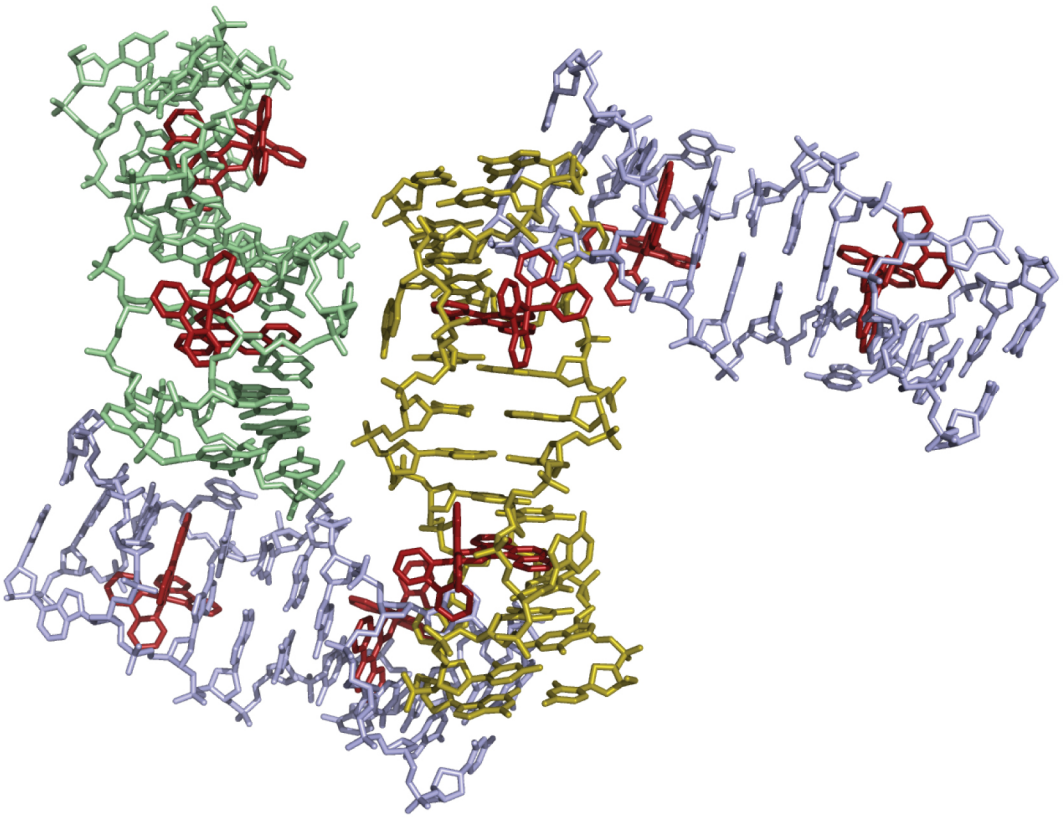

Figure 6.4: Packing of helices in structure 1. The helices are not packed end-to-end, as is commonly observed in crystal structures of DNA oligonucleotides. Instead, inter-duplex π-stacking of the ejected adenosines leads to a packing arrangement that renders the two mismatch sites in a given duplex inequivalent.

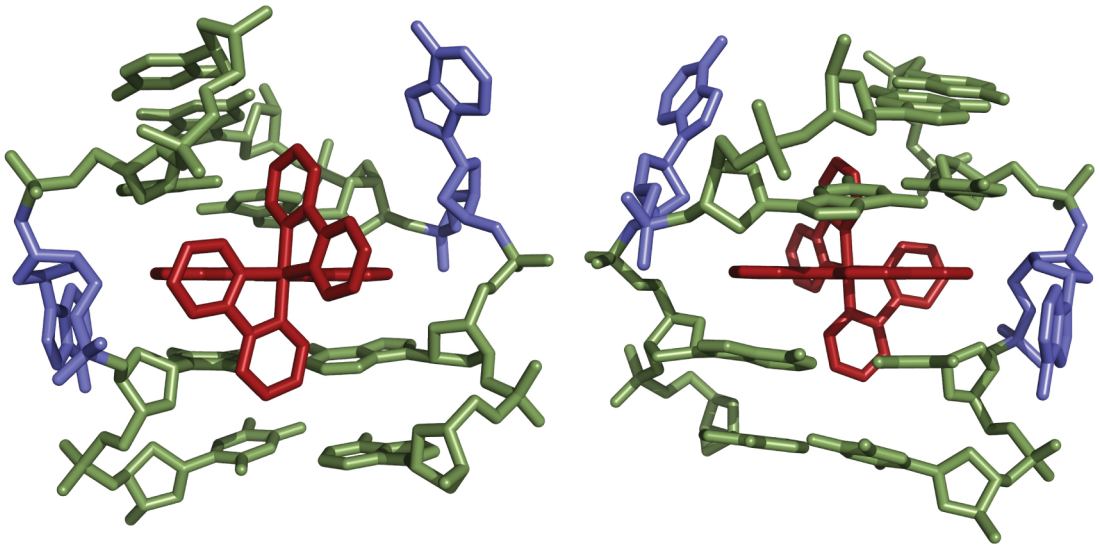

Figure 6.5: Detailed structures of metalloinsertion sites in structure 1. Views of metalloinsertion at an A•A mismatch from the minor (left) and major (right) grooves are shown.

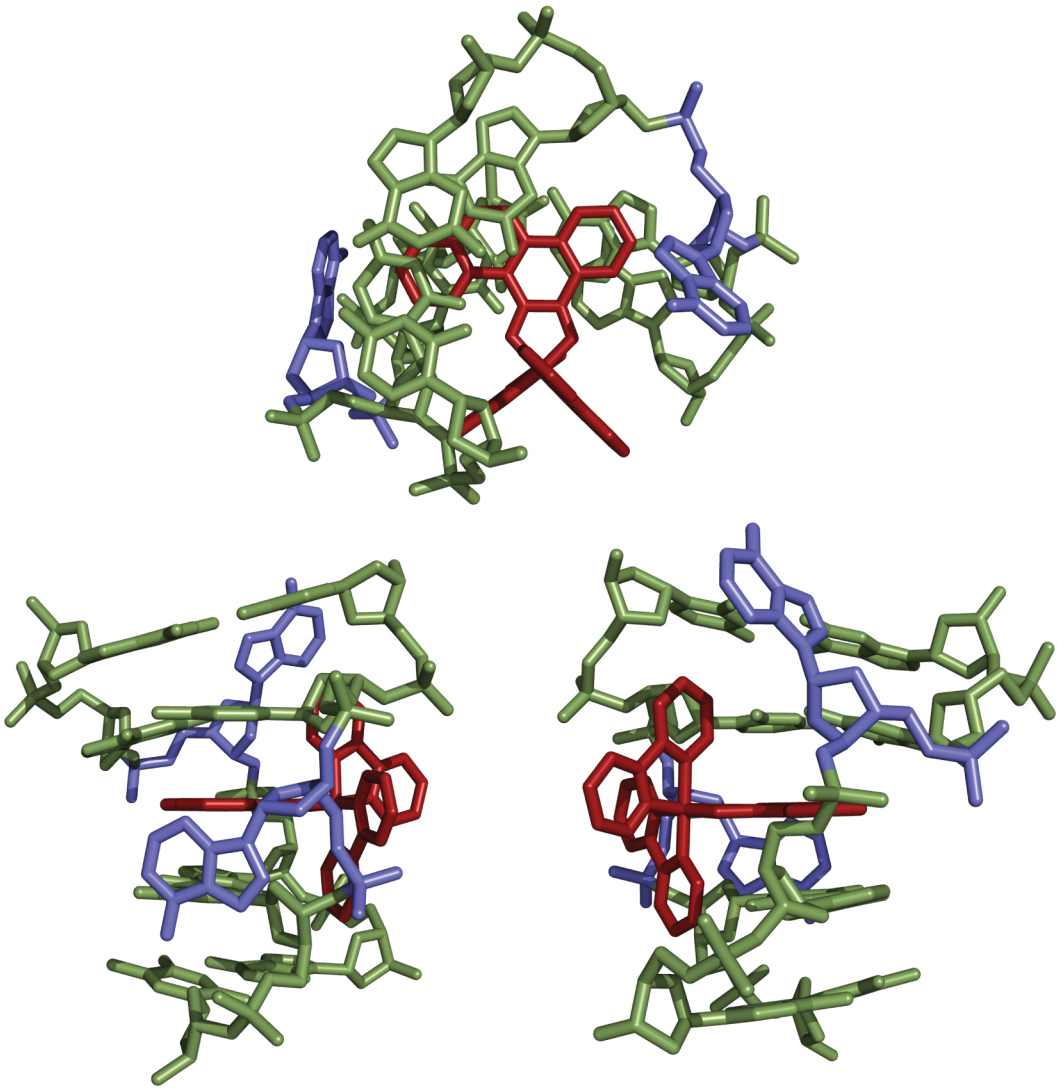

Figure 6.6: Detailed structures of metalloinsertion sites in structure 1. Views of metalloinsertion at an A•A mismatch from along the helical axis (top) and from the phosphate backbone (bottom left, bottom right) are shown.

Upon binding, the rhodium complex inserts deeply to enable complete overlap and stacking with both the purines and pyrimidines of the flanking base pairs. Importantly, these flanking base pairs neither stretch nor shear despite the considerable width of the ligand. All sugars retain their original C_2'-*endo* puckering, and all bases maintain their initial *anti* conformation. To accommodate the inserted rhodium complex, the minor groove at the binding site widens to 19 Å from phosphate to phosphate, between 1 and 1.5 Å wider than other points in the duplex. Aside from the opening of the phosphodiester junctions at the insertion site, however, very little distortion of the DNA is observed (**Tables 6.2** and **6.3**).

The difference between the two insertion sites lies only in the crystal packing of the ejected adenosines. At one of the two insertion sites, one of the ejected adenosines is stacked tightly within the major groove, where it lies perpendicular to the DNA base stack and is not involved in any interduplex interactions or hydrogen-bonding. In contrast, the other adenosine at this site is interwoven with and π-stacks between the ejected adenosine from an adjacent duplex and the ancillary bipyridine ligand of the rhodium complex inserted in that nearby oligonucleotide. At the second insertion site, one of the ejected adenosines again π-stacks between the ejected adenosine from a second adjacent oligonucleotide and the ancillary bipyridine of the rhodium complex intercalated in that nearby DNA. Unlike the first insertion site, however, the other ejected adenosine here does partake in π-stacking, in this case with an extruded adenosine of yet another nearby duplex (**Figure 6.7**).

Base step	Shift (Å)	Slide (Å)	Rise (Å)	Tilt (°)	Roll (°)	Twist (°)
CG/CG	0.8	2.2	3.4	12.0	-1.6	37.6
GG/CC	-0.3	2.7	3.2	-6.1	5.7	34.3
GA/TC	-	-	-	-	-	-
AA/TT	-1.3	1.2	3.3	-4.7	3.8	37.6
AT/AT	0.0	0.1	3.4	1.3	-0.7	29.6
TT/AA	1.3	1.0	3.4	2.2	5.6	36.1
TC/GA	-	-	-	-	-	-
CC/GG	0.4	2.7	3.3	4.7	6.5	34.5
CG/CG	1.0	2.5	3.2	-8.2	2.1	37.3
B-DNA	-0.1	-0.8	3.3	-1.3	-3.6	36

Table 6.2: DNA helical parameters[b] relating consecutive base pairs of structure 1[c]

[b] Geometrical relationships between consecutive base pairs: shift, translation into the groove; slide, translation toward the phosphodiester backbone; rise, translation along the helix axis; tilt, rotation about the pseudo-two-fold axis relating the DNA strands; roll, rotation about a vector between the C1' atoms; and twist, rotation about the helix axis.

[c] Data were calculated by using the program 3DNA.[30]

Base pair	Shear (Å)	Stretch (Å)	Stagger (Å)	Buckle (°)	Propeller (°)	Opening (°)	Pucker
C•G	0.1	-0.1	0.9	-10.0	-2.5	-2.8	C2'-endo
G•C	-0.2	-0.1	-0.0	-0.2	1.1	-3.8	C2'-endo
G•C	-0.4	-0.1	0.6	15.0	-7.2	-1.3	C2'-endo
A•A	-	-	-	-	-	-	C2'-endo
A•T	-0.1	-0.1	0.0	-8.6	7.2	1.5	C2'-endo
A•T	0.1	-0.1	0.1	-0.0	-8.3	3.2	C2'-endo
T•A	-0.0	-0.0	0.0	-0.8	-8.0	1.1	C2'-endo
T•A	-0.1	-0.2	0.1	5.8	9.4	1.7	C2'-endo
A•A	-	-	-	-	-	-	C2'-endo
C•G	0.3	-0.1	0.6	-18.8	-5.8	-0.5	C2'-endo
C•G	0.2	-0.1	0.1	-3.9	2.0	-0.5	C2'-endo
G•C	-0.3	-0.1	0.4	6.2	-5.3	0.7	C2'-endo
B-DNA	0	0.1	0.1	0.1	4.1	-4.1	C2'-endo

Table 6.3: DNA helical parameters for the base pairs of structure 1[d]

[d] Data were calculated by using the program 3DNA.[30]

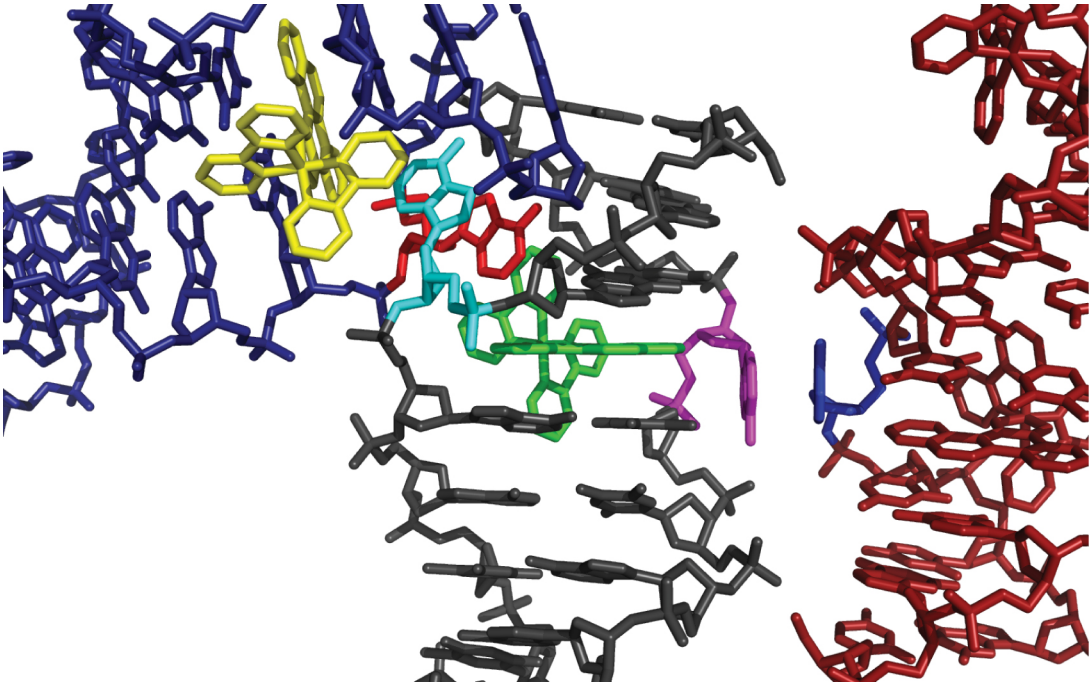

Figure 6.7: Crystal packing by the ejected adenosines at one of the metalloinsertion sites in structure 1. At both insertion sites of the duplex, one ejected adenosine (cyan) π-stacks in an interwoven fashion with the bipyridine ligand of a rhodium complex (yellow) inserted in a nearby crystallographically related oligonucleotide and its corresponding ejected adenosine (red). The bipyridine ligand of the rhodium complex in the original duplex (green) completes the four-component stacking. In only one of the two insertion sites, as shown here, the second mismatched adenosine ejected in the major groove (magenta) π-stacks with a crystallographically equivalent ejected major groove adenosine (blue).

6.3.3: STRUCTURE 2

In crystal **2**, the oligonucleotide co-crystallizes with the metalloinsertor in the space group $P4_32_12$. In this case, the asymmetric unit is a single DNA strand with 1.5 metalloinsertors. Each duplex thus contains three rhodium complexes, one inserted at each of the mismatched sites and a third intercalated between the adenosine and thymine of the central 5'-AT-3' step (**Figure 6.8**). Due to its position on a crystallographic two-fold axis, the central rhodium intercalates in two different orientations. The rhodium complexes at the two mismatched sites are also related by C_2 symmetry, providing a single, independent view of the insertion site (**Figure 6.9**). Interestingly, in all respects other than the identity of the mismatch, this structure is virtually identical to that previously published for Δ-$Rh(bpy)_2(chrysi)^{3+}$ bound to a C•A mismatch.[8]

At the A•A mismatch site, the metalloinsertor approaches the DNA from the minor groove, ejects the mispaired adenines from the helix, and replaces them in the DNA base stack with its own sterically expansive chrysi ligand. Indeed, the metalloinsertor π-stacks with the flanking A•T and C•G base pairs and penetrates so deeply from the minor groove that it is solvent accessible from the major groove. One of the ejected adenosines sits in the major groove, positioned perpendicular to the DNA base stack. The other adenosine bends back into the minor groove, where it π-stacks between the ejected adenosine of an adjacent duplex and a bipyridine ligand of a metalloinsertor bound to that oligonucleotide. Insertion of the rhodium complex into the site is facilitated by a slight widening of the phosphate backbone, from an average of 17.5 Å for well-matched sites to 19 Å for the metalloinsertion sites. Indeed, beyond this

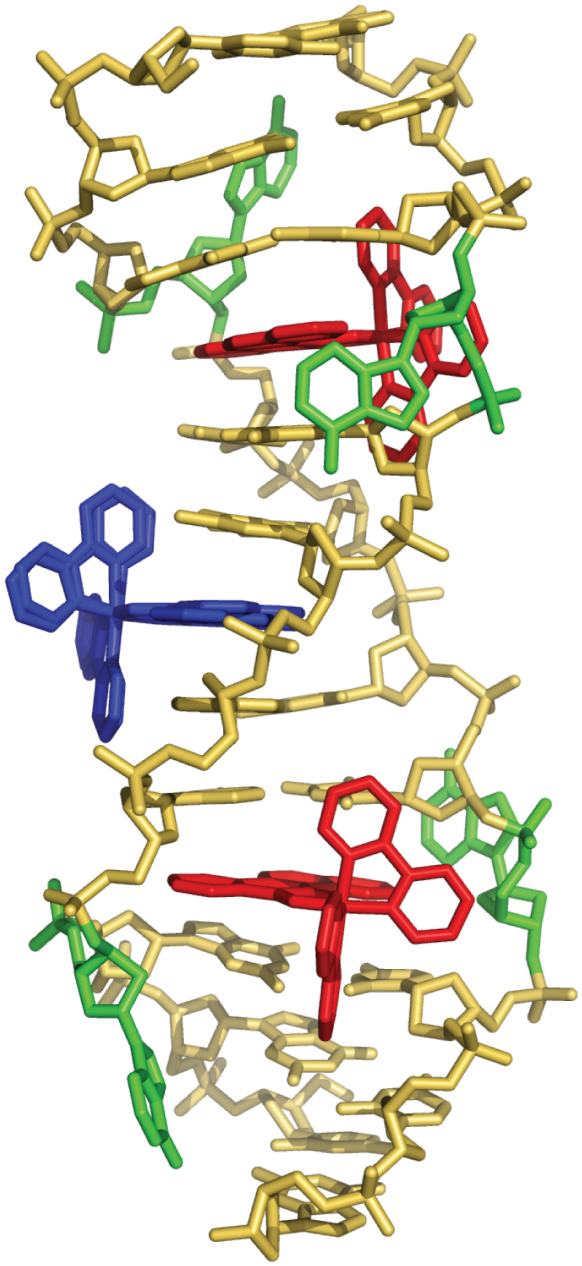

Figure 6.8: Structure 2. Two Δ-Rh(bpy)$_2$(chrysi)$^{3+}$ (red) are inserted, one in each A•A mismatch of the oligonucleotide 5'-CGG*A*AATT*A*CCG-3' (yellow). A third rhodium complex (blue) is intercalated at the central 5'-AT-3' step. The ejected adenosines are shown in green.

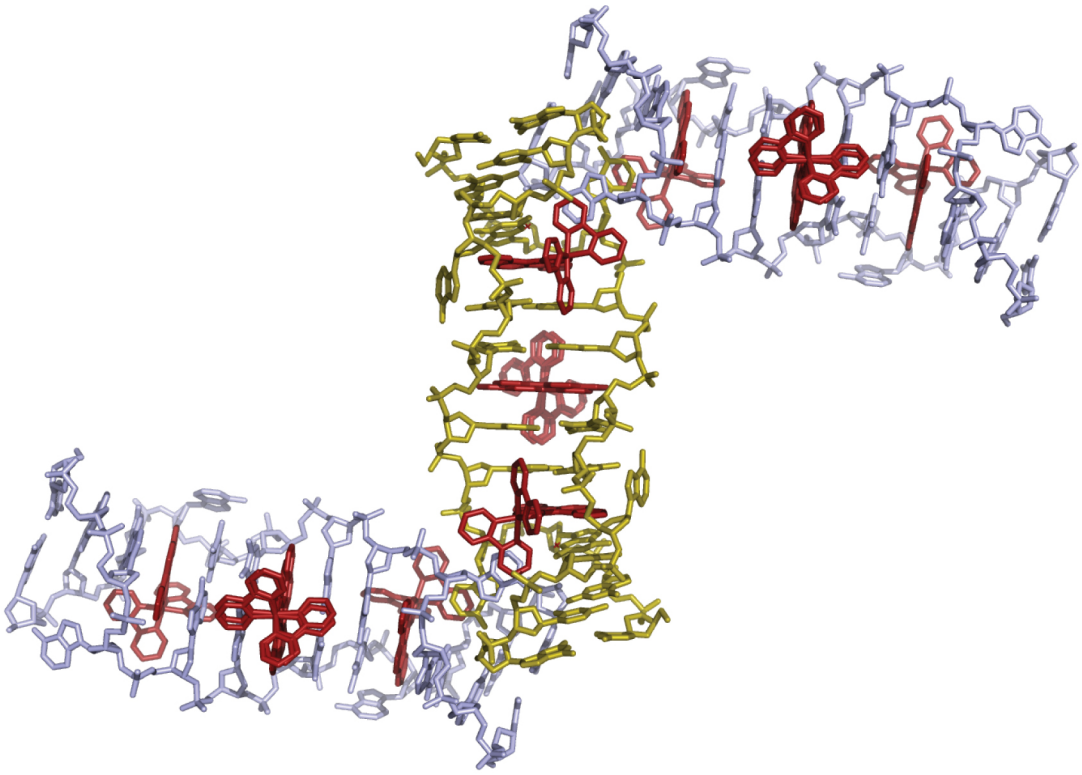

Figure 6.9: Packing of helices in structure 2. The helices are not packed end-to-end, as is commonly observed. Instead, inter-duplex π-stacking of the ejected adenosines leads to packing arrangement in which the two metalloinsertion sites are equivalent.

conformational change, metalloinsertion again distorts the DNA very little. Some buckling of the external flanking C•G base pairs is observed, but all riboses exhibit C2'-*endo* puckering, and all bases retain an *anti* configuration (**Tables 6.4** and **6.5**).

As in the C•A mismatch structure, a third Δ-$Rh(bpy)_2(chrysi)^{3+}$ is also found intercalated at the central 5'-AT-3' step.[8] At this site, the rhodium complex approaches the duplex from the major groove and intercalates the chrysi ligand between adjacent A•T and T•A base pairs, doubling the rise at the intercalation site to 7.1 Å and slightly unwinding the duplex. This binding interaction resembles closely that previously observed in the crystal structure of the sequence-specific metallointercalator Δ-α-$Rh[(R,R)\text{-}Me_2trien](phi)^{3+}$ bound by classical intercalation to its target site.[3] The intercalative binding, like insertion, is accommodated by a slight widening of the phosphate backbone at the intercalation site and is accompanied by some buckling of the adjacent base pairs. Given the exquisite mismatch selectivity of the metalloinsertors in solution, such intercalative binding is a surprise and is almost certainly the result of crystal packing forces. The bipyridines of the intercalated metal complex π-stack with the terminal C•G base pairs of two crystallographically related duplexes, in essence making the intercalated rhodium complex a linchpin for the crystal packing (**Figure 6.10**).

6.3.4: DIFFERENCES BETWEEN THE TWO STRUCTURES

Certainly the most prominent difference between the two structures is the presence or absence of a Δ-$Rh(bpy)_2(chrysi)^{3+}$ intercalated at the central 5'-AT-3' step. Given the similarity in crystallization conditions for crystals **1** and **2**, the rhodium

Base step	Shift (Å)	Slide (Å)	Rise (Å)	Tilt (°)	Roll (°)	Twist (°)
CG/CG	1.1	2.2	3.0	11.0	2.8	40.0
GG/CC	-0.4	2.7	3.3	-6.0	6.1	34.8
GA/TC	-	-	-	-	-	-
AA/TT	-0.8	0.8	3.3	0.4	4.3	32.2
AT/AT	0.0	-0.2	7.1	0.0	-10.4	27.3
TT/AA	0.8	0.8	3.3	-0.4	4.3	32.2
TC/GA	-	-	-	-	-	-
CC/GG	0.4	2.7	3.3	6.0	6.1	34.8
CG/CG	-1.1	2.2	3.0	-11.0	2.8	30.0
B-DNA	-0.1	-0.8	3.3	-1.3	-3.6	36

Table 6.4: DNA helical parameters[e] relating consecutive base pairs of structure 2[f]

[e] Geometrical relationships between consecutive base pairs: shift, translation into the groove; slide, translation toward the phosphodiester backbone; rise, translation along the helix axis; tilt, rotation about the pseudo-two-fold axis relating the DNA strands; roll, rotation about a vector between the C1' atoms; and twist, rotation about the helix axis.

[f] Data were calculated by using the program 3DNA.[30]

Base pair	Shear (Å)	Stretch (Å)	Stagger (Å)	Buckle (°)	Propeller (°)	Opening (°)	Pucker
C•G	0.0	-0.3	0.8	-16.2	-2.4	-4.	C2'-endo
G•C	-0.2	-0.3	0.0	3.4	1.4	-2.1	C2'-endo
G•C	-0.3	-0.1	0.5	18.0	-6.0	0.2	C2'-endo
A•A	-	-	-	-	-	-	C2'-endo
A•T	-0.1	-0.1	0.1	-1.3	8.6	5.0	C2'-endo
A•T	0.1	-0.2	0.2	7.3	-6.9	1.2	C2'-endo
T•A	-0.1	-0.2	0.2	-7.3	-6.9	1.2	C2'-endo
T•A	0.1	-0.1	0.1	-1.3	-8.6	5.0	C2'-endo
A•A	-	-	-	-	-	-	C2'-endo
C•G	0.3	-0.1	0.5	-18.0	-6.0	0.2	C2'-endo
C•G	0.2	-0.3	0.0	-3.4	-1.4	-2.1	C2'-endo
G•C	-0.1	-0.3	0.8	16.2	-2.4	-4.9	C2'-endo
B-DNA	0	0.1	0.1	0.1	4.1	-4.1	C2'-endo

Table 6.5: DNA helical parameters for the base pairs of structure 2[g]

[g] Data were calculated by using the program 3DNA.[30]

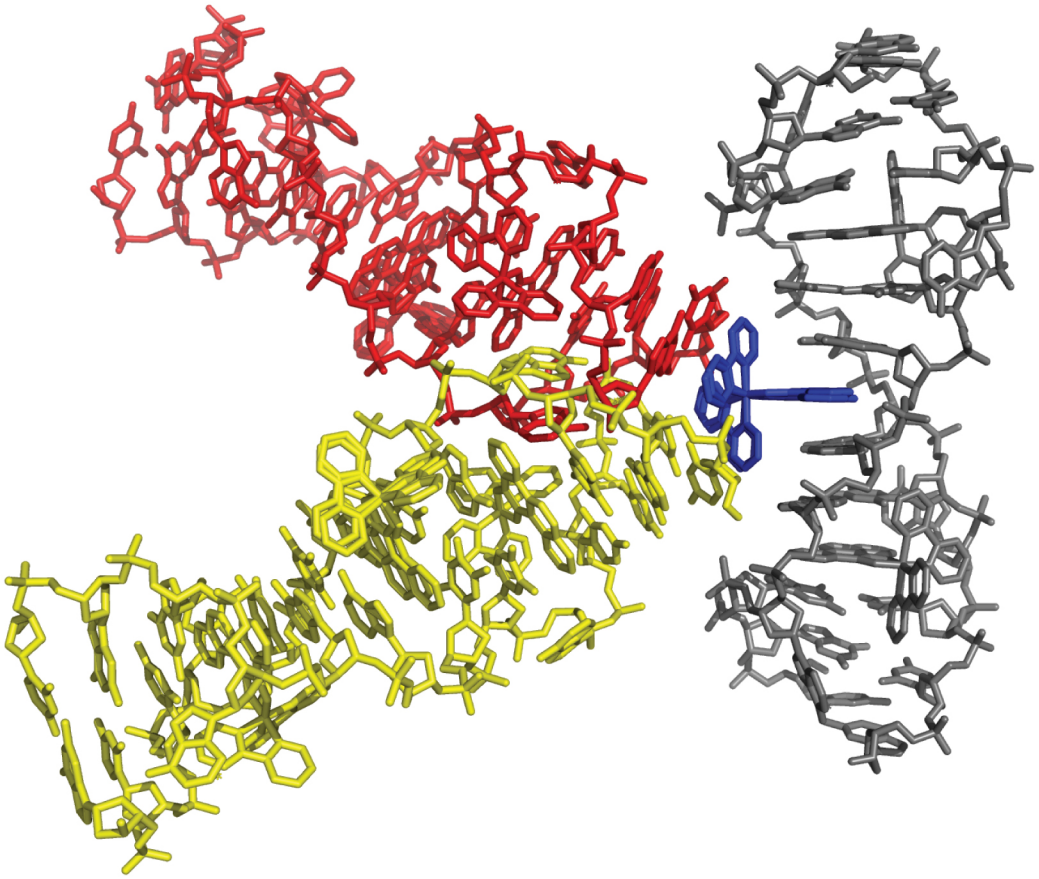

Figure 6.10: Crystal packing of the intercalated $Rh(bpy)_2(chrysi)^{3+}$ in structure 2. Two duplexes (red and yellow) pack against the bipyridine ligands of the intercalated $Rh(bpy)_2(chrysi)^{3+}$ (blue). The metal complex is a linch-pin for the crystal packing.

complex likely has comparable affinity for this central matched site in both cases. That the intercalated rhodium complex *is not* observed in structure **1** therefore strongly substantiates our conclusion that Δ-$Rh(bpy)_2(chrysi)^{3+}$ has negligible affinity for matched DNA and only binds to such sites when intercalation is stabilized by crystal packing-driven π-stacking. In structure **2** and the previously reported C•A mismatch structure, intercalation at the matched site is supported by π-stacking between the ancillary bipyridines of the intercalated rhodium complex and the terminal C•G base pairs of two adjacent helices.[8] Moreover, interwoven stacking between rhodium moieties in these latter duplexes and ejected purines further serves to lock the helices in an orientation that favors intercalative binding. These interactions, taken together, promote the binding of the metalloinsertor in a mode that is not detectable in solution. In fact, the interactions are insufficient to enforce complete intercalation into the double helix (the Rh-helical axis distance in the C•A mismatch structure, for example, is 1.2 Å longer than that of the DNA-bound metallointercalator Δ-α-Rh[(R,R)-Me_2trien](phi)$^{3+}$).[3, 8] These structures thus provide a cautionary example of how crystal packing forces may alter the binding of small molecules to DNA.

The intercalated Δ-$Rh(bpy)_2(chrysi)^{3+}$ in structure **2** is likely also responsible for a second major difference between the structures. Upon superposition of the two structures, it becomes evident that the duplex in structure **1** is slightly bent relative to that in structure **2** (**Figure 6.11**). Examination of the two mismatch-bound chrysi ligands in each structure is particularly instructive in this regard; in structure **2**, the two ligands are nearly coplanar, whereas in structure **1**, they are clearly skew relative to one another (**Figure 6.12)**. Because few perturbations to the duplex are observed beyond the

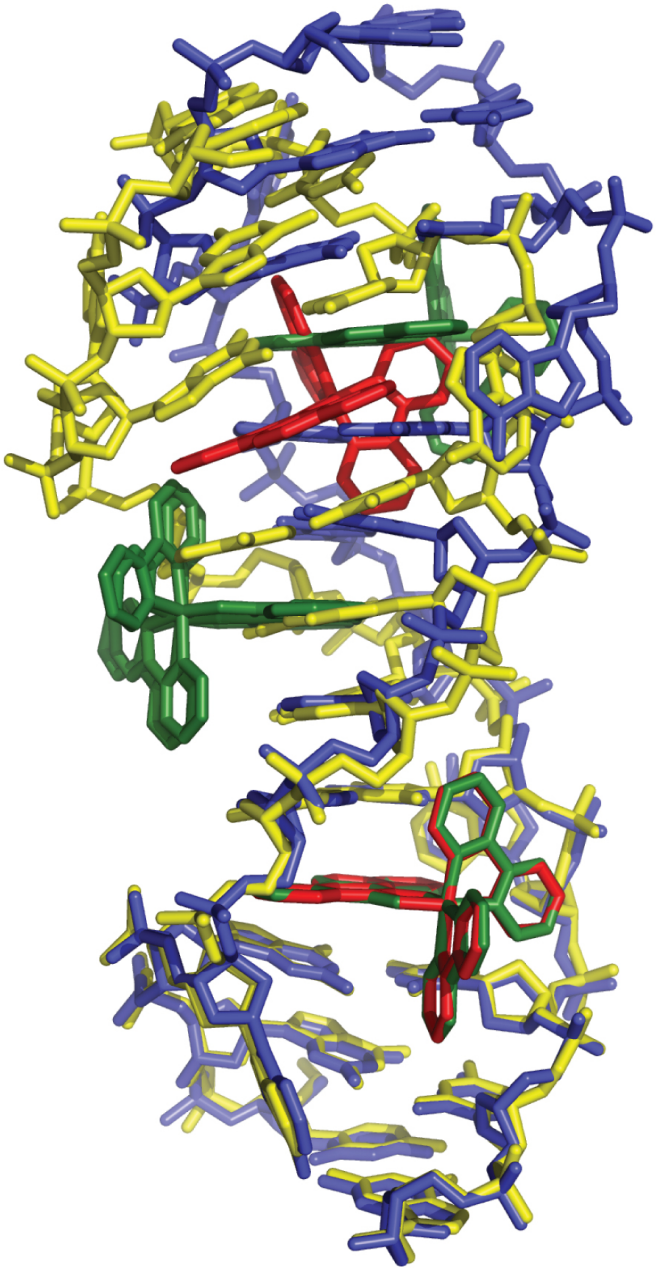

Figure 6.11: Superposition of structures 1 and 2. Structure **1** (yellow DNA with red metal complexes) is contrasted to structure **2** (blue DNA with green metal complexes) by superimposing the bottom, mismatch-bound $Rh(bpy)_2(chrysi)^{3+}$. Note the pronounced bending of the duplex of structure **1**.

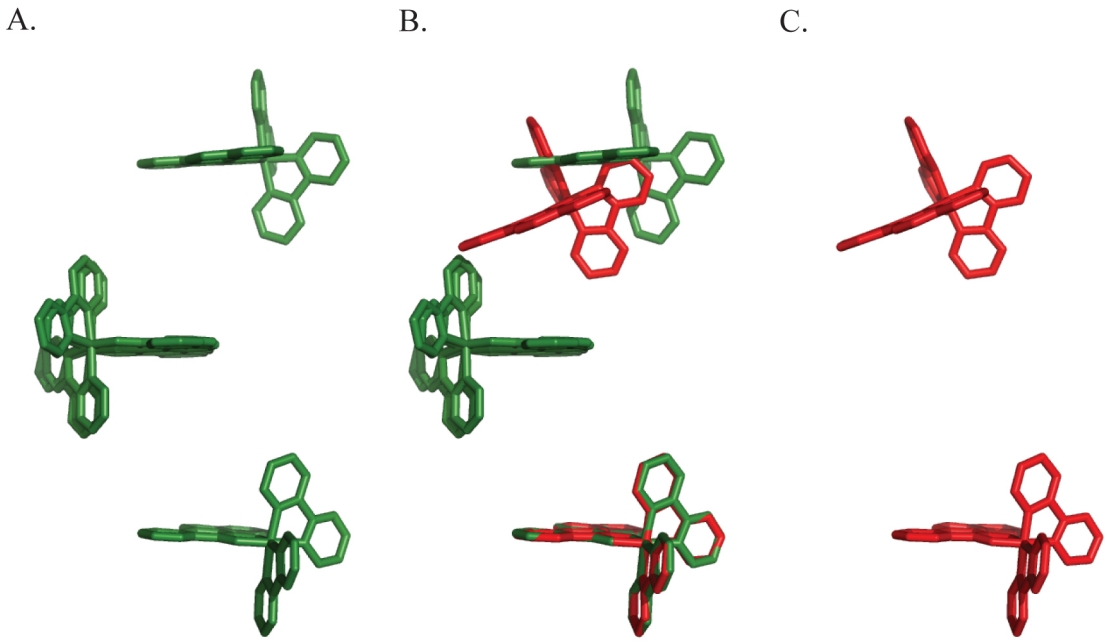

Figure 6.12: The metal complexes of structures 1 and 2. The metal complexes from structure 1 (C) and 2 (A) are shown. A superposition of the two sets of complexes (B) further emphasizes the skewed orientation of those from structure 1 compared to those from structure 2.

mismatched base pair itself in either structure, it is improbable that the metalloinsertors are responsible for this bend in the duplex. Rather, the slight bending is most likely a result of the flexibility associated with the base step. It follows that in structure **2**, the centrally intercalated and well-stacked rhodium complex rigidifies and straightens the helix.

A third major difference between the two structures lies in the stacking of the extrahelical adenosines. The interduplex, four component π-stacking interactions of one of the ejected adenosines at each mismatch site is common to both structures reported here, as well as the previously published C•A mismatch structure.[8] It is with the second ejected base at each mismatch site that differences arise. At each A•A mismatch site in structure **2** and in the C•A mismatch structure, the second ejected adenosine or ejected cytosine, respectively, sits tightly within the major groove, perpendicular to the DNA base stack and uninvolved in any π-stacking or hydrogen bonding. The same is true for the second ejected adenosine at one of the two A•A mismatch sites in structure **1**. At the other A•A site in structure **1**, however, the second ejected adenosine lies near the major groove, remains close to the phosphate backbone, and π-stacks with the ejected adenosine of a nearby duplex (**Figure 6.7**).

6.3.5: GENERAL ARCHITECTURE OF THE INSERTION BINDING MODE

What is perhaps most remarkable about these crystal structures is not their differences but their similarity, not only to one another but also to the earlier structure we obtained.[8] The superposition of the four independent views of Δ-$Rh(bpy)_2(chrysi)^{3+}$ bound to a mismatched site (3 A•A sites, 1 C•A site, **Figure 6.13**) reveals how

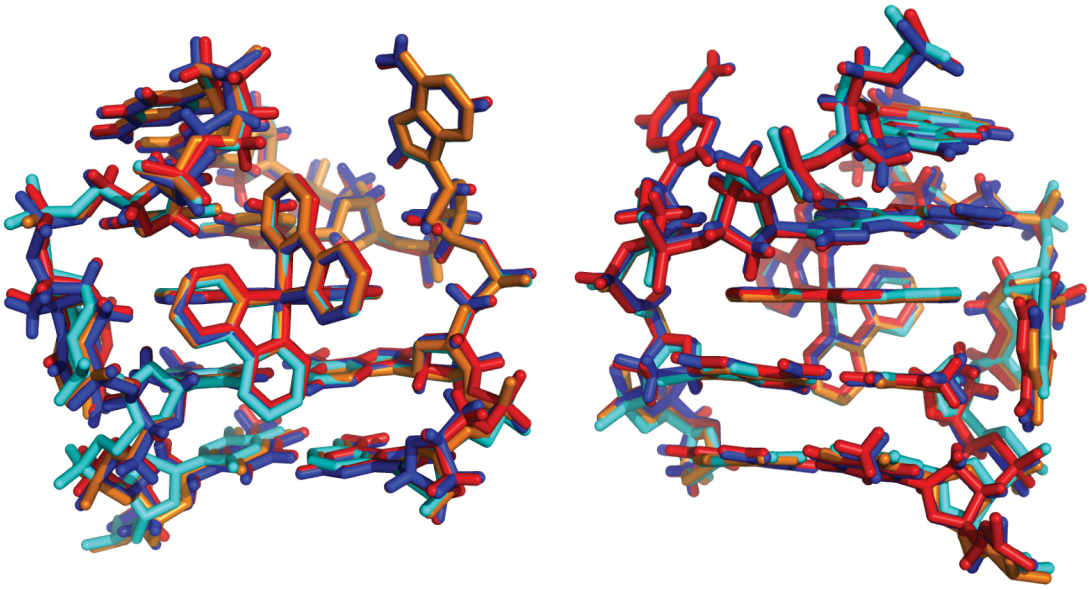

Figure 6.13: General architecture of metalloinsertion. Superposition of the three crystal structures showing insertion of Δ-Rh(bpy)$_2$(chrysi)$^{3+}$ into a single base mismatch viewed looking into the major groove (left) or minor groove (right). The red, blue, and orange structures represent insertion at an A•A mismatch as reported in this work (red and blue are the two sites from structure **1**, and orange is from structure **2**). The cyan structure represents insertion at a C•A mismatch as previously reported.[8]

every detail of the insertion binding mode is maintained regardless of the type of mismatch. In all cases, the DNA conformational changes are localized to the binding site. The metal complex essentially replaces the mismatched base pair; there is no increase in rise, no change in stacking, and no change in sugar puckering. In every case, Δ−$Rh(bpy)_2(chrysi)^{3+}$ is well stacked with the matched DNA bases and penetrates the DNA so deeply that it protrudes from the opposite major groove. Furthermore, in each study, this binding is accommodated by a slight opening in the phosphodiester backbone, and the DNA is only minimally perturbed beyond the insertion site: all bases maintain their original *anti* conformation, all sugars retain a C_2'-*endo* puckering, and flanking base pairs neither stretch nor shear.

Perhaps most remarkable is that the ejected bases, irrespective of their identities, assume nearly identical positions. The ejected bases are not splayed out in random positions, at least not in the structures in the solid state. Instead, their positions seem to be defined, at least in part, by the sugar torsions. In fact, it may be more facile for the bases to be ejected from the minor groove side and accommodated in the major groove; this ejection into the major groove may then be a general characteristic of base pair displacement.[31] Certainly, as evident in **Figure 6.13**, the distinct overlap of these different insertion sites, independent of the identity of the mismatch and crystal packing, must reflect the ease of adopting this type of conformation. These results, all taken together, indicate clearly that insertion into the double helix from the minor groove with ejection of a base pair towards the major groove is a motif that is characteristic of the binding of metal complexes bearing extended ligands to thermodynamically destabilized sites in DNA.

6.4: CONCLUSION

The metalloinsertion of bulky metal complexes at DNA mismatches represents a new paradigm for how small molecules may bind non-covalently to DNA. The structures described here of Δ-$Rh(bpy)_2(chrysi)^{3+}$ bound to thermodynamically destabilized A•A mismatches illustrate the generality of this binding mode. Combined with previous crystallographic and NMR studies on different mismatched oligonucleotides, these structures reveal the architectural characteristics of metalloinsertion: in every case, without regard to the type of mismatch, the metal complex approaches the DNA from the minor groove, ejects the mismatched bases from the helix towards the major groove, replaces the extruded base pair in the π-stack with its own bulky ligand, and perturbs the DNA only minimally beyond the binding site. The similarity in the structures described here along with their clear differences serve furthermore to underscore metalloinsertion as a unique binding interaction, one distinct from intercalation. The presence of an intercalative rhodium in one of the structures also highlights how crystal packing forces can contribute to the solid state structures of small molecules bound non-covalently to DNA. While the information obtained from these structures yields critical and detailed insights, these data must also be considered in context with other data obtained in solution. In future work, it is hoped that these structures will not only prove useful as an illustration of a binding archetype but also in driving the design, synthesis, and application of new generations of small molecules that bind DNA through the insertion mode.

6.5: REFERENCES

1. Lerman, L. S. *Journal of Molecular Biology* **1961,** *3*, 18−30.
2. Neidle, S. *Nucleic Acid Structure and Recognition*. Oxford University Press: 2002.
3. Kielkopf, C. L.; Erkkila, K. E.; Hudson, B. P.; Barton, J. K.; Rees, D. C. *Nature Structural Biology* **2000,** *7* (2), 117−121.
4. Kielkopf, C. L.; White, S.; Szewczyk, J. W.; Turner, J. M.; Baird, E. E.; Dervan, P. B.; Rees, D. C. *Science* **1998,** *282*, 111−115.
5. Bennett, M.; Krah, A.; Wien, F.; Garman, E.; McKenna, R.; Sanderson, M.; Neidle, S. *Proceedings of the National Academy of Sciences U. S. A.* **2000,** *97*, 9476−9481.
6. Coll, M.; Frederick, C. A.; Wang, A. H.; Rich, A. *Proceedings of the National Academy of Sciences U. S. A.* **1987,** *84*, 8385−8389.
7. Lipscomb, L. A.; Zhou, F. X.; Presnell, S. R.; Woo, R. J.; Peek, M. R.; Plaskon, R. R.; Williams, L. D. *Biochemistry* **1996,** *35*, 2818−2823.
8. Pierre, V. C.; Kaiser, J. T.; Barton, J. K. *Proceedings of the National Academy of Sciences U. S. A.* **2007,** *103*, 429−434.
9. Cordier, C.; Pierre, V. C.; Barton, J. K. *Journal of the American Chemical Society* **2007,** *129*, 12287−12295.
10. Junicke, H.; Hart, J. R.; Kisko, J. L.; Glebov, O.; Kirsch, I. R.; Barton, J. K. *Proceedings of the National Academy of Sciences U. S. A.* **2003,** *100*, 3737−3742.
11. Zeglis, B. M.; Pierre, V. C.; Barton, J. K. *Chemical Communications* **2007**, 4565−4579.
12. Jackson, B. A.; Alekseyev, V. Y.; Barton, J. K. *Biochemistry* **1999,** *38* (15), 4655−4662.

13. Jackson, B. A.; Barton, J. K. *Journal of the American Chemical Society* **1997,** *119* (52), 12986−12987.

14. Jackson, B. A.; Barton, J. K. *Biochemistry* **2000,** *39* (20), 6176−6182.

15. Jackson, B. A.; Henling, L. M.; Barton, J. K. *Inorganic Chemistry* **1999,** *38* (26), 6218−6224.

16. Zeglis, B. M.; Barton, J. K. *Nature Protocols* **2007,** *2* (2), 357−371.

17. Zeglis, B. M.; Barton, J. K. *Journal of the American Chemical Society* **2006,** *128* (17), 5654−5655.

18. Lim, M. H.; Lau, I. H.; Barton, J. K. *Inorganic Chemistry* **2007,** *46*, 9528−9530.

19. Zeglis, B. M.; Boland, J. A.; Barton, J. K. *Journal of the American Chemical Society* **2008,** *130* (24), 7530−7531.

20. Zeglis, B. M.; Boland, J. A.; Barton, J. K. *Biochemistry* **2009,** *48* (5), 839−849.

21. Hart, J. R.; Johnson, M. D.; Barton, J. K. *Proceedings of the National Academy of Sciences of the United States of America* **2004,** *101* (39), 14040−14044.

22. Petitjean, A.; Barton, J. K. *Journal of the American Chemical Society* **2004,** *126* (45), 14728−14729.

23. Schatzschneider, U.; Barton, J. K. *Journal of the American Chemical Society* **2004,** *126* (28), 8630−8631.

24. Ernst, R. J.; Song, H.; Barton, J. K. *Journal of the American Chemical Society* **2009,** *131* (6), 2359−2366.

25. Hart, J. R.; Glebov, O.; Ernst, R. J.; Kirsch, I. R.; Barton, J. K. *Proceedings of the National Academy of Sciences U. S. A.* **2006,** *103*, 15359−15363.

26. Collaborative Computational Project Number 4. *Acta Crystallographica* **1994,** *D50*, 760−763.

27. Adams, P. D.; Grosse−Kunstleve, R. W.; Hung, L. W.; Ioerger, T. R.; McCoy, A. J.; Moriarty, N. W.; Read, R. J.; Sacchettini, J. C.; Sauter, N. K.; Terwilliger, R. C. *Acta Crystallographica* **2002,** *D58*, 1948−1954.

28. Murshudov, G. N.; Vagin, A. A.; Dodson, E. J. *Acta Crystallographica* **1997,** *D53*, 240−255.

29. DeLano, W. L. *The PyMOL Molecular Graphics System*, DeLano Scientific: San Carlos, CA, 2002.

30. Lu, X. J.; Olson, W. K. *Nucleic Acids Research* **2003,** *31*, 5108−5121.

31. Peng, T.; Dohno, C.; Nakatani, K. *Angewandte Chemie−International Edition* **2006,** *45*, 5623−5626.

CHAPTER 7: THE DESIGN AND SYNTHESIS OF MISMATCH-SPECIFIC BIFUNCTIONAL CONJUGATES

7.1: INTRODUCTION

The diagnostic and therapeutic potential of mismatch-specific metalloinsertors became evident very soon after their discovery. Therefore, over the past ten years, our laboratory has sought to develop these complexes for various clinical applications.[1, 2] The first generations of metalloinsertors, most notably $Rh(bpy)_2(chrysi)^{3+}$ and $Rh(bpy)_2(phzi)^{3+}$, have shown significant promise as agents for the detection of mismatches[3, 4], single nucleotide polymorphisms[5], and abasic sites.[6, 7] Furthermore, the ability of both these complexes, among others, to preferentially inhibit the proliferation of mismatch repair (MMR) deficient cells makes them attractive candidates for use as chemotherapeutics against MMR-related cancers.[8, 9]

Yet the overall promise of metalloinsertors is not limited to that of the complexes alone. Indeed, these mismatch-specific agents can be employed in conjugates to confer site-specificity on useful but otherwise non-specific agents.[10–14] Structurally, these bifunctional conjugates must necessarily feature a tripartite design, with metalloinsertor, linker, and cargo subunits (**Figure 7.1**). The conjugates are assembled convergently. A linker-modified ligand is first synthesized and then metallated onto a pre-formed $Rh(phen)(chrysi)(NH_3)_2^{3+}$ framework to yield the completed linker-modified, trisheteroleptic metalloinsertor (see Chapter 2 for details and synthetic schemes), for example $Rh(phen)(chrysi)(^{NH2}bpy)^{3+}$. This subunit is then covalently attached to the desired cargo via standard peptide coupling procedures. Importantly, the inherent

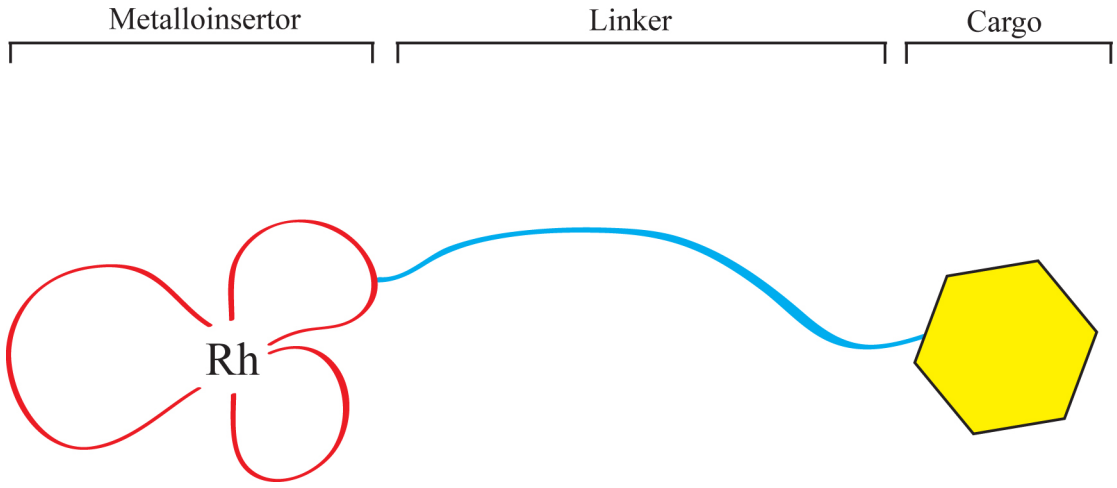

Figure 7.1. The anatomy of a bifunctional conjugate. The metalloinsertor subunit (red) is covalently tethered to the cargo moiety (yellow) by a flexible linker (blue).

modularity of metal complexes and the convergent synthetic approach to these conjugates affords the opportunity to exploit a variety of metalloinsertor, linker, and cargo moieties. To date, our laboratory has designed, synthesized, and tested bifunctional conjugates employing platination agents[13], alkylators[12], DNA-cleaving copper complexes[11], fluorophores[14], and cell-penetrating peptides[10] (**Figure 7.2**). All have enjoyed a measure of success. For example, the metalloinsertor subunit of the DNA alkylator conjugate (**Figure 7.2a)** is able to specifically direct its nitrogen mustard subunit to alkylate DNA near mismatched sites. Further, the metalloinsertor-Oregon Green conjugate discussed earlier in this text (**Figure 7.2c**, Chapter 3) successfully acts as a mismatch-specific fluorescent probe, if only as a proof of concept.

Yet despite these successes, the overall *in vitro* and *in vivo* applicability of the conjugates has remained limited. At fault are two disparate issues, likely acting in concert: poor cell permeability and reduced DNA binding affinity. The former, while outside the scope of this chapter, has been thoroughly investigated in our laboratory.[15, 16] All evidence suggests that the cellular uptake of octahedral metal complexes occurs via passive diffusion, with an increase in the hydrophobicity of the ancillary ligands of a complex dramatically enhancing uptake. These trends, however, were elucidated using the $Ru(L)_2(dppz)^{2+}$ family of complexes, not larger, more complex, bifunctional conjugates. While studies are currently underway involving Ru-peptide conjugates, much remains to be done to fully understand the uptake of these more complex systems.

The second factor, reduced DNA binding affinity, is more central to the investigations at hand. It has been empirically observed that the binding affinity of the

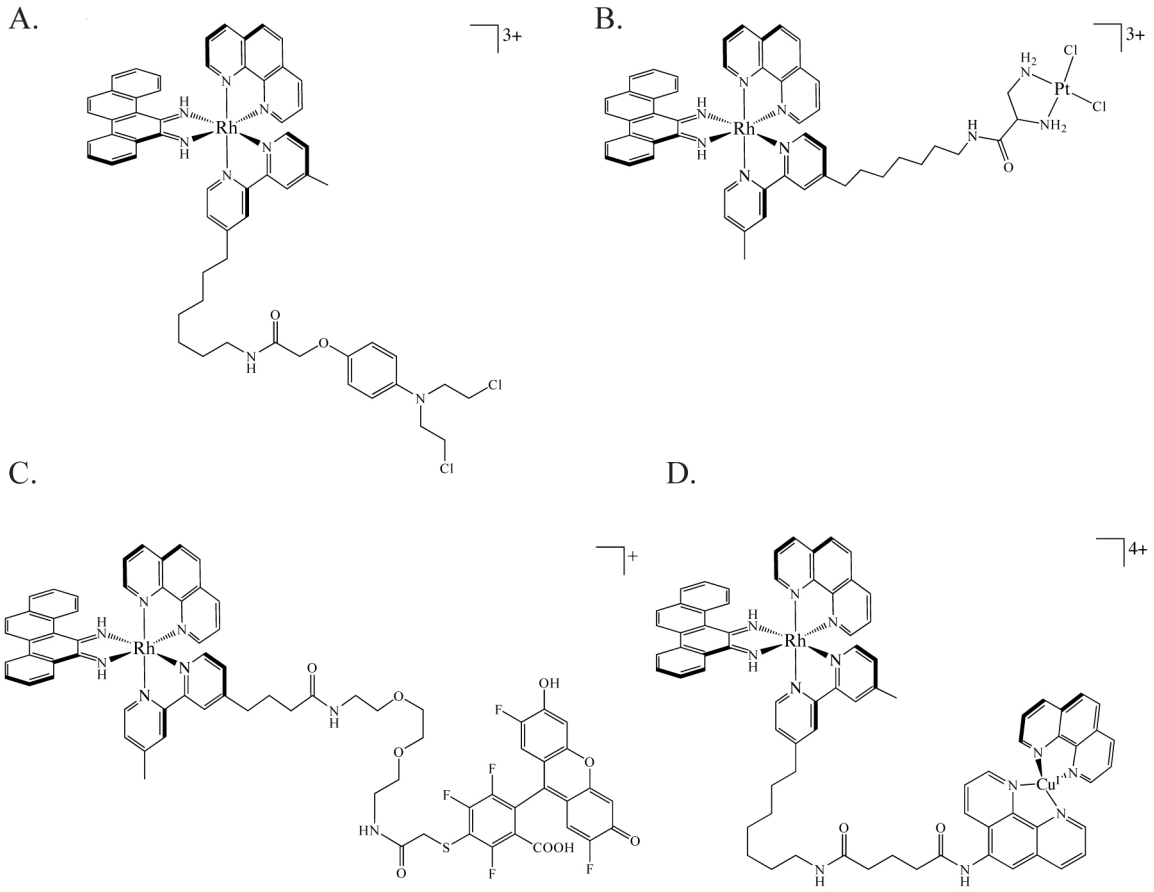

7.2: Some mismatch-specific bifunctional conjugates. Four bifunctional conjugates previously developed by this laboratory. Metalloinsertors were employed to impart mismatch-specificity on pendant alkylating[12] (A), platinating[13] (B), fluorescent[14] (C), and DNA cleaving[11] (D) agents.

mismatch-specific conjugates (and their rhodium subunits alone) are lower than that of their parent $Rh(bpy)_2(chrysi)^{3+}$, $Rh(bpy)(phen)(chrysi)^{3+}$, and $Rh(phen)_2(chrysi)^{3+}$ complexes.[11, 13, 14] All of the bifunctional conjugates to date have employed a $Rh(phen)(chrysi)(^{x}bpy)^{3+}$ framework as their metalloinsertor subunit, where ^{x}bpy denotes a 4,4'-dimethyl-bipyridine ligand with one of the methyl groups alkylated to create a linker moiety. These metalloinsertors exist as a mixture of four stereoisomers, two enantiomers of two diastereomers (**Figure 7.3**).[a] The enantiomers, of course, are born out of the innate chirality of octahedral metal complexes containing three bidentate ligands. The diastereomers, in contrast, are created by the asymmetry of the linker-modified bipyridine ligand; the linker-modified methyl can either be perpendicular (axial diastereomer) or parallel (equatorial diastereomer) to the plane of the chrysi ligand.

It is known from past experiments that neither Λ-enantiomer will effectively bind mismatched DNA.[17–19] This, however, is true of all known metalloinsertors, and thus will not reduce the binding affinity of the conjugates relative to other mismatch-specific complexes. The problem, then, lies in the linker-modified bipyridine ligand, predominantly the linker itself but also the complementary methyl group. The relationship between ancillary ligand bulk and DNA binding affinity has been firmly established: the larger the ancillary ligands, the weaker the complex binds DNA. The recent work of Ernst and Song in our laboratory has illustrated this quite nicely. As the ancillary ligands get larger — from $Rh(NH_3)_4(chrysi)^{3+}$ to $Rh(bpy)_2(chrysi)^{3+}$ to $Rh(DIP)_2(chrysi)^{3+}$ — the binding affinity of a complex for a C•C mismatch drops dramatically, from 1×10^8 M^{-1} to 3.4×10^7 M^{-1} to 9.1×10^4 M^{-1}, respectively.[9] It follows

[a] As they are almost certainly inconsequential from a DNA-binding stand-point, the diastereomers resulting from the asymmetry of the chrysi ligand are typically ignored.

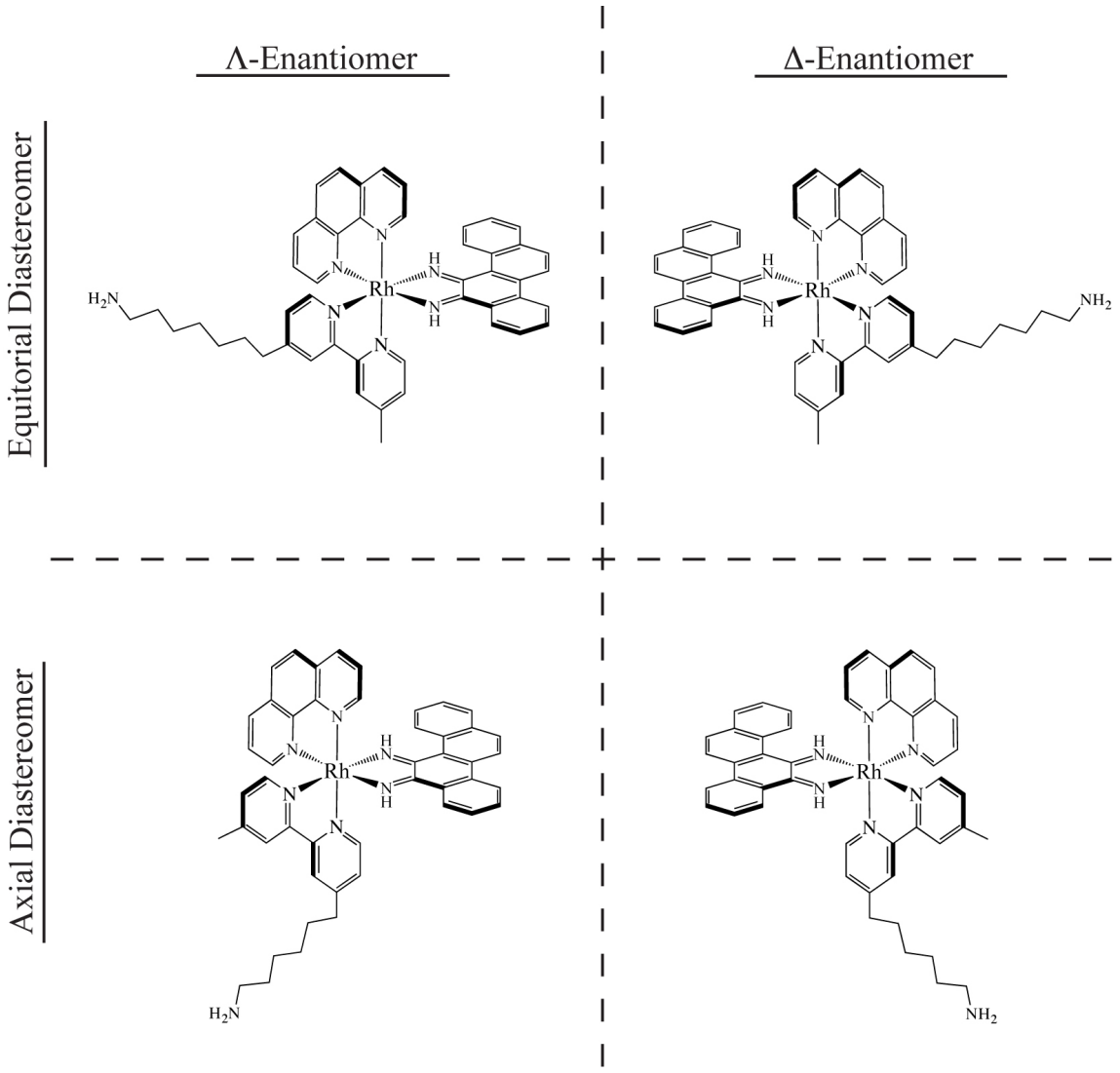

Figure 7.3: The stereoisomers of Rh(phen)(chrysi)(^{NH2}bpy)$^{3+}$. It is almost certain that neither Λ-enantiomer binds mismatched DNA, but it is likely that the affinities of both Δ-enantiomers are reduced relative to the parent complexes as well.

that the Δ-enantiomers of Rh(phen)(chrysi)(^{x}bpy)$^{3+}$ may also have reduced binding affinity relative to their parent complexes. The affinity of the axial diastereomer is likely particularly reduced due to the large linker that likely clashes significantly with the phosphate backbone above or below the binding site of the complex. The equatorial diastereomer may be similarly affected by the bulk of its axially-positioned methyl group, though perhaps to a lesser degree.

Mismatch-specific bifunctional conjugates have tremendous potential, and thus we could not just throw in the towel. Therefore, to remedy this binding affinity problem, we have recently turned to a new platform for linker-modified ligands: 2,2'-dipyridylamine (HDPA, **Figure 7.4**). The key to HDPA is the centrally located, bridging nitrogen. This central amine can be alkylated to yield a linker-modified dipyridylamine (DPA) ligand (see CHAPTER 2 for synthetic protocols). Upon metallation, the linker thus extends diagonally from the metal complex, reducing the steric clash that hindered the binding of the metalloinsertors bearing modified dimethyl-bipyridine ligands. Further, the two-fold symmetry of the modified DPA ligands eliminates any diastereomers in trisheteroleptic complexes; Rh(phen)(chrysi)(DPA')$^{3+}$, for example, exists simply as a mixture of Δ- and Λ–enantiomers.

Experiments with Rh(bpy)$_2$(chrysi)$^{3+}$ and Rh(HDPA)$_2$(chrysi)$^{3+}$ have shown that switching from bipyridine to dipyridylamine ancillary ligands does not result in any substantive reduction in site-specific affinity. More important still, the C•C mismatch-specific binding constant of Rh(phen)(chrysi)(HDPA)$^{3+}$ is 2.5 x 10^{6} M^{-1}, and only a slight reduction in affinity is observed for the analogous complex bearing a DPA ligand with a carboxylate-terminated linker (9.8 x 10^{5} M^{-1}).

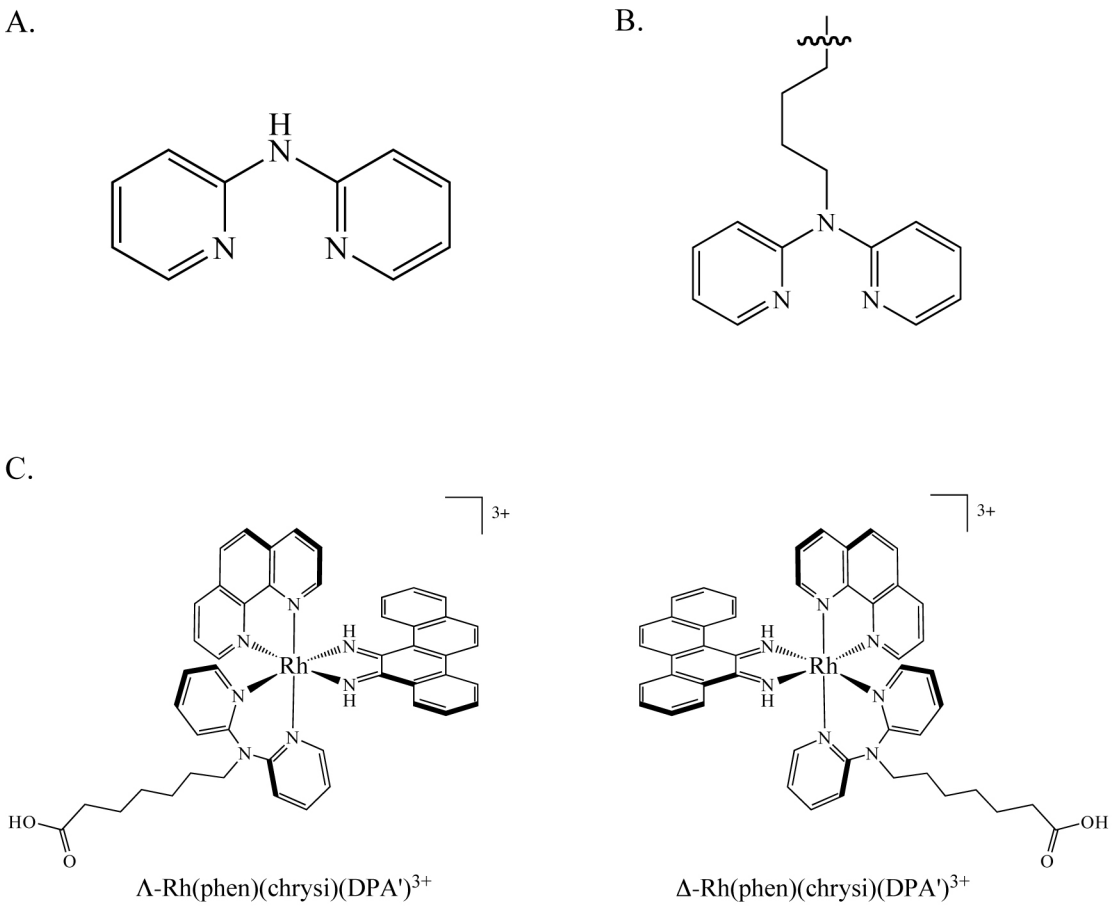

Figure 7.4: A new option for linker-modified ligands. (A) 2,2'-dipyridylamine (HDPA); (B) a linker-modified dipyridylamine (DPA) ligand; (C) the Λ- and Δ-enantiomers of Rh(phen)(chrysi)(DPA')$^{3+}$ (left and right, respectively).

There is, however, one significant limitation to HDPA and modified DPAs as ligands for metalloinsertors: altered photochemistry. $Rh(HDPA)_2(chrysi)^{3+}$, for example, is not photochemically active and, therefore, is unable to affect photocleavage at its binding site.[b] Complexes bearing at least one bipyridine-based ligand fare slightly better; $Rh(phen)(chrysi)(HDPA)^{3+}$ is capable of site-specific, photoactivated strand scission, but at drastically reduced efficiencies compared to $Rh(bpy)_2(chrysi)^{3+}$ or $Rh(phen)(chrysi)(bpy)^{3+}$ (**Figure 7.5**). Fortunately, while photocleavage is useful for the characterization of metalloinsertors and their conjugates, it becomes less important in the *in vivo* applications for which most bifunctional conjugates are intended.[c]

No bifunctional conjugates employing a modified dipyridylamine ligand have yet been published, though a number are currently in development. Herein, we will present two case studies in the design, synthesis, and application of mismatch-specific, bifunctional conjugates. The first, a conjugate bearing a hydrolysable platination agent, was developed in the era of linker-modified bipyridine ligands. The second, a metalloinsertor-radionuclide conjugate, employs a linker-modified dipyridylamine ligand. Both cases offer significant insights into the factors important for the successful development of useful, mismatch-specific bifunctional conjugates and will hopefully inspire continued research into these molecules and others like them.

---

[b] The binding constant for this compound was determined via competition with $Rh(bpy)_2(chrysi)^{3+}$ (see chapter 2 for details).

[c] As an aside, a third option exists that may combine the best features of bipyridine (photochemistry) and dipyridylamine (linker location) ligands: linker-modified 3-methyl-2,2'-bipyridine ligands. 3-methyl-2,2'-bipyridine can be synthesized via the facile cross-coupling of 2-pyridylzinc bromide and 2-chloro-3-methyl pyridine. The bipyridine product can then be alkylated and converted to ligand with a useful linker via the protocols described in Chapter 2. See Notebook 6, Page 116 for a cross-coupling procedure.

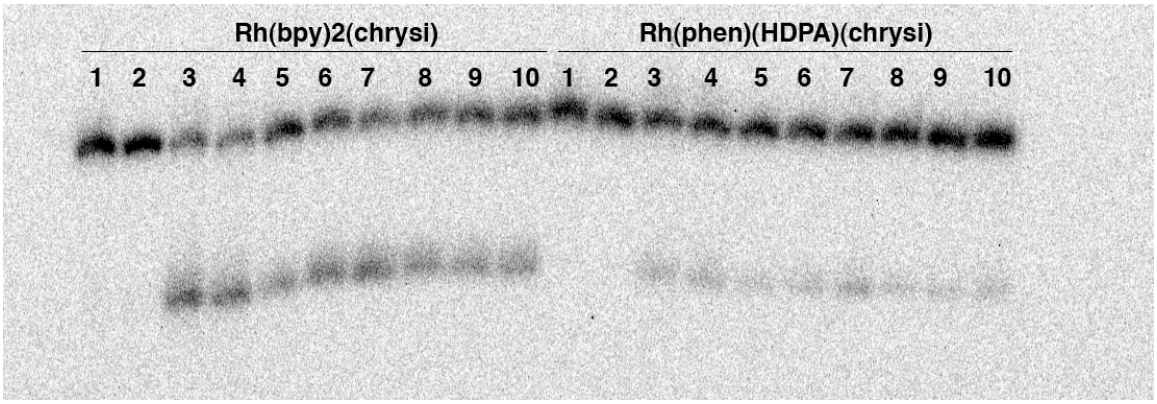

Figure 7.5: The reduced photocleavage efficiency of Rh(phen)(HDPA)(chrysi)$^{3+}$. Autoradiogram of a denaturing 20% polyacrylamide gel showing the mismatch-specific DNA photocleavage of Rh(bpy)$_2$(chrysi)$^{3+}$ and Rh(phen)(HDPA)(chrysi)$^{3+}$ as a function of irradiation wavelength. Conditions are duplex (5 μM), Rh (5 μM) in 20 mM NaCl, 10 mM NaPi, in pH 7.1 followed by irradiation for 12 min. The left set of lanes contains Rh(bpy)$_2$(chrysi)$^{3+}$, while the right set of lanes contains Rh(phen)(HDPA)(chrysi)$^{3+}$. Lane 1: matched DNA, irradiation with solar simulator. Lane 2: mismatched DNA, dark control. Lanes 3−10 contain mismatched DNA irradiated at wavelengths of 300, 320, 340, 360, 380, 400, 420, and 440 nm, respectively. The DNA sequence is 5'-^{32}P-GCA TCG ACA GAC CAG CTT ATC AT**C** CTA AGA GCG – 3' where the bold, red C is complementary to a G in the matched duplex and a C in the mismatched duplex. Note the reduced photocleavage efficiency of Rh(phen)(HDPA)(chrysi)$^{3+}$ at all wavelengths. Independent experiments indicate the binding affinities of the two complexes are similar.

7.2: A SECOND GENERATION METALLOINSERTOR-PLATINUM CONJUGATE

7.2.1: INTRODUCTION

Cisplatin, *cis*-$Pt(NH_3)_2Cl_2$, is the original member of a family of extensively employed and highly effective platinum-based chemotherapeutic agents that have been used to combat a wide variety of cancers, including carcinomas, sarcomas, and lymphomas (**Figure 7.6**).[20, 21] *In vivo*, cisplatin exerts its biological effect by making covalent, intrastrand DNA crosslinks to purine bases, most often guanine doublets; these DNA adducts activate the cellular DNA damage response, interfere with cell division, and ultimately trigger cell death.[22–30] Some cancers, including many linked with mismatch repair deficiency, have proven resistant to cisplatin.[31–37] This phenomenon and the harsh side effects associated with cisplatin chemotherapy have fueled considerable research into the development of new, more effective, and less toxic platinum(II) chemotherapeutics.[38] Two of the most successful, carboplatin and oxaliplatin, are currently widely employed in chemotherapeutic protocols. Carboplatin, like cisplatin, bears two *cis*-ammine ligands.[39] Oxaliplatin, in contrast, employs a 1R,2R-(-)-*trans*-diaminocyclohexyl (dach) ligand that has been shown to restore drug activity in many cisplatin resistant cell lines.[40] Interestingly, in order to improve the ligand exchange kinetics of the Pt(II) center, both drugs employ hydrolysable dicarboxylate ligands in place of the chlorides of cisplatin.

Given the cisplatin resistance of many cancers linked to mismatch-repair deficiency, we have hypothesized that the conjugation of a platinum(II) chemotherapeutic subunit to a mismatch-specific metalloinsertor may successfully modulate the toxicity of

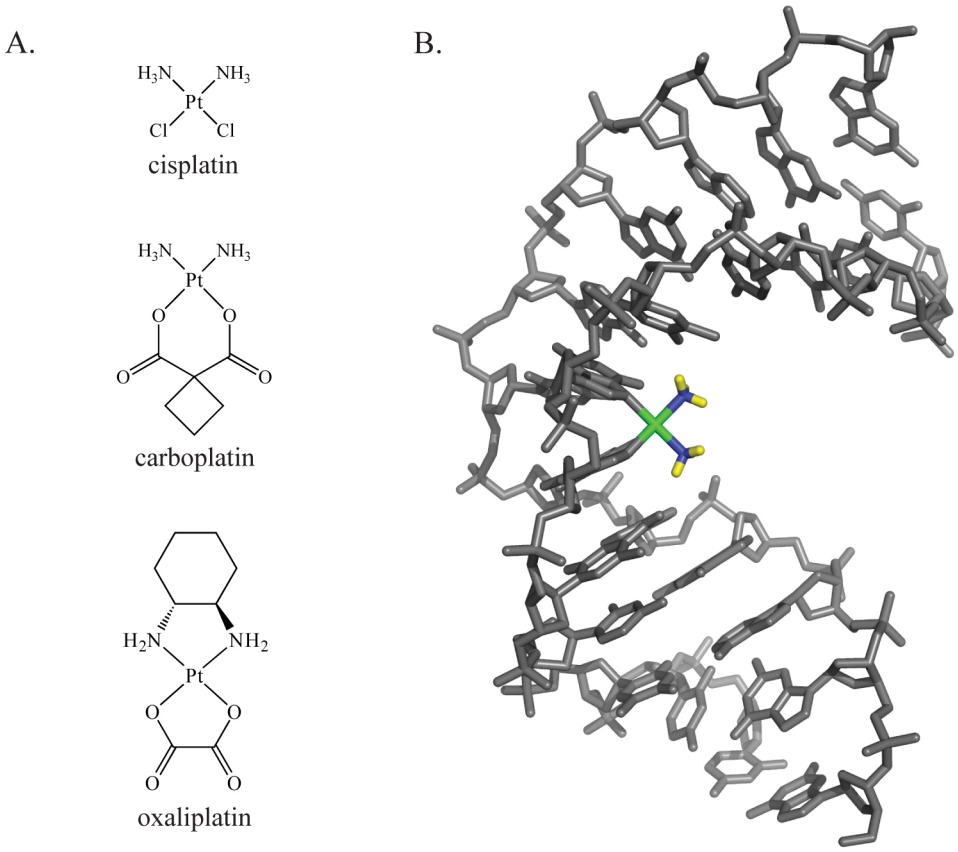

Figure 7.6: Platinum(II)-based chemotherapeutics. (A) Three commonly-employed platinum(II) drugs. (B) An NMR structure revealing the kink induced in DNA upon the formation of a 1,2-intrastrand d(GpG) adduct by cisplatin.[41]

the drug to these types of tumors. In essence, the metalloinsertor would act as a molecular taxi, selectively delivering the platinum agent to mismatched DNA and thus concentrating the drug in those cells replete with mismatches (i.e. MMR-deficient cells). We have previously designed, synthesized, and tested a first generation metalloinsertor-platinum conjugate (RhPt1, **Figure 7.2B**).[13] The conjugate successfully and selectively delivers its platinum cargo to mismatched DNA; however, it is limited by the permanent covalent link between the metalloinsertor and platinum subunits. Because the linker connects the metalloinsertor to the non-labile 1,2-diaminoethane ligand of the platinum moiety, the platinum complex can only form adducts with DNA within a linker-length of the binding site of the metalloinsertor.

We have set out to design and synthesize a second generation metalloinsertor-platinum conjugate, RhPt2, to address these limitations. In this case, the platinum subunit is inspired by oxaliplatin, containing both a diaminocyclohexyl ligand known to combat cisplatin resistance and a dicarboxylate, malonate-derived ligand.[38, 42] The metalloinsertor subunit is linked to the platinum moiety not through the inert diammine ligand but rather through the hydrolysable malonate-derivative ligand. Kinetic studies on oxaliplatin and related platinum complexes have shown that the hydrolysis half-lives of their dicarboxylate ligands is around 3 h at 37 °C.[39] Thus, this conjugate, like RhPt1, will act as a molecular taxi, but this time, however, it will drop its passenger off. The intact conjugate will first seek out and selectively bind mismatched DNA; then, on a longer timescale, the platinum unit will be released from the conjugate by hydrolysis and will be free to form its cytotoxic adducts with any of the DNA in the nucleus of the targeted cell.

7.2.2: SYNTHESIS

The conjugate was synthesized in a convergent manner, with the rhodium and platinum moieties completed separately and coupled in the final step. The trisheteroleptic, linker-modified rhodium subunit, Rh(phen)(chrysi)(^{NH2}bpy)$^{3+}$, was synthesized from $RhCl_3$ according to standard protocols (**Figure 7.7**, see Chapter 2).[2, 12]

The platinum subunit presented a more original, if not slightly more difficult, synthetic challenge.[d,43] First, the dicarboxylate ligand was synthesized. To provide further space between the platinum and rhodium moieties and to enable efficient coupling, a 2-(4-carboxybenzylidene)malonic acid ligand was employed and synthesized via either of two routes from paraformylbenzoic acid (**Figure 7.8**). In method 1, the benzoic acid is protected with a tert-butyl ester, reacted with dibenzyl malonate via a $TiCl_4$-promoted Knovenagel condensation, and selectively deprotected with hydrogen over Pd/C to yield t-butyl-protected 2-(4-carboxybenzylidene)malonic acid (MalBzCOOtBu). In the second, more efficient route, the Knovenagel condensation comes first. Paraformylbenzoic acid is reacted with dibenzyl malonate in the presence of $TiCl_4$, and the free carboxylic acid of this product is protected with a tert-butyl ester via acid-catalyzed reaction with isobutene. A subsequent, selective deprotection step with H_2 over Pd/C yields the completed MalBzCOOtBu.

The completed malonate ligand was metallated via reaction with Pt(dach)$(NO_2)_2$, a platinum(II) species prepared in two steps from K_2PtCl_4 (**Figure 7.9**). Finally, the ready-to-couple Pt2 subunit, Pt(dach)(MalBzCOOH), was obtained via deprotection of

[d] For much of the synthetic work on the platinum subunit of RhPt2, I am deeply indebted to the prodigious talents of Dr. Anne Petitjean, a former postdoctoral researcher in the Barton laboratory.

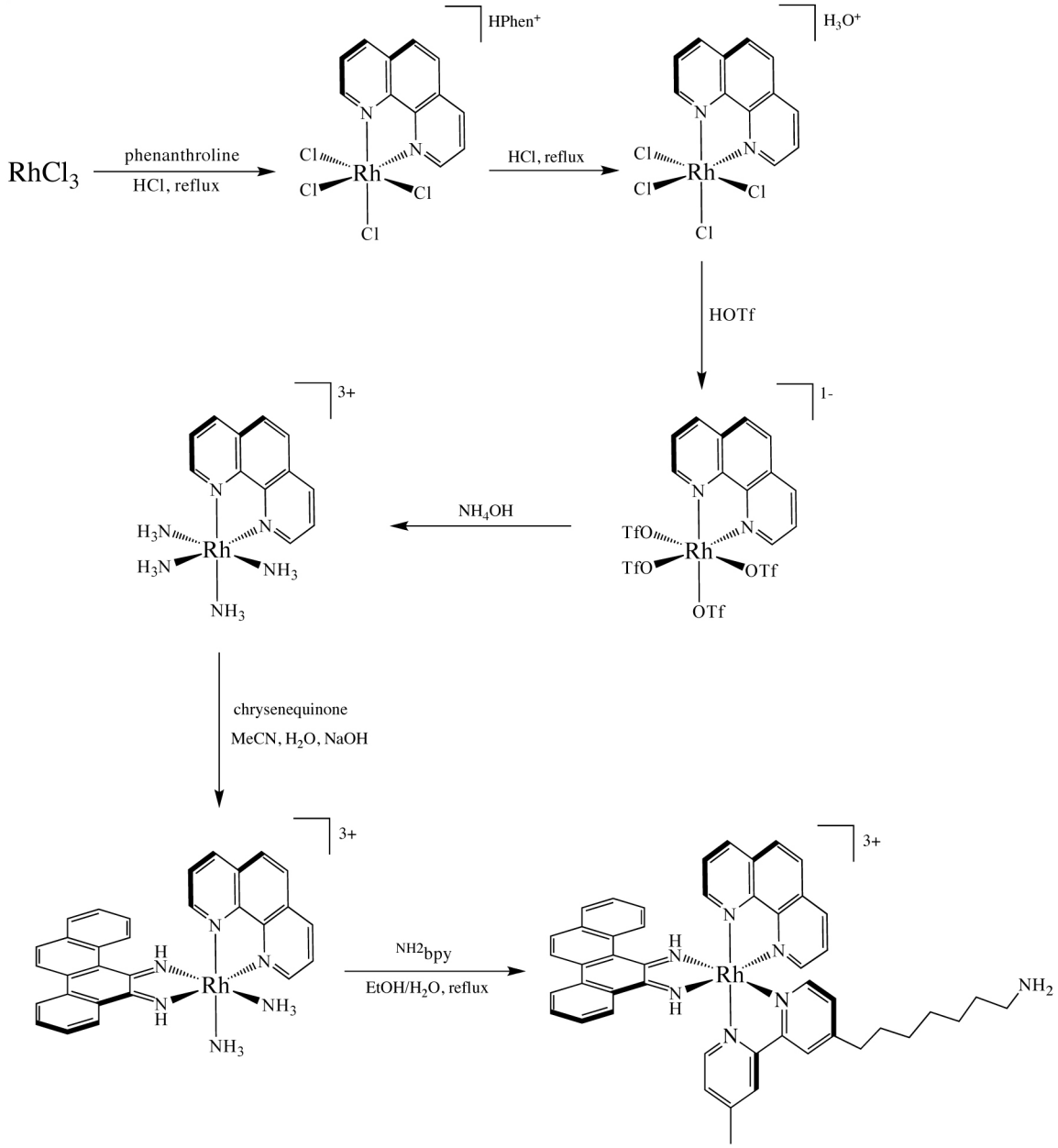

Figure 7.7. **The synthetic route to the trisheteroleptic metalloinsertor subunit.** The conjugate's metalloinsertor subunit was synthesized via the sequential addition of phen, chrysi, and ^{NH2}bpy ligands onto a rhodium center.

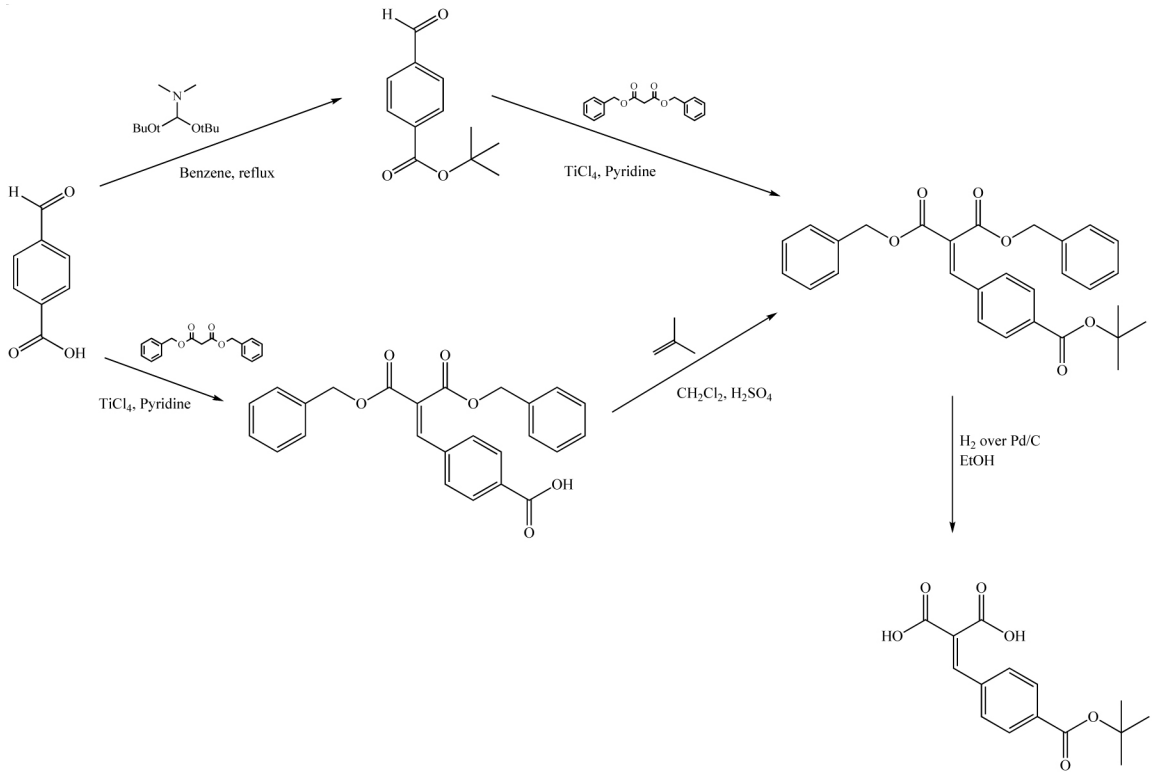

Figure 7.8: The synthetic route to the Pt2 malonate ligand. The ligand can be synthesized from paraformylbenzoic acid via two routes. In method 1 (top), the carboxylic acid is first protected, followed by a Knovenagel condensation with dibenzyl malonate. In method 2 (bottom), the Knovenagel condensation with dibenzyl malonate comes first and is followed by the protection of the free carboxylic acid. Regardless of which method is followed, the benzyl esters of the resultant product are then removed with H_2 over Pd/C, yielding the protected Pt2 malonate ligand that is ready for metallation onto Pt(II).

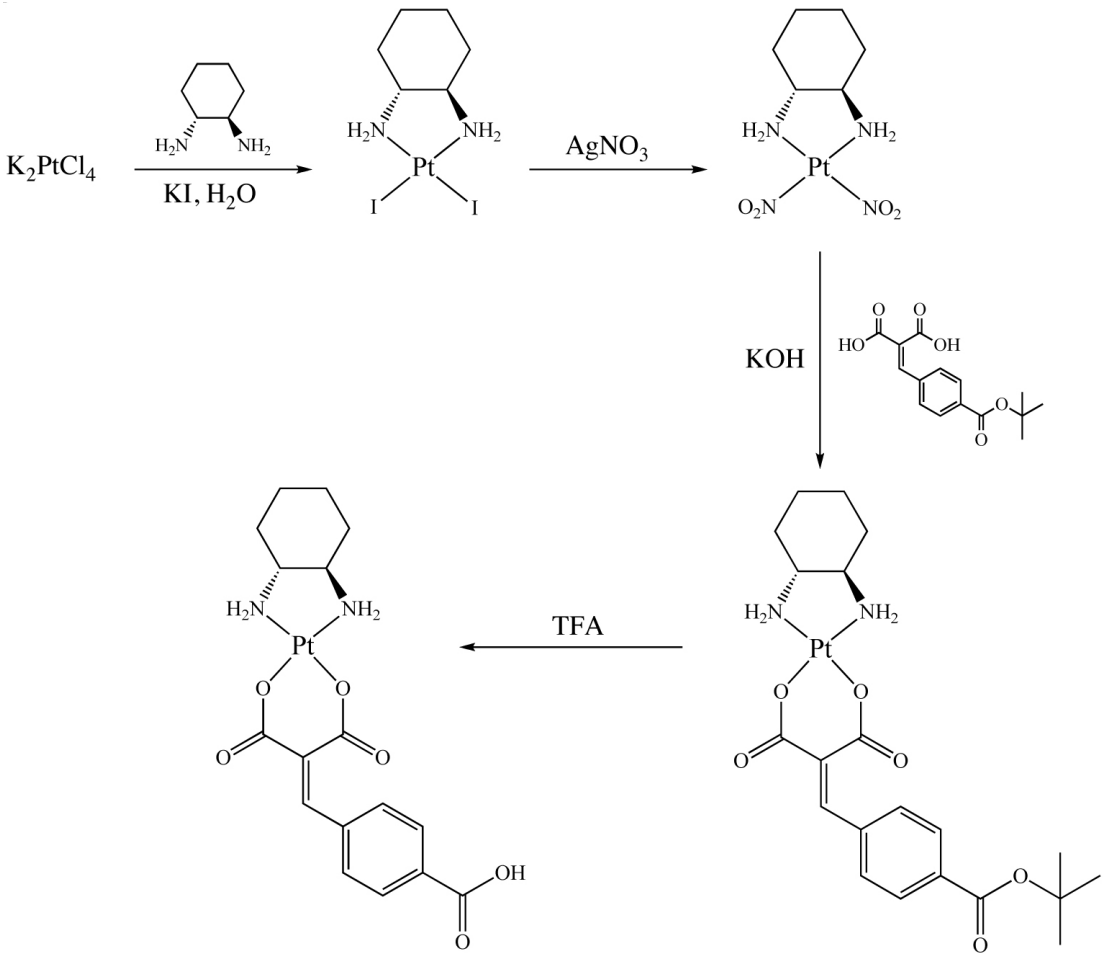

Figure 7.9: The synthetic route to Pt2. Pt(dach)(NO_2)$_2$ is prepared in two steps from potassium tetrachloroplatinate via ligand substitution reactions. The t-butyl ester-protected malonate ligand is then metallated onto the platinum center in the presence of base to produce Pt(dach)(MalBzCOOtBu), and this complex is deprotected with TFA to yield the ready-to-couple Pt2 product.

the tert-butyl ester with trifluoroacetic acid. The completed RhPt2 conjugate was then obtained via peptide coupling with Rh(phen)(chrysi)(^{NH2}bpy)$^{3+}$ using HATU (**Figure 7.10**) and purified via cation exchange (Sephadex CM-25) and reverse-phase HPLC chromatography.

7.2.3: MISMATCH RECOGNITION AND PLATINATION EXPERIMENTS

The mismatch recognition and DNA platination properties of RhPt2 were investigated with denaturing polyacrylamide gel electrophoresis using radiolabeled oligonucleotides that contain both a d(GpG) target site (blue) for platination and a central C•C mismatch (red) for metalloinsertor binding: 5'-^{32}P-TTA GGA TCA TCC ATA TA-3'. Control experiments with matched (C•G) duplexes were also performed, but controls using DNA without a d(GpG) binding site were deemed unnecessary, because the platinum(II) complex will readily bind other purine sites in the absence of its preferred guanine doublet target. Experiments previously performed with the original RhPt1 conjugate tell us what to look for; while mismatch-site strand scission products naturally travel more quickly on a gel than their parent DNA strands, platination products travel more slowly and thus appear above the parent band in the gel.

A simple recognition and photocleavage assay clearly illustrates that the RhPt2 conjugate specifically recognizes and photocleaves mismatched DNA (**Figure 7.11**). In these recognition experiments, RhPt2 was incubated with the DNA for very short amounts of time before irradiation in order to minimize the number of platinum adducts formed. Subsequently, binding constant titrations revealed that the site-specific affinity of

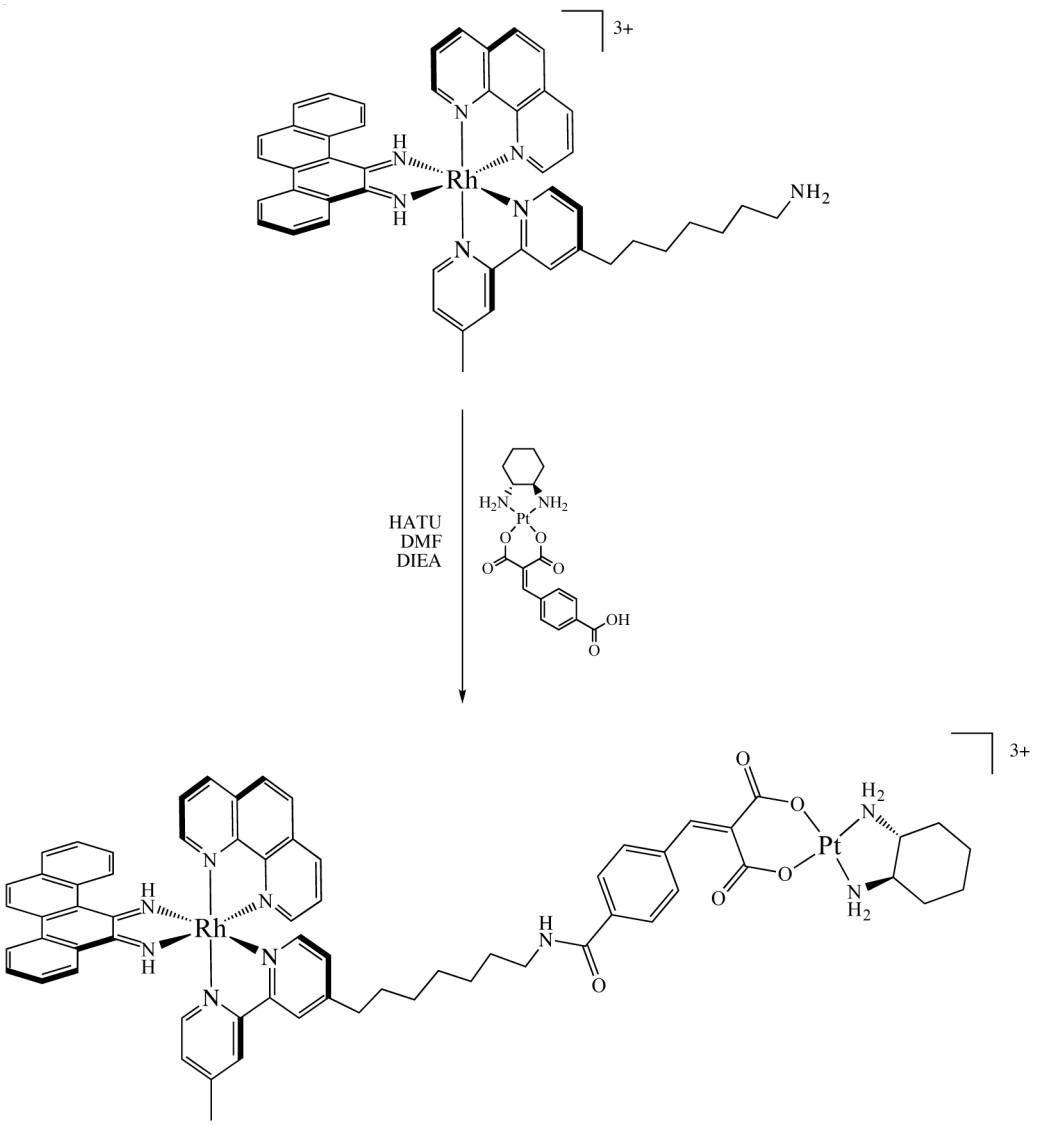

Figure 7.10: The synthesis of RhPt2. To form RhPt2, Pt2 [Pt(dach)(MalBzCOOH)] and Rh(phen)(chrysi)(^{NH2}bpy)$^{3+}$ are coupled with HATU.

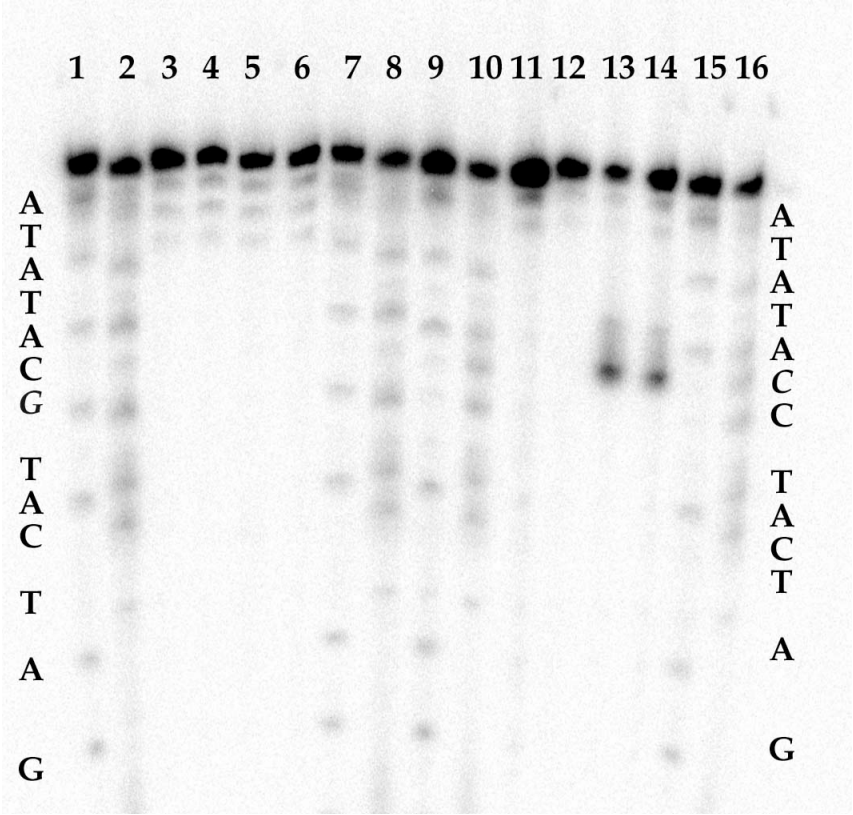

Figure 7.11: Mismatch recognition and photocleavage of RhPt2. Autoradiogram of a denaturing 20% polyacrylamide gel showing the mismatch-specific DNA photocleavage of RhPt2. Conditions are duplex (2 μM) and RhPt2 (2 μM) in 20 mM NaCl, 10 mM NaPi, pH 7.1 followed by irradiation on an Oriel Instruments solar simulator (320−440 nm). Lanes 1, 2, 7, and 8 are Maxam Gilbert A+T (1, 7) and C+G (2, 8) sequencing reactions for matched DNA. Lane 3 contains a matched DNA light control. Lane 4 contains a matched DNA dark control. Lanes 5 and 6 contain matched DNA and metal complex with irradiation for 3 and 6 min, respectively. Lanes 9, 10, 15, and 16 are Maxam Gilbert A+T (1, 7) and C+G (2, 8) sequencing reactions for mismatched DNA. Lane 11 contains a mismatched DNA light control. Lane 12 contains a mismatched DNA dark control. Lanes 13 and 14 contain mismatched DNA and metal complex with irradiation for 3 and 6 min, respectively. The DNA sequence is 5'-^{32}P-TTA GGA TCA TCC ATA TA-3' where the bold, red C is complementary to a G in the matched duplex and a C in the mismatched duplex.

RhPt2 for a C•C mismatch is approximately 1 x 10^6 M^{-1}, though the plot of RhPt2 concentration against photocleavage produces a somewhat skewed sigmoid, so the actual value is likely lower.

Additional electrophoresis experiments allowed for the interrogation of the platination behavior of RhPt2. Simple incubation experiments with radiolabeled matched and mismatched duplexes reveal that clear, slow-moving platination adducts are formed when DNA is incubated with RhPt2 for 3 hours (**Figure 7.12**). A comparison to the products formed upon incubation of DNA with cisplatin suggests that the adducts formed by RhPt2 move more slowly though the gel and thus are slightly different; this is not surprising given the greater steric bulk of the diaminocyclohexyl ligand of the Pt2 complex. Further, more careful examination of the cisplatin-containing lanes reveals that a second, even more slowly moving adduct is formed during these incubations. Notably, the same is true with RhPt1, and in that case, it was hypothesized that the two bands represent intra- and interstrand platination adducts.[13] The greater steric bulk of the diaminocyclohexyl ligand of Pt2 may also be responsible for the absence of a second, likely interstrand platination product in the case of RhPt2.

Perhaps not surprisingly given the hydrolysis of the Pt2 subunit, platination adducts are observed with both matched and mismatched duplexes. Further still, experiments to probe the platination selectivity of RhPt2 in the presence of mixtures of matched and mismatched assemblies reveal that the Pt2 unit shows little specificity for the platination of mismatched DNA. It seems that even though the metalloinsertor subunit of the conjugate selectively binds mismatched DNA, the platinum subunit, once released, is free to bind either matched or mismatched DNA with little discrimination.

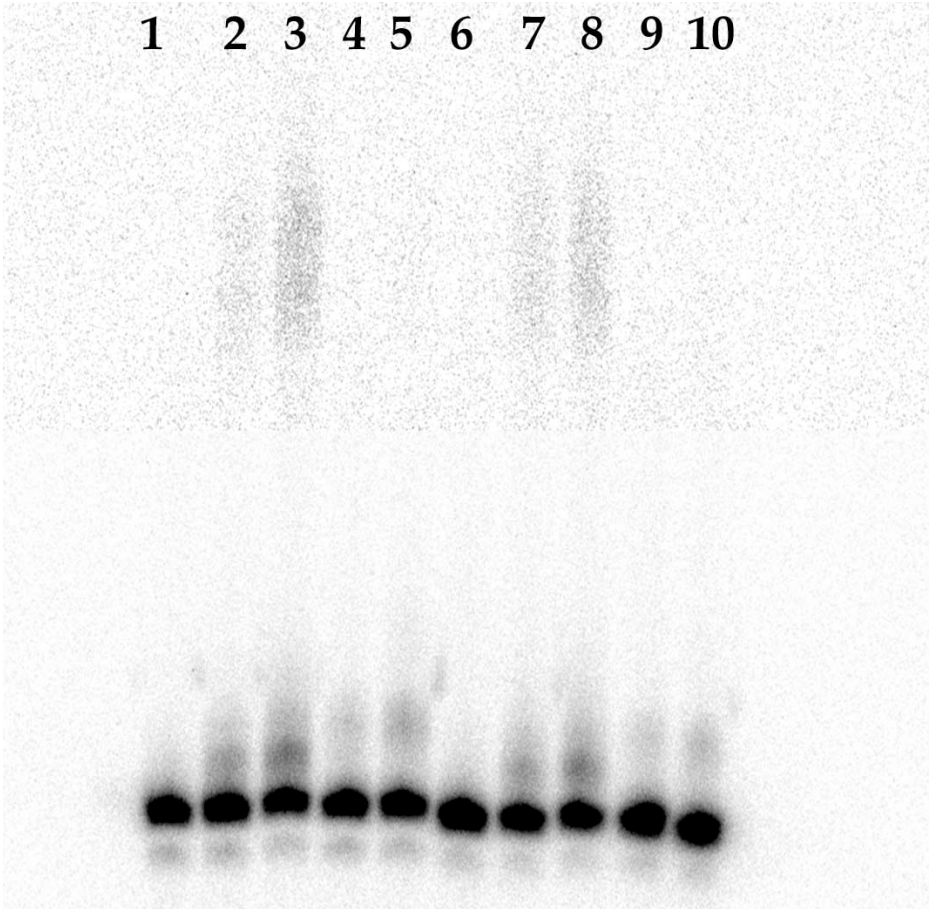

Figure 7.12: DNA platination adducts formed by cisplatin and RhPt2. Autoradiogram of a denaturing 20% polyacrylamide gel showing the platination adducts formed by cisplatin and RhPt2. Conditions are duplex (2 μM) in 20 mM NaCl, 10 mM NaPi, pH 7.1 with three hour incubations. Lanes 1−5 contain matched DNA. Lanes 6−10 contain mismatched DNA. Lanes 1 and 6: control, no metal complex. Lanes 2 and 7: DNA with 1 μM cisplatin. Lanes 3 and 8: DNA with 2 μM cisplatin. Lanes 4 and 9: DNA with 1 μM RhPt2. Lanes 5 and 10: DNA with 2 μM RhPt2. The DNA sequence is 5'-^{32}P-TTA GGA TCA TCC ATA TA-3' where the bold, red C is complementary to a G in the matched duplex and a C in the mismatched duplex. The gain on the top half of the gel has been increased in order to visualize the second platination bands in the cisplatin lanes.

An interesting interplay between platination and photocleavage is also observed at long incubation times (**Figure 7.13**). As expected, the amount of platination adduct increases with time as RhPt2 is incubated with DNA for 3, 6, and 9 hours. Interestingly, a concomitant decrease in the amount of photocleavage is observed with increasing time (**Figure 7.14**). This may be the result of the kink introduced into DNA upon platinum binding. It is almost certain that kinking the DNA would disrupt metalloinsertion at the mismatch. Thus it follows that if more platinum is bound, less rhodium is bound, and less photocleavage will be observed.

7.2.4: DIFFERENTIAL ANTI-PROLIFERATION EXPERIMENTS

The ultimate goal of a metalloinsertor-platinum conjugate is its successful application as a chemotherapeutic agent for mismatch repair deficient tumors. Thus, BrdU cell proliferation assays were performed in order to investigate the differential biological effect of RhPt2 on mismatch repair proficient and mismatch repair deficient cell lines. To be more specific, two variants of the HCT116 colorectal cancer cell line were employed. The two types of cells, HCT116O and HCT116N, are completely isogenic except for the presence or absence of the gene for the essential mismatch repair protein MLH1. HCT116N cells have an intact copy of the gene and are proficient at mismatch repair, while HCT116O cells do not have the gene and are thus mismatch repair deficient.[44] As discussed earlier in this work, $Rh(bpy)_2(chrysi)^{3+}$ and $Rh(bpy)_2(phzi)^{3+}$ both selectively inhibit the proliferation of HCT116O cells, a biological effect that additional evidence has suggested is related to the mismatch-specific binding of the metalloinsertors.[8, 9]

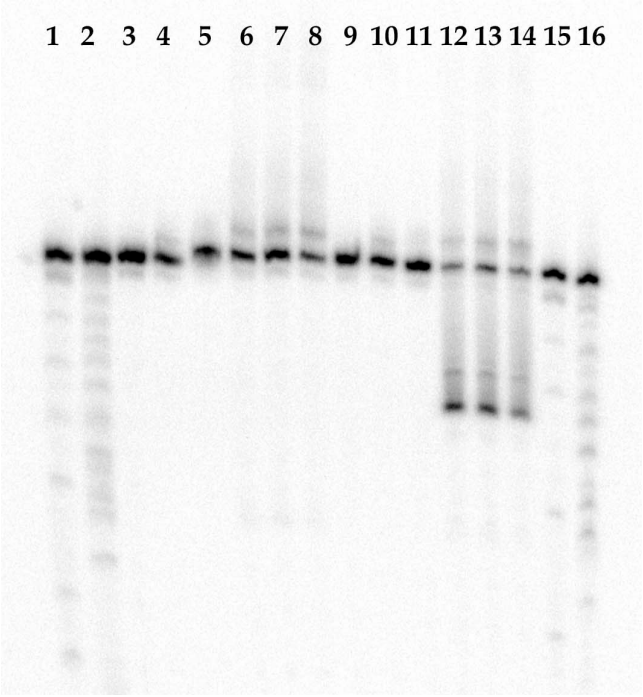

Figure 7.13: The interplay between photocleavage and platination. Autoradiogram of a denaturing 20% polyacrylamide gel showing the DNA photocleavage and platination of RhPt2 as a function of incubation time. Conditions are duplex (2 μM) and RhPt2 (2 μM) in 20 mM NaCl, 10 mM NaPi, pH 7.1 followed by irradiation on an Oriel Instruments solar simulator (320−440 nm). Lanes 1−8 contain matched DNA, and lanes 9−16 contain mismatched DNA. Lanes 1, 2, 15, and 16 are Maxam Gilbert A+T (1, 15) and C+G (2, 16) sequencing reactions. Lanes 3 and 9 contain DNA irradiated for 3 minutes. Lanes 4 and 10 contain DNA with no metal complex and no irradiation. Lanes 5 and 11 contain DNA incubated with RhPt2 for 3 h with no subsequent irradiation. Lanes 5 and 12 contain DNA incubated with RhPt2 for 3 hours with 3 minutes subsequent irradiation. Lanes 6 and 13 contain DNA incubated with RhPt2 for 6 hours with 3 minutes subsequent irradiation. Lanes 7 and 15 contain DNA incubated with RhPt2 for 9 hours with 3 minutes subsequent irradiation. The DNA sequence is 5'-^{32}P-TTA GGA TCA TCC ATA TA-3' where the bold, red C is complementary to a G in the matched duplex and a C in the mismatched duplex.

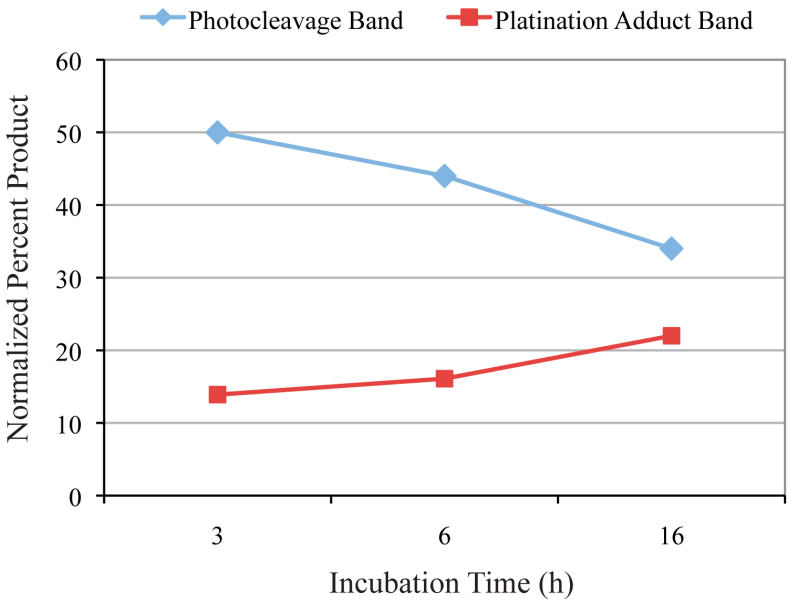

Figure 7.14: The interplay between photocleavage and platination. The quantification of lanes 12, 13, and 14 from the gel shown in **Figure 7.13**. Each product is expressed as a percentage of the total DNA in the lane in question.

For the experiments at hand, the adherent HCT116O/N cells were grown in 96-well plates at a concentration of 2000 cells per well. The cells were then incubated with variable concentrations of metal complex for 24 hours, provided fresh media, allowed to grow for 48 hours, and then labeled with BrdU 24 hours before analysis. The amount of BrdU incorporation and, by extension, cellular proliferation was quantified by ELISA assay according to standard procedures.

Consistent with the literature, cisplatin has very little differential antiproliferative effect in the two cell lines; if anything, the complex is slightly more biologically active in the mismatch repair proficient HCT116N cells (**Figure 7.15**).[33–37] The results with RhPt2 are similar (**Figure 7.16**). The conjugate is certainly biologically active, significantly inhibiting cellular proliferation in both cell lines at concentrations as low as 5 μM. However, no reliable differential effect is observed. The reasons for this phenomenon are unclear. Two explanations seem most likely. First, the metalloinsertor subunit of the conjugate may have attenuated biological activity compared to its parent $Rh(bpy)_2(L)^{3+}$ complexes. Further cell proliferation experiments indicate that this may be at least part of the story, for $Rh(phen)(chrysi)(^{NH2}bpy)^{3+}$ induces significantly less differential antiproliferative effect in HCT116O/N cells than its parent metalloinsertors. As we have discussed earlier in this chapter, this may be a result of the reduced binding affinity characteristic of trisheteroleptic metalloinsertors with linker-modified 4,4'-dimethyl-bipyridine ligands. Second, the hydrolysis of the platinum subunit may occur before the metalloinsertor subunit binds the DNA of the cell in question. This, too, seems like it might be part of the story. For as we have learned more about the cellular uptake of octahedral metal complexes, it has become clear that the average uptake time

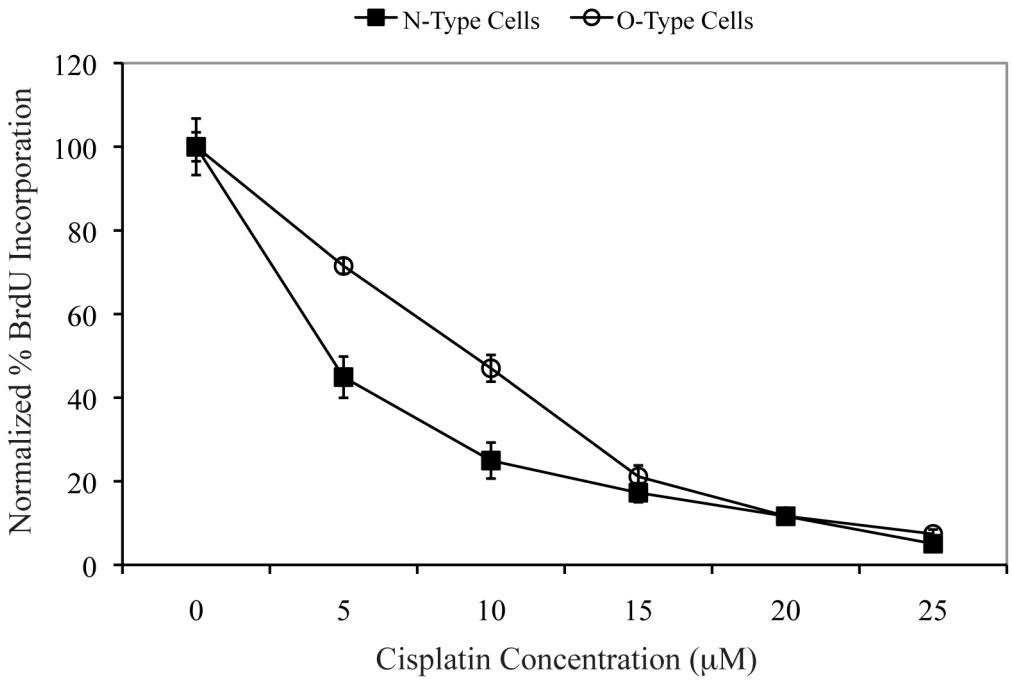

Figure 7.15: The antiproliferative effects of cisplatin on HCT116O/N cells. The normalized percent BrdU incorporation (a marker of cell proliferation) in HCT116O (MMR-) and HCT116N (MMR+) cells is shown as a function of cisplatin concentration.

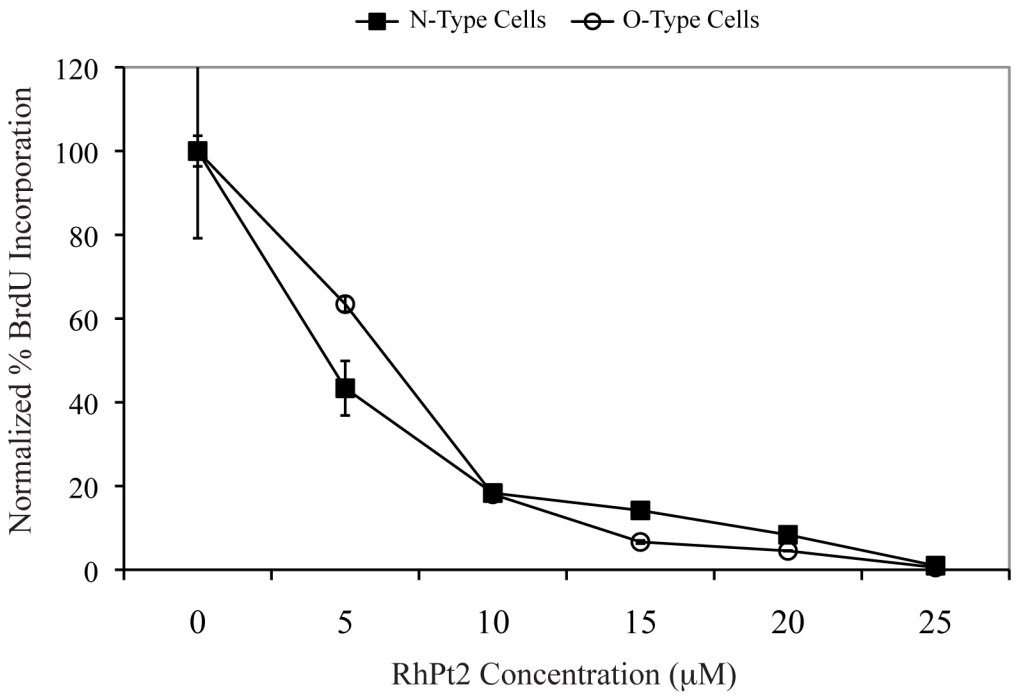

Figure 7.16: The antiproliferative effects of RhPt2 on HCT116O/N cells. The normalized percent BrdU incorporation (a marker of cell proliferation) in HCT116O (MMR-) and HCT116N (MMR+) cells is shown as a function of RhPt2 concentration.

for a complex (approximately 12−24 hours) is far longer than the hydrolysis half life of oxaliplatin-like complexes (approximately 3 hours).

7.2.5: CONCLUSION

Gauging the success of a bifunctional conjugate can be difficult. To be sure, the development of the RhPt2 conjugate met many of its goals. The molecule was successfully synthesized, it binds mismatched DNA with high specificity and affinity, the hydrolysis of the platinum subunit allows for the platination of DNA, and along the way, an interesting interplay between photocleavage and platination was observed. However, the project faltered at its final goal: enhancing the differential antiproliferative effect of metalloinsertors with mismatch repair deficient cells. The reasons for this failure remain unclear. However, it may be that the RhPt2 conjugate was simply a little bit ahead of its time. All conceit aside, we have learned much about both the design of bifunctional conjugates and the cellular uptake of metal complexes since RhPt2 was first developed and tested. Thus, it may ultimately prove advantageous to revisit the idea of a metalloinsertor-platinum chemotherapeutic conjugate, for our newfound understanding of the issues of molecular design and uptake may tip the balance in favor of the successful combination of these two powerful families of molecules.

7.3: A METALLOINSERTOR CONJUGATE BEARING AN AUGER ELECTRON EMITTING RADIONUCLIDE

7.3.1: INTRODUCTION

Radiation therapy plays a central role in the treatment of cancer, and while external beam radiation and brachytherapy undoubtedly remain the most often employed modalities, interest in targeted radiopharmaceutical therapy has grown rapidly over the past three decades in both the laboratory and the clinic.[45−49]

β-Emitters are the most commonly utilized radionuclides for therapeutic purposes, with their low linear energy transfer (LET, <0.2 keV/μm)[e] and high range (100 μm − 5 mm) making them particularly useful for the cross-fire irradiation of large tumors. Indeed, a number of β-emitting radionuclides are currently used in the clinic, including $Na^{131}I$ for thyroid cancer, $^{32}PO_4^{3-}$ for some blood cancers, $^{89}SrCl_2$ for some bone cancers, and ^{131}I-m-iodobenzylguanidine for neuroendocrine cancers.[45] However, while the low LET of β-emitting radionuclides makes them well-suited for large tumor masses, it can render them less effective at killing individual cancer cells. As a result, for some applications, the field is increasingly interested in α-emitting radionuclides. Due to their short range (30−80 μm) and high LET (80−100 keV/μm), α-emitters are tremendously cytotoxic to single cells and small tumors.[50, 51] A large volume of work has centered on the labeling of monoclonal antibodies with α-emitting nuclei; however, the progress has been somewhat limited by the small number of suitable radionuclides. Indeed, to date only ^{211}At, ^{211}Bi, and ^{213}Bi have been actively pursued, though new efforts at designing multi-α-emitting 'nanogenerators' are intriguing.[52]

[e] Linear energy transfer (LET) is the amount of energy lost per unit distance as an ionizing particle travels through a material. It depends on a given particle's type, charge, and energy.

While most of the research into the development of targeted radiopharmaceuticals has centered on α- and β-emitting nuclei, a third class of radionuclides has garnered increasing attention in recent years for its potential in DNA-targeted radiotherapeutic agents: Auger electron emitters. First discovered in the late 1920s by Pierre Auger, Auger electrons are low energy electrons ejected from radionuclides as a result of internal conversion or electron capture processes.[53–55] Indeed, almost half of all radionuclides emit Auger electrons (for a partial list, see **Figure 7.17**). The process is relatively simple (**Figure 7.18**). Taking ^{111}In as an example, the radionuclide in question first undergoes an electron capture process that results in the emission of a γ-ray and the formation of an inner shell electron vacancy. An electron in a higher energy level then drops down to fill this hole, and the energy released during this conversion is transferred to another electron that is consequently ejected from the radionuclide. This ejected electron is an Auger electron. Interestingly, multiple Auger electrons, sometimes as many as 30, can be emitted per decay event. Returning to our model, after the ejection of the first Auger electron, there are now two vacancies, one created by the electron that filled the original hole and one formed by the ejection of the Auger electron. Now, the process repeats itself, with two electrons from higher energy orbitals filling these vacancies and two additional electrons ejected from the atom with the energy released upon these conversions. This process repeats itself in an Auger cascade until the vacancies reach the outermost energy levels. By this time, the radionuclide has emitted many Auger electrons and, as a result, has become a highly charged polycation. In an event provocatively named the Coulombic explosion, the polycation is neutralized by oxidizing the

Radionuclide	Half-Life (d)	Auger Yield	Total Energy (keV)
^{51}Cr	27.7	5.4	3.653
^{55}Fe	997.1	5.1	4.177
^{67}Ga	3.26	4.7	6.264
^{75}Se	120	7.4	5.74
^{77}Br	2.38	6.7	5.218
^{99m}Tc	0.25	4.0	0.899
^{111}In	2.8	14.7	6.75
^{113m}In	0.069	4.3	2.047
^{115m}In	4.5	6.1	2.847
^{123}I	0.55	14.9	7.419
^{125}I	60.1	24.9	12.241
^{193m}Pt	4.33	26.4	10.353
^{195m}Pt	4.02	32.8	22.526
^{201}Tl	3.04	36.9	15.273
^{203}Pb	2.16	23.3	11.63

Figure 7.17. Some Auger-electron emitting radionuclides. Note the considerable differences in Auger yield (the number of electrons emitted per decay), ranging from an average of 4.0 for ^{99m}Tc to an average of 36.9 for ^{201}Tl.[56]

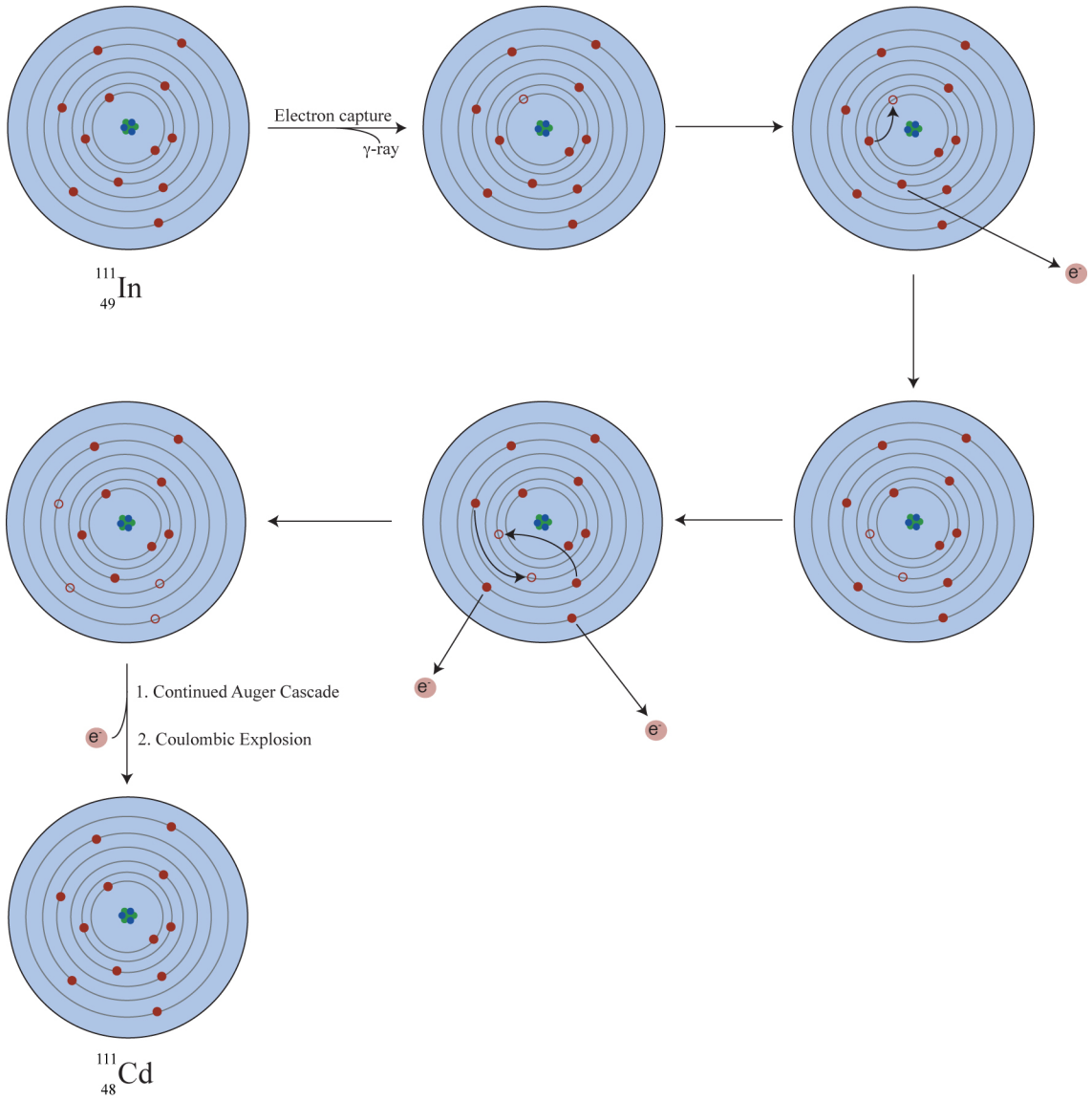

Figure 7.18: Schematic of the Auger electron emission pathway of ^{111}In

surrounding environment, forming the neutral daughter nucleus (^{111}Cd in the case of ^{111}In) and completing the process.

From a biomedical perspective, the high number of electrons per decay, high linear energy transfer (4−26 keV/μm), and short path length (<20 nm in water) are the keys to the therapeutic potential of Auger electron emitters.[56−58] These three factors combine to create tremendous energy densities at, and only at, the site of decay. While this trait may limit the efficacy of these radionuclides in large tumors, it translates to extremely high cytotoxicity if the radionuclei are directed at the appropriate intracellular target, namely DNA. Indeed, if confined to the cytoplasm, an Auger electron emitting agent induces a cytotoxic response that follows a profile characteristic of low-LET radionuclides. If in the nucleus, however, the same agent will induce a cytotoxic response more characteristic of a very high LET radionuclide.[57]

From a mechanistic standpoint, Auger electrons promote cell death by both necrosis and radiation-induced apoptosis by creating double strand breaks in DNA.[59, 60] It is likely that reactive oxygen species created both by the Auger electrons themselves and the Coulombic explosion also play significant roles in mediating the biological effect. Further still, Auger electron emitters are largely non-toxic in the blood or near bone marrow and many undergo concomitant γ-decay that may allow for radiotherapy and diagnostic imaging with a single radionuclide.[56, 57] Given all this potential, it is not surprising that a number of Auger emitting therapeutic agents have been developed, including ^{111}In-peptide conjugates[61], ^{125}I-labeled estrogens[62], ^{125}I- and ^{123}I-labeled nucleosides[63−65], ^{195m}Pt transplatin[66], and ^{99m}Tc-intercalator conjugates[67] (**Figure 7.19**).

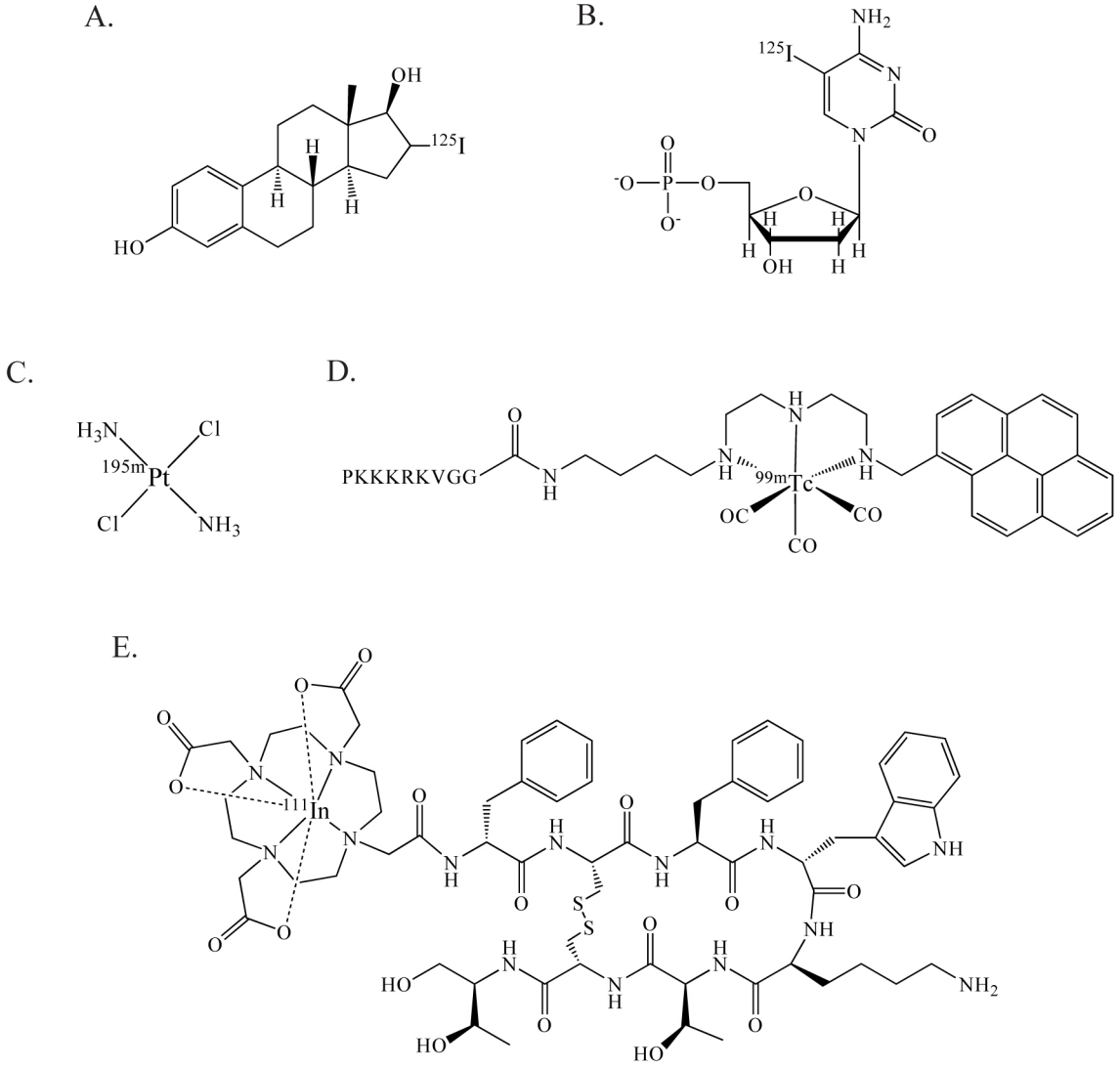

Figure 7.19: Some Auger electron emitting radiotherapeutic agents. (A) ^{125}I-16-α-iodoestradiol[62]; (B) C5-^{125}I-deoxycytosine[63, 64]; (C) *trans*-^{195m}Pt$(NH_3)_2(Cl)_2$[66]; (D) a ^{99m}Tc-nuclear localization signal-pyrene conjugate[67]; (E) ^{111}In-Octreoide, a clinically-employed, γ-emitting imaging agent that is currently being investigated for its efficacy as a Auger-emitting radiotherapeutic.[61]

The mismatch-specific conjugates previously developed by our laboratory for therapeutic applications have undeniably proven successful in oligonucleotide-based experiments.[12, 13] However, their *in vivo* success at preferentially inhibiting the proliferation of mismatch repair deficient cells has been limited. This is likely because the differential antiproliferative activity of these conjugates is predicated on their selective accumulation in mismatch repair deficient cells. For example, because the alkylator subunit of the metalloinsertor-nitrogen mustard conjugate is cytotoxic whether the rhodium subunit is bound to DNA or not, we must rely on the mismatch-specific binding of the metalloinsertor to lead to the selective accumulation of the conjugate in mismatch repair deficient cells.[12] This is a departure from the principles behind the biological activity of $Rh(bpy)_2(chrysi)^{3+}$ and $Rh(bpy)_2(phzi)^{3+}$. While the exact mechanistic details are still murky, it has become abundantly clear that the differential biological effect of these complexes is based on their specific binding of DNA mismatches.[8, 9] It follows, then, that the selective accumulation of these complexes in MMR-deficient cells is likely a minor factor, if one at all, in the observed differential effect. This supposition is further supported by recent ICP-MS experiments that show no differential accumulation of rhodium in MMR-proficient and -deficient cells.

Auger electron emitting radionuclides afford a singular opportunity to create bifunctional metalloinsertor conjugates with antiproliferative effects that are based on specific binding of mismatched DNA rather than selective localization in MMR-deficient cells. Because of the unique properties of Auger electrons, Auger electron emitting radionuclides are only capable of producing a significant cytotoxic response if *bound* to DNA. Importantly, simply being in the nucleus is not good enough. Investigations have

shown that DNA-bound Auger emitters kill cells far more efficiently than nucleus-localized, but non-DNA-bound emitters. The ramifications for a mismatch-specific, bifunctional conjugate are clear. In MMR-deficient cells, the Rh-Auger conjugate will enter the nucleus, bind to mismatches in the DNA, cause double strand breaks upon decay, and prompt cell death. In MMR-proficient cells, the Rh-Auger conjugate will still enter the nucleus, but in this case, the absence of mismatches will prevent DNA binding, and thus the conjugate will be far less effective at killing the cells (**Figure 7.20**). Clearly, a Rh-Auger conjugate holds tremendous potential as a selective cytotoxic agent for mismatch repair deficient cells.

Herein, we present preliminary investigations into the design, synthesis, and study of a mismatch-specific, metalloinsertor-Auger electron emitter conjugate.

7.3.2: DESIGN

The most important design decision in the development of a Rh-Auger conjugate is the choice of radionuclide. The ultimate goal of this line of investigation is, of course, the development of a therapeutic agent. Thus, it was tempting to choose one of the more clinically applicable Auger emitting radionuclides, such as ^{111}In, ^{123}I, or ^{99m}Tc. However, many other preliminary investigations have employed a different radionuclide, ^{125}I, in proof-of-concept model systems. Granted, the 60-day half-life of ^{125}I renders it relatively unusable for clinical applications. However, it is often employed in this manner primarily because ^{125}I has been shown to promote double strand breaks particularly well, most likely a result of its high number of Auger electrons emitted per decay, and thus

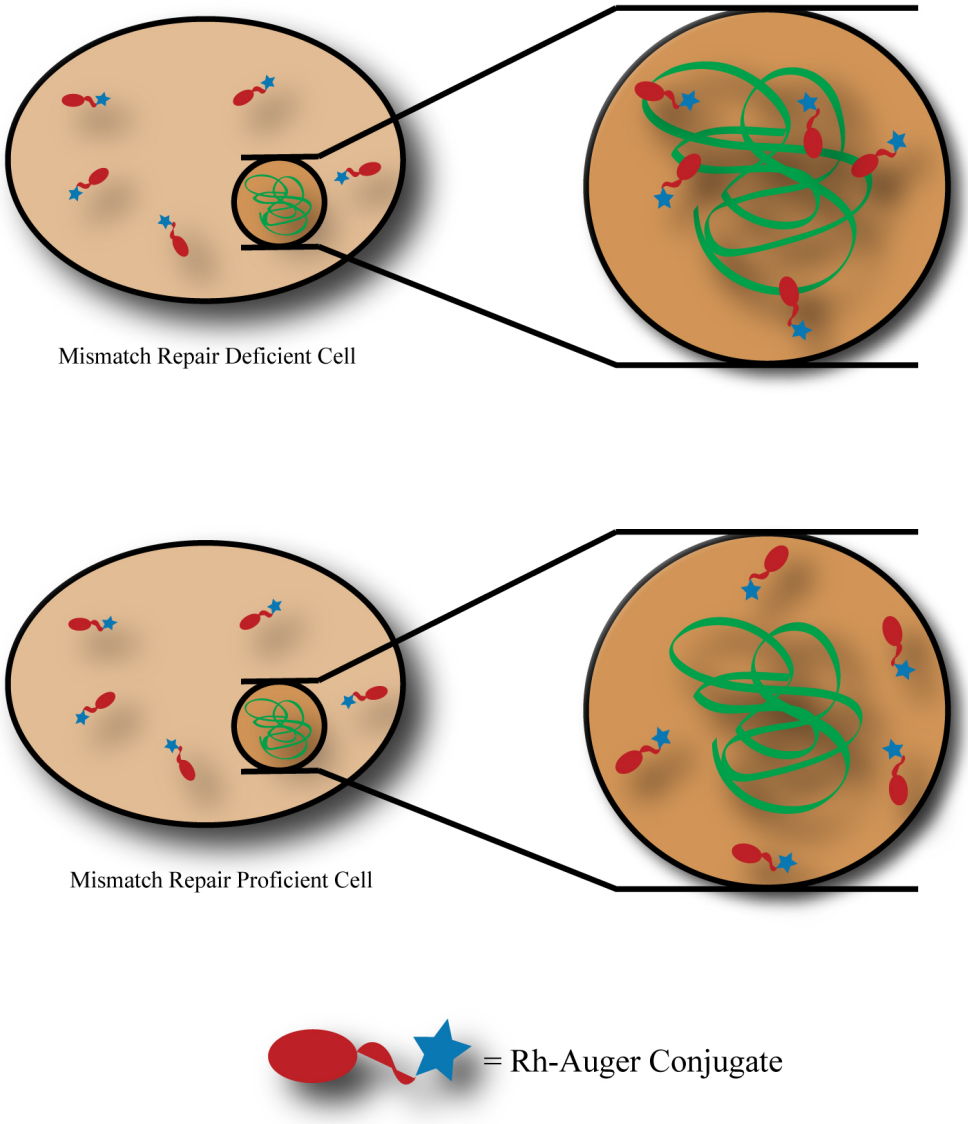

Figure 7.20: A Rh-Auger conjugate in MMR-proficient and -deficient cells. In MMR-deficient cells, the Rh-Auger conjugate will enter the nucleus, bind to mismatches in the DNA, cause double strand breaks upon decay, and prompt cell death. In MMR-proficient cells, the Rh-Auger conjugate will still enter the nucleus, but in this case, the absence of mismatches will prevent DNA-binding, and thus the conjugate will be far less effective at killing the cells.

lends itself well to PAGE electrophoresis studies with radiolabeled oligonucleotides.[63, 64, 68] The well-developed chemistry of iodination reactions may also play a significant role in the frequency of ^{125}I use. At bottom, if a Rh-^{125}I conjugate proves successful in oligonucleotide experiments, a new, more clinically relevant radionuclide such as ^{111}In or ^{123}I can be substituted with relative ease.

7.3.3: SYNTHESIS

The exigencies of radiochemistry required that this conjugate be synthesized in a linear fashion, with the ^{125}I radionuclide introduced last. Based on the structure considerations discussed earlier in this chapter, a trisheteroleptic metalloinsertor bearing a dipyridylamine ligand with a carboxy-terminated linker was employed. The metalloinsertor-linker subunit was synthesized in a step-wise fashion from $RhCl_3$ (**Figure 7.21**). The radioiodination reaction requires a phenolic hydroxyl group for substitution with ^{125}I.[69] Therefore, a tyramine was then coupled to the metalloinsertor subunit using HATU to provide the necessary radioiodination substrate. Next, the Rh-tyramine conjugate was purified by cation exchange chromatography and HPLC and sent to Perkin-Elmer for radioiodination. After one week, the radiolabeled and HPLC-purified Rh-^{125}I conjugate was returned (**Figure 7.22**). The specific activity of the final product was 2200 Ci/mmol (2070 μCi/μg), and it was provided at a concentration of 250 μCi/mL (120 nM Rh). The initial radiochemical purity of the Rh-^{125}I conjugate was >95%.

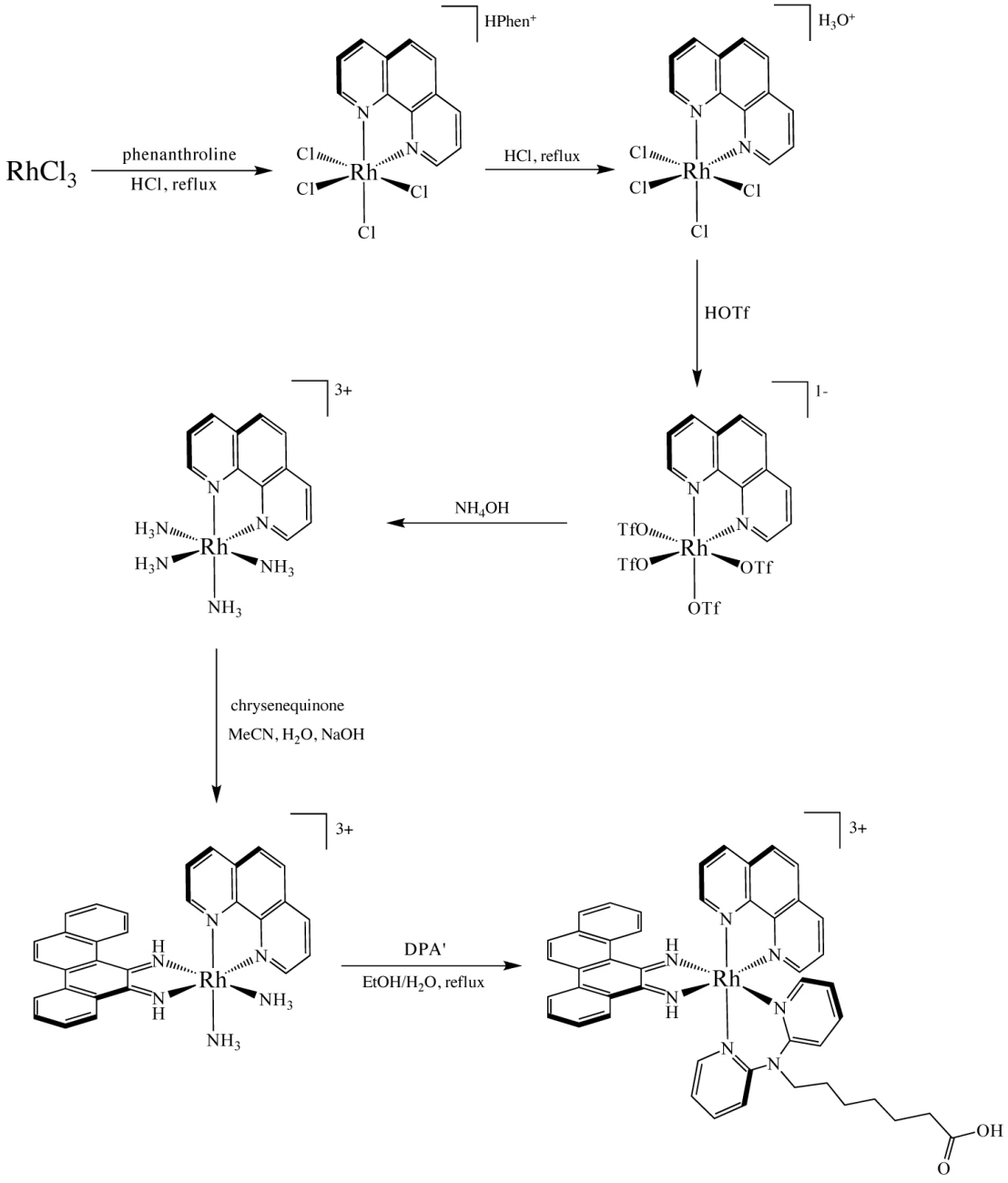

Figure 7.21. **The synthetic route to the trisheteroleptic metalloinsertor subunit.** The conjugate's metalloinsertor subunit was synthesized via the sequential addition of phen, chrysi, and DPA' ligands to a rhodium center.

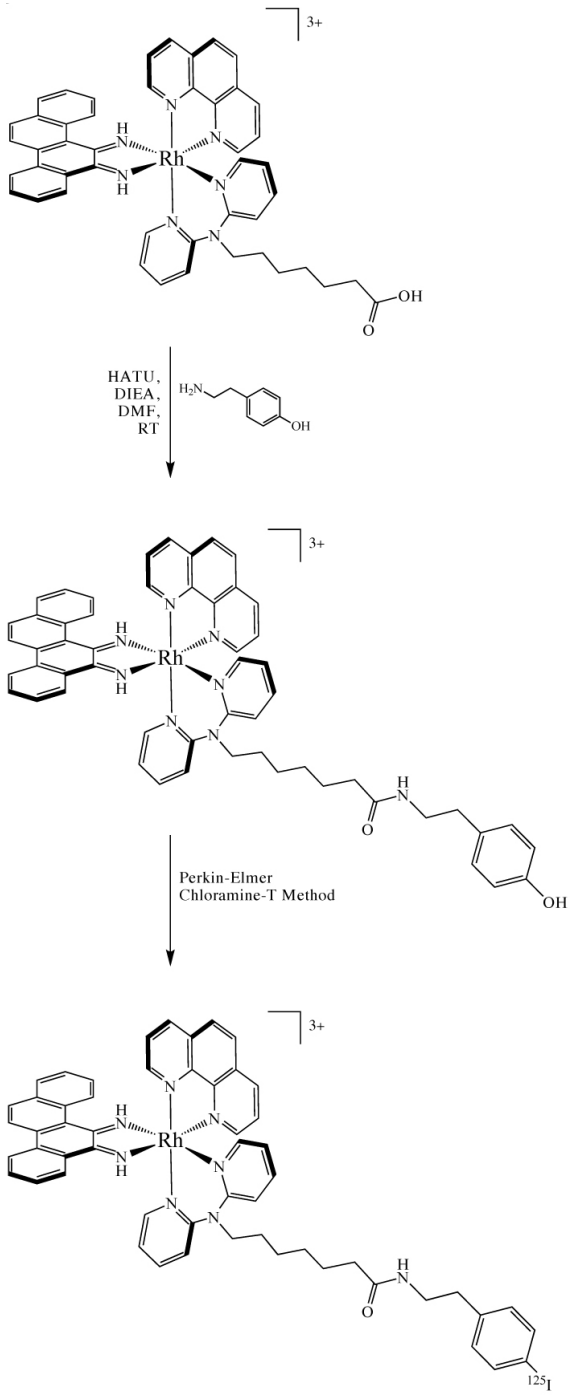

Figure 7.22: The synthetic route to Rh-^{125}I. Tyramine was first coupled to the metalloinsertor subunit to provide a hydroxyl group for the labeling reaction. Then, the completed Rh-tyramine conjugate was sent to Perkin-Elmer for radioiodination via the Chloramine-T method.[69]

7.3.4: DNA CLEVAGE STUDIES

In order to interrogate the mismatch-specific binding and photocleavage of the Rh-^{125}I experiment, the precursor Rh-tyramine conjugate was employed in denaturing PAGE experiments using 5'-^{32}P-labeled oligonucleotides containing or lacking a central C•C mismatch. These experiments illustrate that the Rh-tyramine conjugate (and, by proxy, the Rh-^{125}I conjugate) specifically recognizes mismatched DNA (**Figure 7.23**). Due to the substitution of a linker-modified dipyridylamine for the linker-modified bipyridine ligand, the Rh-tyramine conjugate displays considerably reduced photocleavage efficiency. This loss in photochemistry, however, is inconsequential for the radionuclide conjugates, for in this case, the job of the metalloinsertor unit is simply to bind mismatch DNA and bring the radionuclide moiety in close proximity to the helix.

Next, preliminary PAGE experiments were performed to investigate the Auger electron mediated DNA cleavage of Rh-^{125}I with matched and mismatched oligonucleotides. For these experiments, 5 μL solutions of Rh-^{125}I (60 nM Rh, 1.25 μCi) were combined with equal volume solutions of 5'-^{32}P-labeled oligonucleotides containing a central C•G, C•C, or C•A base pair (50, 100, or 150 nM). The samples were frozen to prevent diffusion of reactive oxygen species and incubated for two, three, or four weeks. Autoradiography of the resultant gels shows little cleavage in any of the DNA strands after 7, 14, or 21 days of incubation (**Figure 7.24**). This is somewhat surprising, considering the conjugate is known to bind selectively to mismatched DNA, and this would almost certainly bring the radionuclide in close enough proximity to the duplex to promote strand scission.

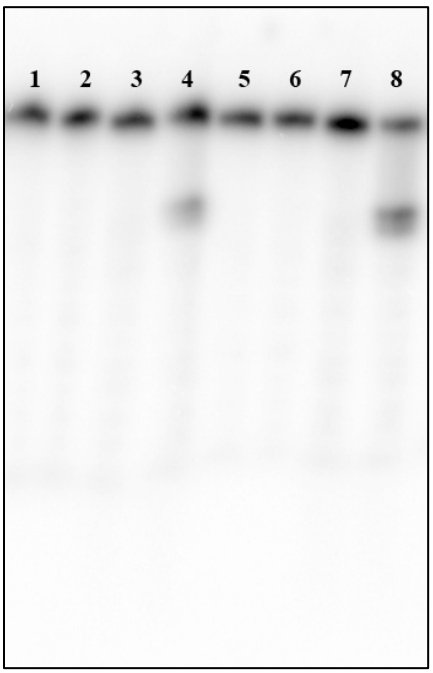

Figure 7.23: Mismatch recognition and photocleavage by Rh-tyramine. Autoradiogram of a denaturing 20% polyacrylamide gel showing the mismatch recognition and photocleavage of Rh-tyramine. Conditions are duplex (1 μM) and Rh complex (1 μM) in 20 mM NaCl, 10 mM NaPi, pH 7.1. Irradiations were performed using an Oriel Instrument Solar Simulator (320−440 nm). Lane 1: matched DNA, light control. Lane 2: matched DNA, Rh-Try, 15 min irradiation. Lane 3: mismatched DNA, light control. Lane 4: mismatched DNA, Rh-Tyr, 15 min irradiation. Lane 5: matched DNA, light control. Lane 6: matched DNA, $Rh(bpy)_2(chrysi)^{3+}$, 15 min irradiation. Lane 7: mismatched DNA, light control. Lane 8: mismatched DNA, $Rh(bpy)_2(chrysi)^{3+}$, 15 min irradiation. The DNA sequence is 5'-^{32}P-GAC CAG CTT ATC AT**C** CCT AGA TTA GCG-3' where the bold, red C is complementary to another C in the mismatched duplexes and a G in the matched duplexes.

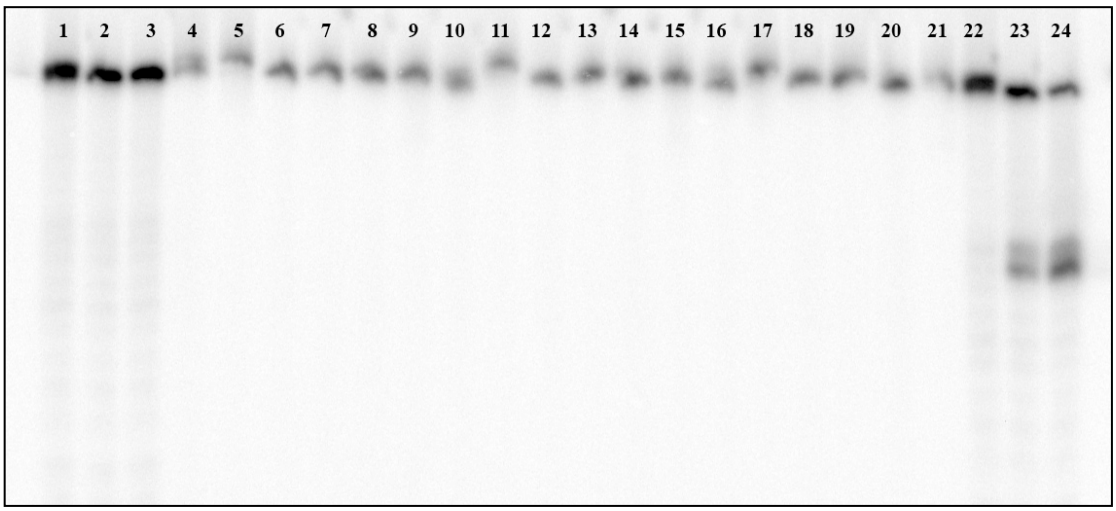

Figure 7.24: DNA cleavage of Rh-^{125}I. Autoradiogram of a denaturing 20% polyacrylamide gel showing DNA cleavage properties of Rh-^{125}I. Conditions are duplex (50, 100, or 150 nM) and Rh complex (60 nM, 1.25 μCi) in 20 mM NaCl, 10 mM NaPi, pH 7.1. Incubations are for 21 days at -80 °C. The forward (F) strand DNA sequence is 5'-GAC CAG CTT ATC AT**C** CCT AGA TTA GCG-3'. The matched sequence (M) is 5'-CGC TTA TCT AGG **G**AT GAT AAG CTG GTC-3'. The C•A mismatched sequence (A) is 5'-CGC TTA TCT AGG **A**AT GAT AAG CTG GTC-3'. The C•C mismatched sequence (C) is 5'-CGC TTA TCT AGG **C**AT GAT AAG CTG GTC-3'. For each assembly, lanes were run with each strand labeled in order to check for double strand breaks. Thus, F*M denotes matched DNA with the forward strand labeled. Lanes 1, 2, and 3 contain dark control experiments with 100 nM F*M, F*A, and F*C, respectively. Lanes 4, 10, and 16 contain F*M DNA. Lanes 5, 11, and 17 contain FM* DNA. Lanes 6, 12, and 18 contain F*A DNA. Lanes 7, 13, and 19 contain FA* DNA. Lanes 8, 14, and 20 contain F*C DNA. Lanes 9, 15, and 21 contain FC* DNA. Lanes 22, 23, and 24 contain $Rh(bpy)_2(chrysi)^{3+}$ photocleavage experiments with 100 nM F*M, F*A, and F*C, respectively. Irradiations were performed using an Oriel Instrument solar simulator (320−440 nm).

A few different factors may be at the root of these results. It is possible that the aliphatic linker and tyramine moiety simply move the radionuclide too far away from the DNA, out of the effective range of the Auger electrons. This, however, is not likely, because the ^{125}I lies only thirteen bonds from the dipyridylamine ligand, and even this distance, which assumes a fully extended linker, is within the range of most Auger electrons. A more likely explanation lies in the low specific activity (1.25 μCi) of the conjugates employed in the Auger electron DNA cleavage experiments. Indeed, other laboratories typically employ specific activities almost two orders of magnitude higher (~70−100 μCi) for similar experiments.[63, 64, 68] This issue will be difficult to remedy in the current experimental environment. Because Perkin-Elmer typically performs ^{125}I-iodinations for imaging applications (which require lower specific activities), the 250 μCi/mL with which they provided our laboratory was the maximum specific activity at which they label. Normally, the solution of radiolabeled conjugate could simply be concentrated *in vacuo*, but our laboratory is not a radiochemistry laboratory, and the Environmental Health and Safety Office strongly discourage using common laboratory equipment in conjunction with the ^{125}I-labeled conjugate.

7.3.5: CONCLUSION

The idea of metalloinsertor-Auger electron emitter conjugate is certainly a work in progress. The principle is sound. In a seminal paper on the topic, O'Donaghue and Whelton distill the issue quite nicely: "For an Auger-targeting therapy based on [DNA-binding], biological specificity would rely on the existence of qualitative or quantitative differences in DNA sequence between tumuor and normal cells."[58] This is precisely the

case in mismatch repair deficient tumors. Further still, mismatch-specific metalloinsertors provide a means to bring Auger electron emitting radionuclides into close range of the DNA of MMR-deficient cells while allowing them to stay at a safer distance from that of MMR-proficient cells.

The Rh-^{125}I conjugate described herein may well provide a proof-of-concept model for this system. To be sure, changes in our radiochemical setup and procedures will be necessary for success and design changes to bring the metalloinsertor and radionuclide moieties closer together may be advisable. Further, a conjugate with a more clinically applicable radionuclide, such as ^{111}In or ^{123}I, will need to be adopted for any future *in vitro* and *in vivo* studies. Ultimately, while it is certain that there is much left to be done, mismatch-specific, Auger electron emitting conjugates hold tremendous potential for the treatment of mismatch repair deficient tumors and will hopefully merit further attention from our laboratory.

7.4: EXPERIMENTAL PROTOCOLS

Many of the procedural details for this investigation are included in Chapter 2 of this text. These include the following: the syntheses of Rh(phen)(chrysi)$(NH_3)_2^{3+}$ (2.3.4.1−2.3.4.5), ^{NH2}bpy (2.3.5.1−2.3.5.3), and DPA' (2.3.5.7, 2.3.5.10, 2.3.5.11), Rh(phen)(chrysi)(^{NH2}bpy)$^{3+}$ (by analogy to 2.3.5.12), and Rh(phen)(chrysi)(DPA')$^{3+}$ (2.3.5.13); the synthesis, purification, and radiolabeling of oligonucleotides (2.4.1−2.4.2); the Maxam-Gilbert sequencing of radiolabeled DNA (2.4.3); and the performance of recognition and binding titration experiments via PAGE (2.4.4.1−2.4.4.2).

7.4.1: MATERIALS AND INSTRUMENTATION

All reagents were obtained from commercial sources and used as received without further purification. $RhCl_3$ was purchased from Pressure Chemicals. K_2PtCl_4 was purchased from Strem Chemicals. Media and supplements were purchased from Invitrogen. BrdU, antibodies, buffers, and peroxidase substrate were purchased in kit format from Roche Molecular Biochemicals. Radioiodination was performed by Perkin-Elmer. All non-aqueous solvents were purchased from Fluka and stored under argon and over molecular sieves. All water used was purified using a MilliQ water purification system. Unless otherwise noted, all reactions were performed under ambient conditions.

^{1}H-NMR spectra were recorded on a Varian 300 MHz spectrometer at room temperature using solvent residual signal as a reference to TMS. Mass spectrometry was performed at either the Caltech mass spectrometry facility or in the Beckman Institute Protein/Peptide Micro Analytical Laboratory (PPMAL). Absorption spectra were recorded on a Beckman DU 7400 spectrophotometer. Extinction coefficients were determined using inductively coupled plasma mass spectrometry (ICP-MS).

Oligonucleotides were synthesized on an ABI 3400 DNA synthesizer and purified via HPLC in duplicate (DMT-off and DMT-on) before use. All reverse-phase HPLC purifications were performed on an HP1100 high-pressure liquid chromatography system equipped with diode array detector using a Varian DynaMax C18 semipreparative column (see Chapter 2, Section 2.4.1). Irradiations were performed using an Oriel Instruments solar simulator (320−440 nm). All PAGE experiments described employed denaturing 20% polyacrylamide gels (SequaGel, National Diagnostics) and were performed according to published procedures. Further, gels were developed using

Molecular Dynamics phosphorimaging screens and a Molecular Dynamics Storm 820 phosphorimager and were subsequently visualized and quantified with Molecular Dynamics ImageQuant software.

7.4.2: Synthesis and testing of RhPt2

7.4.2.1: Synthesis of 4-formylbenzoic acid tert-butyl ester (method 1)

In a 50 mL round-bottom flask, 1.30 g 4-carboxybenzaldehyde (8.7 mmol) were suspended in benzene (15 mL, dry) and brought to reflux under argon. Still under argon, 4.5 mL N,N-dimethyldi-tert-butylacetal (18.8 mmol, 2.2 equiv) were added dropwise over the course of 15 min. The reaction was monitored via TLC (SiO_2, CH_2Cl_2). After 3 h, the yellow reaction mixture was allowed to cool to room temperature, extracted with $NaHCO_3$(aq), washed with brine, dried with $MgSO_4$, and concentrated via rotary evaporation. The residue was purified via column chromatography (SiO_2, 5:1 hexanes:diethyl ether) to yield 1.1 g of the product as a yellow oil (61%).

^{1}H-NMR ($CDCl_3$): 10.11 ppm (s, 1H); 8.17 ppm (d, 2H); 7.94 ppm (d, 2H), 1.66 ppm (s, 9H).

7.4.2.2: Synthesis of 2-(4-tert-butoxycarbonylbenzylidene)-malonic acid dibenzyl ester (method 1)

In a 10 mL round-bottom flask, 500 mg 4-formylbenzoic acid tert-butyl ester (2.4 mmol) and 0.62 mL dibenzylmalonate (2.5 mmol, 1 equiv.) were dissolved in dry THF (3 mL) and cooled down in an ice bath. Then, 0.56 mL titanium tetrachloride (5 mmol, 2 equiv.) were added, and the mixture was stirred under argon at 0 °C for 3 h. After 3 h, 0.8

mL dry pyridine were added, and the mixture was warmed to room temperature and stirred for 48 h. After 48 h, water (20 mL) and dichloromethane (50 mL) were added to the reaction mixture. The organic layer was separated, extracted three more times with dichloromethane, washed with brine, dried with $MgSO_4$, and concentrated via rotary evaporation. The residue was purified via column chromatography (SiO_2, CH_2Cl_2) to yield 550 mg of the product as a white solid (47%).

^{1}H-NMR ($CDCl_3$): 7.83 ppm (d, 2H); 7.79 ppm (s, 1H); 7.25-7.45 ppm (m, 12H), 5.29 ppm (s, 2H), 5.26 ppm (s, 2H), 1.62 ppm (s, 9H).

ESI-MS: 473 $[M+H]^+$

7.4.2.3: SYNTHESIS OF 2-(4-CARBOXYBENZYLIDENE)-MALONIC ACID DIBENZYL ESTER (METHOD 2)

In 10 mL round-bottom flask, 1.9 g 4-carboxybenzaldehyde (12.7 mmol) and 3.2 mL dibenzylmalonate (12.7 mmol, 1 equiv.) were cooled in an ice bath. Dry carbon tetrachloride (5 mL) and 2.5 mL titanium tetrachloride (1.8 equiv.) were then added to the reaction mixture under argon. The yellow mixture was stirred at 0 °C for 3 h. After 3 h, 4 mL dry pyridine were added, and the mixture was warmed to room temperature and stirred for 48 h. After 48 h, water (20 mL) and dichloromethane (50 mL) were added to the reaction mixture. The organic layer was separated, extracted three more times with dichloromethane, washed with brine, dried with $MgSO_4$, and concentrated via rotary evaporation to yield a yellow oil. The oil was then triturated with diethyl ether, and the resultant white solid was filtered and air dried to produce 3.2 g of the desired product (61%).

^{1}H-NMR ($CDCl_3$): 7.96 ppm (d, 2H); 7.81 ppm (s, 1H); 7.25−7.45 ppm (m, 12H), 5.29 ppm (s, 2H), 5.27 ppm (s, 2H).

ESI-MS: 417 $[M+H]^+$

7.4.2.4: SYNTHESIS OF 2-(4-TERT-BUTOXYCARBONYLBENXYLIDENE)-MALONIC ACID DIBENZYL ESTER (METHOD 2)

In a 250 mL round-bottom flask, 3.58 g 2-(4-carboxbenzylidene)-malonic acid dibenzyl ester (8.6 mmol) were suspended in CH_2Cl_2, and 4 drops of neat sulfuric acid were added to the solution. Under argon, isobutene was bubbled through the solution for 5 min. The suspension was stirred under argon at room temperatures for 3 days, and isobutene was bubbled through the solution every 7 h. After 3 days, the mixture was diluted with CH_2Cl_2 (50 mL) and saturated $NaHCO_3$ (aq) (50 mL) and shaken in a separatory funnel, and the organic layer was isolated. The aqueous layer was then further extracted with CH_2Cl_2 (3 x 50 mL). The combined organic layers were washed with brine, dried with $MgSO_4$, and concentrated via rotary evaporation to yield 4.0 g of the product as a colorless oil that solidifies to a white solid with time (>98%). The ^{1}H-NMR and ESI-MS were identical to those obtained for the product of the reaction described in Section 7.4.2.2.

7.4.2.5: SYNTHESIS OF 2-(4-TERTBUTOXYCARBONYLBENZYL)-MALONIC ACID

In a 50 mL Schlenk flask, 40 mg 10% Pd/C were added to 300 mg 2-(4-tert-butoxycarbonylbenxylidene)-malonic acid dibenzyl ester in 15 mL of EtOH. The reaction vessel was evacuated, filled with $H_{2(g)}$, and stirred overnight. After 16 h, the reaction

mixture was opened to the atmosphere and filtered through celite. The resultant solution was concentrated via rotary evaporation to yield 180 mg of the product as a thick colorless oil (>95%).

^{1}H-NMR ($CDCl_3$): 7.92 ppm (d, 2H); 7.28 ppm (d, 2H); 3.74 ppm (t, 1H), 3.31 ppm (d, 2H), 1.57 ppm (s, 9H).

ESI-MS: 295 $[M+H]^+$

7.4.2.6: SYNTHESIS OF PT(DACH)I_2

In a 50 mL round-bottom flask, 1.0 g K_2PtCl_4 (2.40 mmol) was dissolved in water (10 mL) by heating to 50 °C. An aqueous solution of 1.95 g KI in 4 mL water (11.7 mmol, 5 equiv.) was then added dropwise to the reaction mixture, and the dark brown solution was allowed to stir at 50 °C for 10 min. After 10 min, a solution of 0.3 g 1R,2R-(-)-transdiaminocyclohexane (dach) in 3 mL water (2.6 mmol, 1.1 equiv.) was added dropwise to the solution. A dark yellow precipitate then formed nearly immediately, and after 30 min more stirring, the precipitate was centrifuged, washed with water (3 x 10 mL) and cold ethanol (1 x 5 mL), and dried *in vacuo* to yield 1.32 g of the product as a dark yellow solid (98%).

7.4.2.7: SYNTHESIS OF PT(DACH)$(NO_2)_2$

In a 50 mL round-bottom flask, 500 mg Pt(dach)$(I)_2$ and 300 mg $AgNO_3$ (1.83 mmol, 2 equiv.) were suspended in water (20 mL). The resultant mixture was then protected from light and stirred at 60 °C for 30 min. After 30 min, a beige precipitate had formed. This precipitate was filtered and washed with water (2 x 5 mL). The resultant

clear filtrate was checked for silver (dilute HCl), concentrated *in vacuo*, taken up in water (20 mL), and filtered through celite. The filtrate was then concentrated again *in vacuo* and triturated in a mixture of methanol (8 mL) and water (0.1 mL). The off-white residue was filtered, washed with methanol, and dried again *in vacuo* to yield 290 mg of the product as a white solid (70%).

^{1}H-NMR ($CDCl_3$): 7.92 ppm (d, 2H); 7.28 ppm (d, 2H); 3.74 ppm (t, 1H), 3.31 ppm (d, 2H), 1.57 ppm (s, 9H).

ESI-MS: 295 $[M+H]^+$

7.4.2.8: SYNTHESIS OF PT(DACH)(MALBZCOOTBU)

In a 50 mL round-bottom flask, 120 mg Pt(dach)$(NO_2)_2$ were dissolved in water (15 mL) via sonicating and heating. A solution of 90 mg 2-(4-tertbutoxycarbonylbenzyl)-malonic acid (1.1 equiv.) in 5 mL 0.12 M KOH was then added dropwise to the platinum solution at room temperature over the course of 5 min. The resultant mixture was then stirred at 50 °C for 3 h. After 3 h, the mixture was chilled to 4 °C in the cold room and left there over night. The next morning, a white solid had formed and was filtered, washed with water (5 mL) and diethyl ether (5 mL), and dried *in vacuo* to yield 100 mg of the desired product as an off-white powder (60%).

^{1}H-NMR (CD_3OD): 7.84 ppm (d, 2H); 7.39 ppm (d, 2H); 4.14 ppm (t, 1H), 3.43 ppm (d, 2H), 2.25−2.35 ppm (m, 2H), 1.9−2.1 ppm (m, 2H), 1.4−1.6 ppm (m, 11H), 1.1−1.4 (m, 4H).

ESI-MS: 602 $[M+H]^+$

7.4.2.9: SYNTHESIS OF PT(DACH)(MALBZCOOH)

In a 10 mL round-bottom flask, 100 mg Pt(dach)(MalBzCOOtBu) were dissolved in 1.5 mL neat TFA and warmed to 35 °C for 5 min. After 5 min, the TFA was removed *in vacuo*, and the resultant pale yellow solid was washed with 5 mL diethyl ether by suspension, centrifugation, and removal of the supernatant. After 10 repeated rounds of washing, the pale yellow solid was air-dried to produce the 50 mg of the desired product as a grey solid (60%).

^{1}H-NMR (d_6-DMSO): 7.82 ppm (d, 2H); 7.31 ppm (d, 2H); 7.0−6.3 ppm (broad m, 2H), 6.1−5.8 ppm (broad m, 2H), 5.4−5.0 ppm (broad m, 2H), 4.02 ppm (t, 1H), 3.08 ppm (d, 2H), 2.20−1.70 ppm (m, 4H), 1.5−0.9 ppm (m, 6H).

ESI-MS: 545 $[M+H]^+$

7.4.2.10: SYNTHESIS OF RHPT2

In a flame-dried, Argon-filled 10 mL Schlenk flask, Pt(dach)(MalBzCOOH) (25 mg) and Rh(phen)(chrysi)(^{NH2}bpy)$^{3+}$ (5 mg) were dissolved in 2 mL DMF. The resultant vessel was purged with $Ar_{(g)}$ for 5 minutes and then stirred for 2 h at room temperature. After 2 h, 0.5 mL DIEA was added, and the resultant reaction mixture was allowed to stir overnight under argon. After 16 h, H_2O (4 mL) was added to the reaction mixture, and the aqueous solution was loaded onto a C18 reverse-phase cartridge (Waters Sep-Pak), washed with water, and eluted with 1:1:0.001 (H_2O:MeCN:TFA). The purified product was frozen and lyophilized to dryness. Each conjugate was further purified via reverse-phase high-performance liquid chromatography using an HP1100 HPLC system, a Varian

DynaMax C18 semipreparative column, and an elution gradient of 85:15 to 40:60 H_2O (0.1% TFA):MeCN (0.1% TFA) over 60 min.

ESI-MS: 674 $[M-H]^{2+}$, 1347 $[M-2H]^{+}$

UV-Vis (H_2O, pH 7.0): λ_{max} 267 nm (ε = 68,000 M^{-1}), 301 nm (ε = 40,000 M^{-1}), 313 nm (ε = 30,400 M^{-1}), 389 nm (ε = 19,400 M^{-1}).

7.4.2.11: PLATINATION PAGE EXPERIMENTS

The platination PAGE experiments with radiolabeled DNA were performed according to the protocols described for recognition and photocleavage experiments in Chapter 2 Section 2.4.4.1. The only difference here is that in many cases, the samples were permitted to incubate for extended periods of time.

7.4.2.12: CELL CULTURE

HCT116N and HCT116O cells were grown in RPMI medium 1640 supplemented with 10% FBS, 2 mM L-glutamine, 0.1 mM nonessential amino acids, 1 mM sodium pyruvate, 100 units/mL penicillin, 100 μg/mL streptomycin, and 400 μg/mL Geneticin (G418). Cells were grown in tissue culture flasks and dishes (Corning Costar) at 37 °C under 5% CO_2 atmosphere.

7.4.2.13: CELLULAR PROLIFERATION ELISA

HCT116N and HCT116O cells were plated in 96-well plates at 2000 cells/well and allowed 24 h to adhere. The cells were then incubated with the metal complexes of interest for 24 h. After 24 h the metal-containing medium was replaced with fresh

medium, and the cells were allowed to grow for 48 more h. Cells were labeled with BrdU 24 h before analysis. The amount of BrdU incorporation was quantified by antibody assay according to established procedures. Cellular proliferation was expressed as the ratio of the amount of BrdU incorporated by the treated cells to that of the untreated cells.

7.4.3: SYNTHESIS OF TESTING OF RH-^{125}I

7.4.3.1: SYNTHESIS OF RH-TYRAMINE

In a flame-dried, Argon-filled 10 mL Schlenk flask tyramine (25 mg) and Rh(phen)(chrysi)(DPA')$^{3+}$ (5 mg) were dissolved in 2 mL DMF. The resultant vessel was purged with $Ar_{(g)}$ for 5 min and then stirred for 2 h at room temperature. After 2 h, 0.5 mL DIEA were added, and the resultant reaction mixture was allowed to stir overnight under argon. After 16 h, H_2O (4 mL) was added to the reaction mixture, and the aqueous solution was loaded onto a C18 reverse-phase cartridge (Waters Sep-Pak), washed with water, and eluted with 1:1:0.001 (H_2O:MeCN:TFA). The purified product was frozen and lyophilized to dryness. Each conjugate was further purified via reverse-phase high-performance liquid chromatography using an HP1100 HPLC system, a Varian DynaMax C18 semipreparative column, and an elution gradient of 85:15 to 40:60 H_2O (0.1% TFA):MeCN (0.1% TFA) over 60 min.

ESI-MS: 478 $[M-H]^{2+}$, 955 $[M-2H]^{+}$

7.4.3.2: HANDLING OF RH-^{125}I

Unless they are < 20 nm away from one's DNA, the Auger electrons emitted by ^{125}I are more or less harmless. The gamma rays and X-rays that the radionuclide also emits during its decay, however, are not. Therefore, considerable care was taken when working with the radiolabeled Rh-^{125}I conjugate. Protective equipment (goggles, lab coat, nitrile gloves, and dosimeters) were worn at all times when handling the molecule. Further, when possible, all manipulations were conducted behind at least ¼″ of protective lead sheets. Needless to say, all ^{125}I waste was sequestered from non-radioactive or ^{32}P waste. Both scintillation counter and Geiger counter surveys were performed rigorously after any experiments to ensure that no contamination had occurred. Finally, my thyroid was surveyed after every experiment by the Environmental Health and Safety Office to check for ^{125}I accumulation.

7.4.3.3: RH-^{125}I DNA CLEAVAGE EXPERIMENTS

5 μL solutions of Rh-^{125}I (60 nM, 1.25 μCi) were combined in 1.5 μL centrifuge tubes with equal volume solutions of 5'-^{32}P-labeled oligonucleotides in a buffer of 40 mM NaCl, 10 mM NaPi, pH 7.1. Three concentrations of DNA were employed: 50 nM, 100 nM, and 150 nM. Four single stranded oligonucleoties were used to create duplexes with central C•G, C•A, or C•C sites. The forward strand DNA sequence was 5'-GAC CAG CTT ATC ATC CCT AGA TTA GCG-3'. The matched complement was 5'-CGC TTA TCT AGG GAT GAT AAG CTG GTC-3', the C•A mismatched complement was 5'-CGC TTA TCT AGG AAT GAT AAG CTG GTC-3', and the C•C mismatched sequence is 5'-CGC TTA TCT AGG CAT GAT AAG CTG GTC-3'. For each type of

duplex, experiments were run with each of the two strands labeled in order to check for double strand breaks.

After preparing the appropriate samples, the tubes were frozen at -80 °C for 7, 14, or 21 days. After incubation, the samples were thawed, diluted with denaturing loading dye, and electrophoresed on 20% denaturing polyacrylamide gels for 60−90 min at 90 W. Images of the gels were obtained via phosphorimagery and quantified using ImageQuant software.

7.5: REFERENCES

1. Zeglis, B. M.; Pierre, V. C.; Barton, J. K. *Chemical Communications* **2007**, 4565−4579.
2. Zeglis, B. M.; Barton, J. K. *Nature Protocols* **2007,** *2* (2), 357−371.
3. Jackson, B. A.; Alekseyev, V. Y.; Barton, J. K. *Biochemistry* **1999,** *38* (15), 4655−4662.
4. Junicke, H.; Hart, J. R.; Kisko, J. L.; Glebov, O.; Kirsch, I. R.; Barton, J. K. *Proceedings of the National Academy of Sciences U. S. A.* **2003,** *100*, 3737−3742.
5. Hart, J. R.; Johnson, M. D.; Barton, J. K. *Proceedings of the National Academy of Sciences of the United States of America* **2004,** *101* (39), 14040−14044.
6. Zeglis, B. M.; Boland, J. A.; Barton, J. K. *Journal of the American Chemical Society* **2008,** *130* (24), 7530−7531.
7. Zeglis, B. M.; Boland, J. A.; Barton, J. K. *Biochemistry* **2009,** *48* (5), 839−849.

8. Hart, J. R.; Glebov, O.; Ernst, R. J.; Kirsch, I. R.; Barton, J. K. *Proceedings of the National Academy of Sciences of the United States of America* **2006,** *103*, 15359−15363.
9. Ernst, R. J.; Song, H.; Barton, J. K. *Journal of the American Chemical Society* **2009,** *131* (6), 2359−2366.
10. Brunner, J.; Barton, J. K. *Biochemistry* **2006,** *45* (40), 12295−12302.
11. Lim, M. H.; Lau, I. H.; Barton, J. K. *Inorganic Chemistry* **2007,** *46*, 9528−9530.
12. Schatzschneider, U.; Barton, J. K. *Journal of the American Chemical Society* **2004,** *126* (28), 8630−8631.
13. Petitjean, A.; Barton, J. K. *Journal of the American Chemical Society* **2004,** *126* (45), 14728−14729.
14. Zeglis, B. M.; Barton, J. K. *Journal of the American Chemical Society* **2006,** *128* (17), 5654−5655.
15. Puckett, C. A.; Barton, J. K. *Journal of the American Chemical Society* **2007,** *129* (1), 46−47.
16. Puckett, C. A.; Barton, J. K. *Biochemistry* **2008,** *47* (45), 11711−11716.
17. Jackson, B. A.; Barton, J. K. *Journal of the American Chemical Society* **1997,** *119* (52), 12986−12987.
18. Jackson, B. A.; Barton, J. K. *Biochemistry* **2000,** *39* (20), 6176−6182.
19. Jackson, B. A.; Henling, L. M.; Barton, J. K. *Inorganic Chemistry* **1999,** *38* (26), 6218−6224.
20. Wong, E.; Giandomenico, C. M. *Chemical Reviews* **1999,** *99* (9), 2451−2466.

21. Rosenberg, B.; Vancamp, L.; Trosko, J. E.; Mansour, V. H. *Nature* **1969,** *222* (5191), 385−&.

22. Ahmad, S.; Isab, A. A.; Ali, S. *Transition Metal Chemistry* **2006,** *31* (8), 1003−1016.

23. Jamieson, E. R.; Lippard, S. J. *Chemical Reviews* **1999,** *99* (9), 2467−2498.

24. Alazard, R.; Germanier, M.; Johnson, N. P. *Mutation Research* **1982,** *93* (2), 327−337.

25. Ciccarelli, R. B.; Solomon, M. J.; Varshavsky, A.; Lippard, S. J. *Biochemistry* **1985,** *24* (26), 7533−7540.

26. Eastman, A. *Biochemistry* **1986,** *25* (13), 3912−3915.

27. Fichtingerschepman, A. M. J.; Vanderveer, J. L.; Denhartog, J. H. J.; Lohman, P. H. M.; Reedijk, J. *Biochemistry* **1985,** *24* (3), 707−713.

28. Pinto, A. L.; Lippard, S. J. *Proceedings of the National Academy of Sciences of the United States of America* **1985,** *82* (14), 4616−4619.

29. Salles, B.; Butour, J. L.; Lesca, C.; Macquet, J. P. *Biochemical and Biophysical Research Communications* **1983,** *112* (2), 555−563.

30. Zhai, X. Q.; Beckmann, H.; Jantzen, H. M.; Essigmann, J. M. *Biochemistry* **1998,** *37* (46), 16307−16315.

31. Pors, K.; Patterson, L. H. *Current Topics in Medicinal Chemistry* **2005,** *5* (12), 1133−1149.

32. Jiricny, J. *Embo Journal* **1998,** *17* (22), 6427−6436.

33. Aebi, S.; KurdiHaidar, B.; Gordon, R.; Cenni, B.; Zheng, H.; Fink, D.; Christen, R. D.; Boland, C. R.; Koi, M.; Fishel, R.; Howell, S. B. *Cancer Research* **1996,** *56* (13), 3087−3090.

34. Fink, D.; Aebi, S.; Howell, S. B. *Clinical Cancer Research* **1998,** *4* (1), 1−6.

35. Fink, D.; Nebel, S.; Aebi, S.; Nehme, A.; Howell, S. B. *International Journal of Oncology* **1997,** *11* (3), 539−542.

36. Fink, D.; Zheng, H.; Nebel, S.; Norris, P. S.; Aebi, S.; Lin, T. P.; Nehme, A.; Christen, R. D.; Haas, M.; MacLeod, C. L.; Howell, S. B. *Cancer Research* **1997,** *57* (10), 1841−1845.

37. Lin, X. J.; Howell, S. B. *Molecular Cancer Therapeutics* **2006,** *5* (5), 1239−1247.

38. Fuertes, M. A.; Alonso, C.; Perez, J. M. *Chemical Reviews* **2003,** *103* (3), 645−662.

39. Hay, R. W.; Miller, S. *Polyhedron* **1998,** *17* (13−14), 2337−2343.

40. Di Francesco, A. M.; Ruggiero, A.; Riccardi, R. *Cellular and Molecular Life Sciences* **2002,** *59* (11), 1914−1927.

41. Gelasco, A.; Lippard, S. J. *Biochemistry* **1998,** *37* (26), 9230−9239.

42. Laurent, J. P.; Morvan, B. *Journal of the Chemical Society−Dalton Transactions* **1993,** (14), 2141−2145.

43. Petitjean, A. A metallointercalator for the delivery and release of platinum based DNA drugs. California Institute of Technology, Pasadena, 2005.

44. Koi, M.; Umar, A.; Chauhan, D. P.; Cherian, S. P.; Carethers, J. M.; Kunkel, T. A.; Boland, C. R. *Cancer Research* **1994,** *54* (16), 4308−4312.

45. Volkert, W. A.; Hoffman, T. J. *Chemical Reviews* **1999,** *99*, 2269−2292.

46. Blower, P. J. *Transition Metal Chemistry* **1998,** *23* (1), 109−112.

47. Hoefnagel, C. A. *Anti−Cancer Drugs* **1991,** *2* (2), 107−132.

48. Larson, S. M. *Current Pharmaceutical Design* **2009,** *15* (9), 950−956.

49. Okarvi, S. M. *Cancer Treatment Reviews* **2008,** *34* (1), 13−26.

50. McDevitt, M. R.; Scheinberg, D. A. *Cell Death and Differentiation* **2002,** *9* (6), 593−594.

51. McDevitt, M. R.; Sgouros, G.; Finn, R. D.; Humm, J. L.; Jurcic, J. G.; Larson, S. M.; Scheinberg, D. A. *European Journal of Nuclear Medicine* **1998,** *25* (9), 1341−1351.

52. McDevitt, M. R.; Ma, D. S.; Lai, L. T.; Simon, J.; Borchardt, P.; Frank, R. K.; Wu, K.; Pellegrini, V.; Curcio, M. J.; Miederer, M.; Bander, N. H.; Scheinberg, D. A. *Science* **2001,** *294* (5546), 1537−1540.

53. Auger, P. *Comptes Rendus Hebdomadaires Des Seances De L Academie Des Sciences* **1928,** *186*, 758−760.

54. Watson, E. C.; Van den Akker, J. A. *Proceedings of the National Academy of Sciences of the United States of America* **1927,** *13*, 659−662.

55. Anderson, C. D. *Physical Review* **1930,** *35* (10), 1139−1145.

56. Buchegger, F.; Perillo−Adamer, F.; Dupertuis, Y. M.; Delaloye, A. B. *European Journal of Nuclear Medicine and Molecular Imaging* **2006,** *33* (11), 1352−1363.

57. O'Donoghue, J. A. *The Journal of Nuclear Medicine* **1996,** *37* (4), 3S−6S.

58. O'Donoghue, J. A.; Wheldon, T. E. *Physics in Medicine and Biology* **1996,** *41* (10), 1973−1992.

59. Cohen−Jonathan, E.; Bernhard, E. J.; McKenna, W. G. *Current Opinion in Chemical Biology* **1999,** *3* (1), 77−83.

60. Simons, J. *Accounts of Chemical Research* **2006,** *39*, 772−779.

61. Andersson, P.; ForssellAronsson, E.; Johanson, V.; Wangberg, B.; Nilsson, O.; Fjalling, M.; Ahlman, H. *Journal of Nuclear Medicine* **1996,** *37* (12), 2002−2006.

62. Yasui, L. S.; Hughes, A.; DeSombre, E. R. *Acta Oncologica* **1996,** *35* (7), 841−847.

63. Karamychev, V. N.; Panyutin, I. G.; Reed, M. W.; Neumann, R. D. *Antisense & Nucleic Acid Drug Development* **1997,** *7* (6), 549−557.

64. Panyutin, I. G.; Neumann, R. D. *Nucleic Acids Research* **1997,** *25* (4), 883−887.

65. Makrigiorgos, G. M.; Kassis, A. I.; Baranowskakortylewicz, J.; McElvany, K. D.; Welch, M. J.; Sastry, K. S. R.; Adelstein, S. J. *Radiation Research* **1989,** *118* (3), 532−544.

66. Howell, R. W.; Kassis, A. I.; Adelstein, S. J.; Rao, D. V.; Wright, H. A.; Hamm, R. N.; Turner, J. E.; Sastry, K. S. R. *Radiation Research* **1994,** *140* (1), 55−62.

67. Haefliger, P.; Agorastos, N.; Renard, A.; Giambonini−Brugnoli, G.; Marty, C.; Alberto, R. *Bioconjugate Chemistry* **2005,** *16* (3), 582−587.

68. Karamychev, V. N.; Reed, M. W.; Neumann, R. D.; Panyutin, I. G. *Acta Oncologica* **2000,** *39* (6), 687−692.

69. Kometani, T.; Watt, D. S.; Ji, T. *Tetrahedron Letters* **1985,** *26* (17), 2043−2046.

CHAPTER 8: CONCLUSIONS

This thesis is a story about metalloinsertion that began before anyone knew that metalloinsertion exists. Without question, the turning point in our laboratory's study of mismatch-specific metal complexes was the elucidation of the structure of $Rh(bpy)_2(chrysi)^{3+}$ bound to a C•A mismatch. The structure was a revelation, teaching us that these complexes bind their target sites not by traditional metallointercalation but by a new binding mode: metalloinsertion. The bulky metal complex binds the DNA from the minor groove, extrudes the mispaired bases, and replaces the ejected bases in the helical π-stack with its own sterically expansive ligand.

The crystal structure answered one of our most enduring and fundamental questions: how do mismatch-specific metal complexes bind their target sites in DNA? Not surprisingly, the answer to this question illuminated explanations for other puzzling issues, including the enantioselectivity of mismatch recognition and the correlation between binding affinity and mismatch destabilization. Yet as so often happens in science, and discovery in general, the answer to one question sprouted many more inquiries. Many of these focused on the generality of the new binding mode. What sort of sterically expansive ligands can metalloinsertors use to bind mismatches? Does metalloinsertion occur at other thermodynamically destabilized DNA defects? How general is the detailed structure of this new binding mode? How can we apply this new understanding of metalloinsertion to the design of useful bifunctional conjugates?

One by one, these are the questions we have tried to answer in this thesis. First, our studies of $Ru(bpy)_2(eilatin)^{2+}$ clearly illustrate that while ligand width is essential to mismatch-specific metalloinsertion, an excess of steric bulk can lead to a loss of site

selectivity. Next, investigations with other thermodynamically destabilized DNA defects reveal that site-specific metalloinsertion is not exclusive to mismatches, extending almost certainly to abasic sites and most probably to single base bulges. Third, two new crystal structures strongly reinforce the generality of metalloinsertion at mismatched sites and support the binding mode as a new paradigm for interactions between metal complexes and DNA. And finally, the development of new bifunctional conjugates, ranging from mismatch-specific fluorophores to mismatch-targeted radiotherapeutics, reflects our aim to apply our understanding of the detailed structure of metalloinsertion to the design and synthesis of clinically useful agents.

In the end, however, it is our sincere hope that the impact of this work will lie not only in the answers it provides but also in the questions it provokes. It is perhaps then appropriate that we conclude with the words of John Muir: "But in every walk with Nature, one receives far more than he seeks."

Muir, J. *Steep Trails*. Houghton Mifflin Company: New York, 1918.